# Probing extreme configurations in binary compact object mergers

Dissertation
zur Erlangung des Doktorgrades
der Naturwissenschaften

vorgelegt beim Fachbereich Physik
der Johann Wolfgang Goethe-Universität
in Frankfurt am Main

von
Samuel David Tootle
aus Muskegon, Michigan, USA

Frankfurt am Main 2022
(D30)

vom Fachbereich Physik der
Johann Wolfgang Goethe-Universität als Dissertation angenommen.

Dekan: Prof. Dr. Roger Erb

Gutachter: Prof. Dr. Luciano Rezzolla
Prof. Dr. Jürgen Schaffner-Bielich

Datum der Disputation: 25. January, 2023

# Acknowledgments

I am very grateful to my supervisor, Prof. Dr. Luciano Rezzolla, for his continued support both academically and personally throughout my time at Goethe. A considerable amount of my understanding of relativity is owed to him and his lectures which have been the foundation for this work.

I would like to thank my second reviewer Prof. Dr. Juergen Schaffner-Bielich for teaching me formally and informally during my time at Goethe by sharing his expertise in neutron stars, equations of state, and gravitational wave theory. Furthermore, I am grateful for his continued feedback on my seminars which have been beneficial to improving my presentations over the past five years.

I would also like to thank Dr. Roman Gold for his continued support throughout my graduate work both academically and professionally.

Furthermore, I would like to thank Dr. Christian Ecker and Marie Cassing for their help in translating parts of my work necessary to submit this thesis.

I would also like to thank Dr. Elias R. Most for his invaluable collaboration and support. I have benefited greatly from his knowledge and experience in theoretical physics and programming - both implicitly and explicitly - without whom I would not have had the opportunity to explore this line of research. All of the evolution results in this work have been made possible by his code development efforts with L. Jens Papenfort such as `FIL`, `Margherita`, and `Antelope`.

I am indebted to L. Jens Papenfort as a mentor, collaborator, and friend throughout my graduate career and from whom my knowledge in programming and theoretical physics has benefited from immensely. Writing `FUKA` together has easily been one of the greatest joys of my professional career. I do not recall a time in my life that I enjoyed the struggle of learning as much as our time together. May there be more coffee and waffle talks to come.

I would like to thank my mentors Kim and Prof. Dr. Claudio Mazzoleni who have been teachers and mentors to me for more than a decade. I am very grateful for their support as I have navigated life in many aspects and for their encouragement when deciding to return to academia.

Finally, I am forever grateful to my wife and partner, Viola, for her continued support and sacrifice as we've navigated life together these past years. I hope you've found this time as interesting as I have. And, to my two boys, who have helped me to realize how much can be accomplished in a day.

# Notation

**Units:** Unless otherwise specified, geometrized units are used throughout this work such that $G = c = k_B = 1$ where $G$ is the gravitational constant, $c$ is the speed of light, and $k_B$ is Boltzmann's constant. Table A.1 provides a convenient chart for converting between dimensionful and dimensionless quantities. Additionally, relevant variables have been defined that will be used throughout this work.

**Index Notation:** Tensor indices denoted by greek characters e.g., $\mu, \nu$, include the range $[0, 3]$ where as latin indices e.g., $i, j$ include only the subset $[1, 3]$.

**Metric Definitions:** In the construction of initial data using the conformally flat approximation, we will regularly reference the flat background metric. Within a cartesian basis the conformal 4-metric, $\tilde{g}_{\mu\nu}$, and purely spatial conformal 3-metric , $\tilde{\gamma}_{ij}$, take the following form

$$\tilde{g}_{\mu\nu} = \begin{pmatrix} -1 & 0 & 0 & 0 \\ 0 & 1 & 0 & 0 \\ 0 & 0 & 1 & 0 \\ 0 & 0 & 0 & 1 \end{pmatrix} \quad , \quad \tilde{\gamma}_{\mu\nu} = \tilde{\gamma}_{ij} = \begin{pmatrix} 1 & 0 & 0 \\ 0 & 1 & 0 \\ 0 & 0 & 1 \end{pmatrix} ,$$

with the 4-gradient defined by

$$\partial_\mu = \frac{\partial}{\partial x^\mu}.$$

For a generic 4-metric, the Christoffel symbols and covariant derivatives are then given by

$$\begin{aligned} \Gamma^\delta_{\mu\nu} &= \frac{1}{2} g^{\delta\lambda} (\partial_\nu g_{\lambda\mu} + \partial_\mu g_{\nu\lambda} - \partial_\lambda g_{\mu\nu}) \,, \\ \nabla_\mu &= \partial_\mu + \Gamma^\delta_{\mu\nu} \,, \\ D_\mu &= \gamma^\nu{}_\mu \nabla_\nu \,, \end{aligned}$$

where the definitions of the covariant derivative assume a torsion free spacetime such that $\Gamma^\delta_{\mu\nu} = \Gamma^\delta_{\nu\mu}$.

# Abbeviations

| | |
|---|---|
| ADM | Arnowitt-Deser-Misner |
| AH | Apparent Horizon |
| BNS | Binary Neutron Star |
| BBH | Binary Black Hole |
| BHNS | Black Hole-Neutron Star binary |
| COM | center-of-mass |
| CRV | constant rotational velocity |
| CTS | Conformal Thin Sandwich |
| EFE | Einstein's Field Equations |
| EOS | Equation of State |
| FUKA | Frankfurt University/KADATH initial data code |
| GRHD | general relativistic hydrodynamics |
| GRMHD | general relativistic magneto–hydrodynamics |
| GW | Gravitational Wave |
| HMNS | hypermassive neutron star |
| ID | Initial Data |
| KADATH | Kadath spectral solver library |
| LORENE | Langage objet pour la relativité numérique spectral library |
| NR | Numerical Relativity |
| PSD | power spectral density |
| PTTC | phase transition triggered collapse |
| QE | quasi-equilibrium |
| TOV | Tolman-Oppenheimer-Volkoff |
| XCTS | eXtended Conformal Thin Sandwich |
| XPN | Xth ($X =$ [3.5th, 4th, 5th]) order post-Newtonian estimate |

# Author Contributions of S.D.Tootle's Thesis

1. **S.D.Tootle**, C. Ecker, K. Topolski, T. Demircik, M. Järvinen, L. Rezzolla, *Quark formation and phenomenology in binary neutron-star mergers using V-QCD* , arxiv:2205.05691, SciPost in review

   S.D.T. formulated and proposed the idea of this work. S.D.T. constructed the initial data and performed all of the numerical simulations. S.D.T. performed the convergence and the gravitational wave analysis. S.D.T. has written multiple parts of the manuscript as well as discussed and modified the remaining sections which have been authored by the co-authors.

2. L. J. Papenfort, E.R. Most, **S.D.Tootle**, L. Rezzolla, *Impact of extreme spins and mass ratios on the post-merger observables of high-mass binary neutron stars* , arxiv:2201.03632, Mon.Not.R.Astron.Soc., in press

   This work was enabled by the `FUKA` initial data codes which S.D.T. is the co–developer of. S.D.T. has contributed in the discussions during the analysis of the simulation data. S.D.T. has constructed plots relating the remnant dimensionless spin as a function of the initial data parameters $q$, $\chi_1$, and the collapse time to a BH, $\tau_c$. The simulations and analysis were performed by L.J.Papenfort and the manuscript was written by S.D.T. and co-authors.

3. **S.D.Tootle**, L. J. Papenfort, E. R. Most, L. Rezzolla, *Quasi-universal behaviour of the threshold mass in unequal-mass, spinning binary neutron-star mergers* , arxiv:2109.00940, **Astrophys. J. Lett.**, 922 L19

   S.D.T. helped formulate the initial idea and plan for such a parameter study. This work was enabled by the `FUKA` initial data codes which S.D.T. is the co-developer of. S.D.T. constructed the initial data and performed all of the numerical simulations. S.D.T. generated all of the manuscript plots. S.D.T. performed the analysis with L.R. resulting in the quasi-universal relation, and wrote a large portion of the manuscript throughout multiple revisions. The co-authors have helped to refine the idea, discuss the results, and author the manuscript.

4. L. J. Papenfort, **S.D.Tootle**, P. Grandclément, E.R. Most, L. Rezzolla, *New public code for initial data of unequal-mass, spinning compact-object binaries* , arxiv:2109.00940, Phys. Rev. D 104, 024057

   This work outlines the theoretical framework and numerical implementation of a suite of numerical solvers to compute initial conditions for single and binary compact objects. We have named the suite `FUKA` which consists of numerical solvers for black holes (BH) and neutron stars(NS) as well as BH–BH, NS–NS and BH–NS binaries of which S.D.T. is a co-developer of since inception.

   Specifically, S.D.T. wrote the interface enabling the use of tabulated and piecewise polytrope equations of state which was later revised by L.J.P. S.D.T. is also the primary developer for the 3D isolated TOV and BH initial data

codes, co-developed the BBH and BNS solvers, and was the primary developer for the BHNS solver.

Furthermore, S.D.T. implemented eccentricity reduction using 3.5PN and iterative means within the initial data construction with insights from L.J.P in addition to contributing to the formulation of the relativistic Euler equations enabling reliable construction of BNS initial data. The published formulation was finalized by L.J.P.

S.D.T. also developed the Configurator parameter file that is used for initial data construction in addition to co–developing the methods used for iterative resolution increase for all of the initial data solvers.

In the manuscript, S.D.T. constructed the initial data and performed all the necessary simulations related to BBHs and BHNSs including the spectral convergence study. S.D.T. performed the analysis related to the inspiral and convergence analysis for the GW150914 test case as well as the BHNS test case. Finally, S.D.T. wrote multiple sections of the manuscript and made modifications to those authored by the listed co–authors in addition to co–developing the presented plots.

5. E. R. Most, L. J. Papenfort, **S.D.Tootle**, L. Rezzolla, *On accretion disks formed in MHD simulations of black hole-neutron star mergers with accurate microphysics* , arxiv:2106.06391, Mon.Not.R.Astron.Soc., in press

   S.D.T. contributed to the discussions during the analysis of the BHNS simulations. S.D.T. made edits and provided comments throughout the text.

6. E. R. Most, L. J. Papenfort, **S.D.Tootle**, L. Rezzolla, *Fast Ejecta as a Potential Way to Distinguish Black Holes from Neutron Stars in High-mass Gravitational-wave Events* , arXiv:2012.03896, Astrophys. J, in press

   This work was enabled by the FUKA initial data codes which S.D.T. is the co–developer of. S.D.T. generated initial data for a subset of the BHB$\Lambda\Phi$ simulations. S.D.T. contributed to the discussions during the analysis of the BHNS simulations. S.D.T. made edits and provided comments throughout the manuscript.

# Copyright material

# Zusammenfassung


### Motivation

Seit der ersten erfolgreichen numerischen Zeitentwicklung eines schwarzen Loch Binärensystems [1], eines binären Neutronensternsystems (BNS) und gemischter Binärsysteme, die aus einem Neutronenstern und einem schwarzen Loch, bestehen (SLNS) hat die Erforschung von Kollisionen kompakter Objekte mit Methoden der numerischern Relativitätstheorie ein enormes Wachstum erfahren (vgl. [2]–[4]).Mit diesen Erfolgen kommen Fragen bezüglich der Dynamik nach der Verschmelzung, den Signaturen von Gravitationswellen (GW) und der resultierenden elektromagnetischen Signale auf. Die Multi–Messenger Detektion von GW170817[5] hat verdeutlicht, dass der Einfluss der Zustandsgleichung von Dichter Kernmaterie berücksichtigt werden muss, um dieses Ereignis zu erklären und auch die Frage, wie solche Ereignisse die Zustandsgleichung einschränken können. Spätere Ereignisse wie GW190425[6] haben die Wahrscheinlichkeit für ein Doppelsystem aus einem schwarzen Loch und einem Neutronenstern in Frage gestellt, bei dem die Masse des schwarzen Loches ähnlich der maximallen Masse eines Neutronensterns ist, da solche Fusionsszenarien in derzeitigen theoretischen Modellen nur schwer zu erklären sind (vgl. [7], [8]).

In dieser Arbeit untersuchen wir zum ersten Mal den Einfluss der Massenasymmetrie und des Spins auf die (Post–)Fusionsdynamik bei binären Neutronenstern–Simulationen, das heißt die Schwellenmasse, die einen Kollaps zu einem schwarzen Loch auslöst und den kritischen Bereich des Überlapps zwischen binären Systemen aus zwei Neutronensternen (BNS) und binären Systemen aus einem schwarzen Loch und einem Neutronenstern (SLNS). Darüber hinaus untersuchen wir auf welche Weise Ereignisse wie GW170817 Zustandsgleichungen für dichte Kern– und Quarkmaterie, welche mit Ergebnissen aus Kerntheorie und störungtheoretischer Quantenchromodynamik (QCD) übereinstimmen, weiter einschränken können. Für die Untersuchung sind jedoch geeignete Anfangsbedingungen erforderlich. Zu diesem Zweck haben wir den öffentlich verfügbaren Code `FUKA` entwickelt, welcher als erster öffentlicher Code in der Lage ist, verlässliche Anfangsbedingungen für hochgradig asymmetrische und schnell rotierende gemischte Binärsysteme, die aus einem Neutronenstern und ein schwarzen Loch bestehen, zu erzeugen.

### Das Anfangswertproblem in Allgemeiner Relativitätstheorie und Hydrodynamik

Die numerische Simulation kompakter Binärsysteme stellte jahrzehntelang ein ungelöstes Problem in Einsteins Allgemeiner Relativitätstheorie dar. Die Methode, die die Untersuchung binärer kompakter Objekte ermöglicht hat, zerlegt die vierdimensionale Rauzeit in dreidimensionale räumliche Hyperflächen $\Sigma_t$ die mit der Zeitkoordinate $t$ parametrisiert werden [10], [11]. Mit dieser Zerlegung lassen sich die Einstein'schen Feldgleichungen zu einem gekoppelten System elliptischer partieller Differentialgleichungen umformen, die für das Anfangswertproblem auf einer der räumlichen Hyperfläche $\Sigma_t$ gelöst werden müssen

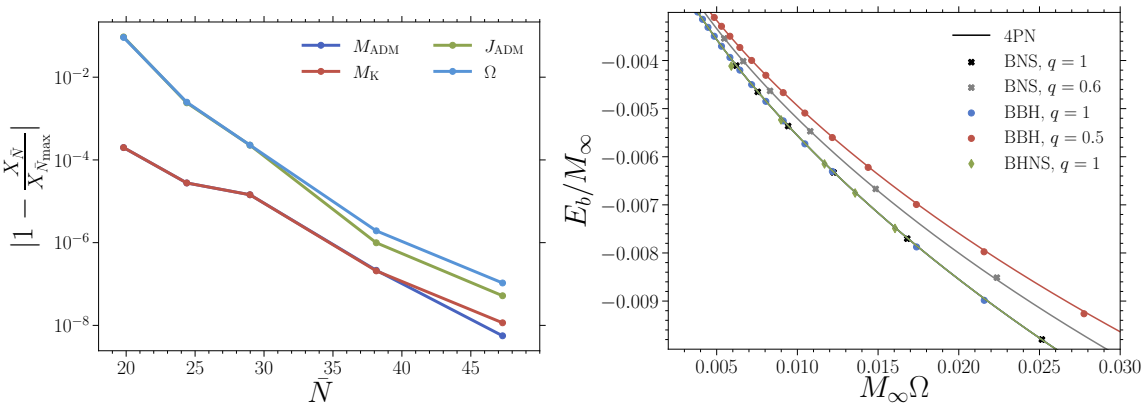


Abbildung 1: *Links:* Konvergenzanalyse für ein BSL–System mit gleicher Masse. Dargestellt ist die absolute relative Differenz für eine gegebene Größe $X$ in Abhängigkeit von der Auflösung $\bar{N}$ (siehe Gl. (2.82)). Hier ist $X$ die Umlaufgeschwindigkeit $\Omega$, die ADM–Masse $M_{\mathrm{ADM}}$, der ADM–Drehimpuls $J_{\mathrm{ADM}}$ und die Komar–Masse $M_{\mathrm{K}}$, die unter der Annahme eines Quasi–Gleichgewichts berechnet wurden. Die relative Differenz dieser Größen bei einer bestimmten Auflösung wird mit dem Datensatz mit der höchsten Auflösung von $\bar{N}_{\max} = 52$ verglichen. *Rechts:* Vergleich der dimensionslosen Bindungsenergie als Funktion der dimensionslosen Orbitalgeschwindigkeit von Quasi–Gleichgewichtssequenzen von BSL– (Kreise), BNS– (Quadrate) und SLNS– (Rauten) Datensätzen gleicher Masse sowie von asymmetrischen BSL–($q = 0.5$) und BNS–($q = 0.6$) Datensätzen zu 4PN–Vorhersagen, die durch Gl. (B.5) gegeben sind (durchgezogene Linien). Diese Grafik wurde aus [9] wiederverwendet.

(vgl. [12]–[16]). Der öffentlich zugängliche Code `LORENE` [17] ist seit über zwanzig Jahren von der physikalischen Gemeinschaft benutzt um das Anfangswertproblem für kompakte binäre systeme zu lösen. Die zuverlässige Konstruktion asymmetrischer binärer Anfangsdaten mit ungleichen Spins ist jedoch sehr begrenzt mit diesen Code und hat das Studium eines großen Teils des verfügbaren Parameterraums nicht ermöglicht.

In Kapitel 2 untersuchen wir das Anfangswertproblem für BSL–, BNS– und SLNS–Systeme und beschreiben die öffentliche Codekollektion `FUKA`[1], der auf der Spektralbibliothek `KADATH`[18] basiert. Um Anfangsbedingungen zu erzeugen, löst `FUKA` die XCTS–Formulierung[16] der Einstein Gleichungen in einem mitrotierenden Koordinatensystem, unter Verwendung einer flocken Hintergrundmetrik und der maximalen Schnittbedingungen. An der asymptotischen Grenze legen wir die Randbedingungen so fest, dass die Raumzeit wiederhergestellt wird. Für schwarze Löcher verwenden wir Randbedingungen bei denen [19], das innere des schwarzen Loches heraus geschnitten wird und der Rand ein scheinbarer Horizont ist, der durch eine *Marginally Outer Trapped Surface* definiert ist. Darüber hinaus ist `FUKA` in der Lage, Anfangsbedingungen für Neutronensterne unter Verwendung einer (stückweise) polytropen oder 1D–tabellierten Zustandsgleichung zu erzeugen.

In Abschnitt 2.7 analysieren wir die Selbstkonsistenz der mit `FUKA` erzeugten Anfangsdaten. Da `KADATH` die Spektralmethode verwendet, erwarten wir eine exponentielle Konvergenz der Lösung in Abhängigkeit von der Anzahl der numerischen Gitterpunkte.

In Abb. 1 (links) zeigen wir ein Beispiel für Quasi–Gleichgewichts–BSL–Anfangsdaten, bei denen eine solche exponentielle Konvergenz gezeigt wird.

[1] https://bitbucket.org/fukaws/

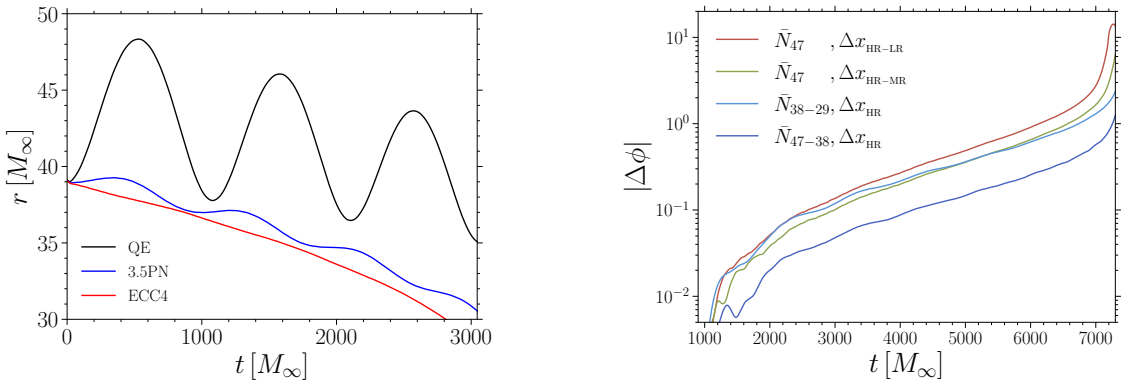


Abbildung 2: *Links:* Beispiel für die gemessene Exzentrizität der Anfangsdaten eines asymmetrischen, sich schnell drehenden BNS–Systems im Quasi–Gleichgewicht (schwarz), unter Verwendung von 3,5PN Schätzungen (blau) und nach Anwendung der iterativen Exzentrizitätsreduktion (rot). Die verwendete binäre Konfiguration ist $M_\infty = 2,7$, $q = 0.6875$, $\chi_1 = 0$ und $\chi_2 = 0.6$, wobei das Fluid mit der `TNTYST` Zustandsgleichung modelliert wird. *Rechts:* Analyse der Evolutionskonvergenz von einem nicht rotierenden BNS–System mit gleicher Masse, dessen Fluid mit der `SLy` Zustandsgleichung modelliert wurde. Die roten und grünen Sequenzen wurden für eine fixe Anfangsdaten–Auflösung ($\bar{N} = 47$) berechnet und vergleichen den Einfluss der Evolutionsauflösung. Die blauen Linien entsprechen einer fixierten Evolutionsauflösung von $\Delta x_{\rm HR}$, so dass die Auswirkungen von den Anfangsdaten zu sehen sind. Diese Grafik wurde aus [9] übernommen.

Dabei vergleichen wir die ADM–Masse (Gesamtenergie in $\Sigma_{t=0}$), die Komar–Masse (gesamte erhaltene Masse in $\Sigma_{t=0}$), den ADM–Spin–Drehimpuls (gesamter Spin–Drehimpulses in $\Sigma_t$ und die Orbitalgeschwindigkeit $\Omega$, mit unterschiedlicher Auflösung $\bar{N}$. Darüber hinaus zeigen wir in Abb. 1 (rechts) Quasi–Gleichgewichtssequenzen von BSL–, BNS– und SLNS–Konfigurationen mit unterschiedlichen Abstanden und Massenverhältnissen $q$, und vergleichen sie mit post–Newtonschen Schätzungen der Bindungsenergie 4. Ordnung. Insgesamt finden wir eine ausgezeichnete Übereinstimmung zwischen unseren numerische Ergebnissen und der post–Newtonschen Annährung.

In Abschnitt 2.8 benutzen wir die mit `FUKA` erzeugten Anfangsdaten um die Zeitentwicklung von kompakten Binärsysteme zu studieren. Konkret analysieren wir die Exzentrizität wärend des Inspirals mit Anfangsdaten unter Quasi–Gleichgewichtsannahmen (QG), post–Newtonschen Korrekturen der Ordnung (3,5PN) sowie iterativen Verfahren zur Reduzierung der Exzentrizität (`ECC4`). In allen untersuchten Konfigurationen stellten wir fest, dass 3.5PN im Vergleich zu den QG–Ausgangsdaten eine deutlich weniger exzentrische Spiralbewegung liefert. Die iterative Exzentrizitätsreduktion verringert diese weiter bis zu $\lesssim 10^{-4}$, wie im linken Feld von Abb. 2 zu sehen ist.

Darüber hinaus haben wir den Einfluss der Auflösung der Anfangsbedingung und der Evolutionsauflösung sowohl für BSL– als auch für BNS–Konfigurationen quantifiziert. Im Fall eines BSL–Systems finden wir, dass die Evolutionsauflösung die dominante Fehlerquelle bei der Messung der absoluten Phasendifferenz ($\phi$) für den $\ell = m = 2$–Multipol der gravitativen Wellenform ist. Dabei könne Unterschiede in der Evolutionsauflösung zu einem Wert von $|\Delta\phi| > 1$ führen. Beim Vergleich unterschiedlicher Auflösung der Anfangsdaten mit der höchsten studierten Evolutionsauflösung stellen wir fest, dass $|\Delta\phi| < 0.1$ ist. Wir stellen ähnliches Verhalten bei nicht rotierenden BNS–Konfiguration mit gleicher Masse

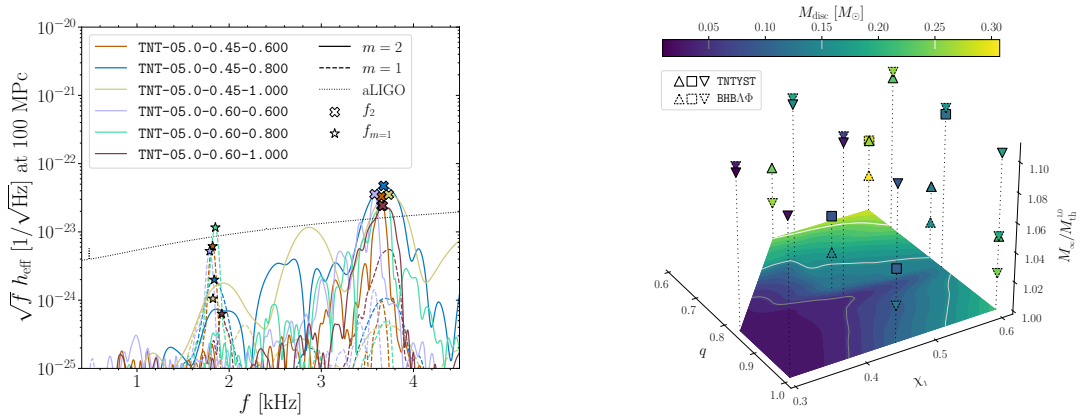


Abbildung 3: *Links:* Die spektrale Leistungsdichte (PSD) der $(\ell, m) \in \{(2,1), (2,2)\}$ Moden des Gravitationswellensignals für die TNTYST Zustandsgleichung. Außerdem zeigen wir die dominanten PSD–Frequenzen $f_{m=1} := \max[\mathrm{PSD}(\ell = 2, m = 1)]$ und $f_2 := \max[\mathrm{PSD}(\ell = 2, m = 2)]$ zusammen mit den aLIGO–Sensitivitätskurve. *Rechts:* Die Massenkritikalität $M_\infty/M_{\rm th}^{1,0}$ ist als Funktion das Massenverhältnisses $q$ und des dimensionslosen Spins $\chi_1$ des schwereren Sternes dagestellt, wobei sich die Farbkodierung auf die Masse, die um den zentrelen Stern rotiert, bezieht. Diese Masse wird gemittelt und auf eine 2D–Ebene projiziert, wodurch die entsprechende kubische Spline–interpolierte Konturdarstellung entsteht, die das stark nichtlineare Verhalten hervorhebt. Diese Grafik wurde aus [20] entnommen.

fest, wie in Abb. 2 (rechts) gezeigt wird. Dabei finden wir, dass der gemessene Wert $|\Delta\phi|$ um etwa eine Größenordnung höher ist als bei der BSL–Konfiguration. Das ist wahrscheinlich darauf zurückzuführen, dass unsere BNS–Konfiguration mit einer Entwicklung 4. Ordnung, wohingegen die BSL–Konstellation mit einer Entwicklung 8. Ordnung beschreiben wird.

**Auswirkungen extremer Spins und Massenverhältnisse auf die Beobachtungen nach der Verschmelzung massereicher Neutronensternbinärsysteme**

Ein wichtiger Aspekt bei der Untersuchung von BNS–Systemen ist eine detaillierte Analyse Dynamik während und nach der Verschmelzung der Sterne. Eine Reihe von Arbeiten mit Focus auf die Dynamik von asymmetrischen und nicht rotierenden BNS–Systemen sind jedoch auf Massenverhältnisse $0.7 \lesssim q \leq 1$ beschränkt [siehe z.B. [21]–[30]]. Es gibt doch nur wenige Studien mit kleineren Massenverhältnissen, z. B. $q \approx 0.5$, unter Verwendung einer polytropen Zustandsgleichung durchgeführt [siehe z.B. [25], [27], [31], [32]] und vor Kurtzem eine Studie mit einer neuartigen tabularisierten Zustandsgleichung die den Phasenübergang von dichter Kernmaterie zu Quarkmaterie beschreibt [33]. Zu den wichtigsten Hauptmerkmalen asymmetrischer binärer Systeme zaehlen die Störung des sekundären Objekts durch Gezeitenkräfte, zu die höre Masse im Materietorus um das zentrale Objekt und die Zunahme der dynamisch ausgeschtoßenen Masse [22], [34].

Parallel dazu wurden auch Studien durchgeführt, um den Einfluss des Spins auf die Kollisionsdynamik zu untersuchen [8], [35]–[40]. Der dominante Effekt den dabei ein zusätzlicher Spin–Drehimpuls hat ist eine veraenderte Lebensdauer das Kollisionsproduktes, sowie dessen Spin der bis zu $\chi \sim 0.89$ [35]–[37], [39] betragen kann. Es wurde jedoch gezeigt, dass der Einfluss des Spin auf die Lebensdauer hypermassiver Neutronensterne im Vergleich zum Einfluss der Mas-

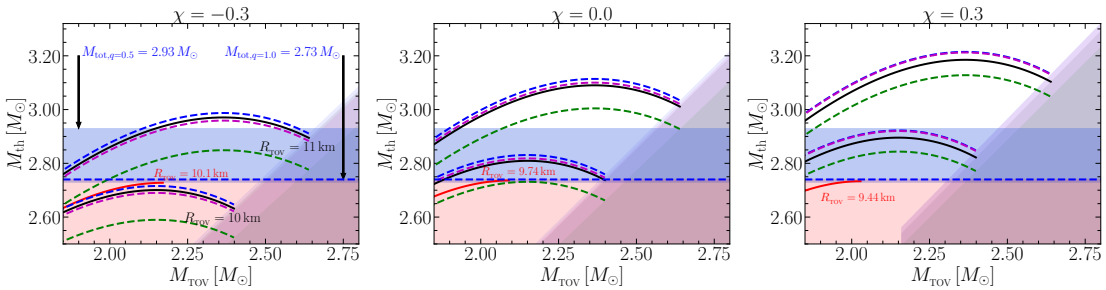


Abbildung 4: Die Säulen in dieser Grafik beziehen sich jeweils auf einen fixierten Spin $\chi \in \{-0.3, 0, 0.3\}$. Wir zeigen die Einschränkungen für die untere Grenze der zulässigen TOV–Radien, indem wir die Schwellenmasse unter Verwendung von Gl. (4.7) entlang von Linien mit konstantem $R_{\rm TOV} \in \{10, 11\}\,{\rm km}$ für jedes Massenverhältnis berechnen. Der horizontale blau schattierte Bereich entspricht dem von GW170817 festgelegten Bereich unter der Annahme von $q \in \{0.5, 0.7, 0.9, 1\}$. Der rot schraffierte Bereich umfasst die EOS, die unter der Annahme ausgeschlossen sind, dass die von GW170817 festgelegte Untergrenze für $q = 1$ gilt, während die grauen Bereiche durch Kausalität ausgeschlossen sind. Diese Grafik wurde aus [41] entnommen.

senasymmetrie gering ist[38]. Eine neuere Arbeit, in der schnell rotierende BNS–Systeme mit $q = 1$ untersucht wurden, in dennen der Spin mit der Richtung der orbitalen Rotationsachse uebereinstimmt, ziegt eine Unterdrückung der dynamischen ausgestoßenen Materie für gleichgerichtete Spins[40].

In Kapitel 3 untersuchen wir erstmals den Einfluss extremer Spins für BNS–Systeme mit Massenasymmetrie $q \in [0.6, 1.0]$ und Gesamtmasse $M_\infty \in [1.025, 1.105] M_{\rm th}^{1,0}$, wobei $M_{\rm th}^{1,0}$ die Schwellenmasse für ein massengleiches irrotierendes System. In Abb. 3 identifizieren wir einen nichtlinearen Zusammenhang zwischen der Massenasymetrie und dem Spin und dessen Auswirkung auf die dynamisch emittierte Masse und die gebundene Masse rund um das zentrale Objekt. Die höchste gemessene emittierte Masse für $q = 1$ finden wir bei maximalen Spin, die minimale emittierete Masse $q \approx 0.8$, jedoch höhere Masse bei $q = 0.6$. Im Gegensatz dazu stellen wir fest, dass die Meiste gebundene Masse rund um das zentrale Objekt bei der höchsten Massenasymmetrie von $q = 0.6$ auftritt, gefolgt von $q = 1$, wobei wiederum den minimale Wert für $q \approx 0.8$ finden (siehe Abb. 3, rechts). Im Gegensatz dazu finden wir in Abb. 3 (links), dass die auffälligste Gravitationswellensignatur für $q = 0.8$ auftritt. Schließlich stellen wir fest, dass der effektive Restspin nach der Kollision zu einem Anstieg der maximalen Leuchtkraft um bis zu einem Faktor 5 führen kann und bis zu einem Tag verzögert ist.

**Quasi–universelles Verhalten der Schwellenmasse bei der Verschmelzung von Neutronensternen mit ungleicher Masse und Spin**

In Kapitel 4 untersuchen wir die BNS–Konfigurationen mit $q \in \{0.5, 0.7, 0.9, 1\}$ und $\chi \in \{-0.3, 0, 0.3\}$, um die Schwellenmasse für den prompten Kollaps unter Verwendung von drei rein hadronischen Zustandsgleichungen (bei endlichen Temperaturen) zu quantizieren. Aus unserer Analyse schließen wir, dass eine quasi–universelle Beziehung, die unabhängig von den untersuchten Zustandsgleichungen ist, existiert. Diese enthält als Spezialfall die universelle Beziehung für die Schwellenmasse massengleicher Systeme aus [42]. In Abb. 4 zeigen wir, dass langlebige Binärsysteme die massiv sind und eine starke Antiorientierung der Spins haben, die stärksten Einschränkungen für die Zustandsgleichung lie-

fern. ´Ahnliche Ergebnisse wurden auch in früheren Arbeiten [43], [44] gezeigt.

**Schnelle Emission als mögliches Unterscheidungsmerkmal von Kollisionen gemischten Systemen und Neutronensternensystemen bei hoher Masse**

Innerhalb eines kritischen Bereichs der Gesamtmasse der Asymmetrie und der Spinparameter können binäre Konfigurationen existieren, bei denen es schwierig zu erkennen ist, ob das primäre (massereichere) Objekt ein massiver Neutronenstern oder ein kleines Schwarzes Loch ist (z.B. GW190418). Frühere Studien haben gezeigt, dass ein wichtiger Unterschied in den Massenströmen bei SLNS–Systemen und BNS–Systemen existiert. Der Matteriefluss in einem SLNS–System ist auf die Gezeitenkraefte des sekundären Objektes zurückzuführen [45]–[48]. Im Vergleich dazu erfolgt in BNS–Systemen zusätzlich zu dem (meta–)stabilen Überrest ein Massenauswurf durch die Schockwellen die bei der Kollision entstehen [49]–[53]. Am auffälligsten ist im Fall eines binären Neutronenstern–Systems die Produktion einer blauen Kilonova, die größtenteils auf die Schockerwärmung an der Kollisionsoberfläche der beiden Neutronensterne zurückgeführt werden kann [54], [55]. Dieses Merkmal ist einzigartig für BNS–Systeme, wobei eine rote Kilonova, die für die langfristigen Massenemissionen aus der Akkretionsscheibe charakteristisch ist [56]–[59], auch bei SLNS-Systemen auftritt.

In Kapitel 5 erforschen wir den kritischen Bereich, in dem sich BNS– und SLNS–Bedingungen natürlich überschneiden. Innerhalb dieses Bereichs verwenden wir numerische Simulationen, um den Einfluss der Massenasymmetrie $q \in [0.486, 0.714]$ und des Spins $\chi_1 \in [0.00, 0.52]$ auf charakteristische Merkmale der SLNS– und BNS–Kollisionen zu berechnen. Insbesondere untersuchen wir die Masse und Zusammensetzung der emittierten Materie in jeder Konfiguration für zwei hardonische Zustandsgleichungen ,wobei wir uns auf Merkmale konzentrieren, die für zukünftige Multi–Messenger–Detektionen von Bedeutung sein könnten. Wir stellen fest, dass ein charakteristisches Merkmal von BNS–Kollisionen die Bildung eines zusätzlichen Emissionsschweifs ist, der durch die Kollision der beiden Neutronensterne entsteht und durch den Materie mit Geschwindigkeiten bis zu $v \sim 0.8c$ ausgeworfen wird. Bei Konfigurationen mit einem rotierenden primären Objekt wird der schnelle Emissionsschweif jedoch zunehmend unterdrückt und schwer von einem SLNS–Ereignis zu unterscheiden.

**Quarkbildung und Phänomenologie bei der Kollision von Neutronensternen mit dem V–QCD Modell**

Die Berechnung der Zustandsgleichung von dichter Kernmaterie ist nach wie vor ein ungelöstes Problem der theoretischen Physik. Kollisionen von BNS–Systemen geben einzigartige Einblicke in das Verhalten von Materie bei hoher Dichte und Temperatur. Die numerische Erforschung dieser Systeme war jedoch bis vor Kurzem auf rein hadronische Zustandsgleichungen oder polytrope Zustandsgleichungen in denen der Übergäng zu Quarkmaterie und die Temperaturabhängigkeit stark vereinfacht beschreiben wird (vgl. [63]).

In Kapitel 6 untersuchen wir erstmals ein neuartiges Modell für die Zustandsgleichung auf der Grundlage von V–QCD, welches einen physikalisch motivierten Rahmen für die thermodynamisch konsistente Beschreibung von Kernmate-

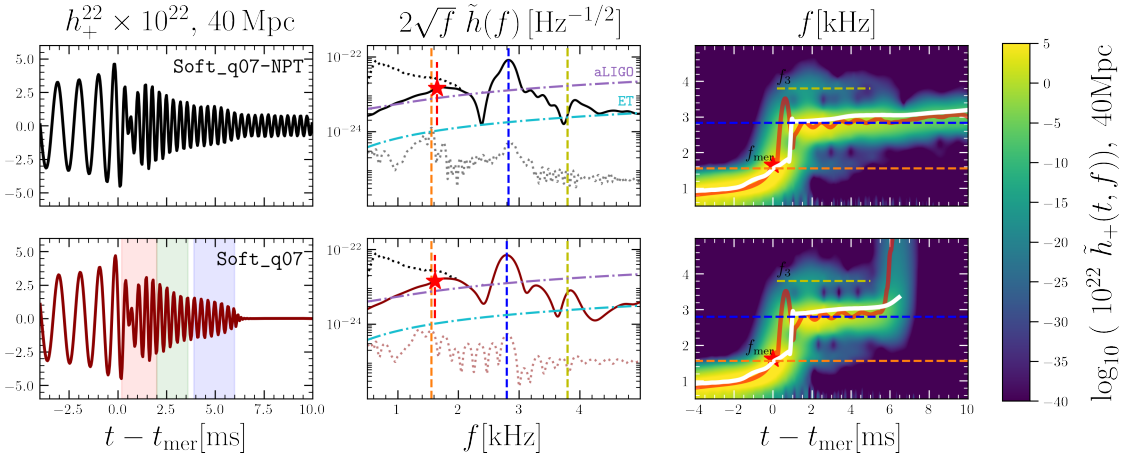


Abbildung 5: *Left:* Die +–Polarisation der $\ell = m = 2$ Mode der Gravitationswellenbelastung. *Mitte:* Die aus Gl. (6.5) berechnete Leistungsspektraldichte $(\ell, m) = (2,1), (2,2)$. Hier zeigt die dunkel gepunktete Linie den Beitrag der Spiralbewegung nur für $(\ell, m) = (2,2)$. Eingeschlossen sind die Empfindlichkeitskurven, die sich auf die derzeitige Empfindlichkeit des aLIGO und des Einstein Teleskops [60], [61] beziehen. *Rechts:* Das Spektrogramm von $h_+^{2,2}$, wobei die weiße Kurve den Betrag des Spektrogramms als Funktion der Zeit zeigt. Hinweis: In den beiden rechten Spalten entsprechen die orangefarbenen und blauen gestrichelten Linien den Spitzenfrequenzen $f^{2,1}$ und $f^{2,2}$ für $(\ell, m) = (2,1), (2,2)$, während die gestrichelte gelbe Linie der aus dem Spektrogramm gemessenen Frequenz $f_3$ entspricht. Der rote Stern bezeichnet die Fusionsfrequenz $f_{\mathrm{mer}}$. Diese Grafik wurde aus [62] entnommen.

rie von niedriger Dichte bis hin zu extrem hohen Dichten bietet. Auserdem kann dieses Modell Vorhersagen für den Phasenübergang von dichte Kernmaterie zu dichte Quarkmaterie machen die mit Ergebnisse der pertubativen QCD konsistent sind. Eine natürliche Folge dieses hybriden Modells ist das Auftreten eines kritischen Punktes bei hoher Temperatur und endlicher Dichte im Phasendiagramm. Neutronensternensimulationen mit dem V–QCD Modell können dabei helfen Erkenntnisse über die Lage des kritischen Punktes im QCD Phasendiagramm zu erlangen.

Wir studieren drei verschiedene Zustandsgleichungen auf der Grundlage des hybriden Modells mit unterschiedlichen Steifigkeiten. Diese Modelle sind in Übereinstimmung mit aktuellen Massen– und Radiusmessungen von Pulsarbeobachtungen und den Gravitationswellenmessungen von GW170817. Diese Modelle wurden verwendet, um numerische Simulationen von BNS–Kollisionen durchzuführen, die mit den gemessene Parametern von GW170817 übereinstimmen. Dabei gehen wir der Frage nach, ob Quarks während der Verschmelzung der beiden Neutronensterne gebildet werden und ob die Lebensdauer des HMNS–Überrests mit der $\sim$ 1s Lebensdauer von GW170817 übereinstimmt. In unserer Analyse identifizieren wir drei Zeitbereiche nach der Kollision mit in denen heiße Quarks, warme Quarks, und kalte Quarks gebildet werden. Besonderes interessant ist die weiche Zustandsgleichung, die bei beiden betrachteten Massenverhältnissen innerhalb von $t_{\mathrm{BH}} < 12\mathrm{ms}$ zur Formation eines schwarzen Loches führt. In Abb. 3 zeigen wir das Gravitationswellensignal, die spektrale Leistungsdichte und das Spektrogramm für die weiche Zustandsgleichung, mit und ohne Übergang zur Quarkmaterie, für die $q = 0.7$ Konfiguration. Außerdem finden wir, dass der Kollaps zu einem Schwarzen Loch auf den Phasenübergang zu Quarkmaterie im kalten und dichten Kern des

Neutronensterns zurückzuführen ist. Darüber hinaus ist der frühe Kollaps zu einem Schwarzen Loch die einzige nennenswerte Auswirkung auf das Gravitationswellenspektrum. Daher werden zukünftige Detektoren, die in der Lage sind das Gravitationswellensignal nach der Kollision zu messen, besonderes wichtig um den Zeitpunkt des Kollapses zu einem Schwarzen Loch festzustellen und da mit etwas über Quarkmaterie in Neutronensternen zu lehrnen.

**Künftige Arbeit**

Die Ergebnisse dieser Arbeit können auf meherer weissen mit zukünftiger Forschung erweitert werden. Im Bereich der Konstruktion von Anfangsdaten könnten die aktuellen Codes in `FUKA` mit Alternativen zur klassischen Relativitätstheorie wie Skalar–/Tensortheorien erweitert werden. Darüber hinaus besteht ein erhebliches Interesse an binären Bosonensternsystemen, die zur Zeit hauptsächlich mit stark vereinfachten Methoden für die Anfangsdatenkonstruktion [64] beschrieben werden. Außerdem könnten Anfangsdaten für Systeme mit extrem schnell rotierenden Schwarzen Löchern mit $\chi \approx 0.99$ implementiert werden.

In Kapitel 3 und Kapitel 5 untersuchen wir Binärsysteme mit kritischer Masse oberhalb der Schwellenmasse mit extremen Spins und kleinen Massenverhältnissen, wobei wir uns auf zwei rein hadronische Zustandsgleichungen beschränken. Eine genauere Untersuchung des Parameterraums für $q$, $\chi$, die Gesamtmasse des Doppelsterns $M_\infty$, und die Zustandsgleichung wäre wertvoll, um die Beziehung zwischen diesen Parametern und der resultierenden Masse um das zentrale Objekt, der dynamischen emittiereten Materie und der Zusammensetzung der Materie zu charakterisieren. Außerdem wäre es interessant Systeme in denen schnell emittierete Materie ($v > 0.6$) gefunden wird genauer zu untersuchen.

In Kapitel 4 haben wir einen erster Blick auf die Schwelle zum prompten Kollaps als Funktion von der Zustandsgleichung, $q$ und $\chi$ geworfen. Seit der ursprünglichen Veröffentlichung wurden mehrere ähnliche Arbeiten veröffentlicht (siehe [65], [66]), die den Parameterraum von $q$ und den Einfluss der Zustandsgleichung gründlich untersucht haben. Daher wäre es wichtig, eine Folgearbeit durchzuführen, die den Spinparameterraum gründlicher untersucht, um eine zuverlässigere Aussage über die in dieser Arbeit diskutierte quasi–universelle Beziehung zu erhalten.

Schließlich wurden in Kapitel 6 die ersten BNS–Simulationen mit einer Zustandsgleichung mit voller Temperaturabhängigkeit und einer Beschreibung der Quark–Materie auf der Grundlage des V–QCD Modells vorgestellt. Zunächst wird es wichtig sein, unsere numerischen Codes so anzupassen, dass sie die Berechnung des Quarkanteils im gesamten numerischen Bereich während der Entwicklung ermöglichen und somit eine genaue 3D–Nachbearbeitung erlauben. Darüber hinaus könnten wir die in den Kapiteln 3–5 durchgeführten Studien ausweiten und die Zustandsgleichungen einbeziehen, die mit dem hybriden V–QCD Modell erzeugt wurden. Das würde uns ermöglichen die Auswirkungen auf die resultierenden Gravitationswellenspektren, die Zusammensetzung der emittierten Materie und das Kollapsverhalten zu ermitteln.

# Contents

# List of Figures

# List of Tables

# Chapter 1

# Introduction

The study of compact object binary mergers using numerical relativity is an exciting field that has experienced incredible growth since the first stable evolution of a binary black hole (BBH)[1], neutron star binaries (BNS) and black hole-neutron star binaries (BHNS) (cf. [2]–[4]). With these successes many questions have been raised with regards to the (post-)merger dynamics, gravitational wave signature, and the resulting electro-magnetic counterpart. The multi-messenger detection of GW170817[5] has highlighted the need to broadened these questions to include the influence of the equation of state (EOS) of nuclear matter in order to explain this event as well as how such events can put constraints on the EOS. Furthermore, later events such as GW190425[6] have brought into question the likelihood of a BHNS binary where the BH has a mass of the order of the maximum irrotational mass $M_{\rm TOV}$ of a neutron star as such formation channels are challenging to explain within current theoretical models (cf. [7], [8]).

Within this introduction we will outline a few key areas of research using numerical relativity that have been explored in this work. Specifically, the exploration of the influence mass asymmetry and spin have on (post-)merger dynamics for BNS simulations, the threshold mass to prompt collapse to a BH, the critical regime of overlap between BNS and BHNS binaries, and the impact multi-messenger observations can have on constraining the EOS. However, for such exploration constraint satisfying initial conditions are required. To that end, a discussion of the initial value problem of numerical relativity will be described as well how we address this in our work.

## 1.1 Initial value problem

Solutions to Einstein's field equations (EFE) for dynamical spacetimes has continued to be a challenging problem for decades. To study binary coalescence and merger the solution to this problem has been the splitting of the 4D spacetime manifold using a 3+1 decomposition such that one obtains purely spatial hypersurfaces $\Sigma_t$ parameterized by a time coordinate $t$. From this splitting, Einstein's field equations can be recast into a coupled system of elliptic partial differential constraint equations that are solved on the initial spatial hypersurface $\Sigma_{t=0}$. The dynamics are then governed by a set of hyperbolic evolution equations (cf. [67]–[70]).

In the case of publicly available initial data for binary objects, only a few options exist. First is the `TwoPuncture` code [71] which has been an asset to the

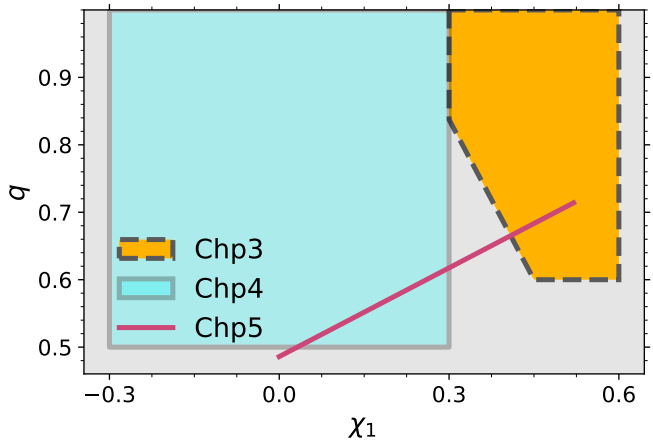


Figure 1.1: Within this work we explore a large portion of the available space of mass ratio $q$ and spin $\chi_1$ for binary neutron star and select black-hole neutron star binaries. Here the mass ratio $q \leq 1$ and the dimensionless spin of the primary (more massive object) $\chi_1 \in [-1, 1]$. The legend refers to the chapter that explores the highlighted region.

community for studying asymmetric spinning BBHs since its development. Secondly, the publicly available `LORENE` spectral solver [17] has been the leading code available for the study of isolated and binary compact objects with community support for over twenty years. Third and more recently, the announcement of the `Elliptica` code for BHNS initial data has been published though a public repository has not been announced [72]. For a semi–complete overview on the state of numerical relativity codes (open and closed source) along with an outlook for future developments, see [73].

However, reliable construction of asymmetric binary ID with compact objects having non–equal spins has been very limited for binaries involving NSs and, as such, has not allowed for the exploration of a large portion of the available parameter space for BNS and BHNS binaries. Pivotal works on excision conditions for black holes [19] has allowed for the construction of high quality binary black hole [74]–[76] and black hole-neutron star [4], [77], [78] initial data which has proven to be efficient when constructing eccentricity reduced initial data using spectral solvers [79]. Furthermore, the construction of BNS initial data allowing for asymmetric binaries with mixed spins has only become well understood in recent years [31], [80] as well as extending these theorems to mixed binaries [81]. However, the codes that currently employ these state-of-the-art approaches such as `SGRID` [25], [31], [82]–[84], `Spells` [4], [75], [80], [81], [85]–[90], and `COCAL` [91]–[95] are closed source; therefore, there is a well known need in the NR community for a collection of initial data codes that can produce eccentricity reduced binary initial data for BHNS and BNS systems such that extremal configurations can be reliably obtained. Moreso, the inclusion of tabulated EOS in the construction of ID is extremely important given the breadth of research dedicated to exploring the EOS parameter space.

In Chapter 2 we will examine the initial data problem as it relates to the construction of BBH, BNS, and BHNS initial data. Furthermore, we will describe our solution to this problem based on the `KADATH`[18] spectral library which has resulted in the public release of our suite of solvers known as `FUKA`[1]. Furthermore, we will examine a series of test configurations to quantify the quality of the resulting ID as it pertains to the resulting evolution. The theory and results discussed in Chapter 2 have been published in [9].

[1] https://bitbucket.org/fukaws/

### 1.2 Exploration of asymmetric spinning BNS mergers

Gravitational wave events such as GW170817 [5] and GW190814 [6] have provided a wealth of insight into the merger of compact objects, but, due to the degeneracy of mass ratio, spin, and tidal deformability; it is challenging to ascertain the constituent mass and spins of the compact objects [96]–[100]. However, multi–messenger events such as GW170817 where an electro-magnetic counterpart was observed have provided considerably more insights which has enabled constraints on the EOS (cf. [28], [42], [101]–[114]) in addition to constraints on the maximum mass of a NS of $M_{\rm TOV} \lesssim 2.3\,M_{\odot}$ to due the expected delayed collapse to a BH (cf. [101], [103], [104], [113], [114]). Furthermore, in each GW event there exists a low-spin and high-spin prior. For instance, for GW190418, the low-spin prior is consistent with an irrotational binary, however, the high-spin prior would result in a dimenionless spin of the primary[2] of $\chi_1 \approx 0.52$.

The uncertainty of the influence mass asymmetry and spin have on merger dynamics, GW spectra, and electro–magnetic counterparts has lead to a wealth of results in numerical relativity which will be discussed in the following sections. In Fig. 1.1 an overview of the parameter space explored within this work is shown where the colored regions correspond to the associated chapter in this work where its results are discussed. However, Fig. 1.1 is slightly misleading as the space of parameters includes as well the total binary mass $M_{\infty}$, the eccentricity of the binary [3] , and the EOS. We have, therefore, identified relevant configurations to explore aimed at identifying prominent characteristics and constraints that will be insightful for future multi-messenger detections.

#### 1.2.1 Dynamics of asymmetric spinning BNS mergers

A key aspect in studying BNS mergers is the detailed analysis of the resulting dynamics during merger and into the post–merger. A number of works focusing on the dynamics of asymmetric irrotational BNS systems have been carried out, but have been limited to $0.7 \lesssim q \leq 1$ [see, e.g., [21]–[30]]. Additionally, limited studies with smaller mass ratios, e.g., $q \approx 0.5$, have been explored using polytropic EOSs [see, e.g., [25], [27], [31], [32]] and, more recently, a study using a novel tabulated EOS with a first–order transition to quark mater [33]. The resulting key features of asymmetric binaries include the disruption of the secondary object for highly asymmetric binaries due to the interaction of tidal forces, a larger remnant disk after collapse, and an increase in dynamical ejecta [22], [34].

Additionally, parallel studies have also been carried out to investigate the influence of spin on merger dynamics [8], [35]–[40]. In these works they find that the addition of spin–angular momentum influences the lifetime of the remnant as well as results in a remnant black hole with spins up to $\chi \sim 0.89$ [35], [36]. It has also been shown that spin as well as highly eccentric orbits can also result in an increased lifetime of the remnant via the onset of a one–arm instability in the HMNS remnant and an increase in the disc mass[37], [39], however, these effects have been shown to be subdominant when compared to the influence of mass asymmetry[38]. Conversely, a more recent work examining strongly spin-

[2]Here we assume the secondary object is irrotational which is consistent with the simulations we have performed throughout this work.

[3]In this work we will only consider quasi-circular orbits with small residual eccentricities that have a negligible influence on the resulting dynamics

ning BNS configurations with $q = 1$ where the spins are (anti-)aligned with the orbital axis of rotation using temperature-dependent EOS models results in an overall suppression of dynamical ejecta for aligned spins[40].

The results from previous studies have focused on the influence of spin or asymmetry which has provided important insights into the dynamics of BNS mergers, however, in this work we will extend the parameter study to include equal–mass binaries with extremal spins up to $\chi_1 = 0.6$ as well as the effective dynamics when considering asymmetric and spinning BNS mergers, the results of which have been published in [20]. In Chapter 3 we will explore the orange region within Fig. 1.1 for massive binaries with $M_\infty \in [1.025, 1.105] M_{\rm th}^{1,0}$ where $M_{\rm th}^{1,0}$ is the threshold mass for an equal-mass irrotational binary for a given EOS as shown in Tab. C.1.

### 1.2.2 Threshold mass to prompt collapse in BNS mergers

Another fascinating regime to explore is that of the threshold mass for binary neutron stars mergers where the threshold mass describes the minimum mass such that a prompt collapse to a BH occurs within the freefall timescale. This has important astronomical implications as prompt collapsing BNS mergers are more electro–magnetically quiet and are challenging to distinguish from BHNS mergers with a similar total mass [115]–[117]. For equal–mass binaries, it would be unlikely for a BH to be involved for $M_{\rm BH} \approx 1.4 M_\odot$ [118], [119], however, for highly asymmetric binaries where the primary mass is of the order of the maximum non-rotating mass for a NS, $M_{\rm TOV}$, such a configuration cannot be ruled out in this critical regime [7], [120].

The threshold mass ($M_{\rm th}$) has been thoroughly studied in order to characterize the quasi–universal behavior of the threshold mass of BNS mergers for irrotational equal–mass and asymmetric mass ratio binaries [23], [42], [65], [66], [121]–[123]. In the case of smaller mass ratios it was originally suggested that the threshold mass decreases with a power–law behavior as a function of decreasing mass ratio $q$ [124] which was later supported by [65]. Hence, it was suggested that a quasi–universal behavior exists and numerous fits are available with $M_{\rm th}$ as a function of various EOS quantities [124]. In contrast, a more recent study was performed which focused on asymmetric irrotational binaries which concluded that no such quasi-universal behavior exists and, as such, the threshold mass as a function of $q$ has an EOS dependent fit of two splines such that, for stiffer equations of state, the maximum threshold mass can occur on the order of $q = 0.8$ whereas, for softer equations of state would only result in a decreasing threshold mass[66].

In Chapter 4 we will discuss the blue region in Fig. 1.1 which is related to BNS mergers in the $q \in [0.5, 1]$ with the dimensionless spin of the primary (more massive) object $\chi_1 \in [-0.3, 0.3]$. Specifically, our work focuses on measuring the threshold mass to prompt collapse in BNS simulations which has been thoroughly explored for equal mass, irrotational binaries[23], [42], [102], [123] and extended later to asymmetric irrotational BNS mergers[65], [66], [122], [125]. Here we explore the asymmetric binaries mass ratios as small as $q = 0.5$ and, for the first time, explore the influence of spin on the mass ratio. The analysis of the quasi–universal relation has been reported in [41].

### 1.2.3 Distinguishing BHNS from BNS

Within a critical region of total binary mass, asymmetry, and spin parameter space; binary configurations may exist such that detections (e.g. GW190418) are challenging to discern whether or not the primary (more massive) object is a massive NS or a small BH. Previous studies have shown that a key feature of a BHNS is discrepancies in the mass flows, specifically, the outflow from a BHNS is due to the tidal disruption of the secondary objects[45]–[48] as compared to BNS mergers which will also produce mass ejection from the collisional shock and, possibly, from the resulting (meta-)stable remnant [49]–[53]. Most prominent in the case of a BNS is the production of a blue kilonova which is largely attributed to the shock heating at the collisional surface of the two NSs [54], [55]. This feature is unique compared to the red kilonova emission characteristic of the long–term mass ejection from the accretion disk [56]–[59].

In Chapter 5 we will explore the critical region where BNS and BHNS configurations naturally overlap. Within this region, we will use numerical simulations to determine the influence of mass asymmetry $q \in [0.486, 0.714]$ and spin $\chi_1 \in [0.00, 0.52]$ on the characteristic feature of BHNS and BNS inspiral and mergers. Specifically, we will examine the ejecta mass and composition of each configuration for two hardonic EOS models (`TNTYST` and `BHB`$\Lambda\Phi$) with a focus on unique characteristics that may inform future multi-messenger detections. The results from this chapter have been previously reported in [8].

## 1.3 Equations of state with quark matter

The equation of state of nuclear matter remains a long standing problem for nuclear theory as well as theoretical physics. Specifically, the low density regions have been fairly well understood using nuclear theory with the extremely high density regions being well described by chiral effective field theory and lattice QCD. Conversely, the intermediate scales between $\sim [1, 10]n_s$, where $n_s$ is nuclear saturation density, are less understood and are only loosely constrained by polytropic EOSs that do not violate causality or more recently, by sound-speed constraints [126]–[128]. Furthermore, merger events of BNS systems provide a unique insight into this intermediate regime, however, the numerical exploration of these systems have been limited to purely hadronic EOSs or polytropic EOSs with artificial transitions to quark matter and an analytical scheme for temperature dependence (cf. [63]).

In Chapter 6 we will explore for the first time a physically motivated temperature and charge fraction dependent EOS with a description of quark matter at densities in excess of nuclear saturation density based on the V-QCD framework [129]. Such a novel framework includes a mixed phase of quark and nuclear matter resulting in a critical point at high temperature and large density. In Chapter 6 we will examine BNS configurations similar to GW170817 to ascertain the mechanisms that influence quark formation, how the formation of quarks influence the GW spectra, and how GW events can constrain the V-QCD model. These results have been reported previously in [62]

Finally, we will close this thesis with a cumulative conclusion in Ch. 7. Here we will review highlighted results from this work in addition to summarizing avenues for future research.

# Chapter 2

# Initial data

The study of compact objects in numerical relativity (NR) is the process of solving the Einstein field equations (EFE) using computers, where the EFE in their original form

$$G_{\mu\nu} = R_{\mu\nu} - \frac{1}{2} g_{\mu\nu} R = 8\pi T_{\mu\nu}, \tag{2.1}$$

represent the description of spacetime as a 4D Lorentzian manifold $(\mathcal{M}\,, g)$ which entails a coupled system of non–linear, second order, partial differential equations. Such a system of equations is vastly more complex than the classical counterpart in Newtonian mechanics such as the two body or effective one body models where only knowledge of the stellar objects are necessary and the initial conditions are trivially defined based on the component mass, separation, and initial momenta. To this end, it is essential to cast the system of equations into a form that reduces computational complexity by taking advantage of relevant symmetries, make meaningful approximations and ensures a convergent solution. This chapter is devoted to the construction of the initial data time slice which will serve as the basis for the numerical simulations discussed in the remaining chapters, however, for a mathematically rigorous review of the decomposition of the EFE to include the evolution equations, the reader is referred to [10], [11].

## 2.1 3+1 decomposition

The first step towards initial data (ID) construction is by employing the standard $3+1$ decomposition which decomposes $\mathcal{M}$ into purely spatial hypersurfaces $\Sigma_t$ which are parameterized by a time coordinate $t$. For a line element of the form

$$ds^2 = g_{\mu\nu} dx^\mu dx^\nu \,, \tag{2.2}$$

such a decomposition is obtained by constructing a projection tensor onto the purely spatial hypersurface as well as a normal pointing vector along the parameterization component, $t$,

$$n_\mu \equiv -\alpha \nabla_\mu t \,, \tag{2.3}$$

$$\gamma_{\mu\nu} = g_{\mu\nu} + n_\mu n_\nu. \tag{2.4}$$

As such, we can define the coordinate time of our hypersurfaces in terms of the normalization factor $\alpha$ and a purely spatial vector, $\beta_\mu$,

$$t_\mu \equiv \alpha n_\mu + \beta_\mu. \tag{2.5}$$

The 4D line element (2.2) can then be rewritten with the help of equations (2.4) and (2.5) into the following form

$$ds^2 = -\alpha^2 dt^2 + \gamma_{ij}(dx^i + \beta^i dt)(dx^j + \beta^j dt). \tag{2.6}$$

The scalar $\alpha$ is commonly referred to as the *lapse*[130] as it describes how the coordinate time is influenced by curved geometry. In the limit of flat spacetime, $\alpha \to 1$ and, as the curvature of the manifold increases e.g., near a massive compact object, $\alpha < 1$. Conversely, $\beta_i$ describes how the spatial coordinates *shift* when traveling along a geodesic which is most easily understood as a loss of parallelism. Therefore, in the limit of flat spacetime, the shift vector $\beta_i \to 0$.

It is now useful to make a few definitions which are used throughout this chapter. First, we can define a covariant derivative that is compatible the projection tensor, $\gamma_{ij}$, as

$$D_i := \gamma^k{}_i \nabla_k.$$

Additionally, we can characterize the curvature of $\Sigma_t$ by measuring the change of the 3-metric along the normal vector $\mathbf{n}$

$$K_{ij} = -\frac{1}{2}\mathcal{L}_{\boldsymbol{n}}\gamma_{ij}\,,$$

which is commonly referred to as the extrinsic curvature. Finally, we define necessary contractions of the energy-momentum tensor

$$E \equiv T_{\mu\nu} n^\mu n^\nu\,, \tag{2.7a}$$

which is the time-like projection of the energy-momentum tensor and

$$j_\alpha \equiv -T_{\mu\nu}\gamma^\mu{}_\alpha n^\nu\,, \tag{2.7b}$$

which is the space-like momentum current. Furthermore,

$$S_{\alpha\beta} \equiv T_{\mu\nu}\gamma^\mu{}_\alpha \gamma^\nu{}_\beta\,, \tag{2.7c}$$

is the purely spatial projection of the stress-energy tensor.

In this way it is possible to recast the EFE as a Cauchy problem such that the EFE are decomposed into a set of evolution equations describing the dynamics of the purely spatial hypersurface which are characterized by a coupled system of second order, partial differential constraint equations. As such, Eq. (2.1) can be cast into the well known Hamiltonian and momentum constraint equations

$$R + K^2 - K_{ij}K^{ij} = 16\pi E\,, \tag{2.8}$$

$$D_j K^j{}_i - D_i K = 8\pi j_i\,, \tag{2.9}$$

$$\tag{2.10}$$

where $R$ is the 3-Ricci scalar on $\Sigma_t$.

### 2.1.1 Conformal Thin Sandwich formulation

Even in the current form of Eq. (2.8) and (2.9), it is unclear what the underlying degrees of freedom of the system of equations are nor are they efficient to be solved directly. To this end, works by Lichnerowicz[13] and York[14], [15] played an important role to dissect the key elements of the constraint equation which has evolved into the Conformal Thin Sandwich decomposition.

The underlying idea is to take the 3+1 decomposition discussed in Sec. 2.1 to the limit where the parameterization of neighboring hypersurfaces are infinitesimally separated such that $\Sigma_t \to \Sigma_{t+\delta t}$. Lichnerowicz proposed the idea of a conformal transformation of the 3-metric such that

$$\gamma_{ij} := \Psi^4 \tilde{\gamma}_{ij} \,, \tag{2.11}$$

where $\tilde{\gamma}_{ij}$ is denoted as the *conformal* or *background* metric and $\Psi$ is a scalar field describing the deviation from the background metric which is, therefore, a coordinate dependent quantity. Furthermore, the extrinsic curvature can be decomposed into its trace and tracefree form

$$K_{ij} = A_{ij} + \frac{1}{3} K \gamma_{ij} \,, \tag{2.12}$$

where $K$ quantifies the mean curvature of $\Sigma_t$. In this work, we utilize the conformal relation for the tracefree extrinsic curvature of

$$\hat{A}^{ij} := \Psi^{10} A^{ij} \,, \tag{2.13}$$

where the exponent of $\Psi$ is chosen to be consistent with the computed result from the momentum constraint (cf. [10], Sec. 6.5.2 for a discussion). With Eq. (2.11) & (2.13), Eq. (2.8) & (2.9) can be rewritten as

$$\tilde{D}^k \tilde{D}_k \Psi + \frac{1}{8} \Psi^{-7} \hat{A}_{ij} \hat{A}^{ij} + 2\pi \Psi^5 E - \frac{1}{8} \tilde{R} \Psi - \frac{1}{12} K^2 \Psi^5 = 0 \,, \tag{2.14}$$

$$\tilde{D}_j \hat{A}^{ij} - \frac{2}{3} \Psi^6 \tilde{D}^i K - 8\pi \Psi^4 j^i = 0 \,, \tag{2.15}$$

where $\hat{A}^{ij}$ is defined as [15]

$$\hat{A}^{ij} = \frac{\Psi^6}{2\alpha} (\tilde{D}^i \beta^j + \tilde{D}^j \beta^i - \frac{2}{3} \tilde{\gamma}^{ij} \tilde{D}_k \beta^k + \partial_t \tilde{\gamma}^{ij}). \tag{2.16}$$

After substituting Eq. (2.16) into (2.15) we obtain

$$\tilde{D}_j \Big( \frac{\Psi^6}{\alpha} (\tilde{\mathbb{L}} \beta)^{ij} \Big) + D_j \Big( \frac{\Psi^6}{\alpha} \partial_t \gamma^{ij} \Big) - \frac{4}{3} \Psi^6 \tilde{D}^i K - 16\pi \Psi^4 j^i = 0 \,, \tag{2.17}$$

$$(\tilde{\mathbb{L}} \beta)^{ij} := \tilde{D}^i \beta^j - \tilde{D}^j \beta^i - \frac{2}{3} \tilde{\gamma}^{ij} \tilde{D}_k \beta^k .$$

A natural first estimate is to set $\tilde{\gamma}_{ij} = f_{ij}$ where $f_{ij}$ is the flat spatial 3-metric which, in a cartesian basis, is simply $f_{ij} = \delta_{ij}$. By using the conformal decomposition with the flat metric the system of equations simplifies considerably as the terms related to the intrinsic curvature of the manifold are zero. Additionally, we can demand a constant background metric such that $\partial_t \gamma_{ij} = 0$. And finally, by imposing maximal slicing we assume the mean curvature $K = 0$. The remaining degrees of freedom to be specified are $\alpha$, $E$, and $j^i$.

### 2.1.2 eXtended Conformal Thin Sandwich

Of the remaining degrees of freedom from the CTS system of equations $\alpha$, $E$, and $j^i$, $\alpha$ is not trivially specifiable since, although it is a smooth distribution it is not uniform in the case of binary compact objects. A later work from York and Pfeiffer [16] introduced an extension to the CTS system coined (XCTS) which derived an equation for $\alpha$ based on the momentum constraint and $\partial_t K$ yielding

$$\tilde{D}_i\tilde{D}^i(\alpha\Psi) - \alpha\Big[\frac{1}{8}\tilde{R} + \frac{5}{12}K^2\Psi^4 + \frac{7}{8}\hat{A}^{ij}\hat{A}_{ij} + 2\pi\Psi^5(E+2S)\Big] \\ +\Psi^5(\partial_t K - \beta^i\tilde{D}_i K) = 0, \tag{2.18}$$

thus resulting in $\partial_t K$ now becoming freely specifiable. With Eq. (2.18) along with Eq. (2.14) and (2.17) we obtain a complete set of elliptic equations. We can then substitute our assumptions of a flat background and maximal slicing along with $\partial_t K = 0$ to obtain the reduced system of equations

$$\tilde{D}^k\tilde{D}_k\Psi + \frac{1}{8}\Psi^{-7}\hat{A}_{ij}\hat{A}^{ij} + 2\pi\Psi^5 E = 0\,, \tag{2.19a}$$

$$\tilde{D}_j\Big(\frac{\Psi^6}{\alpha}(\tilde{\mathbb{L}}\beta)^{ij}\Big) - 16\pi\Psi^4 j^i = 0\,, \tag{2.19b}$$

$$\tilde{D}_i\tilde{D}^i(\alpha\Psi) - \alpha\Big[\frac{7}{8}\hat{A}^{ij}\hat{A}_{ij} + 2\pi\Psi^5(E+2S)\Big] = 0\,, \tag{2.19c}$$

where now only the source terms $E$ and $j^i$ remain to be specified along with appropriate boundary conditions.

### 2.1.3 Stationarity

When generating ID we wish to find an equilibrium solution such that the Hamiltonian and momentum constraints are satisfied throughout their dynamical evolution. This equates to identifying a time-like Killing $\xi^\mu$ vector such that the well known Killing equation is satisfied

$$\tilde{D}_\xi\tilde{\gamma}_{ij} = 0.$$

Within the 3+1 decomposition, this simply results in

$$\xi^\mu := t^\mu = \alpha n^\mu + \beta^\mu. \tag{2.20}$$

In other words, this can also be thought of as computing $\Sigma_t$ in the co-moving frame. However, in the case of binary initial data only an approximate helical killing vector exists that describes quasi-stationary initial conditions which is defined as (cf. [10], [11], [131])

$$\xi^\mu := \partial_t + \Omega\partial^i_\phi(\mathbf{x}_c)\,, \tag{2.21}$$

where $\Omega$ is the orbital velocity of the binary and $\partial^i_\phi(\mathbf{x}_c)$ is the rotation vector field at a coordinate center $x_c$. In this work the formulations presented are completely general, however, we use the analytically known rotation field $\partial_\phi$ due to the strict $z$-symmetry imposed by the `KADATH` library.

### 2.1.4 Matter sources and hydrostatic equilibrium

In the case of binary initial data involving a neutron star, the energy-momentum tensor in the perfect fluid form is used to model neutron star matter

$$T^{\mu\nu} := \rho h u^{\mu} u^{\nu} + p g^{\mu\nu} \,, \tag{2.22}$$

where $\rho$ is the rest-mass density, $h := 1+\epsilon+p/\rho$ is the relativistic specific enthalpy, $u^{\mu}$ is the fluid four-velocity, and $p$ is the pressure. Using Eq. (2.7) projections we can compute the source terms in Eqs. (2.19)

$$E := \rho h W^2 - p \,, \tag{2.23a}$$

$$S^i{}_i := 3p + (E+p) U^i{}_i \,, \tag{2.23b}$$

$$j^i := \rho h W^2 U^i \,, \tag{2.23c}$$

where W is the Lorentz factor which we define as

$$W^2 := (1 - U^i U_i)^{-1} \tag{2.24}$$

A common issue when using spectral methods is the appearance of so-called *Gibbs phenomenon* when attempting to find a spectral fitting function which models a shock or a discontinuous region thereby deteriorating or spoiling the solution. A first step to minimize these effects is to utilize an intelligent domain decomposition such that known shock interfaces e.g., the stellar surface, coincide with a domain boundary, however, this only removes aliasing due to attempting to model the shock with a single interpolating function and does not resolve the issue inside the stellar surface where the gradient of the density is still very steep when approaching the surface. Therefore, even with an optimal domain decomposition one can still obtain a result that includes strong oscillations near the surface especially when increasing the resolution of the stellar domains. To avoid resorting to filtering of higher order terms we instead rescale Eqs. (2.19) in the stellar interior by $p/\rho$ which is more well behaved spectrally and removes explicit terms of $\rho$ from the system of equations thus enabling an accurate description of stellar matter and providing a reliable means for convergence.

As we wish to model a binary in equilibrium, we must ensure the fluid is in hydrostatic equilibrium. This reduces to solving the relativistic conservation equations for the energy-momentum tensor and of the rest-mass current

$$\nabla_{\mu} T^{\mu\nu} = 0 \,, \tag{2.25}$$

$$\nabla_{\mu} (\rho u^{\mu}) = 0. \tag{2.26}$$

In the construction of binary ID we make the assumption that the stellar matter is isentropic ($ds = 0$) which we find reasonable when modeling a cold star that is unperturbed. As such, we can write the relativistic Euler equation obtained by the constraint Eq.(2.25) as

$$u^{\mu} \nabla_{\mu} (h u_{\nu}) + \nabla_{\nu} h = 0. \tag{2.27}$$

In order to decompose Eq. (2.27) we first introduce the projection of the specific enthalpy current onto $\Sigma_t$

$$\hat{u}_i = h \gamma^{\mu}_i u_{\mu}. \tag{2.28}$$

In the presence of Killing vector, we can define the co-rotating fluid 3-velocity as

$$V^i := \alpha U^i - \xi^i \,, \tag{2.29}$$

and, with Eq. (2.28) and (2.29), we can rewrite Eq. (2.27) in a purely spatial form[11], [131]

$$D_i\left(\frac{h\alpha}{W} + \hat{u}_j V^j\right) + V^j(D_j\hat{u}_i - D_i\hat{u}_j) = 0. \tag{2.30}$$

We see by inspection that the isentropic relativistic Euler equation has an exact first integral for configurations where $V^j = 0$ or $\hat{u}_j = 0$. For the case of $V^j = 0$ we see this as the case when the fluid is co-moving with the Killing vector $\xi^i$. Conversely, $\hat{u}_j = 0$ represents the case when the fluid is described by an irrotational flow which we model using a velocity potential $\phi$ such that $\hat{u}_j = D_j\phi$. In a similar fashion, the purely spatial form of Eq. (2.26) is

$$D_i(\rho W V^i). \tag{2.31}$$

Equation (2.31) with (2.29) now form an elliptic equation for the velocity potential $\phi$. However, $D_iV^i$ in fact includes a laplacian term related to the velocity potential $\phi$ which is therefore defined up to a constant and, as such, must be fixed explicitly in order to obtain a unique solution. Given Eq. (2.31) contains explicit appearance of $\rho$, we can define $H := \ln h$ and recast (2.31) such that $\rho$ is no longer present

$$\Psi^6 W V^i \tilde{D}_i H + \frac{dH}{d\ln\rho}\tilde{D}_i(\Psi^6 W V^i) = 0 \,, \tag{2.32}$$

where, in order to obtain Eq.(2.32) we assume $dH/d\ln\rho$ is strictly monotonic.

Up until now only binary configurations containing irrotational or co-rotating fluid profiles have been addressed. In order to extend the formulation to include arbitrary uniform rotating fluid profiles, we follow the constant rotational velocity (CRV) formulation as derived by Tichy[131] which adds a spin component to the specific enthalpy current such that

$$\hat{u}_i := D_i\phi + s_i \,, \tag{2.33}$$

$$s^i := \omega\xi^i_{\rm NS}. \tag{2.34}$$

In the same manner as for black hole initial data, $\xi^i = \partial^i_\phi(\mathbf{x}_{\rm NS})$ is a rotation vector field centered on the neutron star parameterized by rotation parameter $\omega$. From this we can now explicitly define the projection of the fluid 4-velocity as well as the Lorentz factor to be

$$W^2 = \frac{\hat{u}^i\hat{u}_i}{h^2} + 1 \,, \tag{2.35}$$

$$U^i = \frac{\hat{u}}{hW}. \tag{2.36}$$

However, by substituting Eq. (2.33) into (2.30) results in a significantly more complex equation which is discussed in detail in [131], [132]. The conclusion from

these discussions is that many of the new terms introduce a negligible contribution to the first integral allowing the following expression to be sufficient when modeling irrotational and arbitrary uniformly rotating fluids

$$\frac{h\alpha}{W} + V^i D_i \phi = 0. \tag{2.37}$$

Tootle:2022pvd, Finally, to fully constrain the fluid degrees of freedom we must specify an equation of state (EOS) which provides a relation between the pressure $p$, internal energy $\epsilon$, rest-mass density $\rho$, and the relativistic specific enthalpy $h$. Our code is thus able to support both analytical (piecewise-)polytropic EOSs as well as 1D cold or finite temperature tabulated EOSs.

## 2.2 Boundary conditions

To close our system of equations appropriate boundary conditions must be enforced both at the outer boundary of the numerical space, at the matching boundary between each spectral domain, and on the surface of each compact object. The matching condition between spectral domains ensures continuity of the solution as well as it's derivatives, however, the boundary conditions on the outer boundary and compact object surfaces require physical motivations to obtain meaningful ID.

### 2.2.1 Asymptotic boundary conditions

To enforce boundary conditions on $\alpha$, $\Psi$, and $\beta^i$ at the outer boundary, we utilize a a compactified coordinate system which maps numerical infinity to finite values[18]. As such, we can compute $\Sigma_t$ in the asymptotic flat limit and impose the following boundary conditions

$$\lim_{r\to\infty} \alpha = 1\,, \qquad \lim_{r\to\infty} \Psi = 1\,, \qquad \lim_{r\to\infty} \beta^i = \beta^i_{cor}\,, \tag{2.38}$$

such that in the asymptotic limit the shift simply describes the co-moving frame

$$\beta^i_{cor} := \xi^i + \dot{a}r^i = \Omega \partial^i_\phi(\mathbf{x}_c) + \dot{a}r^i\,, \tag{2.39}$$

where the additional factor $\dot{a}r^i$ equates to a relative acceleration between the two objects which will be discussed in detail in Sec. 2.5.

Although well defined analytically, $\partial^i_\phi$ is challenging numerically given it involves coordinate locations up to spatial infinity. To overcome this limitation the shift can be decomposed into

$$\beta^i := \beta^i_0 + \beta^i_{cor}\,, \tag{2.40}$$

where $\beta^i_0$ measures the deviations from the co-moving frame and, as such, is referred to as the *inertial shift*. Therefore, in the asymptotic limit we can enforce $\beta^i_0 = 0$ which is well defined numerically. It has been shown in the case of a conformally flat metric that $(\tilde{\mathbb{L}}\partial_\phi)^{ij} = 0$, therefore, in practice we can freely replace $\beta^i$ by $\beta^i_0$ within the XCTS system of equations[131].

### 2.2.2 Horizon boundary conditions

In this work we utilize excision boundary conditions as developed by Cook et al [19] which excises the black hole interior by defining the excision surface to be an apparent horizon. To do so, we define the excision surface to be a coordinate 2-sphere of constant radius characterized by an outward pointing unit normal vector field ($s^i$) and a projection tensor ($h_{ij}$)

$$s^\mu := [0, s^i] = \Psi^{-2}\tilde{s}^i\,, \qquad\qquad h_{\mu\nu} := \gamma_{\mu\nu} - s_\mu s_\nu = \Psi^4\tilde{h}_{\mu\nu}. \tag{2.41}$$

To demand that the excision surface is in fact an apparent horizon can be achieved by ensuring a vanishing expansion ($\theta$) at the surface. This is equivalent to demanding that the horizon will initially evolve along the out-going null generators of the horizon[11]. We can define such null generators as

$$k^\mu := \frac{1}{\sqrt{2}}\big(n^\mu + s^\mu\big), \tag{2.42}$$

and fix the excision surface to be a null surface by demanding

$$t^\mu k_\mu|_{\mathcal{S}_{\rm BH}} = 0, \implies \beta^i s_i|_{\mathcal{S}_{\rm BH}} = \alpha. \tag{2.43}$$

Furthermore, by decomposing $\beta^i$ into perpendicular and tangent components as derived by Cook et al[19], we can translate Eq. (2.43) into the following boundary conditions on the excision surface

$$\beta^i_\perp|_{\mathcal{S}_{\rm BH}} := \alpha s^i\,, \tag{2.44}$$

$$\beta^i_{||}|_{\mathcal{S}_{\rm BH}} := \omega_{\rm BH}\xi^i_{\rm BH}\,, \tag{2.45}$$

where $\xi^i$ is the rotational killing vector field centered on the black hole

$$\xi^i_{\rm BH} := \partial_\phi(\mathbf{x}_{\rm BH}), \tag{2.46}$$

and the rate of rotation is parameterized by $\omega_{\rm BH}$. In conformal notation, we can express the expansion on the two surface as

$$\theta = \frac{\Psi^{-2}}{\sqrt{2}}(\tilde{h}^{ij}\tilde{D}_i\tilde{s}_j + 4\tilde{s}^k\tilde{D}_k\ln\Psi - \Psi^{-4}\tilde{h}^{ij}\hat{A}_{ij})\,, \tag{2.47}$$

and, by demanding $\theta = 0$, we obtain the boundary condition enforcing our excision surface as an apparent horizon (or Marginally Outer Trapped Surface)

$$\tilde{s}^i\tilde{D}_i\Psi|_{\mathcal{S}_{\rm BH}} = -\frac{\Psi}{4}\tilde{D}^i\tilde{s}_i - \frac{1}{4}\Psi^{-3}\hat{A}_{ij}\tilde{s}^i\tilde{s}^j. \tag{2.48}$$

Finally, a condition for the lapse on the horizon must be specified. In our code there are two possibilities

$$\alpha|_{S_{\rm BH}} = \text{const}\,, \tag{2.49}$$

$$\tilde{s^i}\tilde{D}_i(\alpha\Psi) = 0. \tag{2.50}$$

Cook et al have analyzed both the former fixed lapse condition as well as the later *von Neumann* condition[19] and have found that the later is more sensitive to

tidal forces in binary configurations which lead to a more consistent description of the black hole. As a result the BH characteristics (mass and spin) throughout numerical simulations are retained to higher degree of accuracy compared to a fixed lapse boundary condition. [1]

### 2.2.3 Neutron star boundary conditions

In the case of neutron stars we need to impose boundary conditions on the fluid such that the stellar surface is well defined and is located at a domain boundary. Given the distribution of matter is not uniform due to tidal interactions with the binary companion the surface of the NS is not necessarily spherical. Traditionally the surface is defined by the vanishing of the rest-mass density $\rho$, however, to be consistent with removing explicit use of $\rho$, we instead utilize vanishing log specific-enthalpy

$$H|_{S_{\rm NS}} := 0. \tag{2.51a}$$

In addition to the constraint on the distribution of matter, we must also enforce conservation of the momentum at the boundary. In the limit $\rho \to 0$, Eq. (2.32) can be reduced by ascertaining that the second term goes to zero and that the first term remains real and non-zero resulting in the boundary condition

$$V^i \tilde{D}_i H|_{S_{\rm NS}} = 0. \tag{2.51b}$$

## 2.3 Asymptotic quantities

To characterize the self–consistency of our binary initial data with respect to a quasi–equilibrium ansatz yet to be discussed and in comparison to post-Newtonian estimates; we can measure the total energy contained in the computed spacetime via integration over a spherical surface at spatial infinity of the Arnowitt–Deser–Misner (ADM) Hamiltonian which has been derived from the Hilbert action. In our numerical implementation we utilize a compactified domain such that the solution within the coordinate patch extending to spatial infinity drops off quickly enough to yield a finite value. By taking advantage of the conformal decomposition this integral takes the form

$$M_{\rm ADM} := -\frac{1}{2\pi} \oint_{\rm S_\infty} D^i \Psi ds_i \,, \tag{2.52}$$

where $ds_i$ is a normal pointing surface element on a sphere at spatial infinity and, as such, is compatible with the flat metric and covariant derivative [11].

In contrast to measuring the total mass stored in a spacetime, we can also measure the total conserved mass, or the Komar mass, along a timelike Killing vector. In the case of binary initial data this reduces to measuring the conserved mass along the time component of the binary helical Killing vector which we have defined as Eq. (2.20). In practice we compute this quantity on a sphere at spatial infinity as with the $M_{\rm ADM}$. The basic expression takes the form of

$$M_{\rm K} := \frac{1}{4\pi} \oint_{S_\infty} n_j \nabla^i \xi^j_{(t)} ds_i, \tag{2.53}$$

[1] Within the `FUKA` codebase initial data using fixed lapse or *von Neumann* conditions are possible, however, the results in this work involving BHs are obtained using exclusively the *von Neumann* condition.

and, by substituting Eq. (2.20), reduces to

$$M_{\rm K} := \frac{1}{4\pi} \oint_{S_\infty} D^i \alpha ds_i. \tag{2.54}$$

One such method to quantify the degree to which the initial data is in quasi–equilibrium is by imposing the virial theorem defined as [11]

$$M_{\rm ADM} - M_{\rm K} = 0. \tag{2.55}$$

In the case of BBH initial data we impose the virial theorem in order to fix the orbital velocity $\Omega$ of the binary whereas, in the case of BNS and BHNS initial data, the more reliable force–balance equation is used which will be discussed in more detail in Sec. 2.6.2 - II. With a precise definition of the total mass stored in the spacetime using $M_{\rm ADM}$, we can define the binding energy of the binary as

$$E_b := M_{\rm ADM} - M_1 - M_2 =: M_{\rm ADM} - M_\infty, \tag{2.56}$$

where $M_{\langle 1,2\rangle}$ are the component gravitational masses. Finally, we can compute the total ADM linear and spin-angular momentum of the binary computed at spatial infinity using

$$J_{\rm ADM} := \frac{1}{8\pi} \oint_{\rm S_\infty} \hat{A}^{ij} \xi_i ds_j \,, \tag{2.57}$$

$$P^i_{\rm ADM} := \frac{1}{8\pi} \oint_{\rm S_\infty} \hat{A}^{ij} ds_j. \tag{2.58}$$

## 2.4 Quasi-local quantities

With a closed system of equations we also need a way to constrain the characteristics of our compact objects such as their gravitational mass and spin-angular momentum. To this end, we utilize the previous definition of a rotation vector field centered on each compact object

$$\xi^i_{\rm (NS,BH)} := \partial^i_\phi(\mathbf{x}_{\rm (NS,BH)}) \tag{2.59}$$

For a black hole, quasi–local quantities provide an accurate measurement of mass and spin-angular momentum even in a binary configuration given the excision surface is an apparent horizon. Therefore, the quantities measured on the excision surface should match what is measured by the dynamic horizon finders in an evolution code. We can first employ the use of the proper integral of the black hole area within the conformal approximation employed here

$$A := \oint_{S_{\rm BH}} \Psi^4 \sqrt{\det(\tilde{h}_{ij})} dS \,, \tag{2.60}$$

whose irreducible mass (i.e., the mass without spin contributions) is equivalent to

$$M_{\rm irr} := \sqrt{\frac{A}{16\pi}}. \tag{2.61}$$

Furthermore, the spin-angular momentum of the horizon is measured analogously to Eq. (2.57) on the excision surface

$$\mathcal{S} := \frac{1}{8\pi} \oint_{S_{\rm BH}} \hat{A}_{ij} \xi^i_{\rm BH} \sqrt{\det(\tilde{h}_{ij})} dS^j. \tag{2.62}$$

Furthermore, we can compute the total gravitational mass of the black hole, also known as the Christodoulou mass, which includes the mass contribution from the spin angular momentum

$$M^2_{\rm CH} := M^2_{\rm irr} + \frac{\mathcal{S}^2}{4M^2_{\rm irr}}. \tag{2.63}$$

$M_{\rm CH}$ is an exceptionally useful relation as it provides an accurate measurement of the gravitational mass of the BH when in a binary or isolated configuration. Finally, we can define the dimensionless spin parameter to be

$$\chi := \frac{\mathcal{S}}{M^2_{\rm CH}}\,, \tag{2.64}$$

which provides an accurate and comparable measure of black hole spins along sequences of BH masses and spin-angular momenta.

In the case of neutron stars quasi–local measurements are not as precisely defined since we do not have a strict geometric definition of the mass and spin of the NS. In the case of the gravitational mass that is used to fix the dimensionless spin of the NS, we instead compute the ADM mass of the TOV solution (i.e., at infinite separation)

$$M_{\rm NS_{(1,2)}} := \lim_{d_0 \to \infty} M_{\rm ADM\,,(1,2)}. \tag{2.65}$$

In the same matter, we fix the baryonic mass $M_b$ for each NS in the binary to be equivalent to $M_b$ of the isolated TOV solution which is simply a volume integral over the stellar interior

$$M_b := \int_{\rm V_{NS}} W \rho \Psi^6 dV. \tag{2.66}$$

We can, however, perform a quasi–local measure of the gravitational mass of the neutron star within the binary by computing the ADM gravitational mass as a volume integral outside of the stellar object as proposed in [31]

$$M_{\rm QL} := -\int_{\rm V_{NS}} D_i D^i \Psi dV. \tag{2.67}$$

It is important to note that the measurement of $M_{\rm QL}$ results in a systematic deviation from the gravitational mass measured in the isolated solution. The definition of the spin-angular momentum is also not well defined in the case of NS. Therefore, we follow the procedure as suggested by [80] where we compute the quasi–local spin–angular momentum on a spherical surface outside of the neutron star such that the entire distribution of matter is captured inside this surface

$$\mathcal{S}_{\rm QL} := \frac{1}{8\pi} \oint_{S_{\rm NS}} \hat{A}_{ij} \xi^i_{\rm NS} \sqrt{\det(\tilde{h}_{ij})} dS^j. \tag{2.68}$$

Aside from the gravitational mass definitions, however, a similar characterization of spinning neutron stars can be made as in the case for BHs

$$\chi_{\rm NS} := \frac{\mathcal{S}_{\rm QL\,,(1,2)}}{M^2_{\rm ADM\,,(1,2)}}. \tag{2.69}$$

Therefore, based on these definitions, the total mass of the binary is computed as

$$\begin{aligned} M_\infty &:= M_1 + M_2 \\ M^{\rm NS}_{\rm X} &:= M_{\rm ADM,(X)} \\ M^{\rm BH}_{\rm X} &:= M_{\rm CH,(X)} \end{aligned} \tag{2.70}$$

### 2.5 Eccentricity reduction

As eluded to during the discussion of our approximate helical killing vector Eq. (2.39), we wish to generate initial data that is in quasi–equilibrium as well as initial conditions with an eccentricity reduced inspiral. [2] To accomplish this we follow the iterative methods proposed by Pfeiffer et al which aims at reducing orbital eccentricity by either introducing analytical corrections or iteratively correcting $\Omega$ and the radial infall velocity, $\dot{a}$, based on numerical evolutions of the initial data which has proven effective in prior and this current work [31], [80], [133].

For 3.5PN corrections to $\Omega$ and $\dot{a}$, the analytical expressions utilized within `FUKA` are discussed in Appendix B. The iterative procedure is, however, more involved. To obtain iterative corrections we first evolve an initial dataset for at least four orbits. We can then fit the separation distance (proper or coordinate separation) as a function of time as well as its time derivative to

$$r(t) = S_r(t) - \frac{B_r}{\omega_r}\cos(\omega_r t + \phi_r)\,, \tag{2.71}$$

$$\dot{r}(t) = S_r(t) + B_r \sin(\omega_r t + \phi_r), \tag{2.72}$$

where fitting parameters $B_r$, $\omega_r$, and $\phi_r$ are used to estimate the degree of binary eccentricity

$$e := -\frac{B_r}{\omega_r d_0}. \tag{2.73}$$

Here $d_0$ is the corresponding separation distance between the two objects at $t = 0$.

A freedom in this procedure is the definition of $S_r(t)$ of which there have been various definitions proposed that include higher order terms in $t$, however, in this work we have utilized the simplest which has proven to be robust

$$S_r(t) := A_0 + A_1 t\,.$$

Use of higher order terms in $t$ within $S_r(t)$ as well in the trigonometric terms have been evaluated, however, they had negligible impact on the iterative corrections for the binaries considered in Sec. 2.8 and, thus, we have chosen to ignore them.

[2] In principle the `FUKA` ID solvers with the current definition of a helical Killing vector could be used to generate ID that is intentionally eccentric, however, we have not focused on such binaries within this work

Once a dataset has been evolved for $\sim 4$ orbits, a fit has been made to, for instance, Eq. (2.72), and the fitting parameters have been computed; we can then compute the corrections $\delta\dot{a}$ and $\delta\Omega$ using

$$\dot{a}_{k+1} := \dot{a}_k + \delta\dot{a}\,, \tag{2.74a}$$

$$\Omega_{k+1} := \Omega_k + \delta\Omega\,, \tag{2.74b}$$

$$\delta\dot{a} := -\frac{B_r \sin\phi_r}{d_0}\,, \tag{2.74c}$$

$$\delta\Omega := -\frac{B_r\omega_r \cos\phi_r}{2\Omega_k d_0}\,, \tag{2.74d}$$

such that the portion of the shift that describes co-rotation (2.39) can be written as

$$\beta^i_{\rm cor} = \Omega_{k+1}\partial^i_\varphi(\boldsymbol{x}_c) + \dot{a}_{k+1} r^i. \tag{2.75}$$

The eccentricity reduction procedure is then repeated until the desired threshold is obtained or further corrections no longer prove beneficial.

In this work we have elected to use Eq. (2.72) as it provided the ability to reduce the eccentricity of the binaries considered in this work below $e \approx 10^{-3}$ whereas additional iterations using Eq. (2.71) did not yield beneficial corrections below this threshold. This is likely due to the fact that, in this regime, $r(t)$ is already very linear and, therefore, the fitting parameters are not very sensitive to the small amount of eccentricity that remains in the system.

In practice the process of iterative eccentricity reduction within the `FUKA`codes reduces to defining two parameters `ecc_omega` and `adot` in the parameter file before (re)running the relevant *eccentricity reduction* stage as discussed in Sec. 2.6.2 - IV; where `ecc_omega` and `adot` have been computed by an external analysis code that is not part of the ID solvers.

## 2.6 Numerical implementation

When solving initial value problems it is imperative to utilize a numerical algorithm that is optimally suited for the problem. It has been shown that spectral methods are particularly well suited for initial value problems since, when implemented correctly, the solution will result in exponential convergence when the number of collocation points are increased[85]. Additionally, spectral methods allow for very fast computation of the derivatives and integrals of the basis functions since these are analytically known and, in certain cases, efficient algorithms such as fast fourier transformations can be used. To this end, we have utilized the `KADATH` spectral solver library which has been specifically designed for solving numerical relativity problems[18]. A key advantage of using `KADATH` is that it provides an interface which can ingest equations in a LaTeXlike format similar to how they are formulated within this work. This allows for more readability and extensibility of the application codes.

### 2.6.1 Spectral solver setup

In the previous section, we have defined a highly non-linear system of coupled partial differential equations which are constrained both by physically motivated boundary conditions as well as the desired characteristics of the binary

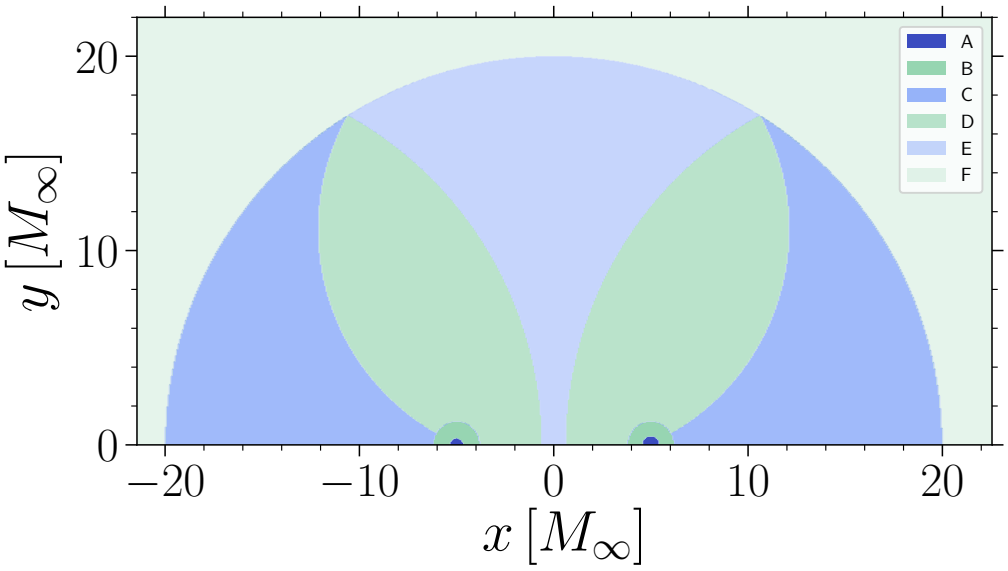


Figure 2.1: This figure describes the domain decomposition of the physical space of a BBH initial dataset. Regions A correspond to adapted spherical shells describing the apparent horizon (AH). Regions B corresponds to the spherical shells exterior to the AH. Regions C, D, and E correspond to the bispherical domains that provide a continuous coordinate map between regions B and F. Region F is the compactified domain which extends to numerical infinity. This figure has been reused from [9].

configuration (i.e., separation, masses and spins). An integral part of this process is the decomposition of the numerical space using a multi-domain approach such that a continuous map is available between numerical and physical coordinates as well as to ensure non-trivial boundaries (e.g., stellar surface, excision surface, numerical infinity) correspond to domain boundaries.

To that end, the binary numerical space is decomposed using a bispherical domain decomposition composed of a minimum of twelve domains[18] which is characterized in Fig. 2.1. Each compact object is composed of at least three domains which cover the interior solution and the matching exterior domain. In the case of a black hole the interior is empty since this region is excised whereas, in the case of a neutron star, the interior is the only region that is composed of nuclear matter. The surface of each object is set as the domain boundary of two spherical–adapted domain boundaries within `KADATH` such that the surface (e.g., stellar surface or excision surface) can adapt to the shape of the object based on its mass and spin configuration. In the case of a black hole this is simply a change in the radius of the 2-sphere in order to obtain the desired irreducible mass. Conversely, the resulting shape for a NS becomes ellipsoidal under the influence of stellar spin frequency and tidal influence from the companion.

The choice of adapted domains describing the compact object surface is two fold. In the case of NS, this allows for non-spherical objects to be accurately modeled by the numerical domains. Secondly, it is possible for Gibbs phenomenon to occur at discontinuities or sharp gradients in the solution when using spectral methods, therefore, it is imperative that the surface lies on a domain boundary. To further reduce the influence of Gibbs phenomenon, trigonometric functions are used as the basis functions to represent periodic variables such as angular components, whereas Chebyshev polynomials are used for non-periodic variables such

as the radial coordinate. As discussed in Sec. 2.1.3, choosing appropriate basis functions not only increases the efficiency of obtaining a numerical solution using spectral methods, but they can also be used to enforce additional constraints such as regularity along the axis of rotation and take advantage of symmetries in the system (e.g., $z$-symmetry).

Once the spherical–adapted surfaces have been defined for each object, a bispherical domain decomposition between the two objects and the external compactified domain is utilized in order to obtain a continuous coordinate map across the entire numerical domain. The addition of the compactified domain results in a mapping of the coordinate systems $\propto 1/r$ such that spatial infinity is mapped to a real value which allows for integrals to be taken at the asymptotic limit [18].

Based on this domain decomposition, a minimum of twelve domains are needed for binary initial data, however, additional spherical shells around each compact object and between the bispherical domains and the compactified domain can be added in order to provide additional local resolution. Addition of spherical shells plays an important role when considering highly asymmetric binaries as well as BHNS binaries in order to adequately resolve the steep gradients in the vicinity of the BH.

The implemented system of equations are solved in bulk directly, i.e., no form of relaxation or zig-zag algorithms are utilized. To this end, the system of equations is ingested and its residual, $R$, is computed in spectral form which utilizes the domain basis functions as the so-called "test-functions", $\xi$, such that the scalar product, $\langle R|\xi\rangle$ goes to zero. This is known as the "tau-method". Within the tau–method additional boundary conditions can be imposed in place of equations for higher order terms. The system of equations are then iteratively solved using a Newton-Raphson method in order to minimize the residuals. A key feature of `KADATH` in this regard is that the fields store not only their value on the collocation points, but also their derivative by means of automatic differentiation[18]. This allows for nearly perfect scaling of `KADATH` and `KADATH`–based applications via MPI parallelization to $\gtrsim 32000$ cores.

An additional feature of spectral codes is the ability to iteratively increase the resolution of the initial data given the spectral solution only improves with resolution. To do so, a given binary configuration is solved at a reasonably coarse resolution as this is quite cheap and fast to do. The solution can then be interpolated onto a new grid that is at the desired higher resolution before attempting to resolve the ID. In this manner, computing high resolution ID iteratively using `KADATH` can be done much more efficient then attempting to solve at high resolution directly.

### 2.6.2 Binary initial data algorithm

The details up til now reflect the theoretical and implementation details as discussed in [9], however, since then a considerably more efficient algorithm has been implemented to reliably construct extremal binary initial data which will now be discussed. The design and implementation of the new algorithm was developed by S.D. Tootle with helpful insights from L.J. Papenfort. We will reference the originally published implementation as v1 and the new implementation as v2 for the remainder of the text.

It is important to note that the v1 implementation documented in [9] leads to

the same constraint satisfying initial data for compact objects as those obtained with v2, however, v1 was very inefficient especially when attempting extremal configurations of highly asymmetric and spinning binaries. As such, the results section remains unchanged. Furthermore, the algorithm for v2 is nearly uniform across the construction of binary ID making it much more easily understood than the published v1 algorithm.

The v2 algorithm is built on a relatively simple principle of superimposed isolated objects which have been used extensively throughout numerical relativity to construct initial conditions for binary and head–on collisions of compact objects including boson stars, neutron stars, black holes, exotic objects, and recently multi–fluid neutron stars including dark matter (cf. [64], [134]). To our knowledge though, only the use of analytical solutions have been used within spectral codes to construct binary initial data which is a very crude estimate when attempting to construct extremal binaries and, at least within KADATH, does not allow for reliable convergence.

Instead, we utilize a slightly different approach. For a given binary configuration the standard inputs to constrain the binary are the mass and spin of each object as well as their relative separation distance. With this information, we can obtain a crude, although reasonable estimate, of the "center-of-mass" (COM) using the classical Newtonian estimate

$$\mathbf{x}_c := \frac{1}{M}\sum_i m_i \mathbf{r}_i. \tag{2.76}$$

With an estimate of the COM, we can compute the 3.5th order post–Newtonian (3.5PN) estimate of the orbital velocity $\Omega$ which will serve as the initial guess for the binary initial data and as the boost to our isolated compact object solutions.

Instead of using analytical solutions of our isolated objects, we now take a moment to compute the 3D solutions of each compact object using the same formulations described previously [see Sec. 2.1,2.3 and 2.4]. In this way, we have the most consistent description of our compact objects within the desired formulation of the EFE. Furthermore, once the isolated object solutions are obtained, we can boost each object using the 3.5PN estimate of $\Omega$ to obtain isolated solutions that resemble the solutions and spin velocities that will be computed in the binary configuration minus the influence of the companion object. It is important to note that computing the isolated solutions even in 3D is computationally inexpensive when compared to the efficiency gained in computing extremal binary solutions.

To generate the initial guess for a given binary ID configuration, we can now superimpose the isolated solutions onto the binary numerical space. To do so, each field, $X$, is superimposed in a similar fashion

$$X_{\rm binary}(\mathbf{x}) := \Xi + \kappa_1 \left(X_1\left(\hat{\mathbf{x}}_1\right) - \Xi\right) + \kappa_2 \left(X_2\left(\hat{\mathbf{x}}_2\right) - \Xi\right), \tag{2.77a}$$

$$\kappa_{<1,2>} := \exp\left[-\left(\frac{r_{<1,2>}}{w}\right)^4\right], \tag{2.77b}$$

$$\hat{\mathbf{x}}_{<1,2>} := \mathbf{x} - \mathbf{x}_{<1,2>}, \tag{2.77c}$$

$$w := \frac{d_0}{2}, \tag{2.77d}$$

where $X$ is substituted by the relevant field (e.g., $\alpha\,, \beta^i_0$, etc), $\Xi$ is the asymptotic value of the field (e.g., $\alpha = \Psi = 1\,, H = 0$, etc), $r_{<1,2>}$ is the coordinate radius from the center of the respective compact object, $w$ is the decay weight factor which controls where the falloff of the isolated solution occurs, $\kappa$ [3] is the overall decay factor such that the solution near each compact object is essentially the isolated solution which is then exponentially decayed to the asymptotic value, and $\hat{\mathbf{x}}_{<1,2>}$ represents the shift in the coordinates such that the isolated solutions are interpolated properly.

This algorithm concludes the generation of the initial guess for the binary solver and is the same irrespective of the binary configuration (BBH, BHNS, BNS). Moreso, the solving procedure is also fairly generic and includes three main stages, however, there are some nuances in binaries involving NS which will be addressed in the following sections.

### 2.6.2 - I Non-equilibrium stage

In the *Non-equilibrium* stage we solve the XCTS system of equations (2.19) while imposing asymptotic boundary conditions on the spacetime fields using Eqs (2.38) with the orbital velocity $\Omega$ as well as the COM fixed within equation (2.39). This is due to the fact that

1. the initial estimates for the COM and $\Omega$ from Newtonian and 3.5PN are not in equilibrium

2. the ADM and linear momentum constraints are evaluated at spatial infinity

As such, fixing $\Omega$ removes an important degree of freedom that would otherwise result in a solver that is prone to convergence issues. Within this stage the spacetime is able to find a consistent solution throughout the numerical space even though the fixed values of COM and $\Omega$ are only approximate. A converged solution from this stage provides a reliable foundation to obtain an equilibrium solution. [4]

**Considerations for a BH -** In the presence of a BH we impose Eq. (2.48) and (2.50) boundary conditions on $\beta^i$ while, at the same time, fixing the irreducible mass (2.61), the Christodoulou mass (2.63), and the dimensionless spin parameter $\chi$ (2.64). Furthermore, source terms in Eq. (2.19) are set to zero.

**Considerations for a NS -** Conversely, when a NS is present, we must also compute the source terms to be included in Eqs. (2.19) and rescale the equations by $p/\rho$ along with imposing (2.38) boundary conditions. Additionally, we solve equation (2.32) and impose boundary conditions (2.51) on the fluid and the velocity potential. In this stage the matter is only rescaled by a constant

$$H \to H = H_{\rm const}(1 + \Delta_H), \tag{2.78}$$

where $H_{\rm const}$ is the distribution of matter from the previous solution (e.g., boosted isolated solution) and $\Delta_H$ is found by enforcing the baryonic mass of the NS is

[3] The functional form of $\kappa$ was motivated by superimposed Kerr initial data[4], [89], however, the utility is quite different in this case.

[4] A converged solution at fixed $\Omega$ does not guarantee convergence to an equilibrium configuration since the respective equilibrium constraint, especially at very close separation, is not easily satisfied. However, for physically reasonable separations (i.e., when equilibrium is a reasonable assumption), convergence is highly expected.

fixed. In a binary setup, the tidal influence of the companion object will result in a change in the velocity profile of the fluid due to Lorentz forces and, from Eq.(2.66), we can see that the volume integral for the measured baryonic mass simply scales as a function of the Lorentz factor, W. Therefore, solving for $\Delta_H$ by enforcing $M_B = \text{const}$ ensures conservation of rest-mass density. There are two key points to mention:

1. Without using a simple rescaling in the initial fixed $\Omega$ stage, the solver will often diverge

2. Without boosting the isolated NS solution prior to import or using an incorrect boost to the NS such as a linear boost, the solution will also diverge even if initially rescaled

Both points highlight the importance of using superimposed boosted isolated objects for the initial guess within the `FUKA` solvers.

### 2.6.2 - II Quasi-equilibrium stage

In the *quasi-equilibrium* stage the same system of equations and boundary conditions as specified in Sec. 2.6.2 - I are used only now the COM and $\Omega$ are no longer fixed and, are instead, found by enforcing quasi–equilibrium conditions and minimizing $P_{\rm ADM}$. In the case of BBH, this is fixed by the virial constraint

$$M_K - M_{\rm ADM} = 0\,,$$

whereas for binaries that include a NS, equilibrium determined based on the "force-balance equation"

$$D_x H|_{x_{c_{1,2}}} = 0\,, \tag{2.79}$$

such that the divergence of the log specific enthalpy is zero along the x-axis where the stellar center(s) are located. This stage is very important as this will provide a binary where the matter is now in hydrostatic equilibrium (i.e., no longer rescaled) in the case of NSs and will compute a COM estimate by finding the location of the axis of rotation $\mathbf{x}_{\rm com}$ such that the ADM linear momenta are minimized

$$P^i_{\rm ADM} = 0. \tag{2.80}$$

Given our domain decomposition is defined *a priori* and as such the coordinate system is always centered about the origin and not the COM, the shift in the coordinate system is implemented by shifting our helical Killing vector

$$\xi^i = \Omega \partial^i_\phi(\mathbf{x}_{\rm com}). \tag{2.81}$$

Furthermore, having a more precise estimate of the COM of the system allows for a more accurate 3.5PN estimate which can be used in the *eccentricity reduction* stage.

### 2.6.2 - III BNS drift removal stage

In the case of BNS initial data there is an additional intermediate stage before proceeding to the *eccentricity reduction stage* stage in order to fix both the $x$ and $y$ components of the COM. During the *quasi-equilibrium* stage, both stars are fixed based on the "force-balance" equation (2.79). As such, only one component of $P_{\rm ADM}$ is minimized during the *quasi-equilibrium* stage, otherwise, the system of equations would be overdetermined. Furthermore, the values of $\Omega$ computed when only one star is constrained by the "force-balance" equation are inconsistent in the regime of highly asymmetric or highly spinning stellar configurations. Even more so, we found that resorting to a averaging of the two values leads to inconsistent and, in extreme cases, non-convergent behavior. Therefore, in this intermediate stage, $\Omega$ is fixed from the equilibrium solution and the fluid solution is rescaled in the same way as in the *non-equilibrium* stage thereby removing Eq. (2.79) for both stars from the system of equation. With this reduced system, we can now enforce that $P^i_{\rm ADM}$ is minimized.

To further elaborate on the quasi-equilibrium nature of this stage, it is important to highlight that, although rescaling ensures conservation of rest–mass, rescaling the fluid solution results in violating the first integral equation (2.37) to a degree. We have found that resorting to this rescaling does result in a slight breathing in the central density, however, we found throughout our exploration of the space of parameters in $q$ and $\chi$ that the impact on the evolution of the binary when comparing solutions from the *quasi-equilibrium* and the *BNS drift removal* stage are insignificant and are, overall, subdominant to the approximations made by resorting to the simplified model leading to Eq. (2.37). Furthermore, the dynamics of the binary when using solutions from the *BNS drift removal* are indistinguishable from solutions from the *quasi-equilibrium* stage aside from the spurious drift still present in the *quasi-equilibrium* solution.

As with the equilibrium stage for the BBH and BHNS ID, this stage is important to further refine the COM of the system in order to remove spurious drifts prior to the *eccentricity reduction* stage and obtain more reliable post-Newtonian estimates for eccentricity reduction.

### 2.6.2 - IV Eccentricity reduction

After the *quasi-equilibrium* stage(s) we have the option to perform an additional stage which will take the ID out of equilibrium, but with the goal to reduce the eccentricity of the binary in order to obtain a more circular inspiral. This is done by either utilizing 3.5PN analytical estimates (See Append B) or through iterative eccentricity reduction procedures as discussed in detail in Sec. 2.5.

Similar to what was discussed in Sec. 2.6.2 - I, since the *eccentricity reduction* stage results in a non-equilibrium configuration by fixing $\Omega$ and $\dot{a}$, we resort to fixing the matter and rescaling it by a constant. For this stage the correction to $\Omega$ is usually quite small ($\sim [10^{-3}, 10^{-5}]$) with the resulting scaling factor $\sim 10^{-4}$. Therefore, the impact to the solution describing the NS very nearly reflects a solution in hydrostatic equilibrium.

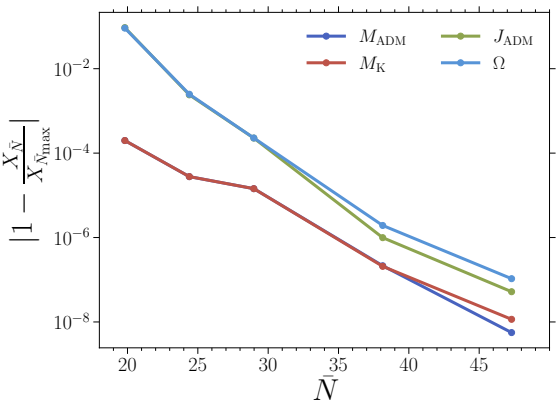


Figure 2.2: Convergence analysis for an equal-mass BBH system where we plot the absolute relative difference for a given quantity $X$ as a function of resolution $\bar{N}$ (see Eq. (2.82)). Here $X$ is orbital velocity $\Omega$, the ADM mass $M_{\rm ADM}$, the ADM angular momentum $J_{\rm ADM}$, and the Komar mass $M_{\rm K}$ computed using the assumption of quasi–equilibrium. The relative difference of these quantities at a given resolution are compared to the highest resolution dataset of $\bar{N}_{\rm max} = 52$. This figure has been reused from [9].

## 2.7 Consistency results

When generating initial data there are multiple aspects that can be analyzed to ensure the solution is consistent with expectations and the utilized analytical models. In this section we will discuss our results which highlight the self-consistency of our solution prior to utilizing an evolution framework.

### 2.7.1 Spectral convergence

A first step when analyzing a solution is to perform a convergence analysis which compares the solution obtained at low resolution to that obtained at the highest possible resolution. The reasoning is two-fold such that we expect with increasing resolution that our solutions will converge to the highest resolution solution and, since we are using a spectral solver, we expect such convergence to be exponential as a function of the global resolution of our spectral grid. In order to characterize the global resolution of our solution, we first reiterate that we utilize a domain decomposition $\mathcal{D}$ such that we obtain a continuous map across the entire physical space. As such, our binary space is decomposed into a minimum of twelve domains each with a given spectral resolution. For a given domain $i$ in $\mathcal{D}$, we denote the total number of collocation points as $N_{(i)}$. Therefore, the global resolution of the numerical space can be quantified as

$$\bar{N} := \left(\sum_{i\in\mathcal{D}} N_{(i)}\right)^{\frac{1}{3}}. \tag{2.82}$$

We can then show convergence for a given quantity, $X$, of which we report on $M_{\rm ADM}$, $M_{\rm K}$, $\Omega$, and $J_{\rm ADM}$. To this end we have computed a sequence of ID at various resolutions $\bar{N}$ for an equal-mass irrotational BBH configuration and extracted these quantities. The absolute relative difference to the highest resolution $\bar{N}_{\rm max}$ has been computed and is shown in Fig. 2.2. We highlight the fact that, although the error for $M_{\rm K}$ and $M_{\rm ADM}$ are consistently lower than $\Omega$ and $J_{\rm ADM}$, we do find exponential convergence among the analyzed quantities.

The discrepancies in the absolute relative difference are not surprising overall. In the case of $M_{\rm K}$ and $M_{\rm ADM}$, these quantities are measured at the asymptotic limit and are dominated by the total mass of the system which are fixed in each solution. However, $\Omega$ is a condition that is fixed by an integral at spatial infinity by imposing the virial theorem which introduces errors from two main sources:

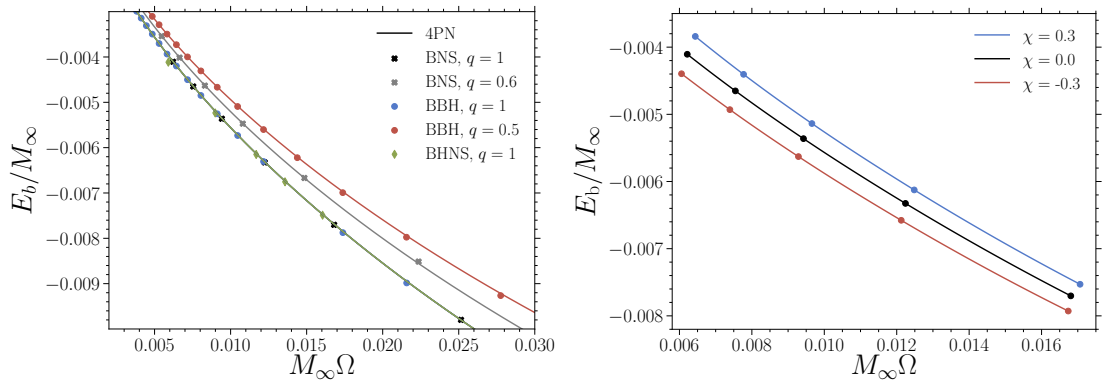


Figure 2.3: Comparison of the dimensionless binding energy as a function of the dimensionless orbital velocity to 4PN predictions given by Eq. (B.5) (solid lines). *Left*: We plot quasi–equilibrium sequences of equal mass irrotational BBH (circles), BNS (squares), and BHNS (diamonds) datasets as well as asymmetric BBH ($q = 0.5$) and BNS ($q = 0.6$) datasets all of which show agreement when compared to 4PN estimates. *Right*: Conversely, we plot sequences of equal mass BNS datasets with dimensionless spins of $\chi = [-0.3, 0, 0.3]$ such that the sign denotes (anti-)aligned spins. We again find good agreement within the range of binary separations considered. This figure has been reused from [9].

1. The virial theorem is the difference between $M_{\rm K}$ and $M_{\rm ADM}$ which already contain errors of their own

2. The calculation at spatial infinity suffers from finite resolution over a large region of physical space

Furthermore, $J_{\rm ADM}$ measures the total spin angular momentum of the binary at spatial infinity which is a function of orbital velocity. Therefore, it is expected that the error in $J_{\rm ADM}$ will correlate with the error in $\Omega$ as we see in Fig. 2.2.

### 2.7.2 Equilibrium sequences

An additional consistency check that can be made is to compare the binding energies measured from *quasi-equilibrium* initial data solutions to post-Newtonian estimates. As such, we compute sequences of *quasi-equilibrium* ID at various separations and compare the dimensionless binding energy $E_b/M_\infty$ to the dimensionless spin orbital velocity $M_\infty\Omega$. We have considered both equal mass ($q = 1$) for BBH, BHNS, and BNS initial data as well as asymmetric initial data ($q = 0.5$ for BBH and $q = 0.6$ for BNS). Initial data involving a neutron star is generated using a polytropic EOS with $K = 100$ and $\Gamma = 2$. In Fig. 2.3 (left panel) we plot $E_b/M_\infty$ of our sequences of BBH (circles), BHNS (diamonds), and BNS (squares) initial data along with the 4PN estimates of which we find they closely agree.

In Fig. 2.3 (right panel) we extend this analysis in the case of BNS initial data by incorporating the influence of spin on the binding energy. In this way we consider sequences of equal mass BNS initial data where the spins are either irrotational or has a dimensionless spin of $\chi = \pm 0.3$ where the sign denotes (anti-)aligned with the axis of orbital rotation. As used in the previous sequences, the fluid is modeled using the same $\Gamma = 2$, $K = 100$ polytropic EOS. We find that the binaries with aligned spin are less bound which is inline with [31] and will result in more orbits prior to merger. Conversely, anti–aligned spins are much more tightly bound and therefore will merge faster. These results overall agree

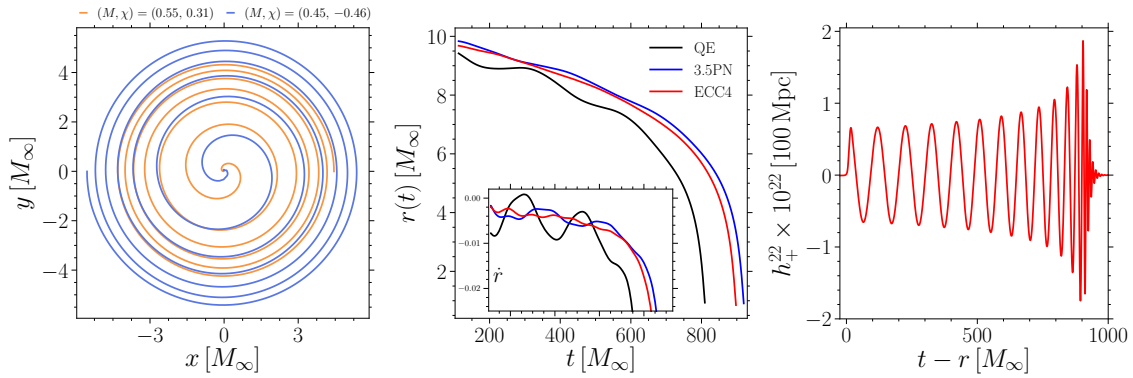


Figure 2.4: Results from the evolution of a BBH configuration with properties similar to GW150914. *Left:* Orbital trajectory of the eccentricity reduced dataset `ECC4`. *Middle:* Coordinate separation timeseries with its time derivative within the inset for the quasi–equilibrium (`QE`), eccentricity reduced using 3.5PN estimates (`3.5PN`), and the resulting solution from four iterations of eccentricity reduction (`ECC4`). *Right:* Gravitational wave strain of the $(\ell, m) = (2, 2)$ mode, $+$-polarization for the `ECC4` dataset. This figure has been reused from [9].

with the 4PN estimates (solid lines) as shown in Fig. 2.3.

## 2.8 Evolution results

The results shown in Sec. 2.7 provide a first estimate to the degree to which our initial data codes provide a consistent solution to the EFE. It is then natural to extend our analysis to the evolution of various initial data sets to ascertain their evolution characteristics. Unless stated otherwise, we have utilized the evolution setup as discussed in Appendix C.

### 2.8.1 Evolution of black-hole binaries

Although other codes exist to generate asymmetric, spinning binary black hole initial data, we include here a test case that encapsulates the features of the `FUKA` BBH initial data solver specifically the ability to perform iterative eccentricity reduction as well as quantify its influence on the resulting evolution.

#### 2.8.1 - I GW150914

As our test case we construct initial data based on the event GW150914. More specifically, we utilize an evolution setup and initial data characteristics inline with [135] which consists of a mass ratio $q = 0.8055$ with $\chi_1 = 0.31$, $\chi_2 = -0.46$, and an initial coordinate separation of $d_0 = 10$M. This includes the use of the `McLachlan` spacetime evolution thorn using the BSSNOK evolution equations. Furthermore, the dimensionless spins are (anti-)aligned with the orbital axis of rotation. In the following we will describe the series of evolutions that have been performed, however, we refer the reader already to Fig. 2.4 for a summary of the dynamics which will be described in detail.

To begin our analysis we initially generate the ID while only assuming quasi-equilibrium (QE) when computing $\Omega$. However, given the asymmetry and spin in the system the eccentricity of the binary is very pronounced as can be seen in the middle panel of Fig. 2.4. As a first attempt to reduce the eccentricity we utilize `FUKA`'s built-in 3.5PN estimates for $\Omega$ and $\dot{a}$. We see already in Fig. 2.4 (mid-

dle) that the eccentricity of the inspiral is already considerably reduced when compared to QE ID. Furthermore we repeated the iterative eccentricity reduction procedure as discussed in Sec. 2.5 until the measured eccentricity fell below $10^{-4}$. The final dataset, referred to as `ECC4`, shows a considerably cleaner evolution of the coordinate separation in the middle panel of Fig. 2.4. Similar to the fitting procedure proposed in[79], we ignore the initial half orbital period which includes spurious junk data in the evolution which is largely attributed to the equilibrium assumptions and, therefore, ignores gravitational radiation present in the system. Moreso, we fit using the time derivative of the coordinate separation ($\dot{r}$) which is much more sensitive to eccentricities on the order of $10^{-3}$ as discussed in Sec. 2.5. It is important to mention that we also found that resulting corrections ($\delta\Omega\,, \delta\dot{a}$) can be sensitive to the fitting procedure used, the number of orbits included, and the initial estimates of the fitting parameters. Therefore, it is important to be consistent throughout each iteration of eccentricity reduction.

In addition to the coordinate separation we include the orbital track (left plot) along with the $\ell = m = 2$ multi–pole of the $+$ polarization of the gravitational wave strain (right plot) within Fig. 2.4 from the evolution of the `ECC4` ID. The orbital track shows a clean inspiral with negligible eccentricity and no apparent linear drift of the binary.

### 2.8.1 - II Influence of ID resolution on gravitational-wave phase

An additional aspect of the initial data that is useful to quantify is the impact of the initial data resolution on the evolution. Furthermore it is useful to determine at which point the ID resolution is the dominant error source compared to the evolution resolution.

To answer this question we perform a total of nine simulations using the `ECC4` set of parameters with different ID resolution, i.e., $\bar{N} \in \{24, 38, 42\}$, and different evolution resolutions, i.e., low resolution ($\Delta x_{\rm LR}/M = 0.024$), medium resolution ($\Delta x_{\rm MR} = 0.019$), and high resolution ($\Delta x_{\rm HR}/M = 0.015$). As a reference quantity, we choose to measure the characteristic GW phase of the $\ell = m = 2$ multi–pole of the $+$ polarization of the GW strain. This quantity has been chosen due to the fact that it is a coordinate independent quantity as well as plays an important role in GW modeling [136]. In all cases, the evolution scheme utilizes an 8th order

| | $\lvert\Delta\varphi\rvert_{\rm LR}$ | $\lvert\Delta\varphi\rvert_{\rm MR}$ | $\lvert\Delta\varphi\rvert_{\rm HR}$ | $M_{\rm ADM}\ [M]$ | $J_{\rm ADM}\ [M^2]$ |
|---|---|---|---|---|---|
| $\bar{N} = 24$ | 12.214 | 1.888 | 0.095 | 0.9897 | 0.9572 |
| $\bar{N} = 38$ | 12.067 | 1.771 | 0.008 | 0.9899 | 0.9573 |
| $\bar{N} = 42$ | 12.067 | 1.770 | 0.000 | 0.9899 | 0.9573 |

Table 2.1: In this table the rows correspond to three difference ID resolutions, $\bar{N} = \{24, 38, 42\}$ whereas the columns of $|\Delta\varphi|$ correspond to the measured gravitational-wave phase differences at merger for the $\ell = m = 2$ multipole of the $+$ polarization for three different evolution resolutions (LR, MR, HR) as compared to the measured GW phase from the highest evolution (HR) and ID resolution ($\bar{N} = 42$). Furthermore, columns of ADM mass $M_{\rm ADM}$ and ADM angular momentum $J_{\rm ADM}$ as computed from the initial data slice are included. This table was original published in [9].

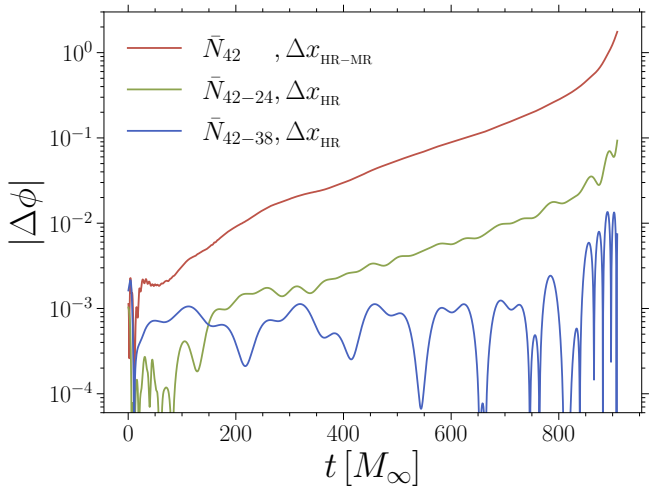


Figure 2.5: The timeseries of the absolute difference of the GW phase $\ell = m = 2$ multipole of the $+$ polarization for configurations with different ID resolution , i.e., $\bar{N} = \{24, 38, 42\}$, or different evolution resolutions, i.e., medium resolution ($\Delta x_{\rm MR}$) or high resolution ($\Delta x_{\rm HR}$) when compared to the GW phase measured from the highest evolution ($\Delta x_{\rm HR}$) and ID ($\bar{N} = 42$) resolution of the ECC4 dataset. This figure has been reused from [9].

finite–differencing scheme to further minimize errors throughout the evolution.

To quantify the influence of ID and evolution resolution, we compute the absolute relative difference $|\Delta\varphi|$ for each configuration as compared to the measured GW phase from the highest evolution (HR) and ID resolution ($\bar{N} = 42$). We include Tab. 2.1 as a tabulated reference which includes the computed absolute GW phase differences when utilizing the values extracted at the time of merger. Included in this table is also the measured ADM mass $M_{\rm ADM}$ and ADM angular momentum $J_{\rm ADM}$ from the ID. We note that the relative difference of $J_{\rm ADM}$ is comparable for all of the resolutions considered. As briefly discussed in Sec. 2.7.1, a significant source of error in low resolution ID for quasi–equilibrium datasets is related to the computed value for $\Omega$ between low and high resolution ID. However, since we are using eccentricity reduced data such that $\Omega$ is fixed, this source of error is removed and consistent measurements for $J_{\rm ADM}$ are obtained regardless of the resolution used for the ID. This already hints that the dynamics of the binary for a given evolution resolution should be fairly similar between ID resolutions.

To further explore this point we include in Fig. 2.5 the timeseries describing $|\Delta\varphi|$ when comparing ID resolutions ($\bar{N}_{42-24}$, $\bar{N}_{42-38}$) at fixed evolution resolution ($\Delta x_{\rm HR}$). As expected, the dynamics of the binary yield a consistent GW phase nearly independent of the ID resolution when $\Omega$ is fixed. We note that for $\bar{N}_{42-24}$ a much more apparent non–linear growth leading up to merger is observed, however, $|\Delta\varphi|$ by merger is still only $\sim 0.1$ rad. In contrast, we include the dark red timeseries which is associated with the comparison of evolution resolutions $\Delta x_{\rm HR}$ and $\Delta x_{\rm MR}$ for fixed ID resolution $\bar{N} = 42$. In this case we see that a change in the evolution resolution results in $|\Delta\varphi|$ that is roughly an order of magnitude higher than the difference obtained when comparing ID resolutions.

These results highlight that, in the case of vacuum evolution, the error introduced by the ID resolution is subdominant compared to the evolution resolution so long as $\Omega$ is fixed either by using iterative eccentricity reduction or PN estimates.

### 2.8.2 Evolution of neutron star binaries

Within this section we include the evolution of representative test cases to characterize the influence of initial data resolution on the dynamics of the evolved

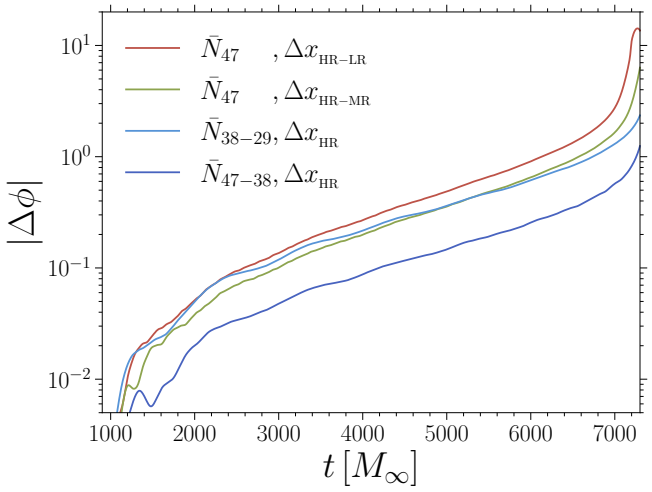


Figure 2.6: Similar to Fig. 2.5 only the ID describes an equal–mass irrotational BNS with the fluid modeled using the SLy EOS. The red and green sequences are computed for fixed ID resolution ($\bar{N} = 47$) and compare the influence of evolution resolution. The blue lines correspond to a fixed evolution resolution of $\Delta x_{\rm HR}$ such that the impact of ID can be seen. This figure has been reused from [9].

binary, to compare to previously published works, and to examine more extreme configuration using the FUKA BNS solver to showcase its capabilities.

### 2.8.2 - I Dependence of evolution dynamics on ID resolution

To ascertain the degree to which the initial data resolution can influence the resulting evolution dynamics we perform an analysis similar to Sec. 2.8.1 - II by performing a series of nine evolutions with varying ID resolution of $\bar{N} \in \{29, 38, 47\}$ and evolution resolutions of, i.e., low resolution ($\Delta x_{\rm LR} = 0.25 M_\odot \approx 369$m), medium resolution ($\Delta x_{\rm MR} = 0.2 M_\odot \approx 295$m), and high resolution ($\Delta x_{\rm HR} = 0.145 M_\odot \approx 215$m). [5] To do so, we use an equal–mass, irrotational binary configuration where each NS has a fixed baryonic mass of $M_b = 1.4946$ with an initial coordinate separation of $52.42$km. Furthermore, we have modeled the fluid using a tabulated version of the SLy EOS. Finally, since the QE computed value of $\Omega$ is heavily dependent on ID resolution used, we have elected to utilize 3.5PN estimates of $\Omega$ and $\dot{a}$ to remove this degree of freedom and overall, reduce the resolution dependence of the ID solution. Alternatively, iterative eccentricity reduction parameters could also have been used, but, overall, should not impact the results presented here.

In Fig. 2.6 we plot the absolute phase difference $|\Delta\varphi|$ for the $\ell = m = 2$ multi–pole of the $+$ polarization for ID resolutions of $\bar{N} = \{29, 38\}$ as compared to $\bar{N} = 47$. In contrast to Fig. 2.5, the sequences are not aligned at $t = 0$ and are, instead, aligned at $t = 1000 M_\odot$. The reason for this is that during the start of the evolution a considerable amount of junk data is produced in the simulation similar to what is seen in the case of the BBH which are compounded given the additional approximations used in the fluid description of the neutron stars. We find that by decreasing the ID resolution from $\bar{N} = 47$ down to $\bar{N} = 29$ results in $|\Delta\varphi| > 1$ whereas decreasing the ID resolution from $\bar{N} = 47$ down to $\bar{N} = 38$ results in $|\Delta\varphi| \approx 1$ which indicates that ID resolution can have an appreciable impact on the inspiral especially for long inspiral simulations.

Furthermore, we contrast the influence of evolution resolution by comparing

[5] Unlike in the BBH simulations, here only a 4th order finite difference scheme is used to evolve the spacetime. This is reasonable given the order of convergence of the hydro evolution code ($< 3$) dictates the accuracy of the results.

evolutions of high ID resolution of $\bar{N} = 47$ using $\Delta x_{\rm LR}$ and $\Delta x_{\rm MR}$ evolution resolutions. The absolute phase difference $|\Delta\varphi|$ is then computed between these runs as compared to the run at high ID and evolution resolution. In this case, we find the impact of evolution resolution is roughly an order of magnitude higher when comparing to the changes in $|\Delta\varphi|$ due to ID resolution. Moreso, in all cases the slope in the growth of $|\Delta\varphi|$ is nearly the same in all simulations indicating that the evolution resolution plays the dominant role in the computed errors.

In conclusion, we have shown that for the given BNS configuration, the errors measured using the $|\Delta\varphi|$ are dominated by the evolution resolution, similar to what was seen in the BBH analysis [c.f. Sec. 2.8.1 - II]. In the case of high evolution resolution, low resolution ID will provide similar evolution dynamics, however, additional accuracy can be obtained by utilizing higher resolution ID on the order of $|\Delta\varphi| \approx 1$. This is likely most important to those studying long inspiral configurations for waveform modeling. Conversely, in the case of decreasing the evolution resolution we find considerably larger errors even at high ID resolution further highlighting the need for high resolution evolutions when modeling binaries that include a NS.

### 2.8.2 - II Comparison of spinning binary neutron star initial data

To verify the accuracy of our initial data we continue our analysis using a benchmark test setup based on previously published results for BNS configurations. As a first setup, we utilize an equal–mass binary configuration with the same characteristics as documented in [31] where each NS has a fixed baryonic mass of $M_b = 1.7745$. Furthermore, two different spin configurations are generated such that each NS has a spin rotation parameter of $\omega \in \{0, 0.01525\}$ and the coordinate separation of the centers of each NS is $d_0 = 47.2 M_\odot$. To close the system of equations the EOS utilized is a single polytrope with $K = 123.6$ and $\Gamma = 2$.

Overall our results which are summarized in Tab. 2.2 agree very well with [31], however, we do note discrepancies in the measured spin-angular momentum for the spinning BNS configuration. We believe this is primarily due to the differences in how the spin–angular momentum is measured in [31] as compared to this work. However, the discrepancy is approximately $0.3\%$ for the configuration considered which still shows close agreement.

| Reference | $\omega\ [M_\odot^{-1}]$ | $M_b\ [M_\odot]$ | $M_{\rm QL}\ [M_\odot]$ | $\mathcal{S}_{\rm QL}\ [M_\odot^2]$ | $\mathcal{S}_{\rm QL}/M^2$ |
|---|---|---|---|---|---|
| Tichy+ 2019 [31] | 0.00000 | 1.7745 | 1.620 | −0.0007 | −0.0003 |
| this work | 0.00000 | 1.7745 | 1.620 | −0.0007 | −0.0003 |
| Tichy+ 2019 [31] | 0.01525 | 1.7745 | 1.626 | 0.8652 | 0.3217 |
| this work | 0.01525 | 1.7745 | 1.626 | 0.8631 | 0.3209 |

Table 2.2: The results for the irrotational and spinning BNS initial data sets that can be compared to [31] published results where $\omega$ is the fixed rotational parameter for each NS, $M_b$ is the fixed baryonic mass, $M_{\rm QL}$ is the quasi–locally measured gravitational mass, $\mathcal{S}_{\rm QL}$ is the quasi–local spin–angular momentum, and the dimensionless spin normalized by $M = 1.64\, M_\odot$. Discrepancies in the results are largely attributed to the different approaches to compute the spins. This table is taken from [9].

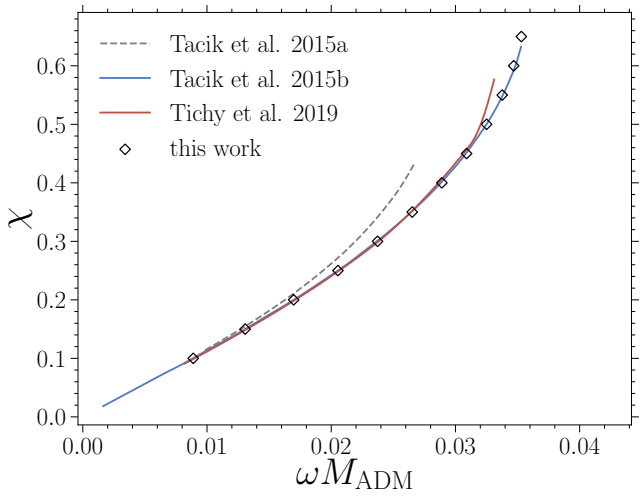


Figure 2.7: Characteristic results showing the relation between the dimensionless spin $\chi$ as a function of the dimensionless spin–rotation parameter $\omega$ for a sequence of $q = 1$ BNS initial data (open symbols) using a polytropic EOS with $K = 123.6$ and $\Gamma = 2$. Solid lines denote previously published fitting functions reported in [31], [80], [87]. This figure has been reused from [9].

To gain further insights into this discrepancy and to gain some confidence regarding our implementation of equations Eq. (2.33) as well as rescaling of Eqs. 2.19 and the relativistic Euler equations, we have generated a sequence of BNS models where the ADM mass of each NS has been fixed to $M_{\rm ADM} = 1.64 M_\odot$. The fluid is described once again by an EOS model using a single polytrope with $K = 123.6$ and $\Gamma = 2$. The variable in these sequences comes from varying the fixed spin rotation parameter $\omega$ from zero until our solver no longer converges. Our results along with those obtained from [87], [80], and [31] have been included to show the overall consistency of `FUKA` ID which are shown in Fig. 2.7. We note that the resulting fit from [87] is based on ID generated using an incorrect first integral which was corrected in a later published erratum [80].

In the slowly spinning regime all codes generate similar results which exhibits, overall, a linear relation between $\chi$ and $\omega$. As $\omega$ increases beyond $\omega M_{\rm ADM} \sim 0.012$, not only do the incorrect results from [87] begin to become apparent, but we also begin to observe non-linear behavior between $\chi$ and $\omega$. Additionally, in the highly spinning regime we see some discrepancy with [31] which is, again, largely attributed to differences in how the spin measurement is being computed.

### 2.8.2 - III Eccentricity reduced asymmetric spinning ID

For an initial test of the full functionality of the `FUKA` BNS ID solver, we have chosen an example configuration with a total mass $M_\infty = 2.7$ and $q = 0.6875$ with component spins of $\chi_1 = 0$ and $\chi_2 = 0.6$ where the spin is chosen to be on the more massive star. Furthermore, the ID is generated using the tabulated `TNTYST` EOS [137]. As observed in the BBH test case, it can be expected that a BNS system where the force-balance constraint Eq. (2.79) has been enforced to obtain ID in quasi–equilibrium will result in an eccentric binary. Therefore, in order to obtain a binary in a circular orbit, we perform the same eccentricity reduction procedure as done in Sec. 2.8.1 - I.

In Fig. 2.8 we plot the binary separation timeseries based on the initial QE ID (blac) along with the datasets utilizing 3.5PN estimates of $\Omega$ and $\dot{a}$ (blue) and, finally, the ID after four iterations of eccentricity reduction which we will refer to as `ECC4` (red). To obtain `ECC4` we initially generate ID using a resolution of

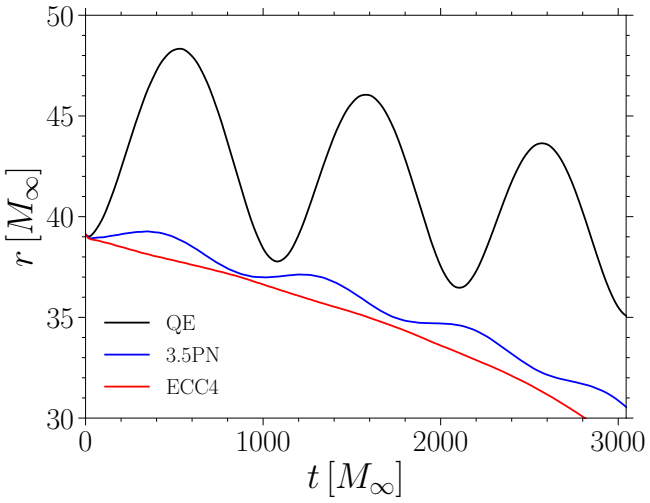


Figure 2.8: Initial test run showing the degree of eccentricity for an asymmetric rapidly spinning BNS ID in quasi–equilibrium (black), using 3.5PN estimates (blue), and after using iterative eccentricity reduction (red). The binary configuration used is a $M_\infty = 2.7$, $q = 0.6875$, $\chi_1 = 0$ and $\chi_2 = 0.6$ where the fluid is modelled using the TNTYST EOS. This figure has been reused from [9]

$\bar{N} = 29$ and an evolution resolution of $\Delta x = 0.2 M_\odot$ for the first iterations of eccentricity reduction. For ECC4 we use a resolution of $\bar{N} = 38$, however, as we discover in Sec. 2.8.2 - I, increasing the resolution beyond $\bar{N} = 29$ has no appreciable influence on the evolution. The eccentricity measured from ECC4 is $\lesssim 10^{-4}$. Further iterative corrections were attempted, however, beyond this point fitting against Eq. (2.72) no longer yields useful corrections.

Figure 2.8 further reinforces that QE ID using Eq. (2.79) results in a highly eccentric inspiral. Furthermore, utilizing the built–in 3.5PN corrections to $\Omega$ and $\dot{a}$ provide orders of magnitude decrease in the eccentricity. Moreso, the eccentricity1 measured from the ID using 3.5PN estimates is similar to those measured from equal–mass non–spinning quasi–equilibrium. Finally, iterative eccentricity reduction can be used to obtain a low eccentricity inspiral. It is therefore recommended to, at a minimum, utilize the 3.5PN estimates for generating BNS ID as it not only allows for a considerably less eccentric binary, but also removes a significant source of resolution dependent error when generating ID by fixing $\Omega$.

### 2.8.2 - IV Extremal BNS configurations

In an effort to probe the limits of the FUKA BNS solver we have chosen a set of final test cases that examines the extremes of what is physically allowed in a BNS configuration. To that end, we model two binaries with a total mass $M_\infty = 3.2$ with mass ratio $q = 0.455$ using the TNTYST tabulated EOS with an initial separation of $d_0 = 30 M_\odot$. Furthermore, in the first binary, the component spins are both irrotational $\chi_1 = \chi_2 = 0$ and thus, the more massive star with $M_1 = 2.2$ is near $M_{\rm TOV}$ for the TNTYST EOS. In the second binary, the dimensionless spin of the primary is $\chi_1 = 0.6$, where such a high spin is motivated by a possibly recycled binary pulsar where the primary has gained a significant amount of matter and angular momentum throughout a phase of accretion. To our knowledge, these are still the smallest mass ratio BNS configurations examined to date and, with the modified algorithm discussed in Sec 2.6.2, can be obtained with minimal effort compared to what was necessary to obtain the original published results in [9].

For each configuration, ID solutions were obtained initially at a coarse resolution of $\bar{N} = 19$ without the need for any form of hand–tuning or modifications to the implemented system of equations or boundary conditions discussed

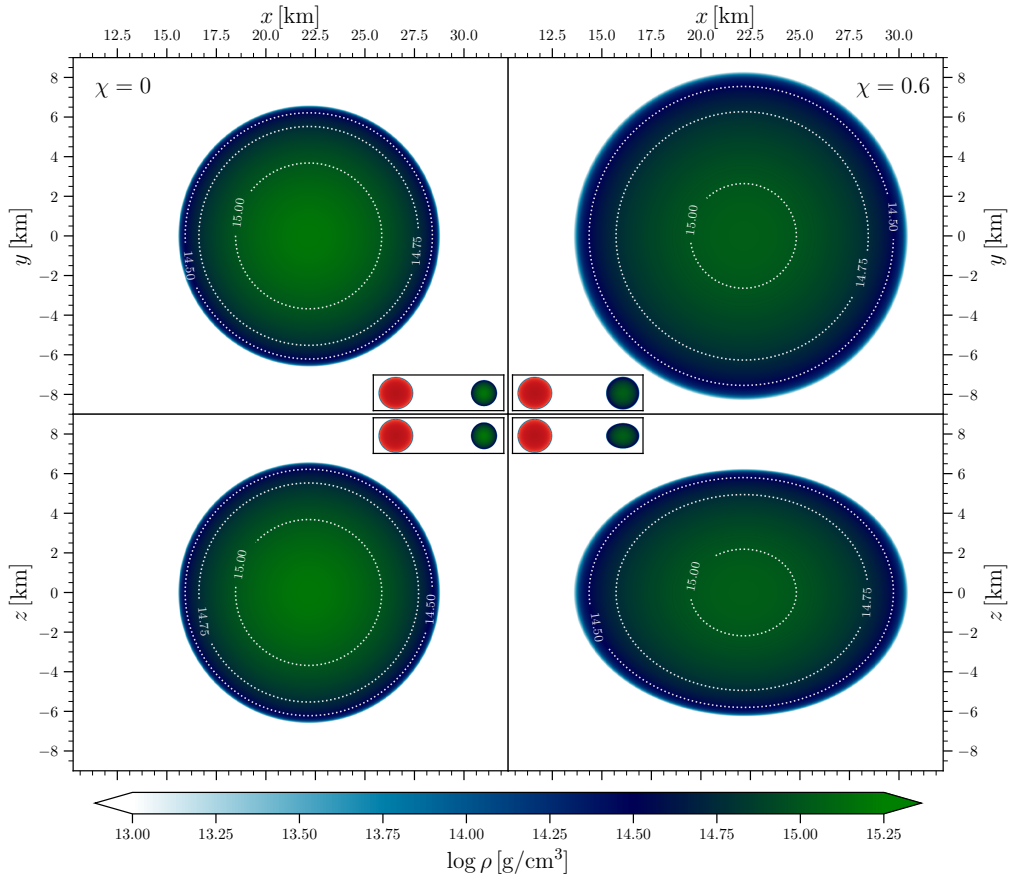


Figure 2.9: 2D slices in the $\langle x, y\rangle$ and $\langle x, z\rangle$ planes of the rest–mass density profile of the two extremal BNS configurations considered with component masses of $M_1 = 2.2\,M_\odot, M_2 = 1.0\,M_\odot$. The left column corresponds to the $\langle x, y\rangle$ and $\langle x, z\rangle$ slices of the binary where both stars are irrotational whereas the right column corresponds to the binary where the more massive star has a dimensionless spin of $\chi_1 = 0.6$. The panels only consider the more massive star, however, the small inset in each panel shows the equivalent binary cross section with the red being the companion star which is the same in both binary configurations. This figure has been reused from [9]

in Sec. 2.1. The coarse solution was then interpolated onto a higher resolution spectral grid of $\bar{N} = 47$ before being resolved. Furthermore, the eccentricity of each binary was reduced using the same iterative reduction procedure discussed in Sec. 2.5 until the eccentricity reached $\lessapprox 10^{-4}$.

To investigate the inherent properties of the irrotational massive star in contrast to the highly spinning configuration, we measure the rest–mass density of both massive stars and include 2D slices in the $\langle x, y\rangle$ and $\langle x, z\rangle$ planes which are shown in Fig. 2.9. The left column of Fig. 2.9 are the $\langle x, y\rangle$ and $\langle x, z\rangle$ density profiles for the irrotational, $2.2M_\odot$ star and the right column is for an equally massive star with a dimensionless spin of $\chi = 0.6$. Furthermore, within each panel is a small subplot showing the corresponding binary cross section where the secondary, which is the same mass and spin for both binaries, is shown in red. Finally, white contours of constant density are provided in order to identify the regions that contain the most mass for a given NS.

In the irrotational case we see a consistent nearly spherical profile between the two slices where the region the density exceeds $10^{15}[\mathrm{g/cm^3}]$ dominates the stellar interior. Conversely, the highly rotating configuration displays a fairly

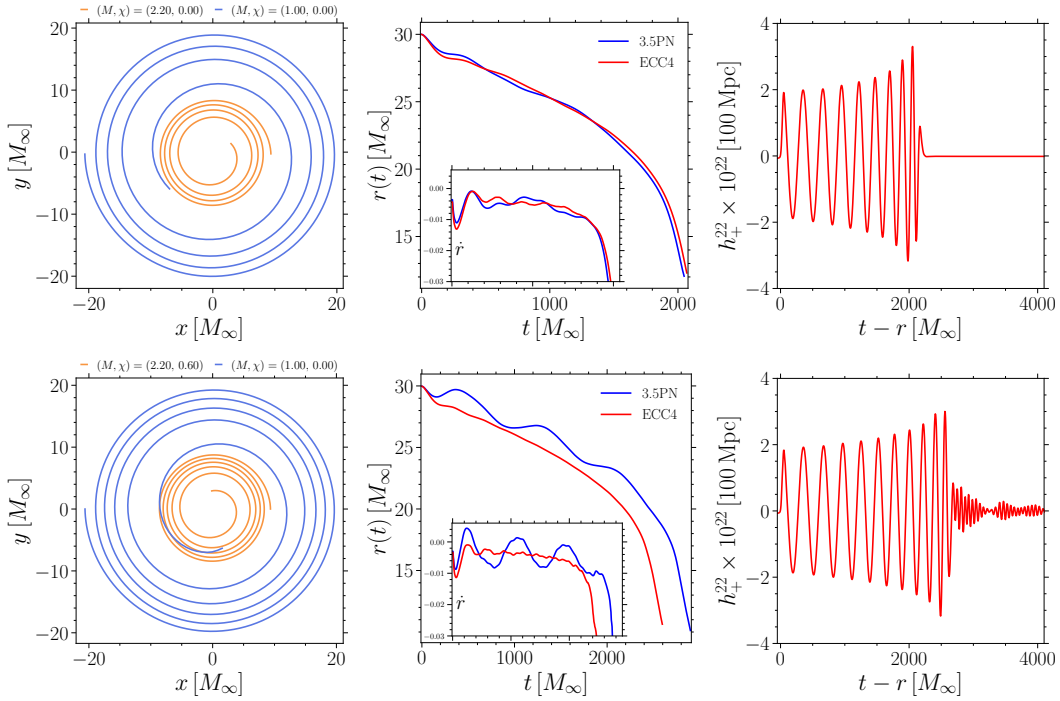


Figure 2.10: In the same manner as Fig. 2.4 only here we provide plots based on the extremal BNS configurations considered in Sec. 2.8.2 - IV with $M_\infty = 3.2\,, q = 0.455$ using the `TNTYST` EOS. *Above:* Includes the orbital track, timeseries of the proper separation, and the GW strain for the irrotational binary configuration. *Below:* The same as *Above* only for the binary configuration where the primary is highly spinning with a $\chi_1 = 0.6$. This figure has been reused from [9]

spherical shape in the $\langle x, y\rangle$ plane, but a highly oblate shape in the $\langle x, z\rangle$ plane. This is matches our expectation given the axis of rotation is along the z-axis and, with a highly spinning fluid, we would expect to see compression of the fluid along the axis of rotation and expansion orthogonal to this axis. Furthermore, we highlight that the spin induced deformation results in the more massive region of the star with density in excess of $10^{15}[\mathrm{g/cm^3}]$ $10^{15}[\mathrm{g/cm^3}]$ becomes quite small and localized in the stellar core.

In order to obtain a first look at the influence an extremal spinning primary can have on the evolution dynamics, we evolve the eccentricity reduced datasets (`ECC4`) for both binaries into the post-merger phase which we have visually summarized in Fig. 2.10 in the same manner as in Sec. 2.8.1 - I. Specifically, we plot the orbital trajectory of the binary, the evolution of the proper separation and its time derivative, and the $\ell = m = 2$ multi–pole of the $+$ polarization of the gravitational wave strain (right plot). In comparing these evolutions, we note that the binary with a highly spinning primary not only takes a longer time to merge due to the additional spin–angular momentum present in the system, but also leads to a metastable hyper–massive neutron star (HMNS) instead of promptly collapsing to a black hole. This is a very exciting result and one that has been the motivation for the exploration of the impact on remnant stability due to spin and mass asymmetry in BNS mergers which will be discussed in Ch. 3 and the study of the threshold mass to prompt collapse for asymmetric spinning BNS configurations in Ch. 4.

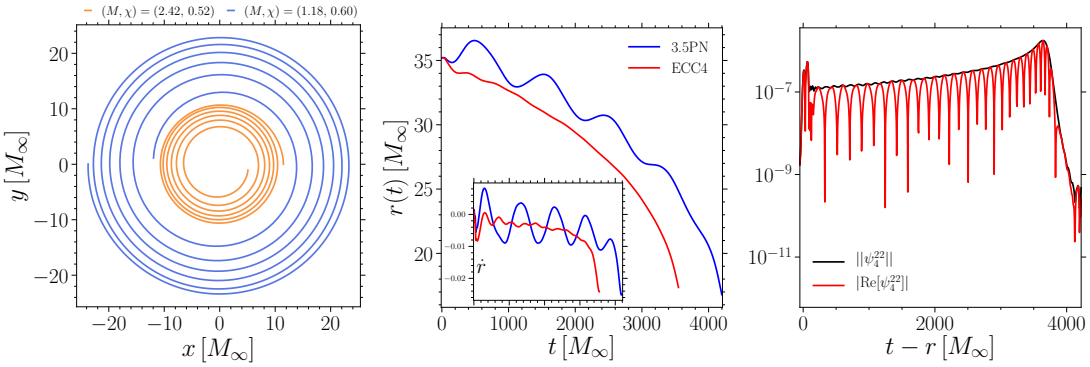


Figure 2.11: Same as in Figs. 2.4 and 2.10 but for a BHNS configuration. Note that the right panel reports the $\ell = m = 2$ multipole the $\psi_4$ Weyl scalar [(both the real part (red solid line) and its norm (black solid line)] in order to highlight the very short ringdown that would not be visible in the gravitational-wave strain. This figure has been reused from [9]

### 2.8.3 Evolution of black hole-neutron star binaries

The last FUKA ID solver is that for the construction of BHNS configurations. For our test case we utilize a fairly extreme configuration that includes a low mass black hole of $M_{\rm BH} = 2.42 M_\odot$ and a dimensionless spin of $\chi_{\rm BH} = 0.52$ with an extremal spinning companion NS with a mass of $M_{\rm NS} = 1.18 M_\odot$ and a dimensionless spin of $\chi_{\rm NS} = 0.6$. The binary components are constructed with a coordinate separation of $d_0 = 35.2 M_\odot$ with a total mass of $M_\infty = 3.6 M_\odot$ as defined by Eq. (2.70).

It is important to note that in the construction of BHNS initial data the resolution of the system, coordinate separation, and domain decomposition are sensitively intertwined in order to obtain a converged solution especially in the case of a low mass BH. The reason for this is that it has been found that in order to reliably obtain a converged solution, the domain decomposition of the bispherical domains should provide a coordinate map between two equal sized spherical shells. However, the coordinate radius of the BH is considerably smaller than that of the NS, so having outer radii that are equal results in insufficient resolution density near the excision region. The same resolution issues can also be obtained when considering highly asymmetric BBH systems with $q \lesssim 0.1$. In order to resolve this issue, additional spherical shells are added near the excision region thus allowing one to solve the BHNS ID at relatively coarse resolution initially as well as utilize resolution increase procedures to obtain a higher resolution solution at lower computational cost. It remains a long-term effort to further refine the procedure to automate the addition of shells around binary components to ensure reliable convergence and consistent solutions.

As performed in our previous results, we begin initially with the eccentricity reduced dataset using 3.5PN estimates for $\Omega$ and $\dot{a}$ where the component masses used are the Christodoulou mass of the BH and the ADM mass of the NS as measured in isolation. Even though we neglect the spins of the component objects this still provides a reasonable first estimate which can then be used as the starting point for iterative eccentricity reduction procedures. For this dataset we have obtained eccentricity reduction estimates using both Eq.(2.71) and (2.72) fitting expressions. After three iterations of eccentricity reduction we obtained an eccentricity $e \sim 5\mathrm{e}{-3}$, however, Eq. (2.71) no longer provided useful corretions

and, as in the case of BBH and BNS, we were only able to use corrections from Eq. (2.72) to obtain ECC4 with a resulting eccentricity of $\lesssim 10^{-4}$.

The results of the evolutions of the ID using 3.5PN estimates as well as ECC4 are included in Fig. 2.11. In the left plot we include the orbital track of the ECC4 dataset which not only demonstrates a smooth inspiral with negligible eccentricity, but also that the COM remains in the center of the evolution grid providing further evidence that the ADM linear momentums have in fact been minimized within the ID solver. Furthermore, during the import of the ID there are no special import considerations other than filling the BH that need to be addressed, e.g., there has been no manual corrections to the shift to remove spurious drifts. Next, the middle panel includes the time evolution of the separation distance and its time derivative. When comparing the middle panel to, for instance, Fig. 2.8 we see that the addition of spin–angular momentum aligned with the orbital axis of rotation from both compact objects results in higher initial eccentricity based on the irrotational 3.5PN estimates. Further testing could be done with implementing effective–one–body estimates where spin–spin and spin–orbital coupling corrections are considered and could be used to obtain more accurate estimates for $\Omega$ and $\dot{a}$; however, these have not been utilized within this work. Finally, the right panel is a semi–log plot of the magnitude of the $\psi_4$ Weyl scalar for the $\ell = m = 2$ multiple of the gravitational wave strain $+$–polarization and the magnitude of its real component as measured from the evolution of the ECC4 dataset. The transition to plotting the raw $\psi_4$ in semi-log scale is to be able to analyze the sharp cutoff due to the tidal disruption of the NS [c.f. [138]].

It is evident that the space of parameters now accessible with the new BHNS solver is incredibly large and will, hopefully, allow for further research into regions previously inaccessible using the previous generation of public ID solvers. Furthermore, we have not fully explored the extremes of the ID capabilities such as the highest spin that can be obtained and the evolutions of highly counter–rotating objects which we leave for future works to investigate. Finally, it is important to note that, in the case of BHs, the choices made for the XCTS degrees of freedom which enforce a conformally flat, maximally sliced background cannot produce black holes with spins $\gtrsim 0.85$. Therefore, moving to black holes with spins in the realm of $\chi \sim 0.99$ would require extensive research and, overall, a new implementation to obtain results similar to [89].

## 2.9 Summary

In this chapter we have laid the foundation for the projects to come which require the ability to reliably generate binary initial data across a broad range of mass ratios $q$ and dimensionless spins $\chi_{\langle 1,2\rangle}$. Furthermore, the use of physically motivated tabulated EOS play a crucial role in the projects to come both in looking at merger dynamics and potential astrophysical observables that are dependent on the EOS as well as our analysis on the quasi–universal relation of the threshold mass.

It is with this in mind that we have developed a suite of elliptic solvers for BBH, BNS, and BHNS ID based on the KADATH spectral solver library which are capable of exploring a large portion of the available parameter space in $q$, and $\chi$ as well as polytropic or finite temperature tabulated EOSs. In this work we have examined representative test cases of the FUKA binary ID solvers that aim

to showcase the capabilities of each solver as well as quantify the contribution of error from the ID on the dynamical evolution. Furthermore, FUKA is the first public code that affords the ability to perform iterative eccentricity reduction of BHNS and BNS ID. Within the FUKA suite, it is now possible for the numerical relativity community to reliably explore a much broader space of parameters in $q$, $\chi$, EOS, and, in principle, eccentricity. Finally, the continued development of the FUKA suite to include the advancements described in Sec. 2.6.2, which have also been made available publically, aims to ensure the highest level of reliability is available to the NR community such that future works can focus on the physics without the labor of the initial value problem.

In FUKA we have constructed initial data using the XCTS system of equations, we have modeled black holes using excision methods such that constraints on the *lapse* and *shift* can be made on our 2-surface which is an apparent horizon by construction, and we have implemented an approximate first integral formulation based on a specific enthalpy fluid velocity profile that is a function of a divergence free potential and uniform rotation component. In this work we have focused on the generation of BHNS and BNS where, in the case of BNS, we have generated and examined the most extreme configurations to date. In all of our results, we have shown the ability and value of performing eccentricity reduction especially for asymmetric and spinning binary ID such that we obtain eccentricities on the order of $\lesssim [10^{-4}, 10^{-3}]$.

Finally, in an attempt to quantify the impact of ID resolution on the evolution dyanmics we have taken a first look at the absolute GW phase difference as a function of both ID and evolution resolution in the case of BBH and BNS ID. In general we find the evolution resolution to be the dominant source of error using this measurement, and, thus, conclude that coarser resolution ID can be justifiably used for evolutions unless high accuracy waveforms are needed. We stress of course that these assessments only hold strictly true for the configurations analyzed here, however, they are representative of commonly used setups.

With FUKA as our foundation we can now begin to explore the space of parameters for extremal binary compact objects in the remaining chapters.

# Chapter 3

# Impact of extreme spins and mass ratios on the post-merger observables of high-mass binary neutron stars

Within the results discussed related to extremal binary neutron star configurations in Sec. 2.8.2 - IV, we found for two binaries using the same equation of state, mass ratio $q$, and total mass $M_\infty$ (as defined by Eq. (2.70)) that the configuration with an extremal spinning primary neutron star can result in a metastable hyper–massive neutron star (HMNS) remnant. Furthermore, based on the numerical and theoretical foundation described in Sec.1.2 we are motivated to quantify the extent mass asymmetry and spin can influence the stability of the HMNS remnant. In this way, the most well established benchmark to compare against is the threshold mass for a given equal–mass, irrotational binary ($M_{\rm th}^{1,0}$) where the value for the threshold mass in this regime has been thoroughly explored for all of the EOSs utilized in the work (cf. [23], [42], [102]). Therefore, in this work we provide the first systematic study of asymmetric and spinning BNS mergers with total masses in excess of $M_{\rm th}^{1,0}$ and up to near extremal spin on the primary NS. To characterize these mergers we identify important characteristic differences in the merger dynamics and the remnant stability. Additionally, we leverage the ability of `FIL` to utilize temperature- and Ye-dependent tabulated EOSs with accurate microphysics and, as such, analyze the ejecta, disk mass and resulting peak luminosity properties while using a grey neutrino leakage scheme.

In Sec. 3.1 we will discuss the details related to the systematic sampling within our parameter space along with the numerical setup used to perform the binary mergers. In Sec. 3.2 we will examine the dynamics and distinguishing characteristics of the various ejecta. Finally, we will provide a brief summary of our results in Sec. 3.2.6.

## 3.1 Methods

Given the large space of parameters in EOS, $M_\infty$, $q$ and $\chi$; we restrict ourselves to performing 14 simulations using the relatively soft `TNTYST` [137] EOS and 14 simulations using the relatively stiff `BHB`$\Lambda\Phi$[139] (see Tab. C.1). Both EOSs are temperature and charge fraction dependent equations of state and are consistent with current astronomical constraints. Hence, these EOSs provide a nice contrast in our results as to the impact stiffness may have on the dynamics and

measured remnant properties. Furthermore, we choose $M_\infty \in [1.025, 1.11] M_{\rm th}^{1,0}$, $q \in [0.6, 1]$ and a dimensionless spin of the primary NS of $\chi_1 \in [0.3, 0.6]$ as defined by Eq. (2.69). In all cases the initial separation of the binary is 45km, the spin of the secondary (less massive) NS is $\chi_2 = 0$ and the axis of rotation for both NSs are aligned with the orbital axis of rotation. Table 3.2 provides a complete list of the configurations investigated along with additional properties that will be described in the results section. The choice of an irrotational secondary is both of convenience as well as to reflect what could be expected in reality where the primary gains additional spin due to accretion of the progenitor star of the secondary NS [7]. Through this process the spin-angular momentum of the secondary is reduced and, therefore, we choose to model it as non-rotating.

For each configuration we simulate the inspiral, merger, and post-merger phase in order to investigate the stability of the HMNS remnant, the mass of the post–collapse disk, and the measured dynamical ejecta. To provide accurate estimates of our ejecta as well as obtain estimates on the peak luminosity, a neutrino leakage scheme within `FIL` is utilized such that neutrino cooling and weak rates are taken into consideration. Furthermore, we utilize the same evolution setup as denoted in Appendix C to perform these evolutions.

When attempting to measure the post-collapse disk mass and ejecta properties, sufficiently high resolution simulations are required. This is in part due to capturing the complex dynamics that occur during the merger process, but also to accurately resolve the small volume of ejecta as they form and are ejected away from the HMNS remnant. To this end, we have performed our simulations with a grid extent up to $\simeq 6,000$km with eight levels of refinement resulting in a grid spacing for the finest level of $\Delta_x = 0.16 M_\odot \simeq 236$m. Furthermore, we have performed additional simulations at a resolution of $\Delta_x = 0.133 M_\odot$ and find that in most cases, the estimates are within a few tens of percent (see Appendix in [20] for a discussion).

## 3.2 Results

The following section describes the results of 28 binary simulations where, for a given EOS and total mass ($M_\infty$), the mass ratio varies between $q \in [0.6, 1]$ and the dimensionless spin of the primary [1] varies between $\chi_1 \in [0.3, 0.6]$. More specifically, we have chosen two mass configurations using the `TNTYST` EOS ($M_\infty / M_{\rm th}^{1,0} \in \{1.050, 1.105\}$) and three mass configurations for the `BHBΛΦ` EOS ($M_\infty / M_{\rm th}^{1,0} \in \{1.025, 1.050, 1.109\}$). In this work the total mass of each binary is chosen in units of $M_{\rm th}^{1,0}$ as measured by [42] from the study of equal–mass irrotational BNS configurations. This normalization provides a measure of the "mass criticality" of the system such that $M_\infty / M_{\rm th}^{1,0} < 1$ is sub-critical and $M_\infty / M_{\rm th}^{1,0} > 1$ is supercritical. A comprehensive list of the binary configurations and the parameters of its constituent objects are summarized in Tab. 3.2.

In the remaining subsections we will focus on the results pertaining to the (post-)merger dynamics, remnant stability, dynamical ejecta, and the remnant disc mass. A comprehensive analysis of these properties is important to understand the secular ejecta and the overall influence on the kilonova emission.

[1] In the case of $q = 1$, the rotating object is chosen at the same coordinate location as the more massive stars in the asymmetric cases for consistency, however, this has no impact on the measured quantities.

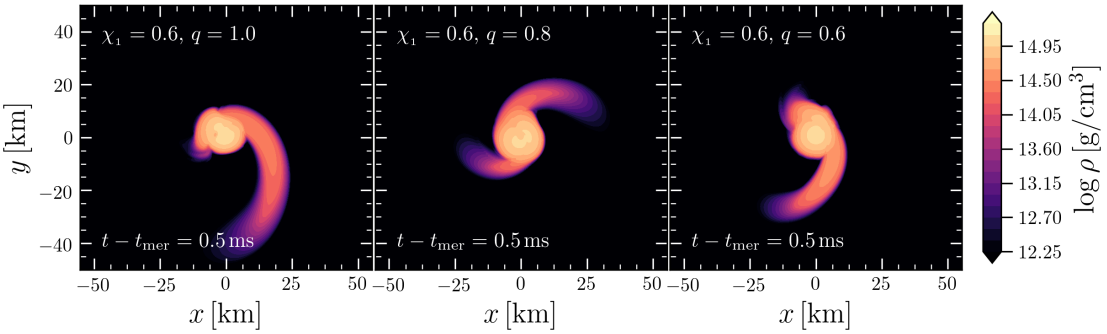


Figure 3.1: 2D slices in the equatorial plane of the rest-mass density at merger time corresponding to $q \in \{1.0, 0.8, 0.6\}$ where the primary NS has a dimensionless spin of $\chi_1 = 0.6$ and the secondary is irrotational $\chi_2 = 0$. Notably, the equal-mass configuration (*left*) results in the tidal disruption of the primary object which is then accreted onto the irrotational secondary. As the binary becomes more asymmetric, the secondary becomes tidally disrupted due to the larger gravitational mass of the primary. This figure has been reused from [20].

### 3.2.1 Merger and post-merger dynamics

In the study of inspiral waveforms via post-Newtonian expansions, the influence of aligned–spins of the component masses has been thoroughly analyzed [140]–[143]. Specifically, the addition of aligned spin–angular momentum of each object as well as the spin–orbital coupling will result in a longer inspiral and, thus, a later merger time. Here, we will instead focus on the violent merger processes and the role extremal spins and asymmetry play.

Given the space of highly spinning mergers has yet to be analyzed, we will start with a qualitative analysis of the dynamics for a subset of binary configurations with an extremal spinning primary with $\chi_1 = 0.6$, $q \in \{0.6, 0.8, 1.0\}$, and $M_\infty/M_{\rm th}^{1,0} = 1.05$ for the TNTYST EOS. In Fig. 3.1 we show a cross section of the rest-mass density in the equatorial plane $\sim 0.5$ms post-merger for each configuration. Interestingly, we find a transition in the disruption characteristics during merger such that, for $q = 1$ (left figure), we see that the primary (spinning) object is tidally disrupted by the more compact secondary object whereas for $q = 0.8$, the merger dynamics are comparable to the irrotational asymmetric case. Furthermore, the disruption dynamics for $q = 0.6$ are analogous to the irrotational configuration where the secondary is tidally disrupted due to the more massive primary. In both cases, the merger or accretion of the secondary NS results in a transfer of angular momentum causing a further spin-up of the primary which also undergoes some disruption as a consequence.

In contrast, we repeat this analysis for binary configurations with $M_\infty/M_{\rm th}^{1,0} = 1.105$. In this case, even for $q = 1$ the disruption of the primary is less due to the higher gravitational mass of each NS. The trend continues as the spin of the primary is further decreased resulting in dynamics similar to an irrotational binary. Similarly for decreasing mass ratio, the impact of the total mass and mass ratio play the dominant role in the resulting merger dynamics, however, the spin of the primary has a noticeable influence on the merger dynamics especially at $q = 0.6$ where the secondary is strongly disrupted.

Furthermore, by repeating this analysis for the BHB$\Lambda\Phi$ EOS we find similar qualitative behavior to that found in the TNTYST configurations, however, the characteristic dynamics are overall milder for BHB$\Lambda\Phi$ and the degree of disrup-

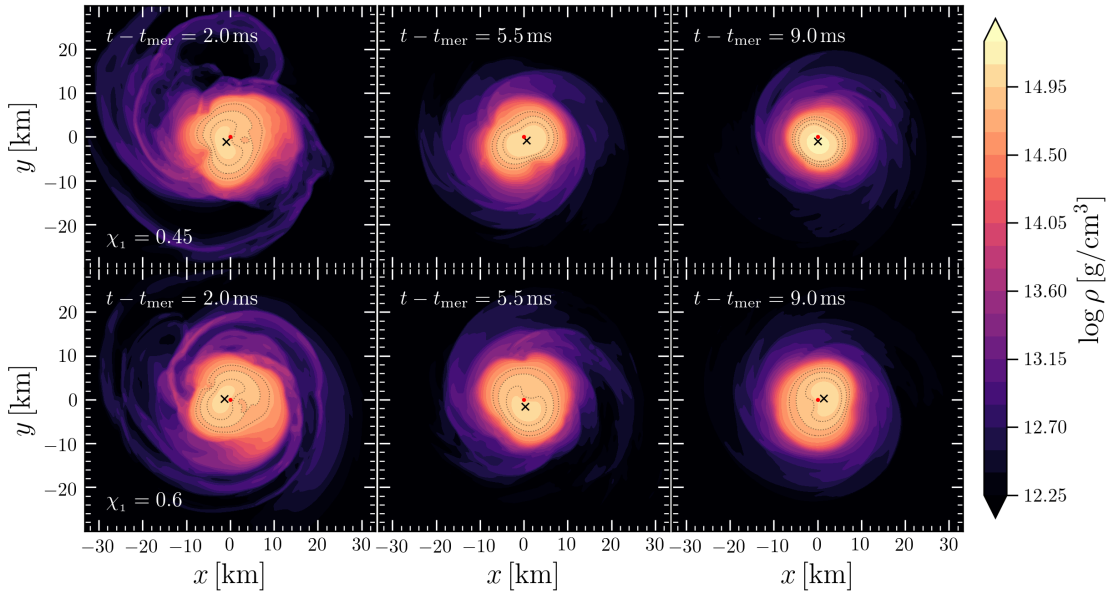


Figure 3.2: 2D slices in the equatorial plane of the rest–mass density at three characteristic post-merger times for two models, `TNT-05.0-0.45-0.800` and `TNT-05.0-0.60-0.800` in order to qualitatively analyze the influence of spin on the HMNS remnant. To do so, we include a marker for the maximum rest-mass density which is denoted by a black cross as well as a red dot to denote the coordinate center. Here we note that by increasing $\chi_1 = 0.45 \rightarrow 0.6$, the distribution of the rest-mass density obtains a higher degree of asymmetry and retains it for longer. By $t - t_{\rm mer} = 9{\rm ms}$, the rest-mass distribution for $\chi_1 = 0.45$ has already started to become more uniform with the maximum density being nearly at the coordinate center whereas, for $\chi_1 = 0.6$, the rest-mass density profile is still highly asymmetric. To further emphasize this feature, we include dotted contours corresponding to $\log \rho \in \{14.7, 14.8, 14.9\}$. This figure has been reused from [20].

tion of the primary is already quite minute even for $M_\infty/M_{\rm th}^{1,0} = 1.05$. From this analysis, we can deduce that the EOS plays an important role in the dynamical (post-)merger processes which sensitively depend on the compactness of the neutron stars. In reality, the (post-)merger dynamics and remnant stability are dictated by a subtle balance between tidal and centrifugal forces as well as the overall strength of the gravitational potential which can be tuned by adjusting $q$, $\chi_1$, and $M_\infty$ respectively. We can therefore characterize the dominant dynamical features in the following manner. First, for $q = 1$, the spin-angular momentum of the primary results in matter being less bound and, thus, is more sensitive to tidal interactions with the non-spinning secondary. Second, for increasingly asymmetric binaries, the secondary NS is instead disrupted due to the stronger tidal interaction with the primary (more massive) object. Third, in the case of extremal spins a second tidal tail can form which carries a significant amount angular momentum and expands quicker than the tidal tail of the secondary thus allowing the possibility for primary tidal tail to cause shocks in the secondary tidal tail.

We now adjust our focus to the post–merger HMNS remnant. In all configurations considered, the distribution of matter within the merger remnant shows various degrees of asymmetry most notably in the equatorial plane. In Fig. 3.2 we show 2D slices of the post-merger remnant at given times for $q = 0.8$, $\chi_1 \in \{0.45, 0.6\}$ and $M_\infty/M_{\rm th}^{1,0} = 1.050$ using the `TNTYST` EOS. Although both binaries demonstrate the development of a strong one-arm instability [see [36], [37], [39], [144]–[147]], we highlight that, especially in the later times (middle and right

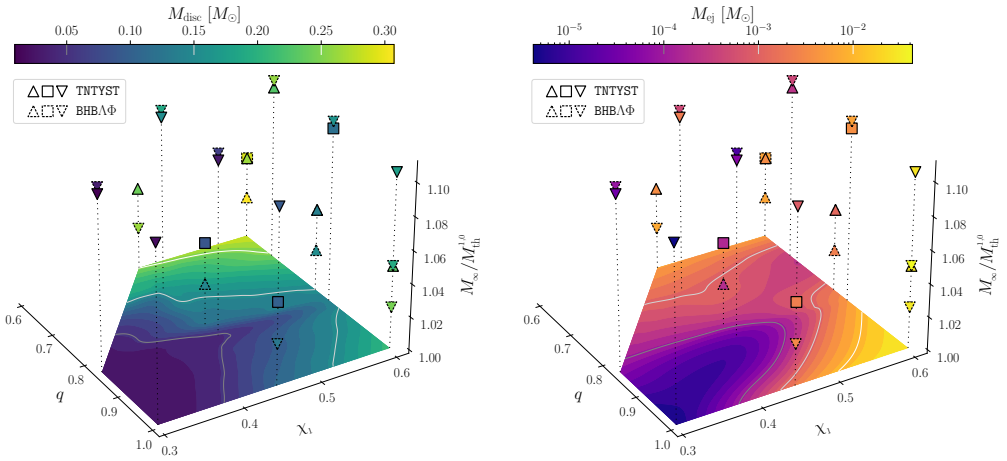


Figure 3.3: Here we analyze the remnant disk mass (*Left*) as well as the total dynamical mass ejected (*Right*) from the merger. In each plot we show the data for both EOSs where the symbol shape denotes the remnant lifetime and the marker line style denotes the EOS where solid lines correlate with the TNTYST EOS and dotted lines correlate with the BHBΛΦ EOS. Furthermore, mass criticality $M_\infty/M_{\rm th}^{1,0}$ is plotted as a function of the mass ratio $q$ and the dimensionless spin of the primary $\chi_1$. Finally, the respective disk (ejecta) masses are projected onto a 2D plane generating a corresponding cubic spline interpolated contour plot which highlights the highly non-linear behavior. This figure has been reused from [20].

panels), the highly spinning HMNS ($\chi_1 = 0.60$) has a highly asymmetric mass distribution as compared to the binary with $\chi_1 = 0.45$. Furthermore, both binary mergers create a HMNS that is (meta-)stable for configurations with a (low) high spinning primary which could result in distinguishable characteristics in the GW emission and disc winds [148].

### 3.2.2 Ejecta analysis

Given the excessively high masses of the configurations studied, a key aspect to understanding the stability of the remnant is by understanding how much mass has been ejected at merger so as to ascertain the mass of the remnant. To this end, we show in Fig. 3.3 3D plots of the mass criticality of each binary as a function of the mass ratio $q$ and the dimensionless spin of the primary $\chi_1$. It is important to note that the color bar represents the disk (dynamical ejecta) mass measured for the binary in the left (right) plot. Furthermore, the data is projected onto a 2D contour plot which is then interpolated using a cubic spline which provides insights into the non-linear relation of the disk (dynamical ejecta) mass as a function of $q$ and $\chi_1$.

We will first focus our attention on the disk mass (left) plot in Fig. 3.3. Unsurprisingly, binaries with low spin and $q > 0.8$ result in very small $M_{\rm disc}$ which correlates well with the short lifetime of the remnant such that the majority of the mass is consumed in the formation of the BH. Additionally, as $\chi_1$ increases for $q = 1$ we see a steady increase in $M_{\rm disc}$ whereas, for $q = 0.6$, we find a sharp increase in $M_{\rm disc}$ resulting in $\gtrsim 50\%$ increase in disk mass compared to $q = 1$ configuration. In contrast, the collapse time ($\tau_c$) to a BH is significantly longer in the case of $q = 0.6$ compared to $q = 1$. This is attributed to the fact that, in the case of $q = 1$, the star that is disrupted is in fact the spinning NS [see Fig. 3.1]. Therefore, matter is accreted onto the equally massive irrotational NS resulting in a

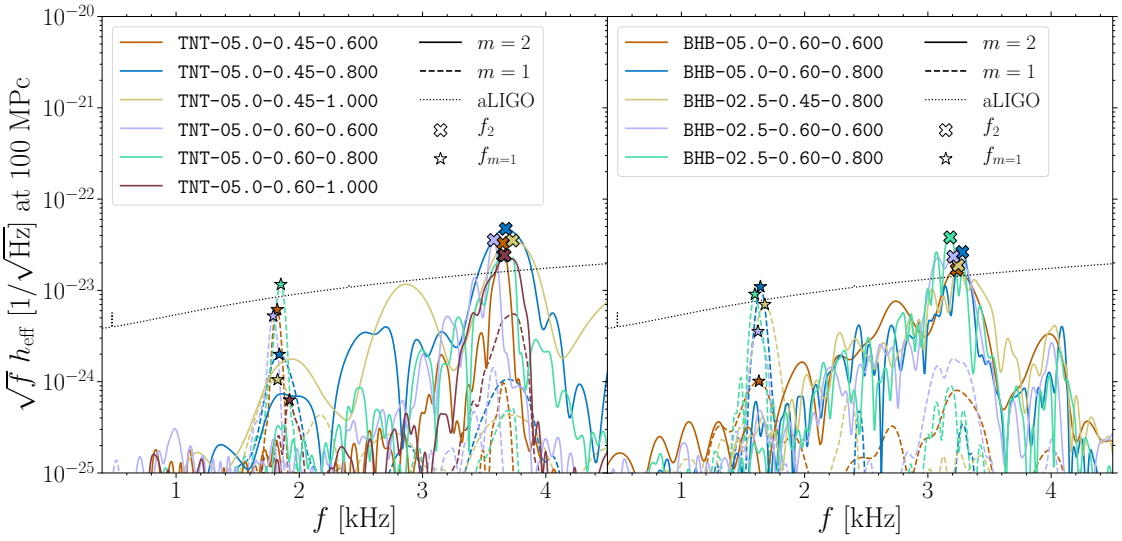


Figure 3.4: The power spectral density (PSD) of the effective gravitational wave strain for the $(\ell, m) \in \{(2,1),(2,2)\}$ modes for the TNTYST (left panel) and BHBΛΦ (right panel). Furthermore, we highlight the dominate PSD frequencies $f_{m=1} := \max[\mathrm{PSD}(l=2, m=1)]$ and $f_2 := \max[\mathrm{PSD}(l=2, m=2)]$. Finally, we include the aLIGO sensitivity curve for reference. This figure has been reused from [20].

prompt collapse for all configurations explored in this study except in the case of TNT-05.0-0.60-1.000. More interesting is the fact that we find a minimum $M_{\rm disc}$ for $\chi_1 \gtrsim 0.4$ and $q \approx 0.82$ highlighting a non–monotonic behavior in $M_{\rm disc}$ as a function of $q$ and $\chi_1$.

As we shift our focus to the ejected mass $M_{\rm ej}$, we find a very similar qualitative behavior as for $M_{\rm disc}$ showing a clear non–monotonic behavior of $M_{\rm ej}$ as a function of $q$ and $\chi_1$. Unlike in the case of $M_{\rm disc}$, we do not see a clear trend in the behavior of a local minimum as the spin of the primary increases. Instead, the minimum shifts from $q \approx 0.82$ towards $q \approx 0.75$. However, it is important to note that the measured ejected mass is prone to precision errors especially for the small quantities noted here. Specifically, the resolution of the evolution numerical grid can result in errors up to $40\%$. Furthermore, the contour plot is constructed using a cubic spline interpolation of the averaged measured quantities. Therefore, for the limited configurations obtained within this large parameter space, the shift in the minium to $q \approx 0.75$ could also be an artifact of insufficient sampling. Overall we see a similar behavior for $q = 1$ and $q = 0.6$, however, opposite to $M_{\rm disc}$, we find larger amounts of dynamical ejecta for $q = 1$ by nearly an order of magnitude. We find this can likely be attributed to the fact that the irrotational star experiences an abrupt spin–up due to accreting matter from the highly spinning star which we'll explore further in Ch.5. In this way, the rapid spin up of the irrotational star results in a second tidal tail formed by the primary NS.

### 3.2.3 Gravitational-wave analysis

Motivated by the results presented in Sec. 3.2.1, it is pertinent to examine the GW properties of the 28 simulations performed. Specifically, we focus our examination during a time window starting at the merger time and extending to the end of the simulation or until collapse to a BH. Out of necessity, we will focus our analysis on configurations that are at least short-lived given the GWs of promptly

collapsing binaries consist predominantly of the collapse and ring-down of the remnant BH.

For the remaining short- and long-lived configurations, we show in Fig. 3.4 the computed power spectral density (PSD) for the $(\ell, m) = (2, 2), (2, 1)$ multi–poles of the gravitational wave strain for the TNTYST (left panel) and BHB$\Lambda\Phi$ (right panel) EOSs along with the sensitivity curve for aLIGO (see [29], [149] for PSD details). Furthermore, the computed PSD is filtered using a Hann windowing function to remove spectral noise followed by a cubic-spline interpolation to provide a smooth function for presentation. All of the configurations examined show a prominent peak in the $(2, 1)$ mode with an approximate relation of $f_{\rm m=1} \approx 0.5 f_2$, where $f_2$ is the frequency associated with the global maximum in the $(\ell, m) = (2, 2)$ spectra. The $f_2$ peak has been thoroughly examined in previous works and is the dominate post–merger frequency[39], [50], [146], [149]–[153].

Interestingly, we find that the maximum value of the $f_{m=1}$ peak in the $(2, 1)$ mode for both EOSs is for the configuration with $q = 0.8$ and $\chi_1 = 0.6$ which hints that there may be an optimal mass ratio resulting in a stronger (2,1) mode. However, the (2,1) mode typically depends sensitively on the mass ratio of the binary thus causing an asymmetry in the HMNS remnant resulting in a one-arm instability. For the simulation times considered here, the collapse time for TNT-05.0-0.60-0.800 and TNT-05.0-0.60-0.600 could not be computed. Thus, the total power in the (2,1) mode due to the remnant lifetime could also play a role in this discrepancy if the simulations were performed until both configurations collapsed. To further emphasize this point, in the case of $\chi_1 = 0.45$, TNT-05.0-0.45-0.800 collapses much earlier than for TNT-05.0-0.45-0.600 resulting in the larger $f_{\rm m=1}$ for TNT-05.0-0.45-0.600 as expected.

In an effort to further analyze the large $f_{\rm m=1}$ peak for TNT-05.0-0.60-0.800, we have chosen to define the total ejected mass as

$$M_{\rm tot} := M_{\rm ej} + \frac{1}{2} M_{\rm disc}, \tag{3.1}$$

which we have included for the 28 configurations studied in this work in Tab. 3.2. When we compare TNT-05.0-0.45-0.800 and TNT-05.0-0.60-0.800, we find a $57\%$ increase in $M_{\rm tot}$ resulting in a collapse time $> 300\%$ longer given TNT-05.0-0.60-0.800 did not collapse by the end of the simulation time. Furthermore, TNT-05.0-0.60-0.800 results in $M_{\rm tot} \sim 45\%$ less than TNT-05.0-0.60-0.600 which implies the HMNS is in fact more massive which could contribute to the strong one-arm instability.

Looking now to the BHB$\Lambda\Phi$ EOS, we see the same dominate (2,1) peak for $q = 0.8$ and $\chi_1 = 0.6$, however, this is limited to $M_\infty / M_{\rm th}^{1,0} = 1.025$ as higher masses result in an early collapse to a BH for $q = 0.6$. Furthermore, $M_{\rm tot}$ increases by only $8\%$ when increasing $\chi_1 = 0.45 \to 0.6$ for $q = 0.8$. Unlike for TNTYST, two mass configurations with $q = 0.8$ do not collapse within the simulation time, namely BHB-05.0-0.60-0.800 and BHB-02.5-0.60-0.800. We see from Fig. 3.4 (right panel) that, in fact, the binary with the more massive HMNS remnant retains the dominant (2,1) mode, specifically BHB-05.0-0.60-0.800.

### 3.2.4 Remnant lifetime

Up until now, the lifetime of the remnant has been mentioned, but not thoroughly discussed. Here we aim to not only quantify the remnant lifetime, but

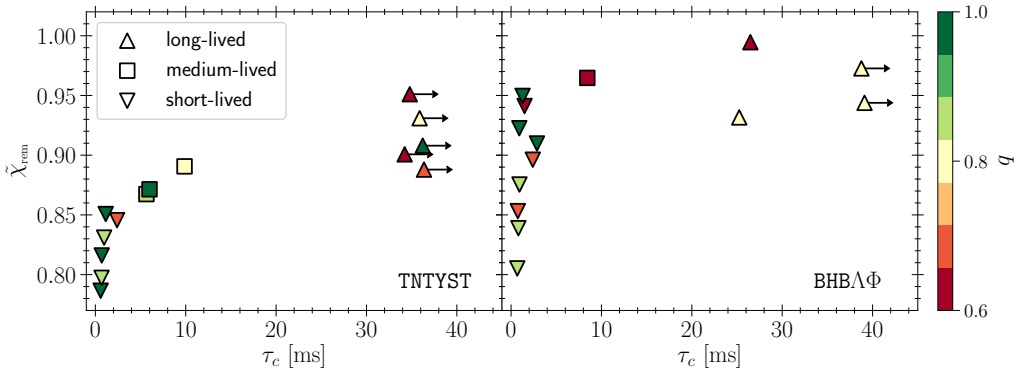


Figure 3.5: The rescaled dimensionless spin of the HMNS remnants $\tilde{\chi}_{\rm rem}$ plotted as a function of the collapse time $\tau_c$ for the TNTYST (left) and BHBΛΦ (right) EOS configurations. The symbols are colored as a function of the mass ratio $Q$ and the symbols denote the lifetime of the remnant. For clarity, we denote remnants that did not collapse within the simulation time with an arrow pointing to increasing $\tau_c$. This figure has been reused from [20].

also characterize the lifetime in an intuitive manner so as to determine the influence of mass and spin as well as EOS. In this work, we utilize the same collapse time ($\tau_c$) measurement as proposed in Ch.4 which are reported in Tab. 3.2. Furthermore, we characterize the lifetime of the remnants as *short lived* for $\tau_c \lesssim 5$ms, *medium lived* for $5 < \tau_c \lesssim 10$ms, and *long lived* for $\tau_c > 10$ms.

From Tab. 3.2 we can already gain an appreciation for the influence of spin and mass asymmetry based solely on the post merger time leading up to collapse to a BH. Specifically for TNTYST, we see for the configurations with a total binary mass $M_\infty/M_{\rm th}^{1,0} = 1.05$ and $\chi_1 = 0.6$ that all models survive up to the end of the simulation time. For $\chi_1 = 0.45$, only TNT-05.0-0.45-0.600 survives til the end of the simulation time with the remaining two mass ratios resulting in a meta-stable remnant that collapses within 10ms. Conversely, for the more massive configurations with $M_\infty/M_{\rm th}^{1,0} = 1.105$, we find all of the configurations have a *short lifetime* except for the long lived TNT-10.5-0.60-0.675 and the meta-stable TNT-10.5-0.60-0.837.

Repeating this analysis for BHBΛΦ shows quite a different behavior. Specifi-

| binary model | $h_{{\rm eff},f_2}$ | $h_{{\rm eff},f_{m=1}}$ | $\frac{h_{{\rm eff},f_{m=1}}}{h_{{\rm eff},f_2}}$ | $\frac{h_{{\rm eff},f_{m=1}}}{h_{{\rm eff},f_2}}\Big\vert_{5{\rm ms}}$ |
|---|---|---|---|---|
| TNT-10.5-0.60-0.675 | 0.500 | 0.032 | 0.064 | 0.173 |
| TNT-10.5-0.60-0.838 | 0.764 | 0.028 | 0.036 | 0.037 |
| TNT-05.0-0.45-0.600 | 0.414 | 0.032 | 0.078 | 0.131 |
| TNT-05.0-0.45-0.800 | 0.682 | 0.023 | 0.034 | 0.030 |
| TNT-05.0-0.45-1.000 | 1.000 | 0.019 | 0.019 | 0.021 |
| TNT-05.0-0.60-0.600 | 0.428 | 0.028 | 0.065 | 0.104 |
| TNT-05.0-0.60-0.800 | 0.594 | 0.033 | 0.056 | 0.341 |
| TNT-05.0-0.60-1.000 | 0.895 | 0.031 | 0.035 | 0.019 |
| BHB-05.0-0.60-0.600 | 0.333 | 0.019 | 0.057 | 0.042 |
| BHB-05.0-0.60-0.800 | 0.371 | 0.029 | 0.079 | 0.295 |
| BHB-02.5-0.45-0.800 | 0.404 | 0.030 | 0.075 | 0.267 |
| BHB-02.5-0.60-0.600 | 0.377 | 0.021 | 0.056 | 0.108 |
| BHB-02.5-0.60-0.800 | 0.428 | 0.027 | 0.063 | 0.169 |

Table 3.1: Here we highlight the power corresponding to the dominate $f_2$ and $f_{\rm m=1}$ frequencies where the total power is computed based on an integration window starting at the merger time and extending until collapse or the end of the simulation time. Finally, we include the relative power $\frac{h_{{\rm eff},f_{m=1}}}{h_{{\rm eff},f_2}}$ for the total integration window and an integration window limit to 5ms post-merger in order to ascertain the relative power for equal integration times. Note: all cells have been normalized by largest value in the table to give a sense of the relative power of each binary and their respective ratios.

cally, we see for $M_\infty/M_{\rm th}^{1,0} = 1.025$ and $\chi = 0.6$ that, even with the addition of extremal spins, $q = 1$ still collapses in a *short* time frame where as $q \in \{0.6, 0.8\}$ survive over a *long* time frame. Surprisingly, for $M_\infty/M_{\rm th}^{1,0} = 1.05$, $q = 0.8$ ends up surviving for a *long* time frame whereas $q = 0.6$ is only meta-stable. Reviewing Tab. 3.1, we see in column 5 that the measured relative effective power in the first $5$ms post-merger for `BHB-05.0-0.60-0.600` is $\lesssim 60\%$ compared to `TNT-05.0-0.60-0.600`. This implies that, for stiffer equations of state, the lack of a strong one-arm instability in the HMNS contributes to a significantly shorter collapse time.

Another avenue to characterize the HMNS remnant is to quantify the effective spin of the remnant as a function of the initial conditions, the mass and spin-angular momentum lost through gravitational waves. To this end, we choose to define the effective dimensionless spin of the remnant as

$$\tilde{\chi}_{\rm rem} := \left(\frac{M_{\rm th}^{1,0}}{M_\infty}\right) \frac{J_{\rm ADM} - J_{\rm GW}}{\left(M_{\rm ADM} - M_{\rm GW}\right)^2}\,, \tag{3.2}$$

where $J_{\rm ADM}$ and $M_{\rm ADM}$ are computed from the initial data and we have chosen to rescale the dimensionless spin by the mass criticality allowing for underlying characteristic behaviors to be realized such that comparison across all the binary configurations can be studied. In practice we compute $J_{\rm GW}$ and $M_{\rm GW}$ by extracting the Weyl scalar $\Psi_4$ on spherical shells at a finite coordinate distance of $735$km from the grid center and integrate from merger up to the BH formation or the end of the simulation (see [154]).

With this definition we show in Fig. 3.5 $\tilde{\chi}_{\rm rem}$ as a function of the computed collapse time $\tau_c$ where the symbols are colored as a function of mass ratio. In this way we find for the `TNTYST` EOS a clear trend such that configurations resulting in $\tilde{\chi}_{\rm rem} \gtrsim 0.9$ result in a long lived remnant. Conversely, for `BHB`$\Lambda\Phi$ configurations such a line is not easily drawn as configurations with $\tilde{\chi}_{\rm rem} \sim 0.95$ can still result in promptly collapsing binary. Furthermore, we see from another view the non–monotonic behavior of the remnant lifetime as a function of spin and mass asymmetry. Specifically, the three `BHB`$\Lambda\Phi$ models with $q = 0.8$ result in a long lived remnant whereas only the extremal spinning $q = 0.6$ configuration survives for a long period. This provides a unique measurement to further support our assessment that, for stiffer EOSs, the lifetime of the remnant is much more dependent on the degree of mass asymmetry and spin of the system.

### 3.2.5 Kilonova emission

In this section we conclude our analysis by approximating the influence $q$ and $\chi_1$ play on the electro–magnetic counterpart for the configurations considered. Therefore we included estimates of the peak luminosity $L_p$ and the time of peak emission $t_p$ in Tab. 3.2 which have been computed using the semi–analytical models by [155] and [156] where we have used a grey opacity of $10{\rm cm}^2/g$. It is important to note that previous modeling and numerical simulations have not considered binaries with such extremal configurations as what has been analyzed here nor have accretion disk simulations been computed with disk masses as large as those measured in this work $M_{\rm disk} \approx 0.3 M_\odot$.

With this in mind, we utilize reference estimates for the amount of the disk mass that will end up being ejected over time ($\sim 50\%$) with an average velocity of

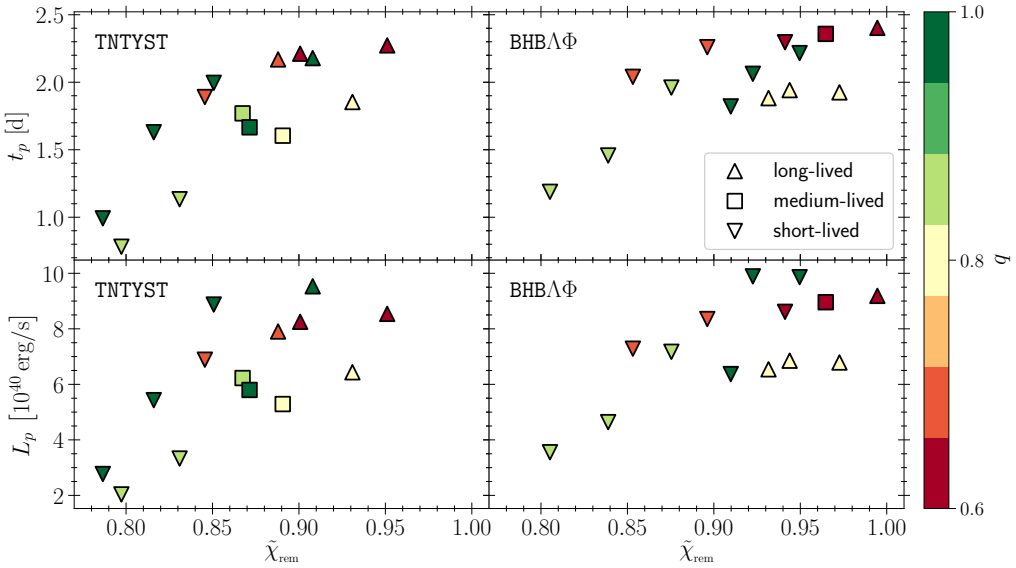


Figure 3.6: The estimated time of peak luminosity $t_p$ (top row) and the peak luminosity $L_p$ (bottom row) as a function of the remnant spin $\tilde{\chi}_{\rm rem}$ for TNTYST (left column) and BHBΛΦ (right column) configurations. In all figures, the color bar denotes the mass ratio $q$ and the symbols correspond to the remnant lifetime. This figure has been reused from [20].

$\langle v \rangle_{\rm disc} = 0.1$. With this we can then compute the mass weighted average velocity of the ejecta using

$$\langle v \rangle := \frac{\langle v \rangle_{\rm ej} M_{\rm ej} + \frac{1}{2}\langle v \rangle_{\rm disc} M_{\rm disc}}{M_{\rm tot}}, \tag{3.3}$$

where $\langle v \rangle_{\rm ej}$ is the average ejecta velocity at infinity and $M_{\rm tot}$ is given by Eq. 3.1. We have included $\langle v \rangle$ in Tab. 3.2, however, we note that for the models that have not collapsed the characteristics of the ejecta and as a result, the kilonova estimates, would be impacted.

To determine the influence of $q$ and $\chi_1$ on the emission properties, we plot in Fig. 3.6 the peak luminosity (bottom) and the time of peak luminosity (top) as a function of $\tilde{\chi}_{\rm rem}$, where the color code is a function of mass ratio. For both EOSs we find that $q = 1$ results in the highest peak luminosities $L_p$ where the time of the peak can be between $\sim 1$ and $\sim 2$ days depending on $\tilde{\chi}_{\rm rem}$. However, the next brightest emissions come from the most asymmetric binaries with $q \sim 0.6$ further pointing towards non-monotonic behavior as a function of $q$. Finally, the weakest emissions are those near equal mass and with lower $\tilde{\chi}_{\rm rem}$ as expected. At the same time we find a consistent trend between $t_p$ and $\tilde{\chi}_{\rm rem}$ such that remnants with higher effective spins will peak more than a day later.

### 3.2.6 Summary

In this work we have computed the inspiral, merger, and post-merger of 28 configurations with $q \in [0.6, 1.0]$ and $\chi \in \{0.3, 0.45, 0.6\}$ for BHBΛΦ and TNTYST EOSs with total binary basses of $M_\infty/M_{\rm th}^{1,0} \in [1.025, 1.109]$. With the availability of the FUKA BNS initial data solver we have analyzed a previously unexplored region of the BNS parameter space by performing GRHD simulations from inspiral up to $\sim 35$ms post-merger. From these simulations we have been

able to analyze the influence mass asymmetry and spin can have on the remnant stability, gravitational wave power spectrum, and electro–magnetic counterparts.

We have found that the imprint on the gravitational waveform, kilonova emission, and remnant stability depend sensitively on the mass ratio and spin. Specifically, the stability of the remnant requires a sufficiently large addition of spin angular momentum to support large mass binaries in excess of the irrotational threshold mass. This behavior is, however, not independent of the EOS as we have found for the stiffer BHB$\Lambda\Phi$ EOS where the examined binaries predominantly have a short lifetime independent of the mass ratio given the HMNS cannot support such a high mass even with $\tilde{\chi}_{\rm rem} > 0.9$. We find this can be partially attributed to the fact that for stiffer EOSs the one-arm instability is significantly weaker by as much as $50\%$ for similar mass criticality TNTYST configurations.

Finally, we find an overall trend between the time of peak luminosity $t_p$ as a function of $\chi_1$ such that configurations with a higher spinning primary will peak up to a day later. Additionally, we find the peak luminosities $L_p$ are often the equal–mass binaries. This phenomena will be discussed further in Ch.5 as it relates to the secondary fast ejection tail.

With a more clear understanding of the merger dynamics, we will focus in Ch. 4 instead on determining how the measured threshold mass changes as a function of $q$ and $\chi$ and whether or not quasi–universal behavior exists similar to what has been found for equal–mass irrotational binaries [42] and asymmetric binaries [125].

| binary model | EOS | $M_\infty$ $[M_\odot]$ | $q$ | $\chi_1$ | $\chi_{\rm eff}$ | $\langle v \rangle$ $[c]$ | $\langle Y_e \rangle$ | $M_{\rm tot}$ $\left[10^{-1} M_\odot\right]$ | $\tau_c$ [ms] | lifetime symbol |
|---|---|---|---|---|---|---|---|---|---|---|
| TNT-10.5-0.30-0.837 | TNTYST | 3.199 | 0.837 | 0.30 | 0.158 | 0.101 | 0.14 | 0.047 | 0.7 | $\triangledown$ |
| TNT-10.5-0.30-1.000 | TNTYST | 3.199 | 1.000 | 0.30 | 0.150 | 0.100 | 0.10 | 0.097 | 0.6 | $\triangledown$ |
| TNT-10.5-0.45-0.675 | TNTYST | 3.199 | 0.675 | 0.45 | 0.268 | 0.103 | 0.08 | 0.783 | 2.4 | $\triangledown$ |
| TNT-10.5-0.45-0.837 | TNTYST | 3.199 | 0.837 | 0.45 | 0.244 | 0.100 | 0.13 | 0.149 | 1.0 | $\triangledown$ |
| TNT-10.5-0.45-1.000 | TNTYST | 3.199 | 1.000 | 0.45 | 0.225 | 0.101 | 0.04 | 0.469 | 0.7 | $\triangledown$ |
| TNT-10.5-0.60-0.675 | TNTYST | 3.199 | 0.675 | 0.60 | 0.358 | (0.100) | 0.06 | (1.142) | $> 36.4$ | $\triangle$ |
| TNT-10.5-0.60-0.837 | TNTYST | 3.199 | 0.837 | 0.60 | 0.326 | 0.102 | 0.04 | 0.627 | 5.7 | $\square$ |
| TNT-10.5-0.60-1.000 | TNTYST | 3.199 | 1.000 | 0.60 | 0.300 | 0.116 | 0.04 | 1.153 | 1.2 | $\triangledown$ |
| TNT-05.0-0.45-0.600 | TNTYST | 3.039 | 0.600 | 0.45 | 0.281 | (0.101) | 0.05 | (1.239) | $> 34.2$ | $\triangle$ |
| TNT-05.0-0.45-0.800 | TNTYST | 3.039 | 0.800 | 0.45 | 0.250 | 0.100 | 0.13 | 0.444 | 9.9 | $\square$ |
| TNT-05.0-0.45-1.000 | TNTYST | 3.039 | 1.000 | 0.45 | 0.225 | 0.103 | 0.07 | 0.525 | 6.0 | $\square$ |
| TNT-05.0-0.60-0.600 | TNTYST | 3.039 | 0.600 | 0.60 | 0.375 | (0.101) | 0.05 | (1.347) | $> 34.8$ | $\triangle$ |
| TNT-05.0-0.60-0.800 | TNTYST | 3.039 | 0.800 | 0.60 | 0.333 | (0.100) | 0.04 | (0.701) | $> 35.9$ | $\triangle$ |
| TNT-05.0-0.60-1.000 | TNTYST | 3.039 | 1.000 | 0.60 | 0.300 | (0.112) | 0.04 | (1.438) | $> 36.2$ | $\triangle$ |
| BHB-10.8-0.30-0.837 | BHBΛΦ | 3.500 | 0.837 | 0.30 | 0.163 | 0.100 | 0.12 | 0.174 | 0.7 | $\triangledown$ |
| BHB-10.8-0.45-0.675 | BHBΛΦ | 3.500 | 0.675 | 0.45 | 0.268 | 0.100 | 0.04 | 0.942 | 0.7 | $\triangledown$ |
| BHB-10.8-0.45-0.837 | BHBΛΦ | 3.500 | 0.837 | 0.45 | 0.244 | 0.100 | 0.10 | 0.327 | 0.8 | $\triangledown$ |
| BHB-10.8-0.60-0.675 | BHBΛΦ | 3.500 | 0.675 | 0.60 | 0.358 | 0.100 | 0.05 | 1.300 | 2.4 | $\triangledown$ |
| BHB-10.8-0.60-0.837 | BHBΛΦ | 3.500 | 0.837 | 0.60 | 0.326 | 0.102 | 0.03 | 0.870 | 0.9 | $\triangledown$ |
| BHB-05.0-0.60-0.600 | BHBΛΦ | 3.314 | 0.600 | 0.60 | 0.375 | 0.101 | 0.04 | 1.509 | 8.4 | $\square$ |
| BHB-05.0-0.60-0.800 | BHBΛΦ | 3.314 | 0.800 | 0.60 | 0.333 | (0.100) | 0.03 | (0.812) | $> 39.1$ | $\triangle$ |
| BHB-05.0-0.60-1.000 | BHBΛΦ | 3.314 | 1.000 | 0.60 | 0.300 | 0.120 | 0.05 | 1.381 | 0.9 | $\triangledown$ |
| BHB-02.5-0.45-0.600 | BHBΛΦ | 3.235 | 0.600 | 0.45 | 0.281 | 0.101 | 0.04 | 1.382 | 1.5 | $\triangledown$ |
| BHB-02.5-0.45-0.800 | BHBΛΦ | 3.235 | 0.800 | 0.45 | 0.250 | 0.100 | 0.14 | 0.732 | 25.2 | $\triangle$ |
| BHB-02.5-0.45-1.000 | BHBΛΦ | 3.235 | 1.000 | 0.45 | 0.225 | 0.101 | 0.04 | 0.674 | 2.9 | $\triangledown$ |
| BHB-02.5-0.60-0.600 | BHBΛΦ | 3.235 | 0.600 | 0.60 | 0.375 | 0.101 | 0.04 | 1.601 | 26.5 | $\triangle$ |
| BHB-02.5-0.60-0.800 | BHBΛΦ | 3.235 | 0.800 | 0.60 | 0.333 | (0.101) | 0.03 | (0.792) | $> 38.8$ | $\triangle$ |
| BHB-02.5-0.60-1.000 | BHBΛΦ | 3.235 | 1.000 | 0.60 | 0.300 | 0.113 | 0.04 | 1.537 | 1.3 | $\triangledown$ |

Table 3.2: The binary models considered in this work are listed including the utilized EOS, the total gravitational mass of the binary $M_\infty$, the mass ratio $q$, the dimensionless spin of the primary NS $\chi_1$, the effective dimensionless spin parameter of the binary $\chi_{\rm eff}$, the mass weighted average velocity of the ejecta, the average $Y_e$ of the ejecta, the mass weighted total ejected mass $M_{\rm tot}$, and the collapse time of the remnant to a black hole $\tau_c$. Additionally, we include the symbol used in later plots which are defined by the survival time of the HMNS remnant for each configuration. Finally, the dimensionless spin of the secondary object is irrotational in all the configurations presented here.

# Chapter 4

# Quasi-universal behavior of the threshold mass in unequal-mass, spinning binary neutron star mergers

In chapter 3 the examination of binaries with a critical mass up to $\sim 10\%$ above the irrotational, equal–mass threshold mass provided both qualitative and quantitative insights into the influence mass asymmetry and spin can have on remnant stability. The addition of spin-angular momenta and mass asymmetry in the binary configuration result in the sensitive interplay of complicated dynamics including mass ejection, tidal disruption, and a possibly strong one–arm instability. We have shown that the collective result of these dynamics can produce a long-live HMNS remnant even for supercritical mass configurations. Furthermore, the relation between many of these dynamical features to $q$ and $\chi_1$ showed a clear non-monotonic behavior (cf. Fig. 3.3).

In this chapter we will shift our focus to the study of the threshold mass to prompt collapse (cf. Sec. 1.2) for given configurations of $q$ and $\chi$. As such, the binary masses used are iteratively changed until an accurate measurement of the threshold mass can be obtained. Within Sec.4.1 we will describe our experimental setup and the binary configurations that will be explored. In Sec. 4.2 we will analyze the measured threshold masses along with the ansatz proposed describing a quasi–universal relation. Finally, in Sec. 4.3 we will summarize the highlighted results from this work.

## 4.1 Methods

Given the large space of parameters in EOS, $M_\infty$, $q$ and $\chi$ we must impose some restrictions in order to reasonably sample the space of parameters while still obtaining accurate results. To this end we have utilized the temperature dependent `TNTYST`, `BHB`$\Lambda\Phi$, and `DD2` EOSs. These EOSs have been chosen since they are still within astronomical constraints while, at the same time, span across a range of stiffnesses. We shown in Tab. C.1 characteristic quantities for the EOSs considered such as their maximum non-rotating (TOV) mass $M_{\rm TOV}$, TOV compactness $\mathcal{C}_{\rm TOV}$, and the associated TOV freefall timescale $\tau_{\rm TOV}$. For the remaining space of parameters ($q\,,\chi$) we choose $q \in \{0.5, 0.7, 0.9, 1.0\}$ where binaries with $q = 0.5$ are at the extreme of physically plausible binaries such that the secondary (less massive) object has a mass $M_{\rm ADM} \sim 1.0 M_\odot$. Additionally, we restrict ourselves

to binaries where only the primary [1] (more massive) object is spinning. Furthermore, we choose to explore dimensionless spins $\chi_1 \in \{-0.3\,, 0\,, 0.3\}$ where $\chi_1$ is defined using Eq. (2.69).

For each configuration we simulate the inspiral, merger, and post-merger phase in order to compute the collapse time $\tau_c$ which is the time from merger until the NS becomes gravitationally unstable and a collapse to a BH is imminent. To this end, we utilize the `FUKA` BNS initial data solver as discussed in Ch. 2 along with the evolution setup described in Appendix C. Specifically, we utilize a numerical evolution grid with an extent of $\approx 3000$km. Using the `Carpet` box-in-box refinement driver, a total of 6 boxes of refinement are utilized resulting in a finest grid spacing of $\Delta x \approx 295$m. In order to minimize the eccentricity for the configurations examined here, we have utilized `FUKA`'s ability to perform eccentricity reduction using 3.5PN estimates as described in Sec. 2.5. This is an important step as appreciable eccentricity can influence the collapse time in BNS mergers[37].

Finally, the key for studying the threshold mass of BNS mergers is to have a rigorous and physically motivated measurement of the collapse time. To this end we have chosen a modified approach to what was originally defined in [42]. Specifically, the minimum of the *lapse*, $\min(\alpha)$, is monitored throughout each simulation [see Eq. (2.6) for a definition of $\alpha$]. This is a precisely tracked quantity throughout numerical simulations and, by definition, characterizes the region of the highest gravitational potential (i.e., small $\alpha$ means a stronger gravitational influence). Therefore, as a NS or HMNS becomes gravitationally unstable such that the fluid pressure can no longer compensate for the gravitational potential, a collapse to a BH is imminent. Furthermore, the collapse to a BH takes place over a finite timescale known as the freefall timescale[157] and is defined as

$$\tau_{\rm ff}(M,R) := \frac{\pi}{2}\sqrt{\frac{R^3}{2M}}\,, \tag{4.1}$$

where, for a given EOS, we can compute $\tau_{\rm ff}$ for the maximum TOV mass, i.e. $\tau_{\rm TOV} := \tau_{\rm ff}(M_{\rm TOV}, R_{\rm TOV})$. However, since $\alpha$ is a gauge dependent quantity its measured value is dependent on the asymmetries in the system. In order to remove this degeneracy so as to compute comparable collapse times, we normalize $\min(\alpha)$ by its maximum which we define as

$$\hat{\alpha} := \frac{\min(\alpha)}{\max(\min(\alpha))}. \tag{4.2}$$

With the necessary definitions in place we can now define thresholds on $\hat{\alpha}$ in order to compute the collapse time. To do so we first set the lower limit on $\hat{\alpha}$ which ensures gravitational instability of the HMNS across the explored parameter space considered. As such we define

$$t_{\rm BH} := t(\hat{\alpha} = 0.1). \tag{4.3}$$

Furthermore, we want to ensure the collapse time never exceeds $\tau_{\rm TOV}$ for a given EOS. As such, we have identified this to be true when

$$t_{\rm merge} := t(\hat{\alpha} = 0.9). \tag{4.4}$$

[1] For $q = 1$ *primary* is only used as a label to describe the NS with spin since they both have equal gravitational mass at infinite separation.

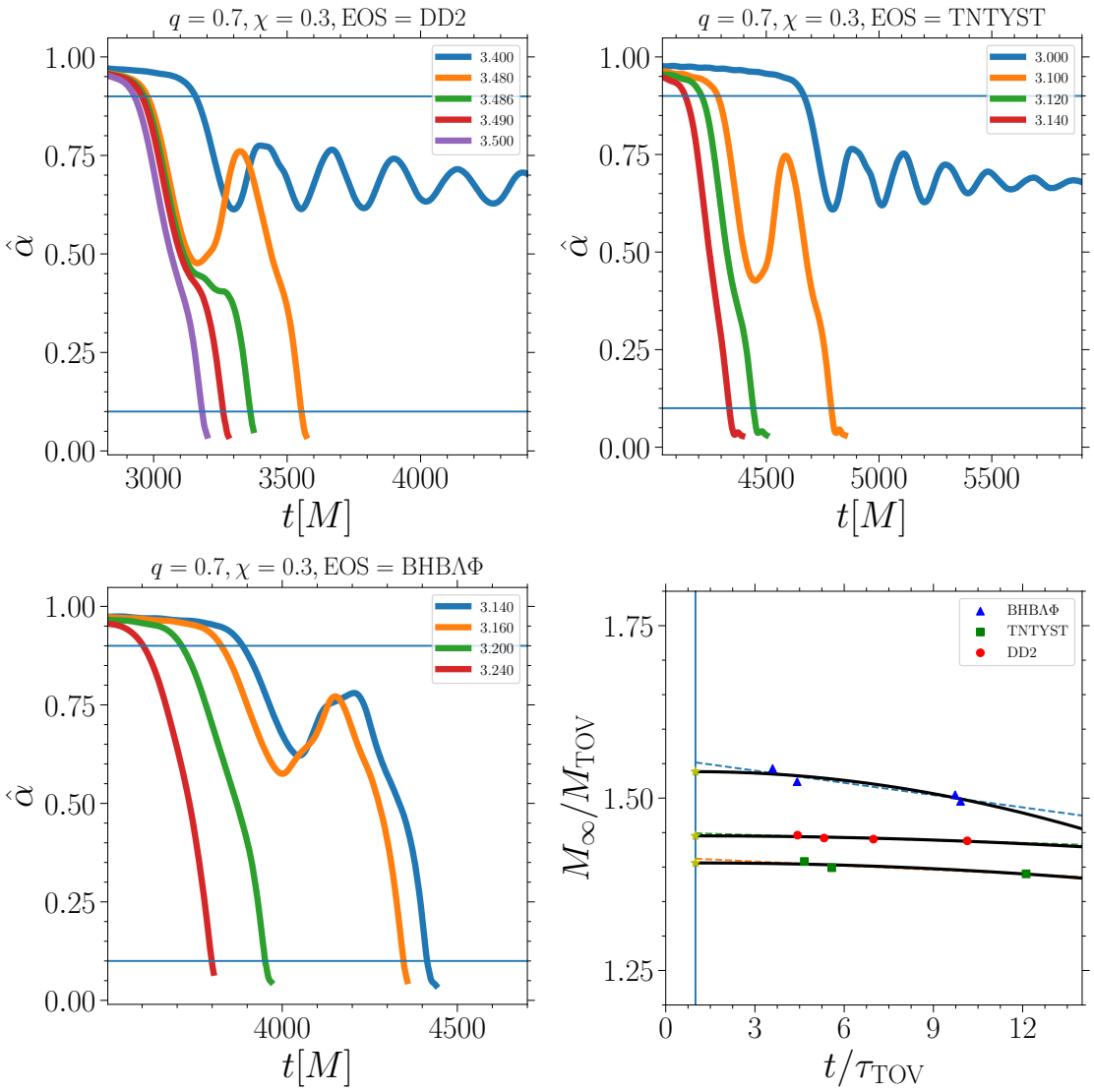


Figure 4.1: *Bottom-right panel*: The total binary mass $M_\infty$ normalized by the TOV mass plotted as a function of the collapse time $t_{\rm col}$ normalized by $\tau_{\rm TOV}$ for a given EOS. *Remaining panels*: Representative examples of the behavior of the normalized minimum lapse $\hat{\alpha}$ as a function of the simulation time for $q = 0.7, \chi = 0.3$ for each EOS. We highlight how sensitive the collapse behavior is for $M_\infty$ especially near $M_{\rm th}$. This figure has been reused from [41].

Therefore, the measurement of the collapse time is simply

$$t_{\rm col} := t_{\rm BH} - t_{\rm merge}. \tag{4.5}$$

With a measure of the collapse time using Eq. (4.5), we can compute the threshold mass for each configuration in a straight forward manner. Each configuration ($q$, $\chi$, and EOS) with variable total mass ($M_\infty$) of the binary is computed up to $\sim 5$ms post–merger. Once three or more points are collected near the threshold mass, e.g., $t_{\rm col}/\tau_{\rm TOV} \lesssim 15$, the data points are fitted to

$$\frac{M_\infty}{M_{\rm TOV}} = b_1 \exp\left[-b_2 \left(\frac{t_{\rm col}}{\tau_{\rm TOV}}\right)^2\right], \tag{4.6}$$

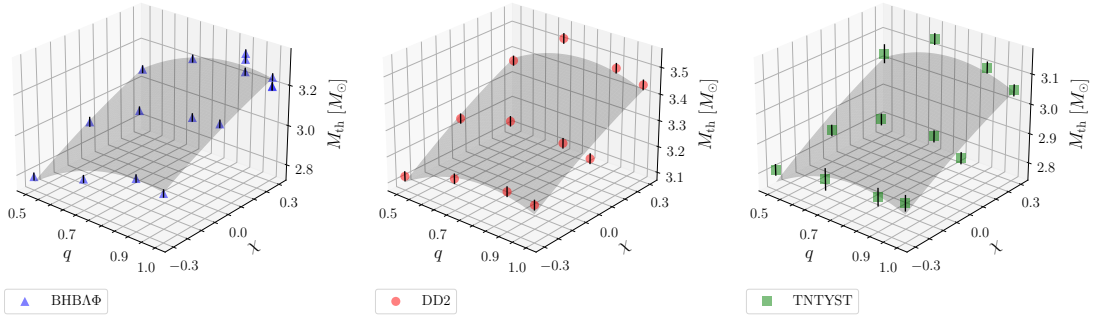


Figure 4.2: The surface representing the fit to Eq. (4.7) for each EOS is plotted as a function of $q$ and $\chi$. This figure has been reused from [41].

in the same way as performed in [42] [2]. The measured $M_{\rm th}$ is, thus, the value obtained by extrapolating the resulting fit using Eq. (4.6) to $t_{\rm col}/\tau_{\rm TOV} = 1$. This process is repeated for all configurations considered which will be analyzed in the following results section. As an example, we show in Fig. 4.1 the timeseries of $\hat{\alpha}$ for the $q = 0.7\,, \chi = 0.3$ BNS configurations; where each panel is for a different EOS. In the bottom right panel we show the fit performed to obtain the measured threshold mass value (solid line) and the related linear fit (dotted line) which tends to overestimate the threshold mass. We note the sensitivity of the resulting timeseries as a function of the binary mass where changes of $\sim 10^{-3}$ are sufficient to transition to collapse behavior at merger time.

## 4.2 Results

In order to gain an insight into the influence of mass asymmetry and spin on the threshold mass we utilize an initial dataset of $36$ configurations spanning across $q$, $\chi$, and EOS. For each configuration the threshold mass is measured by computing a sequence of BNS simulations until an error in the measurement of $M_{\rm th}$ is below $1\%$. For such a parameter study, more than $400$ simulations were performed to enable these results. As such, we have plotted the threshold mass as a function of $q$ and $\chi$ as shown in Fig. 4.2 for each EOS.

### 4.2.1 Quasi-universal behavior

Examination of Fig. 4.2 highlights a highly non–linear relation between $q$, $\chi$, and $M_{\rm th}$ which could be well described by a second-order polynomial. To this end, we propose an ansatz of

$$M_{\rm th}(q,\chi)|_{\rm EOS} := a_1 + a_2(1-q) + a_3\chi + a_4(1-q)\chi + a_5(1-q)^2 + a_6\chi^2\,, \qquad (4.7)$$

where the resulting fit for each EOS results in a chi–squared of $X^2_{\texttt{BHBΛΦ}} = 0.001$, $X^2_{\texttt{DD2}} = 0.001$, and $X^2_{\texttt{TNTYST}} = 0.003$. In all cases, the average deviation from the fit is $1\%$ with a maximum deviation of $\sim 2\%$ which is of the order of $\delta M_{\rm th} = 0.03 M_\odot$.

Upon further inspection, the form of the fit is similar for each EOS and, as such, the question arises as to whether or not a quasi-universal relation can be

[2] Use of non-linear fit continues to be necessary as the use of a linear fit can result in an overestimate of $M_{\rm th}$ of $\sim 1-2\%$.

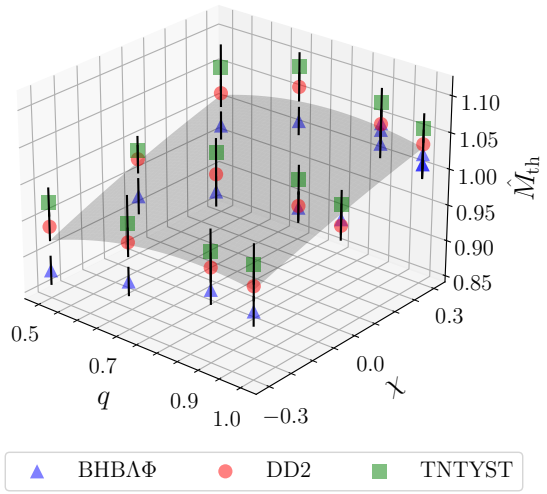


Figure 4.3: The surface representing the fit to Eq. (4.7) using the normalized threshold mass, $\hat{M}_{\rm th}$, which highlights the quasi-universal behavior of $M_{\rm th}$ as a function of mass asymmetry and spin. The measurement of $\hat{M}_{\rm th}$ is shown with a corresponding error bar where the markers denote the data for a given EOS. This figure has been reused from [41].

obtained that effectively rescales the surface depending on the EOS. Within [42] and the study of equal–mass irrotational BNS, the threshold mass is related simply to EOS specific TOV quantities, $M_{\rm TOV}$ and $R_{\rm TOV}$. Although the influence of $q$ and $\chi$ on $M_{\rm th}$ results in a more complicated form we expect, in the limit of $q = 1$ and $\chi = 0$, that the relation from [42] should be recovered. To this end we propose a new ansatz which is that of separability

$$M_{\rm th}({\rm EOS}, q, \chi) = \kappa({\rm EOS})\, f(q, \chi)\,, \tag{4.8}$$

where all of the dependence on the EOS is encapsulated within $\kappa({\rm EOS})$ and the remaining functional dependence on $q$ and $\chi$, i.e. $f(q, \chi)$, is contained within Eq. (4.7). In order to demand that the quasi-universal relation from [42] is recovered for $q = 1\,, \chi = 0$ we have chosen to use this relation as $\kappa({\rm EOS})$

$$\kappa({\rm EOS}) := \left(a - \frac{b}{1 - c\mathcal{C}_{\rm TOV}}\right) M_{\rm TOV}\,, \tag{4.9}$$

where $\mathcal{C}_{\rm TOV} = M_{\rm TOV}/R_{\rm TOV}$ is the stellar compactness and the fitting coefficients are $a = 2b/(2 - c)$, $b = 1.01$, and $c = 1.34$ as documented in [42]. In Fig. 4.3, we plot all of the data as a function of $\hat{M}_{\rm th} := M_{\rm th}/\kappa$ along with the fit of the normalized data to Eq. (4.7). For the EOSs considered we note a non–monotonic behavior in terms of $q$ which has been discussed in [37], [124]. However, it is expected that for neutron stars the dependence on spin should increase monotonically given

| FIT | $a_1$ | $a_2$ | $a_3$ | $a_4$ | $a_5$ |
|---|---|---|---|---|---|
| BHBΛΦ | $0.982 \pm 0.005$ | $0.08 \pm 0.06$ | $0.14 \pm 0.02$ | $0.04 \pm 0.06$ | $-0.4 \pm 0.1$ |
| DD2 | $0.997 \pm 0.007$ | $0.13 \pm 0.08$ | $0.12 \pm 0.02$ | $0.04 \pm 0.08$ | $-0.3 \pm 0.1$ |
| TNTYST | $1.024 \pm 0.008$ | $0.14 \pm 0.08$ | $0.12 \pm 0.03$ | $0.04 \pm 0.09$ | $-0.3 \pm 0.2$ |
| Univ | 1 | $0.11 \pm 0.07$ | $0.12 \pm 0.03$ | $0.07 \pm 0.09$ | $-0.3 \pm 0.2$ |

Table 4.1: The fitting coefficients for each EOS and the universal fit to Eq. (4.7). For Univ, $a_1 := 1$ in order to recover the equal-mass, irrotational result from [42]. This table was originally published in [41].

the addition of angular momentum to the system will result in a more stable and longer lived remnant[158]–[160]. As such, we expect there to be a maximum threshold mass at the maximum allowable spin, $\chi_{\rm max}$. In this work, $\chi = \chi_1 + \chi_2$ which implies $\chi_{\rm max} := 2 \times 0.65$, where $0.65$ is the maximum spin possible for an isolated NS [44]. Furthermore, we can use this reasoning to remove a degree of freedom from Eq. (4.7) by imposing the following constraint

$$\partial_\chi f(q,\chi)|_{\chi_{\rm max}} = 0\,, \tag{4.10}$$

which results in a functional relation for $a_6$ of

$$a_6 := \frac{a_3 + a_4(1-q)}{2\chi_{\rm max}}. \tag{4.11}$$

Shown in Tab. 4.1 are the fitting coefficients for each EOS as well as the universal fit where Eq. (4.11) has been used in all cases. Note that even though $a_1 := 1$ is only fixed in the case of the universal fit, the independent fits for each EOS result in $a_1 \approx 1$ further supporting the separability ansatz. Ultimately the fit results in a chi–squared of $X^2 = 0.028$ and the data deviates from the fit by an average of $2\%$ with a maximum deviation of $\sim 6\%$ which is at the most extreme configurations. Compared to the equal–mass irrotational binary configurations we find the threshold mass can increase by as much as $\sim 6\%$ for aligned spins and decrease by $\sim 10\%$ for anti–aligned spins. In an effort to ensure this result holds not only for $\chi_2 = 0$, we have included an additional small sample of runs with $\chi_2 \neq 0$ and have found that this fit holds equally well. The final fits reported in Tab. 4.1 have used these additional data points for completeness.

### 4.2.2 Constraints on stellar radii

With a robust relation for the threshold mass we can extend the analysis performed in [42] to provide constraints on the lower limit of stellar radii. To this end we have used Eqs. (4.6), (4.9), and (4.8) to compute sequences of $M_{\rm th}$ as a function of $M_{\rm TOV}$ along lines of constant $R_{\rm TOV}$ which are shown in the top panels of Fig. 4.4. Within each panel we use the chirp mass of GW170817 $1.188 M_\odot$ as the lower bound given the electro–magnetic counterpart indicates the merger did not result in a prompt collapse, however, translating this to a gravitational mass results in the shown blue band depending on the mass ratio. This is emphasized in the top left-most panel of Fig. 4.4. This procedure is conducted for each $\chi \in \{-0.3\,, 0\,, 0.3\}$ which corresponds to the left, middle, and right columns in Fig. 4.4 respectively. Looking first at the mass ratio, we find that knowledge of $q \gtrsim 0.7$ does not constrain the stellar radius much more than assuming $q = 1$, however, for $q \sim 0.5$ we see that much stronger constraints can be made given the significantly smaller prediction for the threshold mass. On the other hand, if we look at the spin of the binary, this can play an important role on constraining the EOS especially in the case of anti–aligned spins. For instance, by looking at the left panel and, under the assumption that GW170817 was equal mass with a total spin of $\chi = -0.3$, all EOSs with an $R_{\rm TOV} \lesssim 10.1{\rm km}$ would be excluded. Conversely, under the assumption that GW170817 had an aligned spin of $\chi = 0.3$ would result in a weaker constraint on the EOS.

In the same manner as [42], we can extend this analysis for an arbitrary mass $M$ in order to ascertain an estimate for the associated radius $R_x$ with a functional

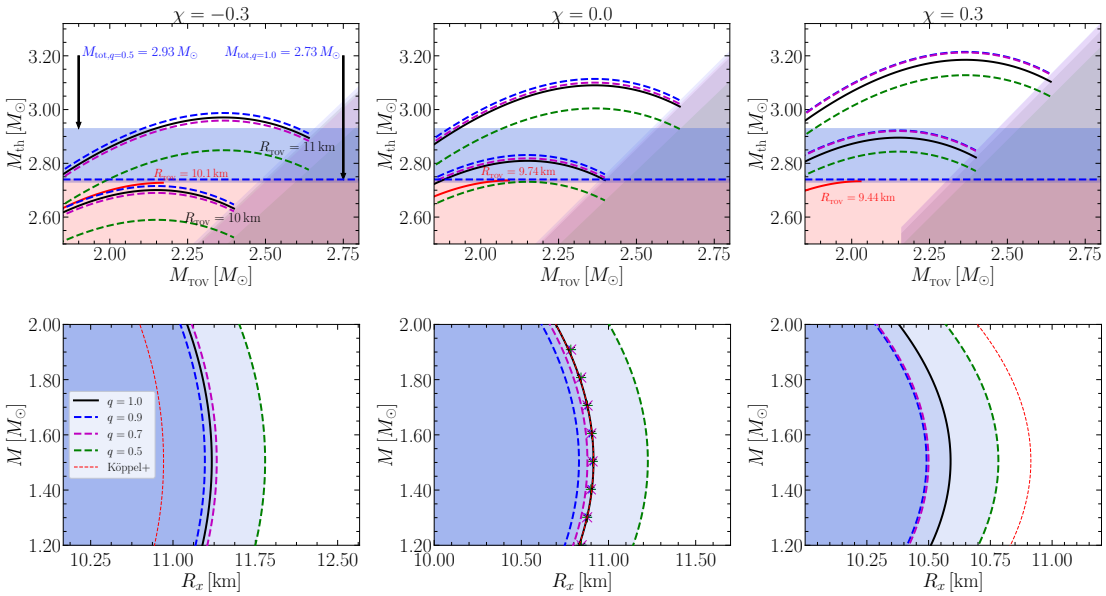


Figure 4.4: The columns within this figure are associated with a fixed spin $\chi \in \{-0.3, 0, 0.3\}$ respectively. *Top:* The constraints set on the lower limit of allowable TOV radii by computing the threshold mass using Eq. (4.7) along lines of constant $R_{\rm TOV} \in \{10, 11\}$ km for each mass ratio. The horizontal blue shaded region corresponds to the constrained region set by GW170817 under the assumption of $q \in \{0.5, 0.7, 0.9, 1\}$. The red shaded region includes those EOSs excluded under the assumption that the lower limit set by GW170817 for $q = 1$ whereas the grey regions are those excluded by causality. *Bottom:* We plot the obtained relation $R_x(M, q, \chi)$ given by Eq. (4.12) for each $q$. In the middle panel, the symbols show that $R_x(M)$ from [42] is recovered when plotting $R_x(M, q, \chi) f(q, \chi)$. In all of the lower panels, the red dashed line is the result $R_x(M)$ presented in [42]. This figure has been reused from [41].

dependence on $q$ and $\chi$, i.e. $R_x(M, q, \chi)$. In the bottom row of Fig. 4.4 we plot the ascertained function $R_x(M, q, \chi)$ for each $\chi \in \{-0.3\,, 0\,, 0.3\}$ which corresponds to the left, middle, and right columns. In our analysis, we have verified that the independently obtained expression can recover $R_x(M)$ presented in [42] by a simple rescaling using $f(q, \chi)$ defined in Eq. (4.7) such that

$$R_x(M, q, \chi) = \frac{R_x(M)}{f(q, \chi)}\,, \tag{4.12}$$

where $R_x(M)$ is the expression presented in [42]

$$R_x(M) = -0.88M^2 + 2.66M + 8.91. \tag{4.13}$$

Within Fig. 4.4 we have shown that the lower limit on the stellar $R_x$ is significantly influenced by spin where, in the case of anti–aligned spin, the lower limit is $\sim 9\%$ larger than in the aligned spin case. Furthermore, as with the top panels, we see only a weak constraint that can be set by knowledge of the mass ratio except in the extreme case where $q < 0.7$.

### 4.3 Summary

In this work we have explored the influence of mass ratio $q$ and spin $\chi$ on the threshold mass to prompt collapse in binary neutron star mergers. To do so we have computed BNS configurations within the range of parameters such that $q \in \{0.5, 0.7, 0.9, 1\}$ and $\chi \in \{-0.3\,, 0\,, 0.3\}$ using three finite temperature

equations of state BHB$\Lambda\Phi$, TNTYST, and DD2. Measuring the threshold mass for these configurations resulted in computing the inspiral and merger of more than $400$ BNS configurations.

From these results we have derived a quasi–universal relation that provides an accurate approximation of the measured threshold masses with an average (maximum) deviation from the acquired universal fit of $\sim 2\%$ ($< 6\%$). Furthermore, we find the influence of asymmetry results in a non–monotonic behavior with a peak threshold mass on the order of $q = 0.8$. Interestingly, this lines up well with the non-monotonic behavior noted in Sec. 3.2.2. Finally, we find the addition of spin-angular momentum from rotating NS solutions results in a monotonic behavior such that the threshold mass can increase by as much as $5\%$ for aligned spins and decrease by as much as $10\%$ for anti–aligned spins.

With a broad understanding of the influence mass asymmetry and spin have on massive binary neutron star mergers as discussed in chapters 3-4, it is pertinent to explore how such mergers can be distinguished from black hole-neutron star configurations with the same mass and spin distribution which we will explore in the following chapter.

# Chapter 5

# Fast ejecta as a potential way to distinguish black holes from neutron stars in high-mass gravitational-wave events

It is well established that the detection of heavy binary neutron star mergers can constrain the equation of state of nuclear matter while, at the same time, also help to constrain the potential mass ratio $q$ and effective spin $\tilde{\chi}$ of the binary [43]. Gravitational wave events such as GW170817[108] provide unique insights into the EOS of nuclear matter as heavy binaries can constrain the EOS via analysis of the threshold mass[23], [42], the lifetime of the remnant, and the electromagnetic counterpart. Furthermore, GW190425[6] poses a unique scenario where the total binary mass $M \approx 3.4 M_{\odot}$ and lack of a detected EM counterpart brings into question whether or not the binary consisted of two neutron stars or a black hole and a neutron star. A difficulty in assessing whether or not GW190425 could have been a BHNS system is due to the fact that current models for formation channels of such a low mass black hole [118], [119], especially for black holes with $M \approx M_{\rm TOV}$ [161]. However, recent observations have provided further evidence to support the formation of massive neutron stars[162] and, as such, could lead to the formation of a black hole with $M \approx M_{\rm TOV}$ in the event of an accretion induced collapse from a companion star or possibly from pulsar spin-down[163].

In this work we seek to analyze this unique regime of overlap for low–mass BHNS systems and high–mass BNS systems. To this end, we perform simulations of BHNS and BNS configurations with constant total mass $M_{\infty} = 3.6 M_{\odot}$ while varying the effective spin, $\tilde{\chi}$, and mass ratio, $q$. Furthermore, we fix the dimensionless spin of the secondary (less massive neutron star) to be irrotational, i.e., $\chi_2 = 0$. In this way, the effective spin of the binary is related to the dimensionless spin of the primary object and the mass ratio by

$$\tilde{\chi} := \frac{m_1 \chi_1 + m_2 \chi_2}{m_2 + m_1} = \frac{\chi_1}{1+q}\left(1 + q\frac{\chi_2}{\chi_1}\right). \tag{5.1}$$

With these constraints, we perform a systematic study for $q \in [0.486, 0.714]$ with an effective spin of $\tilde{\chi} \in \{0, 0.15, 0.35\}$.

In Sec.5.1 we will describe our experimental setup and specify the binary configurations to be examined. Furthermore, in Sec. 5.2 we will compare and contrast

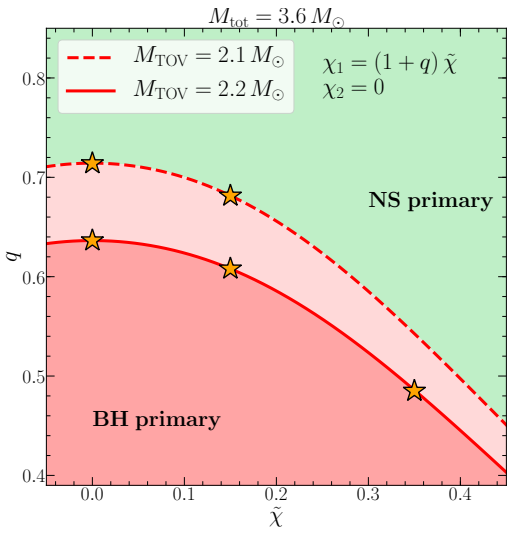


Figure 5.1: The dotted (solid) line describes the critical configurations for the BHBΛΦ (TNTYST) EOSs based on the universal relations derived in [43] for a total mass $M_{\rm tot} = 3.6$, $\chi_1 = (1+q)\tilde{\chi}$, and $\chi_2 = 0$. The green region defines the parameter space resulting in a stable primary NS whereas the red region below the critical lines denotes the region where a BNS is not possible. The stars denote the configurations examined in this work along the critical line which could be either a BNS or BHNS. This figure has been reused from [8].

the resulting dynamics as well as the resulting mass, composition, and distribution of the ejecta. Finally, in Sec. 5.3 we will summarize our results and discuss the potential impact to future multi–messenger observations.

## 5.1 Methods

In this work we utilize the same evolution setup as described in Appendix C. More specifically we use a numerical extent up to $\approx 6,000$km in each coordinate direction with a refinement level setup that provides a finest grid spacing of $\approx 215$m. Furthermore, we perform a full GRMHD evolution where an $\approx 10^{14}$G dipole magnetic field is imbedded into the secondary neutron star. In order to ensure consistency among results we have chosen to not include a magnetic field on the primary NS in the BNS simulation. The BNS initial data has been generated using the FUKA BNS solver as described in Ch. 2, however, at the time these simulations were performed the BHNS solver was not yet complete. Therefore, the publicly available LORENE spectral code was utilized to generate the BHNS

| | $M_1$ | $M_2$ | $M_{b,1}$ | $M_{b,2}$ | $q$ | $\chi_1$ | $\tilde{\chi}$ | EOS |
|---|---|---|---|---|---|---|---|---|
| TNT.BH.chit.0.00 | 2.20 | 1.40 | – | 1.55 | 0.636 | 0.00 | 0.00 | TNTYST |
| TNT.BH.chit.0.15 | 2.24 | 1.36 | – | 1.50 | 0.608 | 0.24 | 0.15 | TNTYST |
| TNT.BH.chit.0.35 | 2.42 | 1.18 | – | 1.28 | 0.486 | 0.52 | 0.35 | TNTYST |
| TNT.NS.chit.0.00 | 2.20 | 1.40 | 2.66 | 1.55 | 0.636 | 0.00 | 0.00 | TNTYST |
| TNT.NS.chit.0.15 | 2.24 | 1.36 | 2.70 | 1.50 | 0.608 | 0.24 | 0.15 | TNTYST |
| TNT.NS.chit.0.35 | 2.42 | 1.18 | 2.87 | 1.28 | 0.486 | 0.52 | 0.35 | TNTYST |
| BHBLP.BH.chit.0.00 | 2.10 | 1.50 | – | 1.65 | 0.714 | 0.00 | 0.00 | BHBΛΦ |
| BHBLP.BH.chit.0.15 | 2.14 | 1.46 | – | 1.60 | 0.681 | 0.24 | 0.15 | BHBΛΦ |
| BHBLP.NS.chit.0.00 | 2.10 | 1.50 | 2.40 | 1.65 | 0.714 | 0.00 | 0.00 | BHBΛΦ |
| BHBLP.NS.chit.0.15 | 2.14 | 1.46 | 2.48 | 1.60 | 0.681 | 0.24 | 0.15 | BHBΛΦ |

Table 5.1: Details of the configurations examined in this study including the EOS, component gravitational ($M_x$) and baryonic ($M_{b,x}$) masses, mass ratio $q$, and the effective binary spin $\tilde{\chi}$. Here, $\chi_2 = 0$ and $\chi_1 = (1+q)\tilde{\chi}$. This table was previously reported in [8].

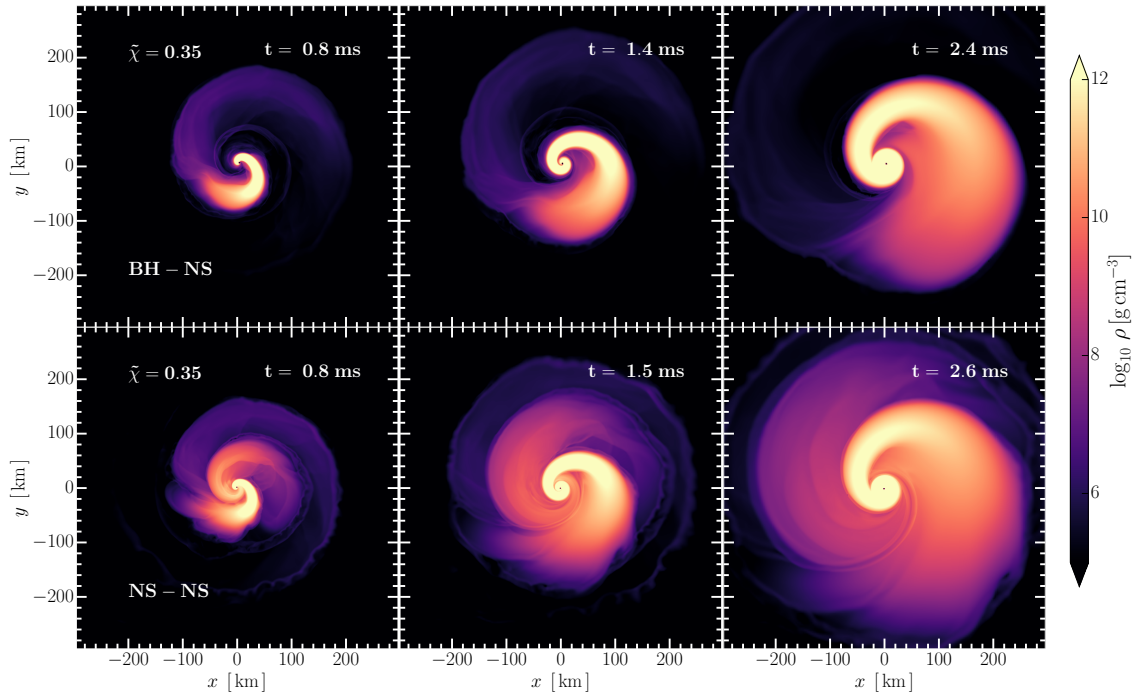


Figure 5.2: The results for the high–spin configuration using the TNTYST EOS with a $\tilde{\chi} = 0.35$ and $q = 0.486$ for the BH–NS (top) and BNS (bottom) at three characteristic post-merger times. For the BNS system, a second mechanism of mass ejection from the primary is clearly seen that is absent in the BHNS. This figure has been reused from [8].

initial data [77], [78], [164]. The LORENE code functions similar to FUKA in that it provides a solution to the EFE in the XCTS formulation (see Sec. 2.1 for details). Furthermore, the black hole is excised from the spectral domain using a fixed lapse boundary condition as discussed in Sec. 2.2.2. Finally, we utilize the BHB$\Lambda\Phi$ and TNTYST EOS to describe the microphysics of nuclear matter such that a range of compactnesses can be examined (see Appendix C.1).

In this work we intend to probe the distinguishing characteristics between BHNS and BNS mergers. As a visual aid we include Fig. 5.1 based on the universal relations discussed in [43] where the green region is the allowed parameter space for a BNS of a given $q$ and $\tilde{\chi}$ such that $\chi_2 = 0$ and the primary object is uniformly rotating with $\chi_1 = (1 + q)\tilde{\chi}$. The dotted (solid) lines mark the critical configuration for BHB$\Lambda\Phi$ (TNTYST) such that, below this line no stable configuration is possible for a BNS system. For $\tilde{\chi} = 0$, the mass of the primary is, therefore, $M_{\mathrm{TOV}}$. A neutron star below (or possibly on) the critical line would, therefore, collapse to a BH resulting in a BHNS system. Within Fig. 5.1 we denote the configurations examined in this work with stars which correspond to $\tilde{\chi} \in [0, 0.15, 0.35]$ [1] The specific configurations including mass ratio, component gravitational and baryonic masses, dimensionless spin of the primary, and the effective binary spin can be found in Tab.5.1.

[1]We note that in the case of BHB$\Lambda\Phi$ a configuration with $\tilde{\chi} = 0.35$ was not possible given the primary, after import into the evolution framework, would lie on the unstable branch and collapse to a BH.

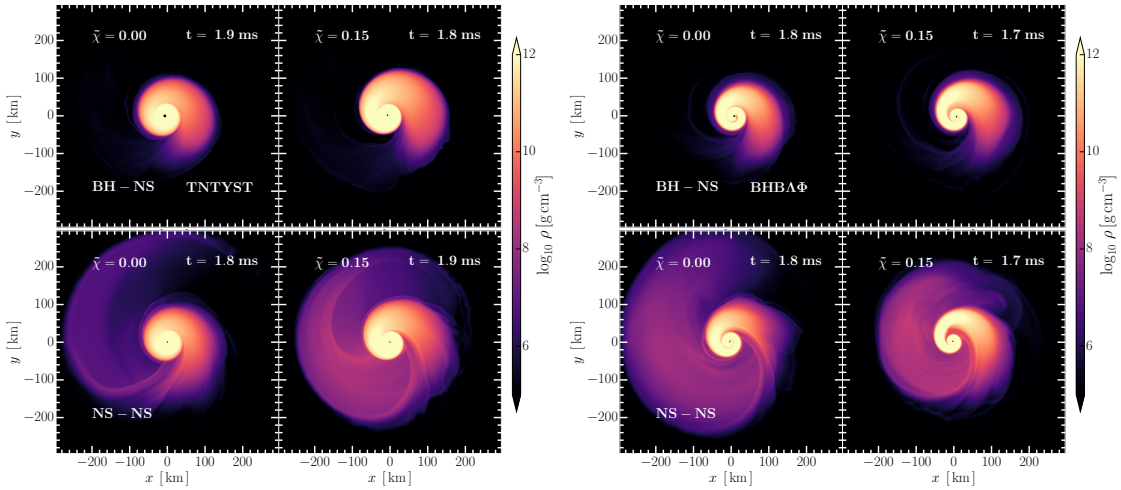


Figure 5.3: The low-spin prior configurations ($\tilde{\chi} \in [0.00, 0.15]$) for the TNTYST EOS (left) and BHBΛΦ (right). This figure has been reused from [20].

## 5.2 Results

In the following we will detail the results of our simulations for the BNS and BHNS configurations tabulated in Tab. 5.1. Specifically, our analysis will highlight the characteristic features that are unique to BNS mergers in the high mass and asymmetric regime. Furthermore, we will examine how robust these features are as the effective spin of the binary varies.

### 5.2.1 Matter Dynamics

As a first step to gain a qualitative insight into the distinguishing characteristics of the merger ejecta, we show in Fig. 5.2 the the rest–mass density during the post-merger of the BHNS (top) and BNS (bottom) systems using the TNTYST EOS with a $\tilde{\chi} = 0.35$ and $q = 0.486$. Shortly after merger (left column), we see already the formation of a secondary mass ejection arm for the BNS configuration which is opposite of the main tail that is observed for both configurations. As the evolution continues we can observe that the secondary tail provides an appreciable amount of ejecta to the system, however, it appears subdominant to the main ejection tail. If we focus on the right column ($\approx 2.4$ms post-merger), the BHNS results in a main tidal arm that is localized to the $+x$ side of the plot whereas in the BNS we see a more isotropic, although asymmetric, distribution.

The dynamical processes contributing to the secondary tidal arm can be attributed to the presence of the primary neutron star instead of a BH. With the presence of the primary NS, the disruption of the secondary object carries angular momentum and can induce a spin–up of the primary object. The rapid spin–up results in the generation of a secondary ejection channel of which can have very high velocities and is absent for the BHNS. It is important to note that the generation of a secondary arm has been identified for asymmetric BNS mergers in [22], [165]. Furthermore, such secondary arms are present in equal-mass BNS simulations at which point they are equal in mass. As the mass ratio decreases, the secondary arm formed by the spin–up of the primary object results in a smaller secondary tail that is sub-dominant to the main tidal arm. Moreso, as the asymmetry increases so to does the mass of the ejecta. In the limiting case of maximal

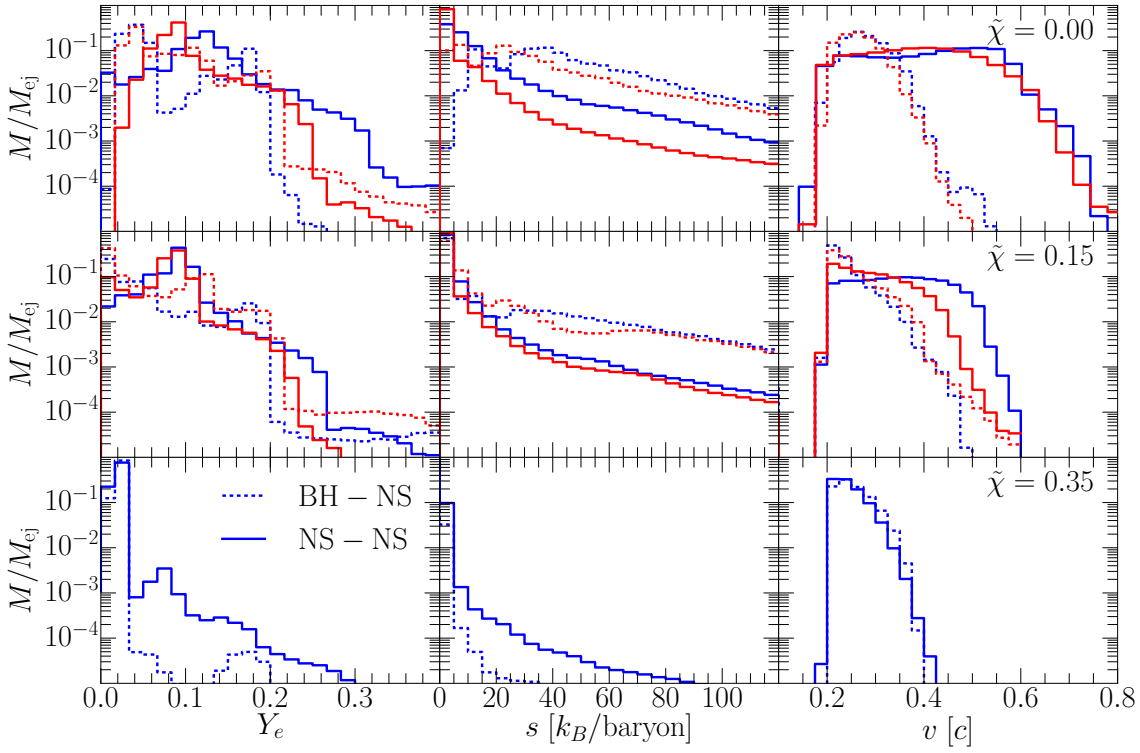


Figure 5.4: Mass fraction of the unbound ejecta mass $M_{\rm ej}$ as a function of the electron fraction $Y_e$ (left column), specific entropy $s$ (middle column), and the fluid velocity $v$ (right column). Each row corresponds to increasing $\tilde{\chi} \in \{0.00, 0.15, 0.35\}$ respectively. Finally, the blue (red) lines correspond to the TNTYST (BHBΛΦ) configurations where solid (dashed) lines denote BNS (BHNS) systems. This figure has been reused from [8].

asymmetry in the BNS merger, the main tidal arm resembles the main tidal arm in the BHNS merger, but the BNS still retains the smaller secondary arm.

We can extend the above analysis to include the influence of smaller effective spins. In Fig.5.3 we see the the low–spin prior for the TNTYST (left pane) and BHBΛΦ (right pane) configurations. Overall, we find the dynamical behavior to be similar, however, we find that with increasing spin (left to right) the total mass of the ejecta appears to increase significantly. We note for BHBΛΦ that the influence of its larger tidal deformability results in a more highly deformed secondary star which, in turn, will yield a more massive remnant disk. In contrast, the velocity of the secondary tail appears to increase as $\tilde{\chi}$ decreases. This can be seen in Fig.5.3 where we see the ejection from the secondary tail already escaping the box for $\tilde{\chi} = 0$ whereas the secondary ejection for $\tilde{\chi} = 0.15$ has not traveled as far. In the following section we will quantify this further upon presenting a detailed analysis of the ejecta composition.

### 5.2.2 Dynamical mass ejection composition

In order to obtain a quantitative understanding of the composition of the dynamical ejecta, we show in Fig. 5.4 the relative composition of the dynamical ejecta in terms of the electron fraction ($Y_e$), specific entropy ($s$), and velocity ($v$) in the first, second, and third column respectively. To discern bound from dynamical ejecta we utilize the Bernoulli criteria of $hu_t < -1$ where $h$ is the specific enthalpy and and $u^\mu$ is the fluid four velocity[53]. In Fig. 5.4 each row corresponds

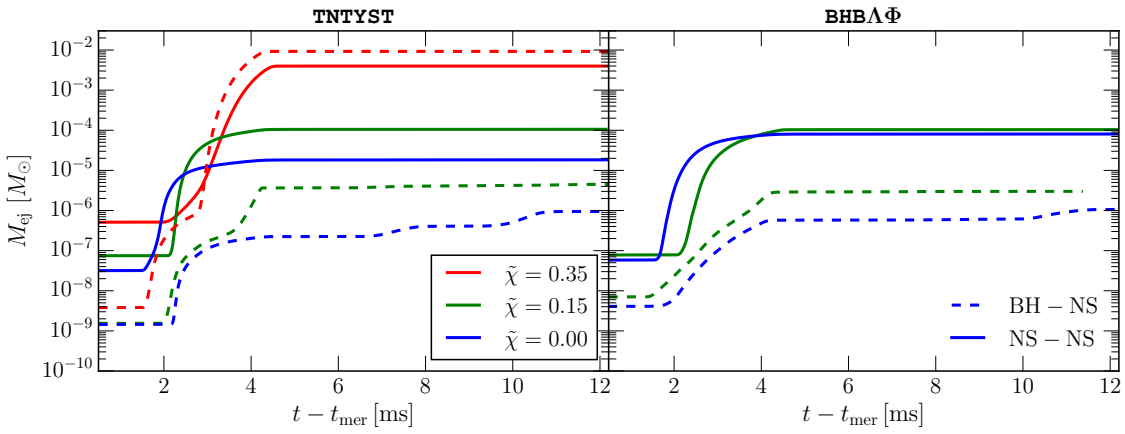


Figure 5.5: Shown is the measured dynamical ejecta post-merger for the TNTYST (left panel) and BHBΛΦ (right panel) binaries where the effective spin $\tilde{\chi} \in [0.00, 0.15, 0.35]$ is denoted by blue, green, and red color respectively. Furthermore, BNS (BHNS) configurations are represented by a solid (dashed) line. This figure has been reused from [8].

to the effective spin of the binary configuration, blue (red) colors corresponds to the TNTYST (BHBΛΦ) configurations, and solid (dotted) lines correspond to BNS (BHNS) configurations.

Focusing first on $Y_e$ we find that the BNS configurations with low–spin results in a peak at higher $Y_e$ values of $Y_e \approx 0.1$ as compared to their BHNS counterparts. This can be understood by considering that the generation of fast ejection occurs as a result of the collision of matter from the surface of the two NSs which is composed of matter with higher $Y_e$ than at the NS core. When comparing the extent of the $Y_e$ distribution for the BHNS and BNS configurations, we see for $\tilde{\chi} = 0.00$ (top row) that the BHBΛΦ (red) configurations are quite similar, however, for TNTYST the BNS configuration includes a much broader distribution reaching $Y_e \approx 0.35$ while the BHNS obtains a maximum $Y_e = 0.3$ which further highlights the influence of the tidal deformability on the dynamical ejecta. As the spin is increased to $\tilde{\chi} = 0.15$ (middle row) the extent of $Y_e$ decreases to 0.3 for the BHBΛΦ BNS configuration and, overall, a decrease in the mass fraction of the ejecta at higher $Y_e$ decreases. Finally, the high–spin configuration for the TNTYST EOS shows a similar peak to the BHNS counter part at low $Y_e \approx 0.02$, however, a secondary peak is still found at $Y_e \approx 0.08$ which is absent in the BHNS configuration. The distribution in $Y_e$ for the high-spin BNS configuration still produces ejected up to $Y_e \approx 0.3$ in contrast to the BHNS with a maximum $Y_e \approx 0.2$.

Looking next at the entropy $s$ (middle column) of Fig. 5.4, we see that a large fraction of the ejecta mass has a peak at lower specific entropy than the BHNS configurations which is attributed to the collision of nuclear matter from the two NSs. However, for the high-spin TNTYST configuration, we see that the fraction of ejecta at low-entropy decreases significantly which implies that rotation provides a more efficient mechanism to absorb the collisional energy resulting in an, overall, less energetic merger.

The most prominent impact to the dynamically ejecta can be readily observed in the velocity distribution (right column) in Fig. 5.4. In the case of $\tilde{\chi} = 0.00$, we find a similar broad distribution for both EOSs with a peak velocity on the order of $v \approx 0.8$ in contrast to the BHNS configuration which have a peak velocity

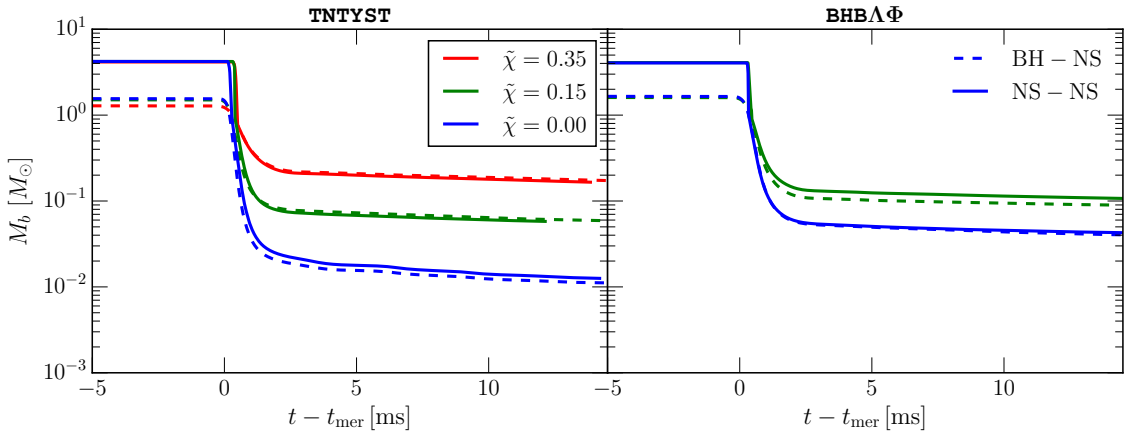


Figure 5.6: The timeseries of the rest-mass density as measured outside of the apparent horizon for the TNTYST (left) and BHBΛΦ (right) configurations. The spin of the configuration $\tilde{\chi} \in [0.00, 0.15, 0.35]$ is denoted by blue, green, and red color respectively whereas the solid (dashed) lines represent BNS (BHNS) configurations. This figure has been reused from [8].

$v \approx 0.5$. Given the main tidal arm is qualitatively similar as shown in Fig.5.3, the distribution of dynamical ejecta at $v > 0.5$ are largely attributed to the secondary tidal arm which appears to be primarily composed of fast-ejecta. For $\tilde{\chi} = 0.15$, a considerable suppression in the velocity distribution is observed such that only a peak of $v \approx 0.6$ is observed, however, we still find there is a broader distribution at a larger mass fraction, i.e., a larger portion of the dynamical ejecta at higher velocities, for the BNS configuration as compared to the BHNS configuration. Interestingly, for the highly spinning TNTYST configuration the velocity distribution of the BNS and BHNS configurations are essentially the same further highlighting, in the limit of highly spinning configurations, that it will very challenging to distinguish a BNS from a BHNS.

Furthermore, we show in Fig. 5.5 the total dynamical ejecta measured up to the end of the simulation. Overall, we find a steady increase in the mass of the dynamical ejecta as $\tilde{\chi}$ increases with a significant increase in the high-spin TNTYST configuration, however, given the second tidal arm is only a small fraction of the ejected mass, there are no significant differences between the BHNS and BNS configurations in terms of total dynamical ejecta. This conclusion is further supported by Fig. 5.6 which shows the total baryonic mass outside of the apparent horizon relative to the merger time. In this case we see that the total baryonic mass in the system is indistinguishable between the BNS and BHNS configurations further solidifying the result that the fast-ejecta is only a small fraction of the resulting mass present in the accretion disk and the dynamical ejecta. We note that this result is in line with previous estimates [166].

Finally, the analysis thus far has given a broad understanding of the influence of the fast–ejection on the bulk properties of the measured dynamical ejecta and disk mass, however, we will focus our attention now on the spatial distribution of the dynamical (unbound) ejecta. In Fig. 5.7 we show the time integration of the dynamically ejected mass (upper hemisphere) and the mass–weighted average $Y_e$ (lower hemisphere) for all of the configurations examined. The upper (lower) panels correspond to the TNTYST (BHBΛΦ) configurations with each row corresponding to increasing $\tilde{\chi}$. Comparing the BHNS with the BNS con-

figurations using the TNTYST EOS and $\tilde{\chi} = 0.00$ (top row) we see that the fast–ejecta produces the bulk of the unbound material which lies dominantly along the equatorial plane with some off-axis ejection which has been examined previously (c.f.[22], [165]). Furthermore the average $Y_e$ of the ejecta is $Y_e > 0.1$ which aligns well with the peak $Y_e$ in Fig.5.4. Conversely, the ejected mass for the low–spin BHNS is much more tightly bound given the lack of a secondary tail. As the spin increases to $\tilde{\chi} = 0.15$ (middle row) we see an increase in $M_{\rm ej}$ for the BHNS, however, the ejecta is still tightly constrained to the equatorial plane. For the BNS configuration, we see not only unbound fluid elements at higher latitudes, but also the prominent secondary tail that is opposite to the primary tail. Once again, the ejecta of the secondary tail has a higher $Y_e > 0.1$ compared to the ejecta of the primary arm which is $Y_e < 0.05$. In the final high-spin configuration with $\tilde{\chi} = 0.35$, we see the main tidal tail becomes the dominant production mechanism for unbound ejecta as seen previously [47], [167] and the secondary fast–ejection arm becomes subdominant. Overall, the same dynamics are seen for the BHB$\Lambda\Phi$ configurations with the notable difference being enhanced dynamical ejection for $\tilde{\chi} = 0.00$ which is attributed to the higher tidal deformability of the EOS.

### 5.2.3 Remarks on multi-messenger signatures

In this work, we've compared and analyzed the merger and post–merger of BNS and BHNS configurations with the same gravitational mass and effective spin. Both binary systems result in a similarly massive BH remnant with a remnant disk of nearly equivalent size (see Fig. 5.6) thus concluding that both configurations will likely result in comparable after glow properties [56]–[58]. In light of this analysis, we conclude that the implication for future multi–messenger detection will likely be limited to potential kilonova precursors drive by the fast–ejecta produced by the second tidal arm[53] which could result in a bright kilonova precursor[168].

## 5.3 Summary

In this work we have performed a first systematic study of the distinguishing characteristics between BNS and BHNS systems using a high binary mass of $M_{\rm tot} = 3.6 M_\odot$ with an effective spin of $\tilde{\chi} \in \{0.00, 0.15, 0.35\}$ which is within the critical overlap region in the parameter space of $q$ and $\tilde{\chi}$ (c.f. Fig.5.1). To do so we have performed state-of-the-art GRMHD simulations using a neutrino leakage scheme of five configurations using the TNTYST and BHB$\Lambda\Phi$ EOSs (see Tab.5.1).

When comparing the ejecta results between BHNS and BNS configurations, we find the resulting total remaining rest–mass density profile outside of the remnant BH is essentially the same thereby implying that the dominant kilonova and afterglow will be similar between BNS and BHNS configurations. However, the distribution of the dynamical ejecta's spatial and physical composition is quite diverse. Specifically, we find for the BNS configurations the formation of the secondary spiral arm due to the rapid spin–up of the primary NS. The rapid spin–up is largely attributed to the torque applied by the collision of the secondary NS resulting in fast ejecta up to $v \approx 0.8$ for $\tilde{\chi} = 0.0$. In contrast, the same BHNS configuration produces dynamical ejecta with only $v < 0.5$. Furthermore the secondary arm results in dynamical ejecta that is proton rich with $Y_e > 0.1$. The

fast ejection arm provides the most prominent characteristic to distinguish a BNS from a BHNS merger for the configurations examined. It has been shown previously that fast dynamical ejecta can lead to a brighter kilonova precursor[168], however, such a rebrightening has yet to be observed[169]. Furthermore, for the high–spin configuration examined using the TNTYST EOS we find that the secondary arm becomes considerably less pronounced thereby reducing the ability to distinguish the two configurations. As shown in Fig. 5.4, the high–spin configurations are similar although the BNS still results in a more proton rich ejecta.

In the works leading up til now the focus has been on extreme BNS configurations, however, these results have been restricted to purely hadronic equations of state. In the final chapter we will discuss a promising framework that includes a novel treatment of the transition to quark matter while still providing a physically motivated temperature and charge fraction dependence.

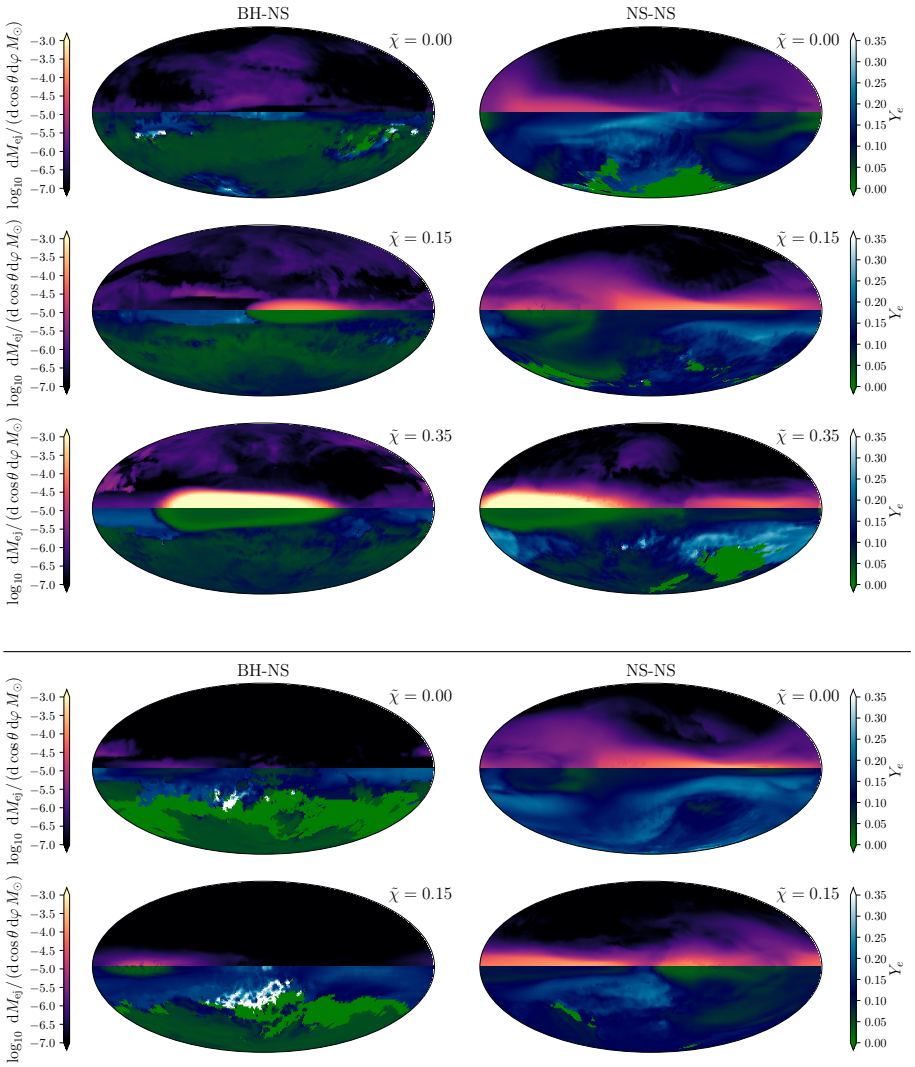


Figure 5.7: In each panel the time-integrated ejected mass $M_{\mathrm{ej}}$ (upper hemisphere) and mass-weighted average electron fraction $Y_e$ (lower hemisphere) projected onto a sphere at radius $r = 295\,\mathrm{km}$ from the origin. The upper (lower) panels are for the TNTYST (BHB$\Lambda\Phi$) configurations which contain in the the left (right) panels the results for the BHNS (BNS) respectively. The time integration is performed up to a short period after the fluid elements of both arms have passed through the detector. Finally, the rows correspond to increasing $\tilde{\chi}$ for a given EOS. In the high latitude regions with low $M_{\mathrm{ej}}$, artificially high/low values of $Y_e$ appear due to low density dynamics within the evolution framework, however, these regions can be ignored since they do not contribute to the total ejected mass properties. This figure has been reused from [8].

# Chapter 6

# Quark formation and phenomenology in binary neutron-star mergers using V–QCD

In the previous chapters we have been restricted to purely hadronic equations of state, however, probing densities above nuclear saturation density without a description of quark matter may overestimate characteristic features such as the threshold mass[125]. Therefore, we are inclined to find an EOS which includes a physically motivated treatment of the transition from nuclear to quark matter specifically one that is both temperature and charge fraction dependent. Previous works focusing on EOSs with a first–order phase transition have used constructions such as polytropic equations of state where a Gibbs-like construction is used to model the phase transition to quark matter and the temperature dependence is imposed using the standard $\Gamma_{\rm th}$ component for an ideal fluid (cf. [63]). This is of particular relevance to binary neutron star mergers given densities reached can be in excess of five times nuclear saturation density ($n_s = 0.16\mathrm{fm}^{-3}$) and temperatures far above $100$MeV. Therefore, it is expected that matter during and after merger will exist outside of $\beta$–equilibrium. Furthermore, a physically motivated model that includes both temperature as well as charge fraction dependence is needed given simpler polytropic models or tabulated models which utilize a $\Gamma_{\rm th}$ law allow for exotic configurations that are potentially non-physical, (e.g. metastable remnants with hot quark cores).

In a recent work[129], a novel hybrid solution to this problem is presented which provides a description of the deconfinement phase of dense nuclear matter to quark matter based on the V–QCD model. Within this framework the temperature dependence is obtained using a van der Waals model which extrapolates the cold $\beta$–equilibrium slice to finite temperature in the high density regime. Additionally, a Gibbs construction is used to construct the mixed phase region such that the baryon and charge chemical potentials are treated consistently for nuclear and quark matter. A natural consequence of this framework is the appearance of a critical point at a high finite temperature and large density. Finally, the low-density and temperature regime is described using the APR [170] and the Hempel-Schaffner-Bielich(DD2)[171] models. In the following section we will highlight the relevant model details for completeness, however, a thorough description of the construction as well as the individual components of the hybrid

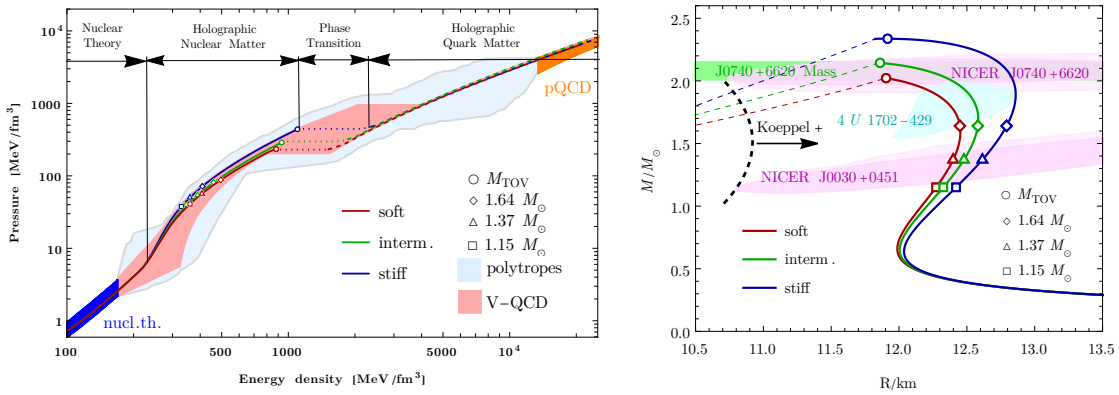


Figure 6.1: *Left:* The breakdown of the cold, $\beta$–equilibrium slice of the V–QCD model which is matched to the dark blue region described by nuclear theory[172] and the high density orange band described by perturbative QCD[173] calculations. In the intermediate density region the light–blue shaded region is constrained by polytropic equations of state and the pink region describes the remaining freedom within the V–QCD model after imposing constraints based on NS observations. Within the pink region we include the resulting model for the `Soft` (red), `Inter` (green), and `Stiff` (blue) EOSs where the dotted line represents the first–order phase transition to quark matter. *Right:* The resulting mass–radius diagram for the three models considered along with direct mass [174], [175] and radius [176]–[180] measurements of heavy pulsars. Finally, the mass–radius constraint ($R_x(M)$) as derived in [42] is shown as the dotted-black line. This figure has been reused from [62].

framework can be found in [129] and the references therein.

With the appearance of a new EOS the space of parameters to explore are quite vast. A well established test case is GW170817 since it was not only a moderately heavy binary, but also one that is expected to produce a meta-stable remnant that survived $\gtrsim 1s$ prior to collapsing to a BH. Additionally, since the mass ratio of GW170817 is not well constrained, we can explore the influence $q$ has on the resulting dynamics. Finally, by using numerical simulations to compute the inspiral and merger of GW170817-like configurations we can explore the stages and distribution of quark formation during the (post-)merger and infer how gravitational wave events can provide insights into and constrain the V–QCD framework.

## 6.1 EOS model

In this work we have utilized the soft (`Soft`), intermediate (`Inter`), and stiff (`Stiff`) models as described within [129] and have been made publicly available on `CompOSE` [181]. The novel approach described in [129] and the references therein utilize gauge/gravity duality in order to circumvent issues that arise within quantum field theory in the finite density and high coupling regime by reformulating the problem within classical five-dimensional gravity. More specifically, the framework described by Demircik et al, V–QCD, is rooted in string theory in the Veneziano limit [182], [183], however, an effective theory is needed which reduces to tuning the action of the model such that it agrees with QCD data at finite number of colors ($N_c$) and flavors ($N_f$). Specifically, the model must be tuned in order for characteristic features such as asymptotic freedom, confinement, linear glueball and meson trajectories and chiral symmetry breaking are reproduced. However, this only partially constrains the available space of tuning parameters available within V–QCD. To fully constrain the model lattice QCD data is leveraged for large-$N_c$ pure Yang-Mills theory [184] and data for

$N_c = 3$ QCD with $N_f = 2 + 1$ flavors at physical quark masses [185], [186] at small baryon-number density. Furthermore, the model utilizes a homogeneous prescription which is effective at describing the high density regime, but quickly breaks down when the density is of the order of $n_s$.

In order to accurately describe the low density regime a hybrid approach has been taken which utilizes the most accurate model for the density regime of interest. To this end, the V–QCD description of nuclear matter at low temperature and near nuclear saturation is paired with the APR model at $\beta$–equilibrium. The remainder of the low density and temperature regime is governed by a combination of the HS(DD2) and APR models. In this way a series of hybrid EoSs are obtained that agree well with all current observational constraints by tuning the remaining degrees freedom of the V–QCD model. However, the V–QCD suffers from a trivial dependence on temperature which must be rectified to obtain an EOS with predictive power. Therefore, a van der Waals model is used with an excluded volume correction for the nucleons and an effective potential. In this way, the temperature dependence is solved by matching the V–QCD predictions for the cold EOS and extrapolating to finite temperature. Furthermore, a dependence on charge fraction is also achieved by utilizing the charge fraction dependence of the `DD2` EOS in the low density and temperature regime while a simple free electron model is utilized in the quark phase. Finally, a meson gas model is used near the cross over in the high temperature regime. To ensure proper treatment of the baryon and charge chemical potential of nuclear and quark matter, a Gibbs construction is used to model the transition between the two phases of matter which not only results in the appearance of a mixed phase within the phase diagram, but also the appearance of a critical point at finite high temperature and large density.

Within this framework three EOS models have been developed which span the allowed space of the mass–radius diagram as constrained by current astronomical observations. In the left panel of Fig. 6.1 we highlight the regions pertaining to the individual models that, together, result in the utilized hybrid EOS framework. Here the three EOS models (`Soft`, `Inter`, and `Stiff`) are shown in order to emphasize their discrepancies which are quite significant given the pres-

| | $q$ | $M_{\rm TOV}$ $[M_\odot]$ | $M_1$ $[M_\odot]$ | $M_2$ $[M_\odot]$ | $R_1$ [km] | $R_2$ [km] | $\tilde{\Lambda}$ | $f_{\rm mer}$ kHz | $f_3$ kHz | $f^{2,1}$ kHz | $f^{2,2}$ kHz | $t_{\rm BH}$ [ms] |
|---|---|---|---|---|---|---|---|---|---|---|---|---|
| `Soft_q10` | 1.0 | 2.02 | 1.37 | 1.37 | 12.37 | 12.37 | 537 | 1.77 | 4.00 | 1.44 | 2.92 | 9.5 |
| `Soft_q07` | 0.7 | 2.02 | 1.64 | 1.15 | 12.42 | 12.24 | 517 | 1.63 | 3.80 | 1.55 | 2.80 | 5.8 |
| `Soft_q10-NPT` | 1.0 | 2.06 | 1.37 | 1.37 | 12.37 | 12.37 | 537 | 1.76 | 4.00 | 1.62 | 2.85 | $> 37$ |
| `Soft_q07-NPT` | 1.0 | 2.06 | 1.64 | 1.15 | 12.42 | 12.24 | 517 | 1.64 | 3.85 | 1.47 | 2.79 | 11 |
| `Inter_q10` | 1.0 | 2.14 | 1.37 | 1.37 | 12.45 | 12.45 | 565 | 1.74 | 4.00 | 1.51 | 2.73 | $> 35$ |
| `Inter_q07` | 0.7 | 2.14 | 1.64 | 1.15 | 12.56 | 12.30 | 543 | 1.63 | 3.70 | 1.42 | 2.67 | $> 37$ |
| `Stiff_q10` | 1.0 | 2.34 | 1.37 | 1.37 | 12.58 | 12.58 | 617 | 1.74 | 3.90 | 1.39 | 2.49 | $> 37$ |
| `Stiff_q07` | 0.7 | 2.34 | 1.64 | 1.15 | 12.76 | 12.38 | 591 | 1.59 | 3.50 | 1.39 | 2.48 | $> 38$ |

Table 6.1: Here we tabulate the analyzed binary configurations to include the mass ratio $q$; the maximum non-rotating mass for the given EOS $M_{\rm TOV}$; the component gravitational masses; the component stellar radii; the binary tidal deformability; the instantaneous gravitational wave frequency at the maximum strain amplitude; characteristic frequencies of the post-merger phase $f_3$ , $f^{2,1}$, and $f^{2,2}$; and the post-merger time when the remnant collapsed to a BH ($t_{\rm BH}$) for the models that collapsed within the simulation time. This table was reused from [62]

sure is plotted in a log scale. Furthermore, a strong first order phase transition is denoted by dashed lines at intermediate energy densities. The associated mass–radius curve for each EOS model is shown in the right panel of Fig. 6.1 where we see the `Stiff` model being at the edge of the constraint set by the X-ray binary `4 U 1702-429` [178] whereas the `Soft` EOS is near the minimum allowed $M_{\rm TOV} = 2.0 M_\odot$ set by `PSR J0740+6620` [174], [175]. Finally, all the models are well within the constraint set by GW170817 such that $\tilde{\Lambda} < 720$ and with sound speed profiles consistent with the recent general sound speed parameterization inside of a NS [128].

## 6.2 Methods

To explore the `Soft`, `Inter`, and `Stiff` EOS models, we have chosen to use the event GW170817 as a basis for this work. The measured chirp mass from GW170817 was $\mathcal{M}_{\rm chirp} = 1.186 M_\odot$ where the chirp mass is related to the total binary mass $M_\infty$ and the mass ratio $q$ by

$$\mathcal{M}_{\rm chirp} = \left[\frac{q}{(1+q)^2}\right]^{3/5} M_\infty \,. \tag{6.1}$$

Due to the degeneracy in measuring the mass ratio and spin, we choose to use $q \in \{0.7, 1\}$ with $\chi_1 = \chi_2 = 0$ in order to explore the influence mass asymmetry has on the merger remnant and quark production. The resulting binary configurations along with the binary tidal deformability $\tilde{\Lambda}$ and the related $M_{\rm TOV}$ for each EOS model considered can be found in Tab. 6.1. Within Tab. 6.1 are two models labeled with `-NPT` which do not include a phase transition to quark matter. These configurations will be discussed in Sec. 6.3.4 during the discussion of the lifetime of the `Soft` model. Furthermore, Tab. 6.1 includes characteristic frequencies of the binary merger which will be discussed during the GW analysis in Sec. 6.3.2.

The BNS initial data has been generated using the `FUKA` ID solvers described in Ch. 2 with the inclusion of eccentricity reduction performed using 3.5PN estimates as discussed in Sec. 2.5. Additionally, we have used the same evolution scheme as described in Appendix C where a finest grid spacing of $\Delta_{\rm HR} := 221$m has been used. The use of this resolution is the result of a convergence study based on the gravitational wave spectra and production of quark matter which will be discussed in Sec. 6.3.3. In their current form the EOS models utilized do not include the relevant microphysics in order to describe neutrino radiation; therefore, the leakage scheme within `FIL` has not been used nor have magnetic fields been introduced.

### 6.2.1 Extraction radii of thermodynamic quantities

As a first estimate of the distribution of quark formation during a BNS merger, the location of quark matter is computed in post–processing as a function of $n_b$, $T$, and $Y_e$ which can be used to construct 2D plots for a qualitative understanding of the distribution of quark matter. In order to obtain a more quantitative result, we instead compute the average amount of quark matter within three extraction radii of $3$km, $6$km, and $9$km which we label as *inner core*, *outer core*, and *inner crust* respectively; which are centered at $(n_b)_{\rm max}$ for $t < t_{\rm merge}$ and at the center-of-mass for $t \gtrsim t_{\rm merge}$. Furthermore, as shown in Fig. 6.2, these radii roughly correspond to

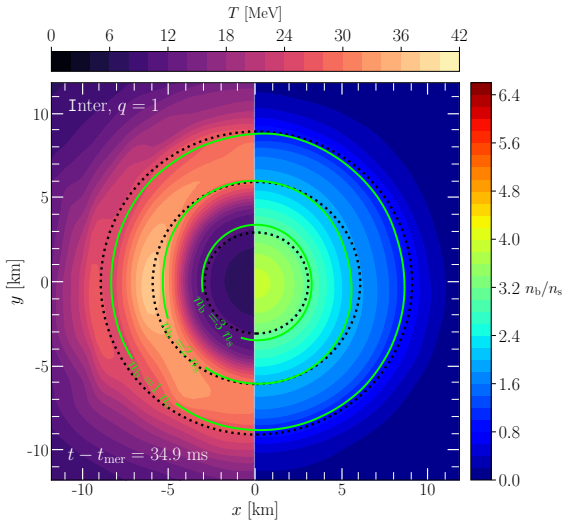


Figure 6.2: The green contours define the extraction radii for thermodynamic quantities in as described in 6.2.1 which have been overlayed with the 2D slice in the $xy$–plane of the computed density profile of the HMNS remnant 31.9ms post-merger for the `Inter_q10-MR`. Here the `MR` denotes that an evolution resolution of $\Delta_{\rm MR} = 295$m was used. The chosen radii of $[3, 6, 9]$km have been chosen since they line up with dashed contours corresponding to $n_b = [3, 2, 1]n_s$ respectively. This figure has been reused from [62].

$3n_s$, $2n_s$, and $1n_s$ respectively based on the late post–merger of the `Inter_q10-MR` simulation, however, we have verified a similar density distribution is observed for the `Soft` and `Stiff` models for both mass ratios considered. It is important to stress that these radii do not always align with these densities especially during the violent merger process. Instead these radii serve as a reference point for discussion and analysis. Only in the limit of a long–term stable remnant do these radii approximately line up with the previously mentioned densities.

We can extend the utility of these extraction radii by including the ability to compute the average of various thermodynamic quantities within each radii

$$\langle f \rangle := \frac{1}{A} \int_\Omega f d^2x \,, \qquad A := \int_\Omega d^2x \,. \tag{6.2}$$

Using Eq. (6.2) we can compute timeseries of the average quark volume produced within each extraction radii. It is important to note that in this simplistic expression the average is computed over a volume assuming a flat spacetime metric determinant. We have verified that even with the inclusion of the computed metric determinant during a simulation the results are minimally influenced due to the fact that, by averaging over the volume, the contribution of the computed metric determinant more–or–less cancels during the averaging procedure. We leave it to future work to not only enable the real–time computation of the quark fraction during a numerical simulation, but to do so using the computed metric. These advancements will allow for accurate 3D analysis of the quark volume and its distribution. Finally, when discussing the maximum temperature $T_{\rm max}$ and density $(n_b)_{\rm max}$, these values are measured within these annuli.

## 6.3 Results

In this section we will explore the results from the previously described BNS configurations using the three EOS models. Specifically, we will analyze the (post-)merger dynamics and quark formation with a focus on when quarks are formed and their dependence on the temperature $T$ and density $n_b$ as will be discussed in Sec. 6.3.1. In Sec. 6.3.2 we will analyze the influence of quark formation on the gravitational wave spectra to determine consistency with the lifetime from GW170817 as well as how future GW detectors will be able to ascertain whether

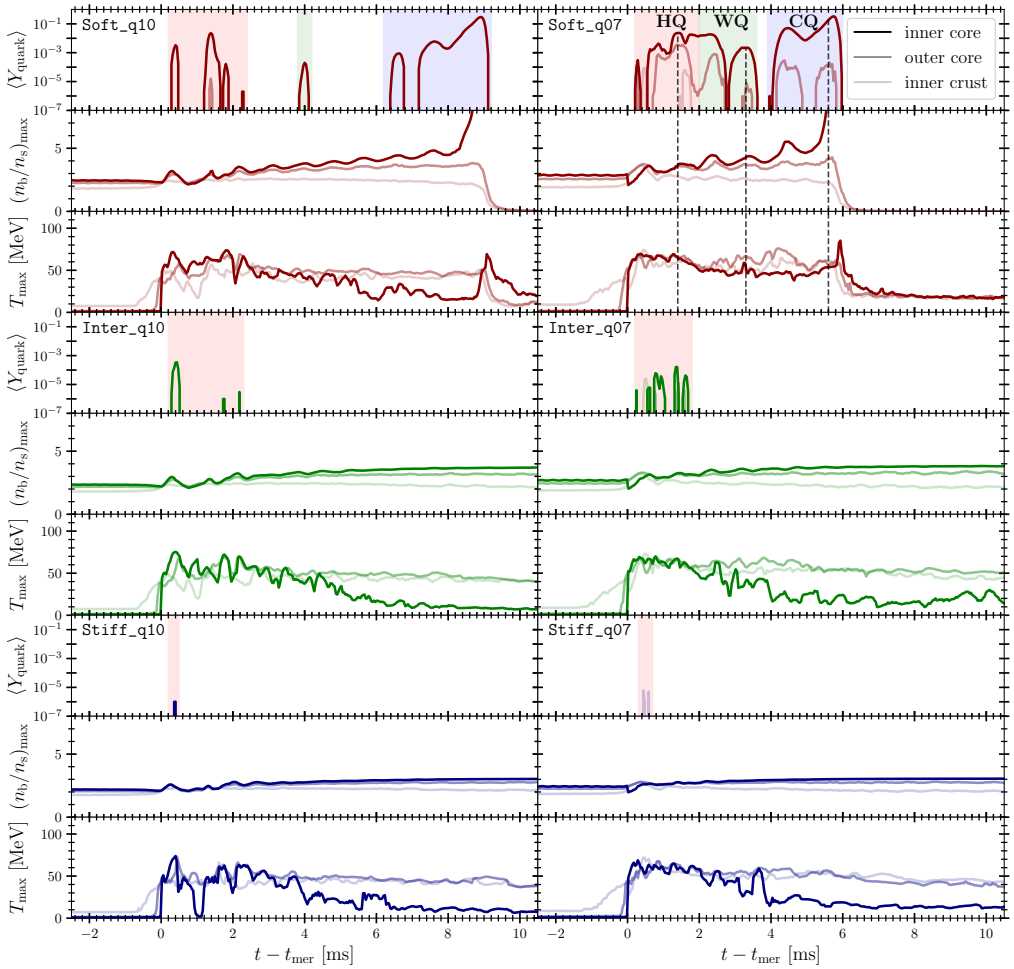


Figure 6.3: The measured maximum temperature $T_{\rm max}$, the maximum number density $(n_b)_{\rm max}$ normalized by $n_s$, and the average quark fraction $\langle Y_{\rm quark}\rangle$ as measured within the three extraction radii for the three EOSs considered. The vertical black dashed lines in the upper-right panel correspond to the time slices used to produce Fig. 6.4. Finally, we characterize the stages of quark formation as hot quarks (HQ), warm quarks (WQ), and cold quarks (CQ) based on the temperature profile. This figure has been reused from [62].

or not a merger remnant has undergone a phase transition to quark matter. Along this line, in Sec. 6.3.4 we will focus on the remnant lifetime and how this compares to the expected $1s$ lifetime of GW170817. Finally, we include a convergence study in Sec. 6.3.3 which provides the basis for the resolution used in our numerical simulations to obtain the GW spectra and lifetime results.

### 6.3.1 Merger dynamics and quark formation

When exploring a numerical simulation for the first time it is useful to gain some initial insights into the characteristics of the binary and the merger remnant by analyzing the 1D timeseries of interesting thermodynamic quantities. Given $Y_{\rm quark}$ is a function of $n_b$ and $T$, we begin by analyzing these quantities as well as computing the average quark fraction $\langle Y_{\rm quark}\rangle$ for the six configurations of interest. In the case of $Y_{\rm quark}$ we choose to look at $\langle Y_{\rm quark}\rangle$ instead since this will provide some insight into the magnitude of quark production at a given time. Furthermore, we are interested in $(n_b)_{\rm max}$ and $T_{\rm max}$ to see how $\langle Y_{\rm quark}\rangle$ is corre-

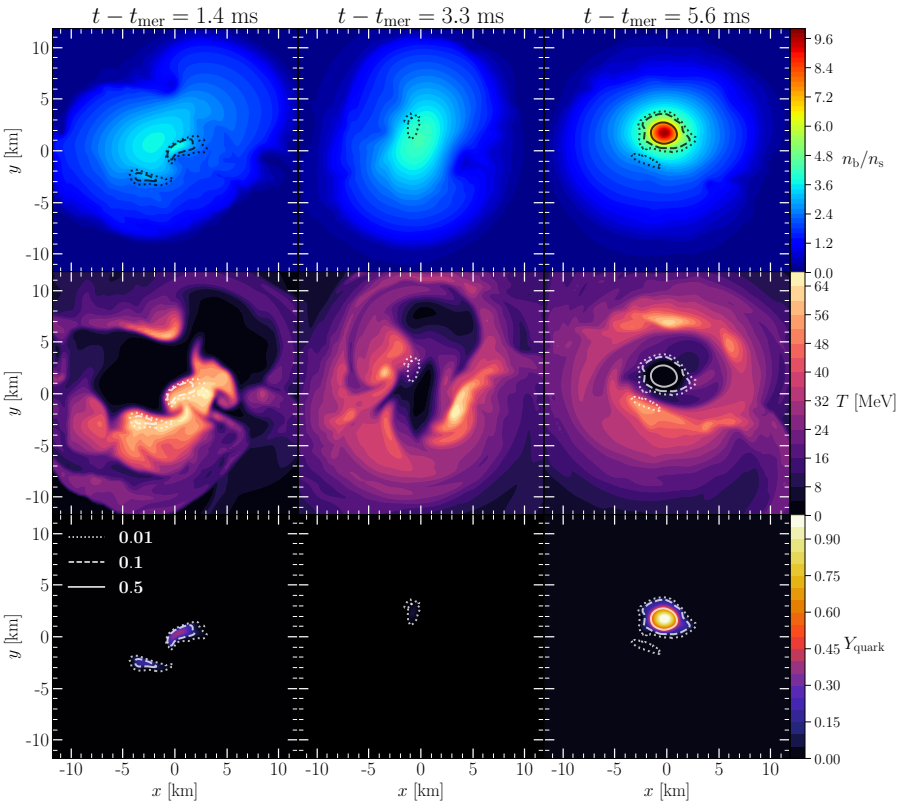


Figure 6.4: 2D slices in the $xy$-plane for $n_b/n_s$ (first row), $T$ (second row), and $Y_{\rm quark}$ at three characteristic post-merger times for the `Soft_q07` configuration that highlight the stages of HQ, WQ, and CQ. In all images we overlay contours of constant $Y_{\rm quark}$ to highlight the interplay between temperature and density in the formation of quark matter. This figure has been reused from [62].

lated to these maximum values. The plot of these timeseries are shown in Fig. 6.4 where the red, green and blue shaded regions correspond to the production of hot quarks (HQ), warm quarks (WQ), and cold quarks (CQ) respectively which will be discussed next.

At the time of merger we see a clear correlation between the formation of quarks and the maximum temperature for all of the models considered. For this reason, we will denote the quarks produced during this stage as hot quarks (HQ) since they appear at the extremely hot shock interface that forms between the two NSs at merger. In the `Soft` model we consistently observe a much higher production of HQ which we attribute to having higher compactness (i.e., higher density profile) for the same gravitational mass as compared to `Inter` and `Stiff` models. Similarly, the asymmetric models also result in a higher amount of HQ production both due to the higher compactness of the more massive object as well as the additional heating mechanisms due to the asymmetry in the system. Interestingly, in the asymmetric cases we find that quark formation is no longer limited to the *inner core*, but are now seen in the *outer core* and *inner crust* as well.

As the formation of the HMNS attempts to equilibrate, a bar–mode instability is present due to the resulting differential rotation. As the remnant begins to settle down due to loss of angular momentum, matter not only begins to cool, but a slight breathing in $(n_b)_{\rm max}$ appears. In the `Soft` model we find there is a sensitive interplay between $T$ and $n_b$ such that the appearance of an intermediate stage of

quarks is produced which we denote as warm quarks (WQ). In our simulations, we only find the production of WQ for the `Soft` model, however, we deduce that the formation of WQ is likely for the `Inter` and `Stiff` models in the case of heavier binaries which will be the subject of future work.

As the remnant continues to cool and transitions to a more uniformly rotating configuration, the density profile increases while the temperature decreases. In the case of the `Inter` and `Stiff` models, the remnant settles into a meta–stable remnant for the remainder of the evolution (Sec. 6.3.4 will revisit their lifetime); however, both configurations from the `Soft` model result in an early collapse at $t - t_{\rm merge} =: \Delta t_{\rm merge} = 9$ms for $q = 1$ and $\Delta t_{\rm merge} = 6$ms for $q = 0.7$. Prior to the collapse of the `Soft` configurations, we see a steady growth of $(n_b)_{\rm max}$ leading to a large production of quarks within the cold, dense core of the NS. Intuitively, we refer to this as the cold quark (CQ) stage which results in a phase-transition-triggered collapse (PTTC) to a black hole which has been observed in previous studies[63].

To further explore these quark production stages we choose characteristic times of high quark production from the `Soft_q07` simulation. The time slices chosen are also denoted by vertical dashed black lines in Fig. 6.3 (upper-right panel). At the defined times of $\Delta t_{\rm merge} \in \{1.4, 3.3, 5.6\}$ ms we plot 2D profiles of the density $n_b$, temperature $T$, and $Y_{\rm quark}$ in the $xy$-plane as shown in Fig. 6.4. In all of the presented profiles we include contours of constant $Y_{\rm quark}$ to highlight the regions pertaining to quark production. For $\Delta t_{\rm merge} = 1.4$ms, we find that the production of HQs overlap with the hottest regions of the remnant. At $\Delta t_{\rm merge} = 3.3$ms, we see that the production of WQs is in a region near the core that is neither the hottest nor the most dense. Finally, at $\Delta t_{\rm merge} = 5.6$ms, we find that the highest concentration of CQs overlaps with the coldest and most dense region of the remnant, however, there is a small, low-concentration region of quarks that forms towards the outer core which appears to form under similar conditions as quarks in the WQ stage. Furthermore, the appearance of a pure quark core results in a PTTC. Interestingly, the appearance of a cold core is in contrast with [187] where the core is hot, however, this is not unexpected since they use the standard $\Gamma_{\rm th}$ law which results in the temperature scaling rather simply with the density and ignores the change in the composition.

With this in mind we turn now to see how the composition of matter in the BNS remnant probes the phase diagram of the `Soft` model. Shown in Fig.6.5 (left) is the phase diagram for the `Soft` model in the $T$ and $n_b/n_s$ space along with the measured values of $T_{\rm max}$, $(n_b)_{\rm max}$, and $Y^{\rm max}_{\rm quark}$ which appear as square, star, and circle markers respectively. Furthermore, the color of the markers of red, green, and blue correspond to specific post–merger time periods of peak quark production. Given the composition of matter will go out of $\beta$–equilibrium, we include dashed and dotted lines which denote the phase boundaries for the minimum (maximum) $Y_e = 0.05$ $(0.09)$ measured in the HMNS. During the HQ (red) stage, we see $Y^{\rm max}_{\rm quark}$ overlap with $T_{\rm max}$ and at later times overlap with $(n_b)_{\rm max}$ as the system transitions to the WQ stage. Note that it appears necessary for the mixed-phase to be out of beta–equilibrium as shown by the dotted and dashed lines for $Y^{\rm max}_{\rm quark}$ at low densities in order for HQ and WQ to form for certain markers. In the WQ (green) stage, we see a complete disconnect of $Y^{\rm max}_{\rm quark}$ from $T_{\rm max}$ and $(n_b)_{\rm max}$ while at the same time WQs lie exactly on the phase boundary further

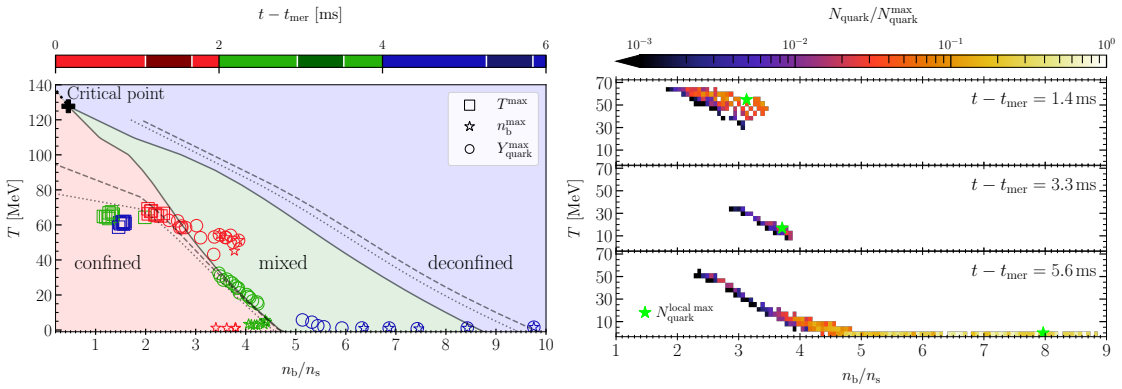


Figure 6.5: *Left:* The phase diagram for the `Soft` model at $\beta$–equilibrium indicated by solid lines where the dashed and dotted lines are the phase boundaries for the minimum (maximum) $Y_e = 0.05\ (0.09)$ measured in the HMNS. The squares, stars, and circles correspond to $T_{\rm max}$, $(n_b)_{\rm max}$, and $Y_{\rm quark}^{\rm max}$ respectively as measured from the evolution of the `Soft_q07` configuration. The color of the markers correspond to the dark regions in the color bar which are related to the post-merger time. *Right:* The number of quarks ($N_{\rm quark}$) measured at characteristic post-merger times, their distribution in the space of $T$ and $n_b/n_s$, and local maximum. Note that we have normalized all of the data based on the global maximum $N_{\rm quark}^{\rm max}$ as measured from these three time slices. This figure has been reused from [62].

highlighting the sensitive interplay between $T$, $n_b$, $Y_e$ and the remnant dynamics. Finally, during the CQ (blue) stage $Y_{\rm quark}^{\rm max}$ and $(n_b)_{\rm max}$ predominantly overlap as expected.

With a firm understanding with how $Y_{\rm quark}^{\rm max}$ probes the phase diagram, it is important to understand the distribution of $Y_{\rm quark}$ as a function of $T$ and $n_b$ which can be seen in Fig.6.5 (right). Here we capture the entire domain of quark production by utilizing $126 \times 35$ bins with equal size in linear space, in the $[n_s,\ 10\,n_s] \times [0, 140\,{\rm MeV}]$ region of the number density–temperature $(n_b, T)$ plane. Furthermore each bin is evaluated independently such that in each bin, $N_{\rm quark}$ is computed as

$$N_{\rm quark} = \sum_j V_j Y_{{\rm quark},j} n_{b,j}\ , \tag{6.3}$$

where the sum is over all $Y_{\rm quark}$ within the $jth$ grid cell with volume $V_j$ encapsulated by each bin for a fixed time slice. Finally each row represents the quark distribution normalized by the global maximum, $N_{\rm quark}^{\rm max}$, as a function of $T$ and $n_b$ at the same characteristic times used for the 2D plots in Fig. 6.4. In the HQ stage (top) we see the local maximum (green star) of quark production at $T \approx 50{\rm MeV}$ and the bulk of quarks being produced between $T \approx [30, 60]{\rm MeV}$ and at lower densities of $n_b/n_s \approx [2, 3.5]$. Next, during the WQ stage (middle) we see a significant drop in temperature where the local maximum occurs at around $T \approx 10{\rm MeV}$ with a span of $T \approx [5, 30]{\rm MeV}$ and $n_b/n_s \approx [2.7, 4]$. Finally, we see in the CQ stage (bottom) the local maximum of $Y_{\rm quark}$ occurs at $n_b/n_s \approx 8\,, T \lesssim 5{\rm MeV}$, but the distribution of $Y_{\rm quark}$ spans $T \approx [0, 50]{\rm MeV}$ and $n_b/n_s \approx [2.3, 9]$. The quark distribution during the CQ stage further highlights that, although the bulk of the quarks produced are located in the coldest and most dense regions, there are regions of quark production that take place at higher temperatures and lower densities similar to the WQ stage.

### 6.3.2 Gravitational wave analysis

Given the primary signature of a binary merger event is the gravitational waveform, it is imperative to quantify the influence the EOS models may have on the GW signature. To do so we use the Newman-Penrose formalism [154], [188] such that we can relate the obtained Weyl curvature scalar $\psi_4$ to the second time derivative of the polarization amplitudes of the gravitational wave strain $h_{+,\times}$

$$\ddot{h}_+ + i\ddot{h}_\times = \psi_4 := \sum_{\ell=2}^{\infty}\sum_{m=-\ell}^{m=\ell} \psi_4^{\ell,m}{}_{-2}Y_{\ell,m}\,, \tag{6.4}$$

where ${}_sY_{\ell,m}(\theta,\phi)$ are spin-weighted spherical harmonics of weight $s=-2$. To this end, we have sampled $\psi_4$ during our simulations with a frequency of $\approx 26\,\mathrm{kHz}$ from a spherical surface with a radius of $\approx 440\,\mathrm{km}$ centred at the origin of our computational domain. The integration is performed using the fixed frequency method derived in [189] to obtain an accurate waveform from our numerical simulations. Furthermore, we extrapolate the result to the estimated luminosity distance of $40\,\mathrm{Mpc}$ of the GW170817 event [190]. Additionally, we fix the angular dependence of the spherical harmonics part by the viewing angle $\theta = 15^\circ$ determined from the jet of GW170817 [191]. Finally, we set $\phi = 0^\circ$ without loss of generality.

In addition to analyzing the features of the raw strain, it is advantageous to integrate over the signal to obtain its power spectral density (PSD) such that prominent frequencies can be identified. To do so, we follow [192] and compute the PSD as

$$\tilde{h}^{\ell,m}(f) := \frac{1}{\sqrt{2}}\Bigg( \left|\int \mathrm{d}t\, \mathrm{e}^{-2\pi i f t} h_+^{\ell,m}(t)\right|^2 + \left|\int \mathrm{d}t\, \mathrm{e}^{-2\pi i f t} h_\times^{\ell,m}(t)\right|^2 \Bigg)^{1/2}. \tag{6.5}$$

A complementary mode of analysis to the PSD is that of spectrogram analysis which highlights the GW frequency distribution as a function of time. To do so the spectrogram is computed using time-windows of 3ms centred at every $\approx 0.04\,\mathrm{ms}$ of our waveform data.

A last method of analysis includes the computation of the phase frequency which is a function of the phase difference between $h_\times^{2,2}$ and $h_\times^{2,1}$

$$f_{\mathrm{GW}} := \frac{1}{2\pi}\frac{d\phi}{dt}\,, \qquad \phi := \arctan\left(\frac{h_\times^{2,2}}{h_+^{2,2}}\right), \tag{6.6}$$

from which we can measure the merger frequency $f_{\mathrm{mer}} := f_{\mathrm{GW}}(\Delta t_{merge} = 0)$.

By carrying out the previously mentioned calculations, we show in Fig. 6.6 the $+$–polarization of the $\ell = m = 2$ mode of the gravitational wave strain, the power spectral density as computed from Eq. (6.5) for the $(\ell, m) = (2,1)\,, (2,2)$ modes and the spectrogram of $h_+^{2,2}$ where the white curve shows the magnitude of the spectrogram as a function time. For the raw strain, the stages of HQ, WQ, and CQ are highlighted with red, green, and blue backgrounds respectively.

Focusing first on the raw strain, we see a very similar behavior for all the binaries up to merger which is expected since they all have essentially identical

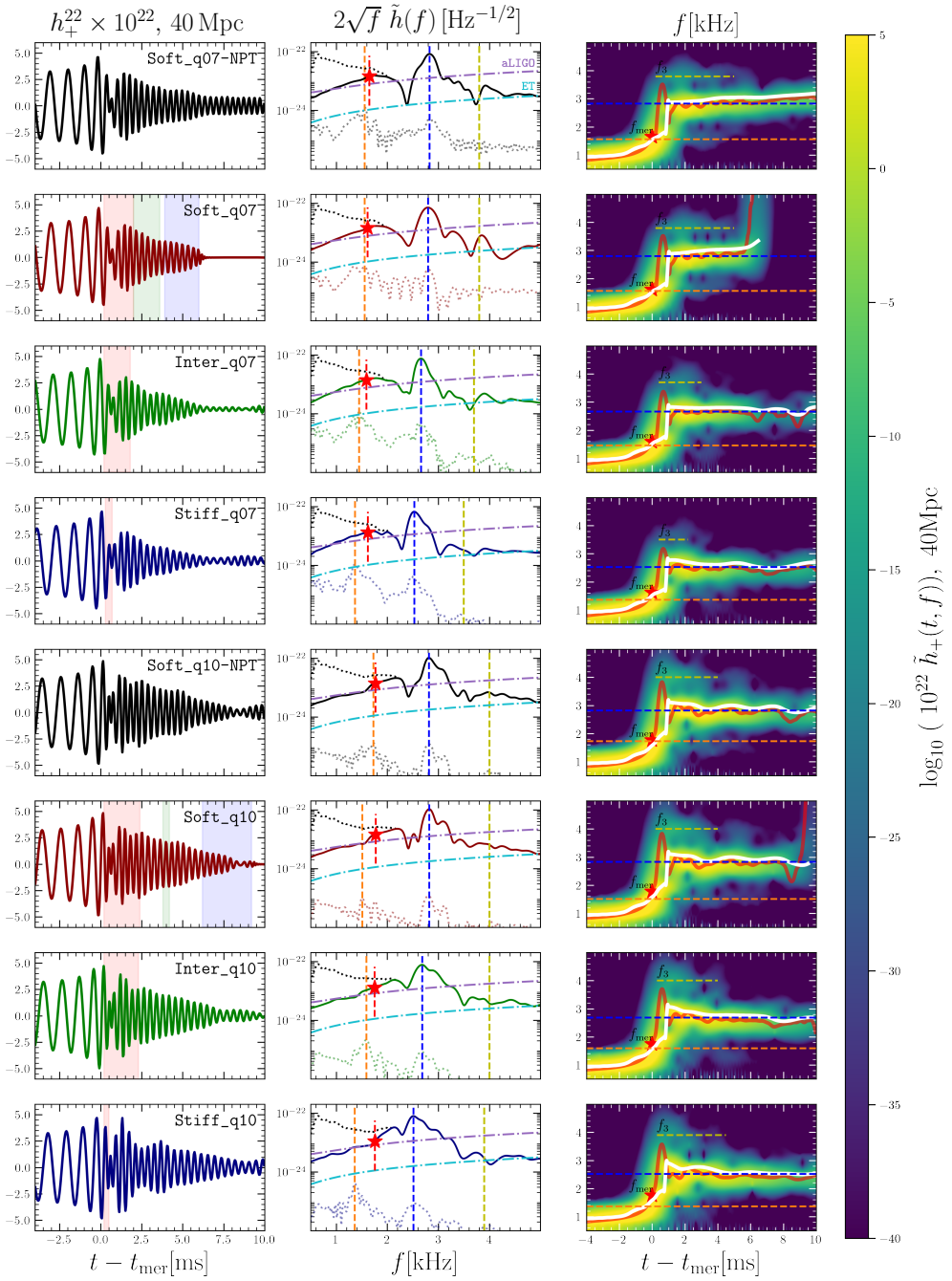


Figure 6.6: *Left:* The $+$–polarization of the $\ell = m = 2$ mode of the gravitational wave strain. *Center:* The power spectral density as computed from Eq. (6.5) for the $(\ell, m) = (2,1)\,, (2,2)$. Here the dark dotted line shows the contribution from the inspiral for the $(2,2)$ mode only. Included are the sensitivity curves related to the current sensitivity of advanced LIGO and the Einstein Telescope respectively [60], [61]. *Right:* The spectrogram of $h_+^{2,2}$ where the white curve shows the magnitude of the spectrogram as a function of time. Note: In the right two columns the orange and blue dashed lines correspond to the peak frequencies $f^{2,1}$ and $f^{2,2}$ for the $(\ell, m) = (2,1)\,, (2,2)$ respectively whereas the dashed yellow line corresponds to the $f_3$ frequency measured from the spectrogram. The red star denotes merger frequency, $f_{\rm mer}$. This figure has been reused from [62].

prescriptions for the cold, $\beta$–equilibrium portion of their models at low densities. In the post–merger the most prominent feature is the early collapse for both of the binaries using the `Soft` model. We find that this collapse can be understood as a PTTC which is attributed to the core of the HMNS remnant undergoing a rapid

softening due to the transition to pure quark matter. It is important to note that similar collapse behavior has also been observed in models that include hyperons [193]–[195]. For the `Soft_q10` and `Soft_q07` configurations we estimate the time of black hole formation ($t_{\rm BH}$) at the onset of exponential decay of the strain amplitude which is indicative of the black hole ringdown. For the remaining configurations that do not collapse within the evolution time, we use the time at the end of the medium resolution simulations as a lower bound on $t_{\rm BH}$. These times are included in Tab. 6.1.

Within the tabulated PSDs there are two curves associated with the $(\ell, m) = (2, 2)$ mode such that the dark dotted line shows the contribution of the inspiral to the PSD (i.e., the PSD is integrated from $t = 0$ up to $\Delta t_{\rm merge} = 10{\rm ms}$) and the solid line (i.e., the PSD that is integrated from $\Delta t_{\rm merge} = [0, 10]{\rm ms}$). As we can see, the portion of the inspiral is again, essentially identical for all the models considered for a given $q$. Below the PSD for the $(\ell, m) = (2, 2)$ is the subdominant $(\ell, m) = (2, 1)$ mode which we see is roughly an order of magnitude weaker for $q = 0.7$ and nearly two orders of magnitude weaker for $q = 1$. In each PSD, the dashed orange line denotes the $f^{2,1}$ peak frequency for $(\ell, m) = (2, 1)$, the dashed blue line denotes the $f^{2,2}$ peak frequency, and the yellow line denotes the $f_3$ frequency as measured from the spectrogram. The red star denotes the merger frequency $f_{\rm mer}$. Upon comparing the $q = 0.7\,, 1.0$ configurations for the three models we see a similar behavior overall with a systematic shift in both peak frequencies which we attribute to the differences in stiffness. For $q = 1$ this is less apparent for $f^{2,1}$ given the (2,1) mode is prone to numerical errors due to its small values.

Similarly, in the right column of Fig. 6.6 are the spectrograms where lines denoting $f^{2,1}$, $f^{2,2}$, and $f_3$ have been included as well as the star denoting $f_{\rm mer}$. We note that although $f_3$ is similar among the EOS models, there is a systematic dampening of the $f_3$ frequency going from the `Soft` to the `Stiff` model for $q = 0.7$. For $q = 1$ no such observation can be made. Furthermore, we note that $f^{2,1}$ and $f^{2,2}$ line up especially well with the $f_1$ and $f_2$ peaks in the spectrogram, however, no apparent peak is found in the PSD that lines up with the $f_3$ frequency which is only measured in the spectrogram.

### 6.3.3 Convergence analysis

Based on the results shown in Sec.6.3.1-6.3.2, it is important to ascertain the influence evolution resolution has on the obtained results. We know already from Ch.2 that the influence of the ID on the evolution will be sub-dominant, therefore, we can logically extend this result to the current study since the ID is only dealing with the cold $\beta$–equilibrium slice of the EOS models. With this in mind, we choose to perform additional simulations to ascertain the influence of evolution resolution on the GW strain as well as the production of quark matter. For this, we perform three simulations up to $10{\rm ms}$ post-merger using resolutions of $\Delta_{\rm LR} = 369{\rm m}$ (`Soft_q10-LR`), $\Delta_{\rm MR} = 295{\rm m}$ (`Soft_q10-MR`), and $\Delta_{\rm HR} = 221{\rm m}$ (`Soft_q10`) where $\Delta_{\rm HR}$ is the resolution used for the results discussed in the previous sections. We note that in our simulations we use a constant courant factor $\mathcal{C} = 0.2$, therefore, the temporal resolution increases as the spatial resolution increases.

In Fig.6.7 (left) we show the $+$–polarization of the $(\ell, m) = (2, 2)$ mode of the

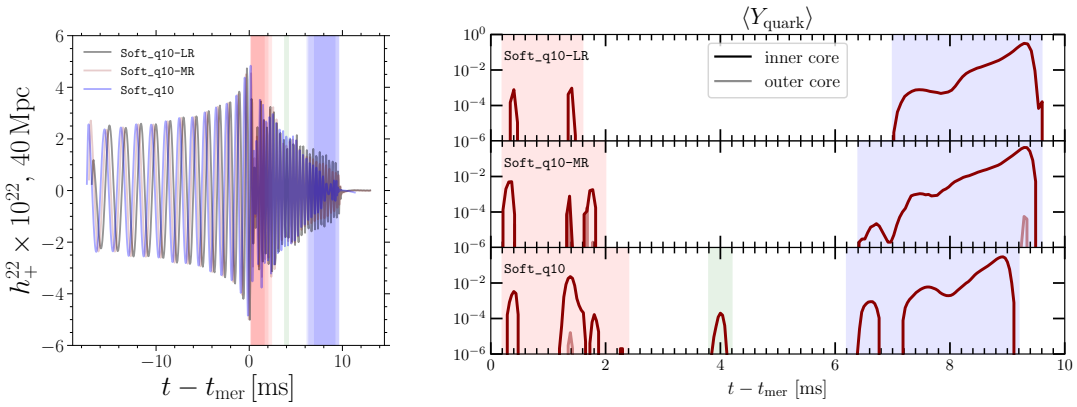


Figure 6.7: *Left:* Convergence analysis of the $h_+^{22}$ gravitational wave strain for the three different evolution resolutions considered. We note a slight phase difference in the inspiral and a difference in the post–merger amplitude, however, the collapse time is robust across these resolutions. *Right:* The average quark abundance measured for the three resolutions considered. Our results highlight the need for higher resolutions to capture fine-structure details such as the appearance of WQ which is only seen for the highest resolution considered. This figure has been reused from [62].

gravitational wave strain for the three resolutions mentioned aligned at merger (i.e., the strain maximum). Here we note a small phase difference to the inspiral waveforms, but with nearly equal amplitude up to merger. In the post–merger we do notice discrepancies in the amplitude, but the phase is essentially the same and the computed collapse time is robust across the resolutions considered. Therefore, the early collapse of the `Soft` configurations is a feature that needs to be analyzed more closely which is discussed further in Sec. 6.3.4.

In Fig.6.7 (right) we show the time series for $\langle Y_{\rm quark} \rangle$for $\Delta_{\rm LR}$ (top), $\Delta_{\rm MR}$ (middle), and $\Delta_{\rm HR}$ (bottom). We find that the time of quark production seen in $\Delta_{\rm LR}$ is mostly retained, however, with increasing resolution we find that the abundance of quarks not only increases in magnitude, but also in time. This includes the appearance of WQ only for the $\Delta_{\rm HR}$ resolution. Furthermore with increased resolution we also see regions of constant quark production (e.g., 6-9ms) start to form independent peaks in $\Delta_{\rm HR}$ (e.g., $\Delta t_{\rm merge} = 6.5$ms). Finally, with higher resolution we also identify the regions of quark production in the outer core further emphasizing the need for high resolution.

Although these convergence results give confidence to the results presented thus far, a future study will focus on identifying the convergent regime of these models. Specifically, a more sophisticated computation of the quark fraction during the numerical simulation (as opposed to post-processing) is needed in order to enable a full 3D analysis of the quark distribution in order to quantify the convergent regime.

### 6.3.4 Remnant lifetime

Based on the convergence analysis performed in Sec. 6.3.3, we are confident that the early collapse of the `Soft` models are not an artifact of evolution resolution and, as such, poses an important question as to the degree to which the phase transition to quark matter has an impact on the result. To that end, we have performed two additional simulations for $q \in \{0.7, 1\}$ for the `Soft` model

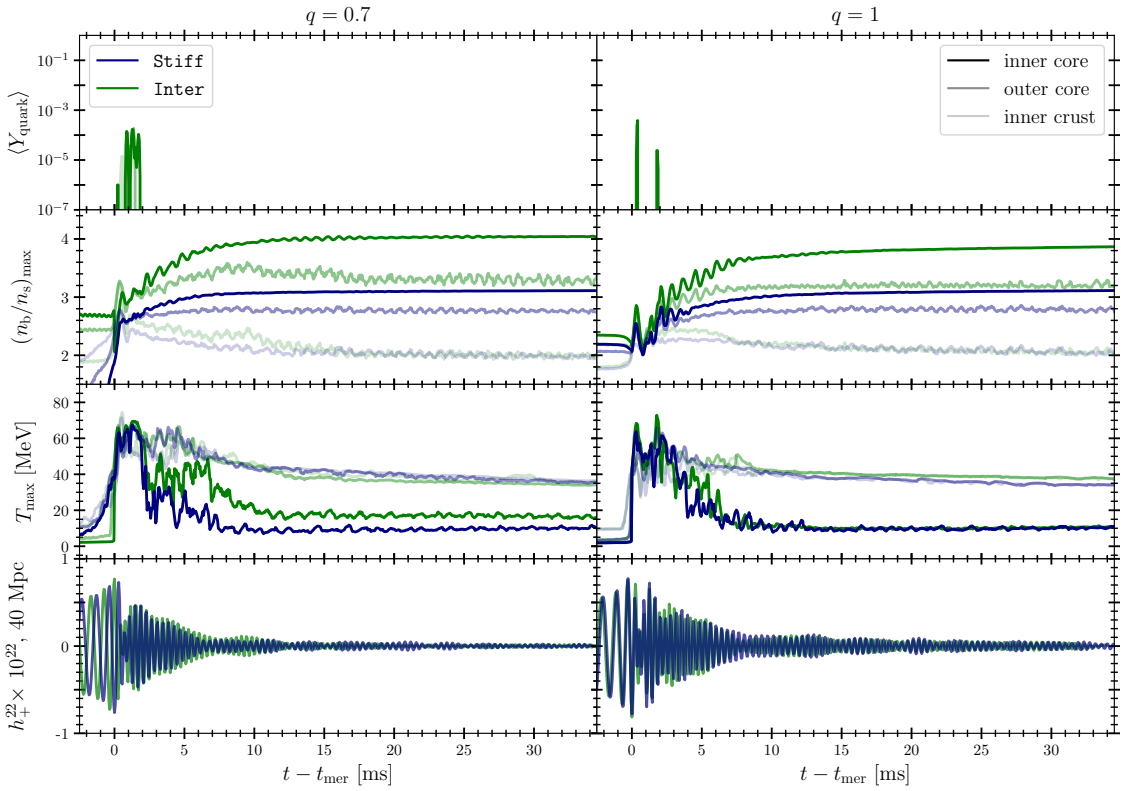


Figure 6.8: The results for the long–term simulations of the `Inter` and `Stiff` configurations which have been performed using $\Delta_{\rm MR}$. Overall, the results are comparable to the simulations performed at high resolution in the early post–merger phase and provide a lower limit on the collapse to a black hole which is the end of the simulation time $\Delta t_{\rm merge} \approx 35$ms. This figure has been reused from [62].

where the phase transition to quark matter is artificially suppressed. We denote these configurations in Tab. 6.1 and Fig. 6.6 as `Soft_q07-NPT` and `Soft_q10-NPT` respectively.

For the equal–mass configuration we can see in Fig. 6.6 (row 5 and 6) that the PSDs of `Soft_q10-NPT` and `Soft_q10` are quite similar as to be expected with the only discrepancy being a shift in the $f^{2,1}$ frequency. The frequency shift is attributed to the PTTC which causes a softening of the EOS. Furthermore, `Soft_q10-NPT` did not collapse within the simulation time $\Delta t_{\rm merge} \approx 15$ms, however, for `Soft_q07-NPT` a collapse to a black-hole occurs at $\Delta t_{\rm merge} \approx 11$ms. Even so, the PTTC of `Soft_q07` occurs $\approx 5$ms prior to `Soft_q07-NPT`. In spite of the `Soft` model being consistent with current constraints on the EOS, the soft configurations studied here are in tension with the expected lifetime of GW170817. Although there are many uncertainties of the mass ratio and spin of the GW170817 binary, this result shows that future multi–messenger detections can help to constrain the V–QCD model.

In contrast, the same cannot be said for the `Inter` and `Stiff` models which did not collapse within the evolution time. However, the convergence results in Sec. 6.3.3 indicate that the impact of performing evolutions with a resolution of $\Delta_{\rm MR}$ may be sufficient to ascertain the long-term stability of the `Inter` and `Stiff` models. As such, we repeated the simulations for the `Inter` and `Stiff` configurations with an evolution resolution of $\Delta_{\rm MR}$ to ascertain the sta-

bility of the remnant; the results of which are shown in Fig. 6.8. We note with this resolution that for the `Inter` configurations the measured $\langle Y_{\rm quark} \rangle$ is fairly similar to the $\Delta_{\rm HR}$ evolutions, however, the very small quantities of quarks produced during the `Stiff` evolutions no longer appear. Overall, the results from this show stable remnants that will survive long after the current simulation time of $\Delta t_{\rm merge} \gtrsim 35{\rm ms}$. However, given the current models do not yet include the microphysic quantities to compute the influence of neutrino cooling and weak interactions, long–term evolutions of these binaries to ascertain their fate is not reasonable as such processes play an import role on these timescales. Furthermore, the current simulations do not include magnetic fields which are also important for long–term evolutions given the growth in the magnetic field can influence the overall stability of the remnant.

### 6.4 Summary

In this work we performed an explorative analysis of the influence a physically motivated EOS with a physically motivated first order phase transition can have on the (post-)merger dynamics and gravitational wave spectra. Given there were many unknowns at the beginning of this research such as where and when quark formation would occur, the approximate distribution of quark matter, and the resolution needed to perform these simulations; the choice of using GW170817 as a test case made for multiple exciting observations.

First, three stages of quark formation have been observed. The HQ stage during the violent merger process where temperatures in excess of $50{\rm MeV}$ can cause a mixed–phase of quark and nuclear matter. Next, the WQ stage can appear during relaxation of the HMNS remnant as it loses its differential rotation thus causing an increase in density and a reduction in temperature. Finally, the CQ stage appears when the cold dense core of the HMNS begins to form pure quark matter starting once it reaches densities of roughly $6n_s$ at which point the strong softening of the EOS causes the core to saturate with pure quark matter reaching densities in excess of $9n_s$ prior to a PTTC to a BH. The appearance of quark production during the HQ and WQ stage is likely to appear in other models, however, the production of CQ is in strong contrast to previous results such as [187] as the use of the $\Gamma_{\rm th}$ law results in the formation of a hot quark core.

Secondly, the impact to the gravitational wave spectra when comparing the three models was minimal and is largely attributed to the differences in stiffness. Interestingly, even though the `Soft_q07` configuration produces a large quantity of quarks up to its PTTC, there is no imprint on the waveform when compared to `Soft_q07-NPT`. However, the primary feature that separated the `Soft` model from the `Soft` model without a phase transition was the early PTTC. Although this is outside of the detectable range even for an ideal candidate such as GW170817, the detection of the post–merger waveform by future GW detectors will shed considerable light on the EOS as we've seen in this study.

Finally, future GW detections with an electro-magnetic counterpart resulting from a long–lived HMNS remnant formed from a heavy BNS merger will shed further insights into the possible parameter space available within the V–QCD model. Although the `Soft` model cannot be fully ruled out based purely on GW170817 due to the uncertainties in its configuration and lifetime, we have shown that GW events can provide valuable insights into the model. For in-

stance, if we use the tension between the `Soft` model and GW170817 to constrain the V–QCD parameter space, this would imply that the critical point would appear at a critical temperature $T_c < 130$MeV as the `Soft` model had the highest $T_c$ of the models studied in this work[129].

# Chapter 7

# Conclusion

This works explores for the first time a broad range of the available parameter space of highly asymmetric ($q << 1$) and spinning ($\chi_1 \neq 0$) binary neutron star configurations using GR(M)HD numerical simulations where the equation of state of nuclear matter has been modeled by finite temperature equations of state consistent with current pulsar observations and GW170817. The results from this work has a direct and meaningful impact on understanding not only the influence $q$ and $\chi$ have on the resulting dynamics, but also to ascertain the extent the resulting dynamics have on multi–messenger signatures.

To enable this work we first describe in chapter 2 the initial value problem (IVP) as it relates to numerical relativity specifically for the generation of initial conditions for binary black holes, binary neutron stars, and black-hole neutron star binaries. Furthermore, we have described our numerical solution to the IVP which has resulted in the `FUKA` (Frankfurt University/Kadath) suite of elliptic solvers for BBH, BNS, and BHNS initial data. `FUKA` is based on the `KADATH` spectral library and have been made publicly to enable further exploration into the vast parameter space of BNS and BHNS configurations. For binaries that include a NS, a considerable level of uncertainty exists not only in $q$ and $\chi$, but also the equation of state. `FUKA` is the first public code to provide a robust solution to obtain highly asymmetric and spinning binary initial data to include the ability to utilize tabulated equations of state as well as perform iterative eccentricity reduction. For such extremal configurations eccentricity reduction proves to be invaluable as the resulting orbital velocity obtained from quasi–equilibrium assumptions results in highly eccentric inspirals. We have found that even the use of 3.5th order post-Newtonian corrections to the orbital velocity and radial infall velocity results in eccentricities up to two–orders of magnitude lower than the inspiral using quasi–equilibrium initial data. Finally, we have shown that the obtained initial data solutions not only show exponential convergence as expected for spectral solvers, but we have also analyzed realistic mass asymmetric and spinning binary test cases that exemplify the resulting eccentricity reduction capabilities and convergence of the initial data solution on the evolution.

In chapter 3 we explored the impact of mass asymmetry $q \in [0.6, 1.0]$ and extremal spins $\chi_1 \in [0.3, 0.6]$ for super–critical binaries with a total binary mass $M_{\rm tot} \in [1.025, 1.109]\, M_{\rm th}^{1,0}$, where $M_{\rm th}^{1,0}$ is the equal-mass irrotational threshold mass to prompt collapse for a given EOS. We find that both the mass ratio $q$ and spin of the primary neutron star $\chi_1$ can have a significant influence on the

mass of the dynamical ejecta, the disk mass, and the lifetime of the remnant hyper–massive neutron star. Interestingly, configurations with an extremal spin of $\chi_1 = 0.6$ result in an average electron fraction $\langle Y_e \rangle < 0.06$ independent of the EOS which points to a more neutron rich ejecta. Additionally, the influence of $\chi_1$ and $q$ on the mass of the dynamical ejecta and disk mass has shown to be very non–linear in the parameter space explored where, for instance, at extremal spins the minimum of the produced dynamical (unbound) ejecta is at $q \approx 0.8$ with a maximum for $q = 1$. This is an important result as shown in Fig. 3.6 as we see the peak luminosity (bottom) reflects the relation between dynamical ejection, $q$, and $\chi$. Furthermore, the influence of $\chi_1$ on the remnant lifetime results in a later time for peak luminosity. Conversely, we have analyzed the influence of $q$ and $\chi_1$ on the resulting gravitational wave spectra by computing the power spectral density of the $(\ell, m) = (2, 2), (2, 1)$ modes of the gravitational wave strain. Surprisingly, we find that configurations with $q = 0.8$ produce the most prominent peak in the $(\ell, m) = (2, 1)$ even though these configurations do not survive nearly as long as the $q = 0.6$ configurations with equivalent $\chi_1$. This further highlights the sensitive interplay between asymmetry and spin in the resulting merger dynamics.

A parallel effort to chapter 3 was the study of the influence of spin and mass asymmetry on the threshold to prompt collapse which we present in chapter 4. In this work we systematically explored BNS configurations with $q \in \{0.5, 0.7, 0.9, 1\}$ and $\chi \in \{-0.3, 0, 0.3\}$ in order to measure the threshold mass to prompt collapse using three purely hadronic, finite temperature equations of state. From our analysis we concluded that a quasi–universal relation exists independent of the EOSs explored and we recover the well defined universal relation for the threshold mass for equal–mass irrotational configurations obtained in [42]. Additionally we have shown that long–lived binaries that are either heavy and (or) have strong anti–aligned spins provide the strongest constraints on the nuclear EOS which is consistent with previous works[43], [44].

A final test case for extremal configurations is the comparison of high–mass binary neutron star and low–mass black hole-neutron star binaries where a potential overlap exists. In this study we use two purely hadronic, finite temperature equations of state to explore binary configurations with a fixed total mass of $M_\infty = 3.6 M_\odot$, $q \in [0.486, 0.714]$ and $\tilde{\chi} \in [0.00, 0.35]$. We find that the most distinguishing characteristic of a BNS merger is the production of a second ejection tail that is absent in the BHNS simulations. F Furthermore, the low-spin configurations result in the secondary ejecta tail producing dynamical ejecta with velocities $v \in [0.4, 0.8]$ which could result in a bright kilonova precursor. However, for the one high–spin configuration examined with $\tilde{\chi} = 0.35$, the ejecta profile is similar between the BHNS and BNS configurations with the second tidal tail being significantly suppressed compared to the low–spin configurations. Overall, the low–spin prior configurations show the possibility for distinguishing a BNS from a BHNS configuration, however, in the high–spin regime, these events are challenging to distinguish even numerically.

Finally, in chapter 6 we examine for the first time a novel EOS framework based on V–QCD which provides a physically motivated description of matter consistently from low density nuclear matter up to the extremely high densities resulting in quark matter. To build this framework the description of nuclear matter is enabled by the DD2 and APR equations of state for the low–density

regime while the solution for cold, high density matter above nuclear saturation are computed using the V–QCD model and matched to lattice QCD results. Furthermore, using a van der Waals construction this framework extends the cold solution of the equation of state of quark matter to finite temperature. Finally, by using a Gibbs construction a consistent description is obtained for the transition from nuclear matter to a mixed-phase, and finally to pure quark matter. A natural consequence of this hybrid framework is the appearance of a critical point at finite high temperature and large density in the phase–diagram. The appearance of a critical point opens many questions as to how binary neutron star mergers probe the phase diagram of this hybrid model and to what extent astronomical observations such as GW170817 could provide constraints to the V–QCD model and, as a consequence, provide insights on the location of the critical point.

To this end three EOS models based on the hybrid framework with varying stiffnesses have been used which are consistent with current mass and radius constraints set by pulsar observations and the tidal deformability constraint set by GW170817. These models were used to perform numerical simulations of irrotational BNS mergers consistent with GW170817 for $q \in \{0.7, 1.0\}$ , $\chi_1 = \chi_2 = 0$ to determine how quarks are formed during the merger of the two NSs and if the lifetime of the HMNS remnant agrees with the $\sim 1$s lifetime of GW170817. From our analysis we identify three stages of quark production related to hot quarks which form during the violent merger, warm quarks which form during the relaxation of the hyper–massive remnant, and cold quarks which form prior to a phase transition triggered collapse. Most interesting is that of the `Soft` EOS which, for both mass ratios considered, collapses to a black hole within $t_{\rm BH} < 12{\rm ms}$. To ascertain the influence of the transition to quark matter, a second EOS model was constructed that suppresses the transition to quark matter and was used to perform the same numerical simulations. Overall we found that the collapse to a black hole is responsible due to the transition to quark matter in the cold dense core of the neutron star. Furthermore, the only prominent impact on the GW spectra is in fact the early collapse to a BH. Therefore, future detectors capable of accurately detecting the collapse time to a BH will play a crucial role in determining whether or not the EOS includes a 1st–order phase transition to quark matter.

In addition to providing valuable insights into the extremal regime of BNS mergers and the influence novel EOS model on the GW specta, many avenues of exploration are still open for consideration. In the realm of initial data construction, the current solvers within `FUKA` could be extended to include alternatives to classical relativity such as scalar/tensor theories in order to gain insights into the influence scalarization has on the (post-)merger dynamics and the resulting GW spectra. Furthermore, considerable interest exists in the field of boson star binaries which still utilizes super–imposed initial data construction which can not only lead to large constraint violations, but also unphysical pertubations[64]. Finally, binary initial data including a BH could also be extended to alternative approaches that allow for the generation of extremal spinning black holes with $\chi \approx 0.99$. This has been previously done for BBHs[89], BHNS[4], and charged black holes with spin[196] (only ID for low spins are shown); however, these codes are not publicly available which is prohibitive to enable further exploration of extremal binaries.

Secondly, the results from chapter 3 and chapter 5 focus on critical mass binaries above the threshold mass with extremal spins and small mass ratios which has been limited to two purely hadronic equations of state (BHB$\Lambda\Phi$ and TNTYST). A more rigorous sampling of the parameter space in $q$, $\chi$, total binary mass $M_\infty$, and EOS would be valuable in order to characterize the relation between these parameters and the resulting disk mass, dynamical ejecta, and ejecta composition specifically in the regime where fast ejecta (i.e., , $v > 0.6$) is found. This could be valuable for kilonova and precursor modeling in preparation for future multi–messenger observations. Furthermore, rigorous analysis of these results could highlight patterns useful for distinguishing BNS from BHNS binaries in the high mass regime. Finally, such an exploration would also provide further details to enable accurate GW modeling as these models suffer from a lack of high resolution simulations especially for BNS and BHNS mergers due to the computational expense.

Third, chapter 4 provided a first look into the threshold to prompt collapse as a function of EOS, $q$ and $\chi$. Since the original publication, multiple parallel works have also been published (see [65], [66]) that have thoroughly probed the parameter space of $q$ and EOS to include EOSs with a 1st–order phase transition to quark matter. Therefore, it would be important to conduct a follow–on work that more thoroughly examines the spin parameter space in order to obtain a more reliable fit for the quasi–universal relation discussed in this work.

Finally, chapter 6 presented the first BNS simulations using an finite temperature EOS with a description of quark matter based on the V-QCD model. Initially, it will be important to adapt our numerical codes to allow for computation of the quark fraction across the numerical domain during the evolution thus allowing for accurate 3D post–processing. These advancements will provide important insights into the distribution of quark matter throughout the (post-)merger as well as enable a study to quantify the convergent regime for numerical simulations. Furthermore, we could extend the studies conducted in chapters 3-5 to include the EOS models generated using the hybrid V–QCD framework so as to determine the impact on the resulting GW spectra, ejecta composition, and collapse behavior.

# Appendix A

# Variables and Units

| Quantity | SI dimension | Geometric dimension | Factor |
|---|---|---|---|
| Length ($L$) | [L] | [L] | 1 |
| Time ($t$) | [t] | [L] | $c$ |
| Mass ($M$) | [M] | [L] | $Gc^{-2}$ |
| Velocity ($v$) | [L t$^{-1}$] | 1 | $c^{-1}$ |
| Angular Velocity ($\Omega$ , $\omega$) | [t$^{-1}$] | [L$^{-1}$] | $c^{-1}$ |
| Acceleration ($a$) | [L t$^{-2}$] | [L$^{-1}$] | $c^{-2}$ |
| Energy ($E$) | [M L$^2$ t$^{-2}$] | [L] | $Gc^{-4}$ |
| Energy Density ($e$) | [M L$^{-1}$ t$^{-2}$] | [L$^{-2}$] | $Gc^{-4}$ |
| Angular Momentum ($\mathcal{S}$ , $J$) | [M L$^2$ t$^{-1}$] | [L$^2$] | $Gc^{-3}$ |
| Pressure ($p$) | [M L$^{-1}$ t$^{-2}$] | [L$^{-1}$] | $Gc^{-4}$ |
| Density ($\rho$) | [M L$^{-3}$] | [L$^{-2}$] | $Gc^{-2}$ |

Table A.1: SI and Geometric dimensions provided for relevant quantities utilized or inferred within this text. This table was modified from [197] to include only relevant quantities to this work.

# Appendix B

# post-Newtonian Estimates

The focus in this body of work is to perform numerical calculations on high performance computers in order to obtain solutions to EFE either at some arbitrary initial timeslice or to compute the evolution of this initial data to further understand the dynamics that result from the evolution of spacetime in vacuum and in the presence of NSs. However, such computations are extremely expensive and, therefore, are restricted to the late inspiral through the post-merger phase. The inspiral, however, has seen a wealth of theoretical modeling support of which the most successful is that of post-Newtonian corrections. For a thorough review the reader is referred to [198] and the references therein. Here we describe only the features of 3.5th order post-Newtonian corrections that are used to perform eccentricity reduction within initial data generation B.1. Furthermore, 4th order post-Newtonian corrections that describe the binding energy of an inspiraling compact object binary are utilized to determine the consistency of quasi-equilibrium initial data within section 2.7.2.

## B.1 Circular orbit estimates

In order to compute the necessary corrections to obtain a more circular inspiral using post-Newtonian corrections, we follow the formulation described in Ref. [198], Sec 7.4, whose formulation describes the circular motion of a binary measured in the COM, co-rotating frame. Specifically, the corrections relevant to generating eccentricity reduced ID are the quantities $\dot{a}$ and $\Omega$ which are defined as

$$\dot{a}_{3.5\mathrm{PN}} = \frac{1}{r}\left[ -\frac{64}{5}\frac{M^3\nu}{r^3}\Big(1+\gamma\Big(-\frac{1751}{336}-\frac{7}{4}\nu\Big)\Big)\right], \tag{B.1}$$

$$\begin{aligned}\Omega^2_{3.5\mathrm{PN}} = \frac{M}{r^3}\Bigg[&1+\Big(-3+\nu\Big)\gamma+\Big(6+\frac{41}{4}\nu+\nu^2\Big)\gamma^2\\ &+\Big(-10-\frac{75707}{840}+\frac{41}{64}\pi^2+22\ln\left(\frac{r}{r_0}\right)\nu+\frac{19}{2}\nu^2+\nu^3\Big)\gamma^3\Bigg].\end{aligned} \tag{B.2}$$

where $\mu := M_1M_2/M_\infty$ is the reduced mass, $\nu := q/(1+q)^2 = \mu/M_\infty$ is the symmetric mass ratio, $r$ is the (coordinate) separation between the centres of the

two compact objects, and $r_0$ is the logarithmic barycentre defined by,

$$\ln r_0 := \frac{1}{M_\infty}\left(M_1 \ln r_1 + M_2 \ln r_2\right) , \tag{B.3}$$

where $r_1$ and $r_2$ are the separation distance of each object to the center-of-mass.

### B.2 Equilibrium binding energy estimate

A common benchmark for determining the consistency of initial data that has been generated using the assumption of quasi-equilibrium is to compare against post-Newtonian estimates which have been shown to be quite accurate up until the late inspiral so long as a sufficiently high order post-Newtonian estimate is utilized. To this end, we document the formulations for binding energy that have been utilized to obtain the results shown in 2.7.2

$$\begin{aligned} E_{b,3.5\mathrm{PN}} = -\frac{\mu x}{2}\Bigg[1 + \Big(-\frac{3}{4} - \frac{1}{12}\nu\Big)x + \Big(-\frac{27}{8} + \frac{19}{8}\nu - \frac{1}{24}\nu^2\Big)x^2 \\ + \Big(-\frac{675}{64} + \Big(\frac{34445}{576} - \frac{205}{96}\pi^2\Big)\nu - \frac{155}{96}\nu^2 - \frac{35}{5184}\nu^3\Big)x^3\Bigg] , \end{aligned} \tag{B.4}$$

$$\begin{aligned} E_{b,4\mathrm{PN}} = E_{b,3.5\mathrm{PN}} + -\frac{\mu x}{2}\Bigg[\Big(-\frac{3969}{128} + \frac{448}{15}\nu \ln x + e_4\nu \\ + \Big(-\frac{498449}{3456} + \frac{3157}{576}\pi^2\Big)\nu^2 + \frac{301}{1728}\nu^3 + \frac{77}{31104}\nu^4\Big)x^4\Bigg] , \end{aligned} \tag{B.5}$$

where $x := \Omega^{2/3}$ and $e_4$ is the 4PN coefficient given by

$$e_4 := -\frac{123671}{5760} + \frac{9037}{1536}\pi^2 + \frac{1792}{15}\ln 2 + \frac{896}{15}e\,. \tag{B.6}$$

# Appendix C

# Evolution Setup

Within this work a considerable number of numerical simulations have been performed. This Appendix documents the relevant details that are consistent throughout these simulations such that only the discerning details will be discussed within the relevant chapters.

The simulations performed in this work have leveraged the open-source and community driven evolution framework, the `Einstein Toolkit`. Within the `Einstein Toolkit`, a fixed-mesh box-in-box refinement driver `Carpet` is used. A key advantage of using the `Einstein Toolkit` is the diverse catalog of community provided "thorns" to compute relevant surfaces and quantities throughout the evolution. In this work we have made extensive use of `AHFinderDirect` thorn in order to find the apparent horizon during the evolution of binaries that include or result in the formation of a BH. Additionally, we utilize `QuasiLocalMeasures` in order to compute the quasi-local irreducible mass, Christodoulou mass, and spin angular momentum on the apparent horizon of binaries including a BH.

In order to evolve the initial data generated with `FUKA`, a separate code is required that implements the evolution equations of our Cauchy problem. In this work we have exclusively used the Frankfurt/IllinoisGRMHD (`FIL`) to solve the general relativistic magnetohydrodynamics equations which implements a fourth order finite difference scheme and includes the ability to handle polytropic and tabulated equations of state. `FIL` also includes a simple neutrino leakage scheme that takes into account neutrino driven cooling and weak interactions.

`FIL` is paired with a separate module `Antelope` which handles the spacetime evolution of EFE which can be acheived using the `BSSNOK`[67], `CCZ4`[68], or `Z4c`[69] formulations. Unless otherwise stated, `Antelope` has been used to handle the spacetime evolution using the `Z4c` formulation.

| EOS | $M_{\rm TOV}$ $[M_\odot]$ | $R_{\rm TOV}$ [km] | $\mathcal{C}_{\rm TOV}$ | $\tau_{\rm TOV}$ $[\mu s]$ | $R_{1.4}$ [km] | $\mathcal{C}_{1.4}$ | $M_{\rm th}^{1,0}$ $[M_{\rm TOV}]$ | $M_{\rm th}^{1,0}$ $[M_\odot]$ |
|---|---|---|---|---|---|---|---|---|
| TNTYST+ | 2.23 | 10.17 | 0.32 | 66.12 | 11.15 | 0.18 | 1.298 | 2.894 |
| BHB$\Lambda\Phi$ | 2.10 | 11.64 | 0.26 | 83.31 | 12.65 | 0.16 | 1.503 | 3.156 |
| DD2 | 2.42 | 11.94 | 0.30 | 80.60 | 12.65 | 0.16 | 1.364 | 3.301 |

Table C.1: Within this thesis the following EOSs have been used in one or more works. Here we provide a central location of the important quantities for the `TNTYST` [137], BHB$\Lambda\Phi$ [139], and the `DD2`[171] EOSs. The listed TOV quantities were previously reported in [42].

# Bibliography


[1] F. Pretorius, "Evolution of binary black hole spacetimes", *Phys. Rev. Lett.*, vol. 95, p. 121 101, 2005. eprint: gr-qc/0507014.

[2] M. Shibata and K. Uryū, "Simulation of merging binary neutron stars in full general relativity: $\Gamma$=2 case", *Phys. Rev. D*, vol. 61, no. 6, 064001, p. 064 001, Mar. 2000. DOI: 10.1103/PhysRevD.61.064001. eprint: gr-qc/9911058.

[3] M. Shibata and K. Taniguchi, "Merger of black hole and neutron star in general relativity: Tidal disruption, torus mass, and gravitational waves", *Phys. Rev. D*, vol. 77, no. 8, p. 084 015, Apr. 2008. DOI: 10.1103/PhysRevD.77.084015. eprint: arXiv:0711.1410.

[4] F. Foucart, L. E. Kidder, H. P. Pfeiffer, and S. A. Teukolsky, "Initial data for black hole neutron star binaries: A flexible, high-accuracy spectral method", *Phys. Rev. D*, vol. 77, no. 12, 124051, p. 124 051, Jun. 2008. DOI: 10.1103/PhysRevD.77.124051. arXiv: 0804.3787 [gr-qc].

[5] The LIGO Scientific Collaboration and The Virgo Collaboration, "Gw170817: Observation of gravitational waves from a binary neutron star inspiral", *Phys. Rev. Lett.*, vol. 119, no. 16, 161101, p. 161 101, Oct. 2017. DOI: 10.1103/PhysRevLett.119.161101. arXiv: 1710.05832 [gr-qc].

[6] B. P. Abbott, R. Abbott, T. D. Abbott, S. Abraham, F. Acernese, K. Ackley, C. Adams, R. X. Adhikari, V. B. Adya, C. Affeldt, and et al., "GW190425: Observation of a Compact Binary Coalescence with Total Mass $\sim 3.4\,M_\odot$", *Astrophys. J. Lett.*, vol. 892, no. 1, L3, p. L3, Mar. 2020. DOI: 10.3847/2041-8213/ab75f5. arXiv: 2001.01761 [astro-ph.HE].

[7] T. M. Tauris, M. Kramer, P. C. C. Freire, N. Wex, H.-T. Janka, N. Langer, P. Podsiadlowski, E. Bozzo, S. Chaty, M. U. Kruckow, E. P. J. van den Heuvel, J. Antoniadis, R. P. Breton, and D. J. Champion, "Formation of Double Neutron Star Systems", *Astrophys. J.*, vol. 846, 170, p. 170, Sep. 2017. DOI: 10.3847/1538-4357/aa7e89. arXiv: 1706.09438 [astro-ph.HE].

[8] E. R. Most, L. J. Papenfort, S. D. Tootle, and L. Rezzolla, "Fast Ejecta as a Potential Way to Distinguish Black Holes from Neutron Stars in High-mass Gravitational-wave Events", *Astrophys. J.*, vol. 912, no. 1, 80, p. 80, May 2021. DOI: 10.3847/1538-4357/abf0a5. arXiv: 2012.03896 [astro-ph.HE].

[9] L. J. Papenfort, S. Tootle, P. Grandclement, E. R. Most, and L. Rezzolla, "" *in preparation*, 2020. arXiv: inpreparation.

[10] E. Gourgoulhon, "3+1 Formalism and Bases of Numerical Relativity", *ArXiv General Relativity and Quantum Cosmology e-prints*, Mar. 2007. eprint: gr-qc/0703035.

[11] T. W. Baumgarte and S. L. Shapiro, *Numerical Relativity: Solving Einstein's Equations on the Computer*. Cambridge, UK: Cambridge University Press, 2010. DOI: 10.1017/cbo9781139193344.

[12] S. Brandt and B. Brügmann, "A simple construction of initial data for multiple black holes", *Phys. Rev. Lett.*, vol. 78, no. 19, pp. 3606–3609, 1997. eprint: gr-qc/9703066.

[13] A. Lichnerowicz, "L'intégration des équations de la gravitation relativiste et la problème des n corps", *J. Math. Pures et Appl.*, vol. 23, p. 37, 1944.

[14] J. W. York, "Conformally invariant orthogonal decomposition of symmetric tensors on riemannian manifolds and the initial value problem of general relativity", *J. Math. Phys.*, vol. 14, p. 456, 1973.

[15] ——, "Conformal 'thin-sandwich' data for the initial-value problem of general relativity", *Phys. Rev. Lett.*, vol. 82, pp. 1350–1353, 1999.

[16] H. P. Pfeiffer and J. W. York, "Uniqueness and Nonuniqueness in the Einstein Constraints", *Phys. Rev. Lett.*, vol. 95, no. 9, 091101, p. 091 101, Aug. 2005. DOI: 10.1103/PhysRevLett.95.091101. arXiv: gr-qc/0504142 [gr-qc].

[17] *Langage objet pour la relativité numérique*, Langage Objet pour la RElativité Numérique, www.lorene.obspm.fr. [Online]. Available: http://www.lorene.obspm.fr.

[18] P. Grandclement, "Kadath: A Spectral solver for theoretical physics", *J. Comput. Phys.*, vol. 229, pp. 3334–3357, 2010. DOI: 10.1016/j.jcp.2010.01.005. arXiv: 0909.1228 [gr-qc].

[19] G. B. Cook and H. P. Pfeiffer, "Excision boundary conditions for black hole initial data", *Phys. Rev. D*, vol. 70, 2004. eprint: gr-qc/0407078.

[20] L. J. Papenfort, E. R. Most, S. Tootle, and L. Rezzolla, "Impact of extreme spins and mass ratios on the post-merger observables of high-mass binary neutron stars", *Mon. Not. Roy. Astron. Soc.*, vol. 513, no. 3, pp. 3646–3662, 2022. DOI: 10.1093/mnras/stac964. arXiv: 2201.03632 [astro-ph.HE].

[21] M. Shibata, K. Taniguchi, and K. Uryū, "Merger of binary neutron stars of unequal mass in full general relativity", *Phys. Rev. D*, vol. 68, no. 8, 084020, p. 084 020, Oct. 2003. DOI: 10.1103/PhysRevD.68.084020. eprint: gr-qc/0310030.

[22] L. Rezzolla, L. Baiotti, B. Giacomazzo, D. Link, and J. A. Font, "Accurate evolutions of unequal-mass neutron-star binaries: properties of the torus and short GRB engines", *Class. Quantum Grav.*, vol. 27, no. 11, p. 114 105, Jun. 2010. DOI: 10.1088/0264-9381/27/11/114105. arXiv: 1001.3074 [gr-qc].

[23] A. Bauswein, T. W. Baumgarte, and H.-T. Janka, "Prompt Merger Collapse and the Maximum Mass of Neutron Stars", *Phys. Rev. Lett.*, vol. 111, no. 13, 131101, p. 131 101, Sep. 2013. DOI: 10.1103/PhysRevLett.111.131101. arXiv: 1307.5191 [astro-ph.SR].

[24] D. W. Neilsen, S. L. Liebling, M. Anderson, L. Lehner, E. O'Connor, and C. Palenzuela, "Magnetized neutron stars with realistic equations of state and neutrino cooling", *Phys. Rev. D*, vol. 89, no. 10, 104029, p. 104 029, May 2014. DOI: 10.1103/PhysRevD.89.104029. arXiv: 1403.3680 [gr-qc].

[25] T. Dietrich, N. Moldenhauer, N. K. Johnson-McDaniel, S. Bernuzzi, C. M. Markakis, B. Brügmann, and W. Tichy, "Binary neutron stars with generic spin, eccentricity, mass ratio, and compactness: Quasi-equilibrium sequences and first evolutions", *Phys. Rev. D*, vol. 92, no. 12, 124007, p. 124 007, Dec. 2015. DOI: 10.1103/PhysRevD.92.124007. arXiv: 1507.07100 [gr-qc].

[26] D. Radice, F. Galeazzi, J. Lippuner, L. F. Roberts, C. D. Ott, and L. Rezzolla, "Dynamical Mass Ejection from Binary Neutron Star Mergers", *Mon. Not. R. Astron. Soc.*, vol. 460, pp. 3255–3271, Aug. 2016. DOI: 10.1093/mnras/stw1227. arXiv: 1601.02426 [astro-ph.HE].

[27] T. Dietrich, M. Ujevic, W. Tichy, S. Bernuzzi, and B. Brügmann, "Gravitational waves and mass ejecta from binary neutron star mergers: Effect of the mass ratio", *Phys. Rev. D*, vol. 95, no. 2, 024029, p. 024 029, Jan. 2017. DOI: 10.1103/PhysRevD.95.024029. arXiv: 1607.06636 [gr-qc].

[28] D. Radice, A. Perego, F. Zappa, and S. Bernuzzi, "GW170817: Joint Constraint on the Neutron Star Equation of State from Multimessenger Observations", *Astrophys. J. Lett.*, vol. 852, L29, p. L29, Jan. 2018. DOI: 10.3847/2041-8213/aaa402. arXiv: 1711.03647 [astro-ph.HE].

[29] L. J. Papenfort, R. Gold, and L. Rezzolla, "Dynamical ejecta and nucleosynthetic yields from eccentric binary neutron-star mergers", *Phys. Rev. D*, vol. 98, 104028, p. 104 028, Nov. 2018. DOI: 10.1103/PhysRevD.98.104028. arXiv: 1807.03795 [gr-qc].

[30] E. R. Most and C. A. Raithel, "Impact of the nuclear symmetry energy on the post-merger phase of a binary neutron star coalescence", *arXiv e-prints*, arXiv:2107.06804, arXiv:2107.06804, Jul. 2021. arXiv: 2107.06804 [astro-ph.HE].

[31] W. Tichy, A. Rashti, T. Dietrich, R. Dudi, and B. Brügmann, "Constructing binary neutron star initial data with high spins, high compactnesses, and high mass ratios", *Phys. Rev. D*, vol. 100, no. 12, 124046, p. 124 046, Dec. 2019. DOI: 10.1103/PhysRevD.100.124046. arXiv: 1910.09690 [gr-qc].

[32] M. Ujevic, A. Rashti, H. Gieg, W. Tichy, and T. Dietrich, "High-accuracy high-mass-ratio simulations for binary neutron stars and their comparison to existing waveform models", *Phys. Rev. D*, vol. 106, no. 2, p. 023 029, 2022. DOI: 10.1103/PhysRevD.106.023029. arXiv: 2202.09343 [gr-qc].

[33] A. Prakash, D. Radice, D. Logoteta, A. Perego, V. Nedora, I. Bombaci, R. Kashyap, S. Bernuzzi, and A. Endrizzi, "Signatures of deconfined quark phases in binary neutron star mergers", *Phys. Rev. D*, vol. 104, no. 8, p. 083 029, 2021. DOI: 10.1103/PhysRevD.104.083029. arXiv: 2106.07885 [astro-ph.HE].

[34] M. Shibata and K. Taniguchi, "Merger of binary neutron stars to a black hole: Disk mass, short gamma-ray bursts, and quasinormal mode ringing", *Phys. Rev. D*, vol. 73, no. 6, 064027, p. 064 027, Mar. 2006. DOI: 10.1103/PhysRevD.73.064027. eprint: astro-ph/0603145.

[35] W. Kastaun, F. Galeazzi, D. Alic, L. Rezzolla, and J. A. Font, "Black hole from merging binary neutron stars: How fast can it spin?", *Phys. Rev. D*, vol. 88, no. 2, 021501, p. 021 501, Jul. 2013. DOI: 10.1103/PhysRevD.88.021501. arXiv: 1301.7348 [gr-qc].

[36] S. Bernuzzi, T. Dietrich, W. Tichy, and B. Brügmann, "Mergers of binary neutron stars with realistic spin", *Phys. Rev. D*, vol. 89, no. 10, 104021, p. 104 021, May 2014. DOI: 10.1103/PhysRevD.89.104021. arXiv: 1311.4443 [gr-qc].

[37] W. E. East, V. Paschalidis, F. Pretorius, and S. L. Shapiro, "Relativistic simulations of eccentric binary neutron star mergers: One-arm spiral instability and effects of neutron star spin", *Phys. Rev. D*, vol. 93, no. 2, 024011, p. 024 011, Jan. 2016. DOI: 10.1103/PhysRevD.93.024011. arXiv: 1511.01093 [astro-ph.HE].

[38] T. Dietrich, S. Bernuzzi, M. Ujevic, and W. Tichy, "Gravitational waves and mass ejecta from binary neutron star mergers: Effect of the stars' rotation", *Phys. Rev. D*, vol. 95, no. 4, 044045, p. 044 045, Feb. 2017. DOI: 10.1103/PhysRevD.95.044045. arXiv: 1611.07367 [gr-qc].

[39] W. E. East, V. Paschalidis, F. Pretorius, and A. Tsokaros, "Binary neutron star mergers: Effects of spin and post-merger dynamics", *Phys. Rev. D*, vol. 100, no. 12, 124042, p. 124 042, Dec. 2019. DOI: 10.1103/PhysRevD.100.124042. arXiv: 1906.05288 [astro-ph.HE].

[40] E. R. Most, L. J. Papenfort, A. Tsokaros, and L. Rezzolla, "Impact of High Spins on the Ejection of Mass in GW170817", *Astrophys. J.*, vol. 884, no. 1, 40, p. 40, Oct. 2019. DOI: 10.3847/1538-4357/ab3ebb. arXiv: 1904.04220 [astro-ph.HE].

[41] S. D. Tootle, L. J. Papenfort, E. R. Most, and L. Rezzolla, "Quasi-universal Behavior of the Threshold Mass in Unequal-mass, Spinning Binary Neutron Star Mergers", *Astrophys. J. Lett.*, vol. 922, no. 1, p. L19, 2021. DOI: 10.3847/2041-8213/ac350d. arXiv: 2109.00940 [gr-qc].

[42] S. Koeppel, L. Bovard, and L. Rezzolla, "A General-relativistic Determination of the Threshold Mass to Prompt Collapse in Binary Neutron Star Mergers", *Astrophys. J. Lett.*, vol. 872, no. 1, L16, p. L16, Feb. 2019. DOI: 10.3847/2041-8213/ab0210. arXiv: 1901.09977 [gr-qc].

[43] E. R. Most, L. R. Weih, and L. Rezzolla, "The heavier the better: how to constrain mass ratios and spins of high-mass neutron star mergers", *Mon. Not. R. Astron. Soc.*, vol. 496, no. 1, pp. L16–L21, May 2020. DOI: 10.1093/mnrasl/slaa079. arXiv: 2003.10391 [astro-ph.HE].

[44] E. R. Most, L. J. Papenfort, L. R. Weih, and L. Rezzolla, "A lower bound on the maximum mass if the secondary in GW190814 was once a rapidly spinning neutron star", *Mon. Not. R. Astron. Soc.*, vol. 499, no. 1, pp. L82–L86, Sep. 2020. DOI: 10.1093/mnrasl/slaa168. arXiv: 2006.14601 [astro-ph.HE].

[45] F. Foucart, "Black-hole–neutron-star mergers: Disk mass predictions", *Phys. Rev. D*, vol. 86, no. 12, 124007, p. 124 007, Dec. 2012. DOI: 10.1103/PhysRevD.86.124007. arXiv: 1207.6304 [astro-ph.HE].

[46] F. Foucart, M. B. Deaton, M. D. Duez, L. E. Kidder, I. MacDonald, C. D. Ott, H. P. Pfeiffer, M. A. Scheel, B. Szilagyi, and S. A. Teukolsky, "Black-hole-neutron-star mergers at realistic mass ratios: Equation of state and spin orientation effects", *Phys. Rev. D*, vol. 87, no. 8, 084006, p. 084 006, Apr. 2013. DOI: 10.1103/PhysRevD.87.084006. arXiv: 1212.4810 [gr-qc].

[47] K. Kyutoku, K. Ioka, H. Okawa, M. Shibata, and K. Taniguchi, "Dynamical mass ejection from black hole-neutron star binaries", *Phys. Rev. D*, vol. 92, no. 4, 044028, p. 044 028, Aug. 2015. DOI: 10.1103/PhysRevD.92.044028. arXiv: 1502.05402 [astro-ph.HE].

[48] K. Kyutoku, K. Kiuchi, Y. Sekiguchi, M. Shibata, and K. Taniguchi, "Neutrino transport in black hole-neutron star binaries: Neutrino emission and dynamical mass ejection", *Phys. Rev. D*, vol. 97, no. 2, 023009, p. 023 009, Jan. 2018. DOI: 10.1103/PhysRevD.97.023009. arXiv: 1710.00827 [astro-ph.HE].

[49] L. Baiotti, B. Giacomazzo, and L. Rezzolla, "Accurate evolutions of inspiralling neutron-star binaries: Prompt and delayed collapse to a black hole", *Phys. Rev. D*, vol. 78, no. 8, p. 084 033, Oct. 2008. DOI: 10.1103/PhysRevD.78.084033. arXiv: 0804.0594 [gr-qc].

[50] F. Foucart, R. Haas, M. D. Duez, E. O'Connor, C. D. Ott, L. Roberts, L. E. Kidder, J. Lippuner, H. P. Pfeiffer, and M. A. Scheel, "Low mass binary neutron star mergers: Gravitational waves and neutrino emission", *Phys. Rev. D*, vol. 93, no. 4, 044019, p. 044 019, Feb. 2016. DOI: 10.1103/PhysRevD.93.044019. arXiv: 1510.06398 [astro-ph.HE].

[51] Y. Sekiguchi, K. Kiuchi, K. Kyutoku, and M. Shibata, "Dynamical mass ejection from binary neutron star mergers: Radiation-hydrodynamics study in general relativity", *Phys. Rev. D*, vol. 91, no. 6, 064059, p. 064 059, Mar. 2015. DOI: 10.1103/PhysRevD.91.064059. arXiv: 1502.06660 [astro-ph.HE].

[52] L. Lehner, S. L. Liebling, C. Palenzuela, O. L. Caballero, E. O'Connor, M. Anderson, and D. Neilsen, "Unequal mass binary neutron star mergers and multimessenger signals", *Classical and Quantum Gravity*, vol. 33, no. 18, 184002, p. 184 002, Sep. 2016. DOI: 10.1088/0264-9381/33/18/184002. arXiv: 1603.00501 [gr-qc].

[53] L. Bovard, D. Martin, F. Guercilena, A. Arcones, L. Rezzolla, and O. Korobkin, "On r-process nucleosynthesis from matter ejected in binary neutron star mergers", *Phys. Rev. D*, vol. 96, p. 124 005, Dec. 2017. arXiv: 1709.09630 [gr-qc].

[54] A. Perego, R. M. Cabezón, and R. Käppeli, "An Advanced Leakage Scheme for Neutrino Treatment in Astrophysical Simulations", *The Astrophysical Journal Supplement Series*, vol. 223, 22, p. 22, Apr. 2016. DOI: 10.3847/0067-0049/223/2/22. arXiv: 1511.08519 [astro-ph.IM].

[55] S. Fujibayashi, Y. Sekiguchi, K. Kiuchi, and M. Shibata, "Properties of Neutrino-driven Ejecta from the Remnant of a Binary Neutron Star Merger: Pure Radiation Hydrodynamics Case", *Astrophys. J.*, vol. 846, 114, p. 114, Sep. 2017. DOI: 10.3847/1538-4357/aa8039.

[56] R. Fernández, D. Kasen, B. D. Metzger, and E. Quataert, "Outflows from accretion discs formed in neutron star mergers: effect of black hole spin", *Mon. Not. R. Astron. Soc.*, vol. 446, pp. 750–758, Jan. 2015. DOI: 10.1093/mnras/stu2112. arXiv: 1409.4426 [astro-ph.HE].

[57] R. Fernández, E. Quataert, J. Schwab, D. Kasen, and S. Rosswog, "The interplay of disc wind and dynamical ejecta in the aftermath of neutron star-black hole mergers", *Mon. Not. R. Astron. Soc.*, vol. 449, pp. 390–402, May 2015. DOI: 10.1093/mnras/stv238. arXiv: 1412.5588 [astro-ph.HE].

[58] D. M. Siegel and B. D. Metzger, "Three-Dimensional General-Relativistic Magnetohydrodynamic Simulations of Remnant Accretion Disks from Neutron Star Mergers: Outflows and r -Process Nucleosynthesis", *Physical Review Letters*, vol. 119, no. 23, 231102, p. 231 102, Dec. 2017. DOI: 10.1103/PhysRevLett.119.231102. arXiv: 1705.05473 [astro-ph.HE].

[59] J. M. Miller, B. R. Ryan, J. C. Dolence, A. Burrows, C. J. Fontes, C. L. Fryer, O. Korobkin, J. Lippuner, M. R. Mumpower, and R. T. Wollaeger, "Full transport model of GW170817-like disk produces a blue kilonova", *Phys. Rev. D*, vol. 100, no. 2, 023008, p. 023 008, Jul. 2019. DOI: 10.1103/PhysRevD.100.023008. arXiv: 1905.07477 [astro-ph.HE].

[60] L. Barsotti, S. Gras, M. Evans, and P. Fritschel, "The updated advanced ligo design curve", *LIGO Document No. T1800044-v5*, Apr. 2018.

[61] M. Punturo *et al.*, "The third generation of gravitational wave observatories and their science reach", *Class. Quant. Grav.*, vol. 27, p. 084 007, 2010. DOI: 10.1088/0264-9381/27/8/084007.

[62] S. Tootle, C. Ecker, K. Topolski, T. Demircik, M. Järvinen, and L. Rezzolla, "Quark formation and phenomenology in binary neutron-star mergers using V-QCD", May 2022. arXiv: 2205.05691 [astro-ph.HE].

[63] L. R. Weih, M. Hanauske, and L. Rezzolla, "Postmerger Gravitational-Wave Signatures of Phase Transitions in Binary Mergers", *Phys. Rev. Lett.*, vol. 124, no. 17, 171103, p. 171 103, May 2020. DOI: 10.1103/PhysRevLett.124.171103. arXiv: 1912.09340 [gr-qc].

[64] T. Helfer, U. Sperhake, R. Croft, M. Radia, B.-X. Ge, and E. A. Lim, "Malaise and remedy of binary boson-star initial data", *Class. Quant. Grav.*, vol. 39, no. 7, p. 074 001, 2022. DOI: 10.1088/1361-6382/ac53b7. arXiv: 2108.11995 [gr-qc].

[65] M. Kölsch, T. Dietrich, M. Ujevic, and B. Bruegmann, "Investigating the mass-ratio dependence of the prompt-collapse threshold with numerical-relativity simulations", *arXiv e-prints*, arXiv:2112.11851, arXiv:2112.11851, Dec. 2021. arXiv: 2112.11851 [gr-qc].

[66] A. Perego, D. Logoteta, D. Radice, S. Bernuzzi, R. Kashyap, A. Das, S. Padamata, and A. Prakash, "Probing the incompressibility of nuclear matter at ultra-high density through the prompt collapse of asymmetric neutron star binaries", *arXiv e-prints*, arXiv:2112.05864, arXiv:2112.05864, Dec. 2021. arXiv: 2112.05864 [astro-ph.HE].

[67] T. W. Baumgarte and S. L. Shapiro, "Numerical integration of Einstein's field equations", *Phys. Rev. D*, vol. 59, no. 2, 024007, p. 024 007, Jan. 1999. DOI: 10.1103/PhysRevD.59.024007. eprint: gr-qc/9810065.

[68] D. Alic, C. Bona-Casas, C. Bona, L. Rezzolla, and C. Palenzuela, "Conformal and covariant formulation of the Z4 system with constraint-violation damping", *Phys. Rev. D*, vol. 85, no. 6, 064040, p. 064 040, Mar. 2012. DOI: 10.1103/PhysRevD.85.064040. arXiv: 1106.2254 [gr-qc].

[69] D. Hilditch, S. Bernuzzi, M. Thierfelder, Z. Cao, W. Tichy, and B. Brügmann, "Compact binary evolutions with the Z4c formulation", *Phys. Rev. D*, vol. 88, no. 8, 084057, p. 084 057, Oct. 2013. DOI: 10.1103/PhysRevD.88.084057. arXiv: 1212.2901 [gr-qc].

[70] H. Olivares, I. M. Peshkov, E. R. Most, F. M. Guercilena, and L. J. Papenfort, "New first-order formulation of the Einstein equations exploiting analogies with electrodynamics", *Phys. Rev. D*, vol. 105, no. 12, p. 124 038, 2022. DOI: 10.1103/PhysRevD.105.124038. arXiv: 2111.05282 [gr-qc].

[71] M. Ansorg, B. Brügmann, and W. Tichy, "A single-domain spectral method for black hole puncture data", *Phys. Rev. D*, vol. 70, p. 064 011, 2004. eprint: gr-qc/0404056.

[72] A. Rashti, F. M. Fabbri, B. Brügmann, S. V. Chaurasia, T. Dietrich, M. Ujevic, and W. Tichy, "New pseudospectral code for the construction of initial data", *Phys. Rev. D*, vol. 105, no. 10, p. 104 027, 2022. DOI: 10.1103/PhysRevD.105.104027. arXiv: 2109.14511 [gr-qc].

[73] F. Foucart, P. Laguna, G. Lovelace, D. Radice, and H. Witek, "Snowmass2021 Cosmic Frontier White Paper: Numerical relativity for next-generation gravitational-wave probes of fundamental physics", Mar. 2022. arXiv: 2203.08139 [gr-qc].

[74] H. P. Pfeiffer, S. A. Teukolsky, and G. B. Cook, "Quasi-circular orbits for spinning binary black holes", *Phys. Rev. D*, vol. 62, p. 104 018, 2000. eprint: gr-qc/0006084.

[75] S. Ossokine, F. Foucart, H. P. Pfeiffer, M. Boyle, and B. Szilágyi, "Improvements to the construction of binary black hole initial data", *Class. Quant. Grav.*, vol. 32, p. 245 010, 2015. DOI: 10.1088/0264-9381/32/24/245010. arXiv: 1506.01689 [gr-qc].

[76] P. Grandclement, E. Gourgoulhon, and S. Bonazzola, "Binary black holes in circular orbits. II. Numerical methods and first results", *Phys. Rev. D*, vol. 65, p. 044 021, 2002. DOI: 10.1103/PhysRevD.65.044021. arXiv: gr-qc/0106016.

[77] P. Grandclément, "Accurate and realistic initial data for black hole–neutron star binaries", *Phys. Rev. D*, vol. 74, no. 12, p. 124 002, Dec. 2006. DOI: 10.1103/PhysRevD.74.124002.

[78] K. Taniguchi, T. W. Baumgarte, J. A. Faber, and S. L. Shapiro, "Quasiequilibrium black hole-neutron star binaries in general relativity", *Phys. Rev. D*, vol. 75, p. 084 005, 8 Apr. 2007. DOI: 10.1103/PhysRevD.75.084005. [Online]. Available: http://link.aps.org/doi/10.1103/PhysRevD.75.084005.

[79] H. P. Pfeiffer, D. Brown, L. Kidder Lawrence E.and Lindblom, G. Lovelance, and M. A. Scheel, "Reducing orbital eccentricity in binary black hole simulations", eprint: gr-qc/0702106.

[80] N. Tacik, F. Foucart, H. P. Pfeiffer, R. Haas, S. Ossokine, J. Kaplan, C. Muhlberger, M. D. Duez, L. E. Kidder, M. A. Scheel, and B. Szilágyi, "Erratum: Binary neutron stars with arbitrary spins in numerical relativity [Phys. Rev. D 92, 124012 (2015)]", *Phys. Rev. D*, vol. 94, no. 4, 049903, p. 049 903, Aug. 2016. DOI: 10.1103/PhysRevD.94.049903.

[81] N. Tacik, F. Foucart, H. P. Pfeiffer, C. Muhlberger, L. E. Kidder, M. A. Scheel, and B. Szilágyi, "Initial data for black hole–neutron star binaries, with rotating stars", *Class. Quant. Grav.*, vol. 33, no. 22, p. 225 012, 2016. DOI: 10.1088/0264-9381/33/22/225012. arXiv: 1607.07962 [gr-qc].

[82] W. Tichy, "Black hole evolution with the bssn system by pseudospectral methods", *Phys. Rev. D*, vol. 74, p. 084 005, 8 Oct. 2006. DOI: 10.1103/PhysRevD.74.084005. [Online]. Available: https://link.aps.org/doi/10.1103/PhysRevD.74.084005.

[83] ——, "A New numerical method to construct binary neutron star initial data", *Class. Quant. Grav.*, vol. 26, p. 175 018, 2009. DOI: 10.1088/0264-9381/26/17/175018. arXiv: 0908.0620 [gr-qc].

[84] ——, "Long term black hole evolution with the bssn system by pseudospectral methods", *Phys. Rev. D*, vol. 80, p. 104 034, 10 Nov. 2009. DOI: 10.1103/PhysRevD.80.104034. [Online]. Available: https://link.aps.org/doi/10.1103/PhysRevD.80.104034.

[85] H. P. Pfeiffer, L. E. Kidder, M. A. Scheel, and S. A. Teukolsky, "A multidomain spectral method for solving elliptic equations", *Comput. Phys. Commun.*, vol. 152, pp. 253–273, 2003. eprint: gr-qc/0202096.

[86] H. Pfeiffer, "Initial data for black hole evolutions", Ph.D. dissertation, Cornell University, Ithaca, New York State, 2003. eprint: gr-qc/0510016.

[87] N. Tacik, F. Foucart, H. P. Pfeiffer, R. Haas, S. Ossokine, J. Kaplan, C. Muhlberger, M. D. Duez, L. E. Kidder, M. A. Scheel, and B. Szilágyi, "Binary neutron stars with arbitrary spins in numerical relativity", *Phys. Rev. D*, vol. 92, no. 12, 124012, p. 124 012, Dec. 2015. DOI: 10.1103/PhysRevD.92.124012. arXiv: 1508.06986 [gr-qc].

[88] A. H. Mroue and H. P. Pfeiffer, "Precessing Binary Black Holes Simulations: Quasicircular Initial Data", Oct. 2012. arXiv: 1210.2958 [gr-qc].

[89] G. Lovelace, R. Owen, H. P. Pfeiffer, and T. Chu, "Binary-black-hole initial data with nearly extremal spins", *Phys. Rev. D*, vol. 78, no. 8, p. 084 017, Oct. 2008. DOI: 10.1103/PhysRevD.78.084017. arXiv: 0805.4192 [gr-qc].

[90] L. T. Buchman, H. P. Pfeiffer, M. A. Scheel, and B. Szilágyi, "Simulations of unequal-mass black hole binaries with spectral methods", *Phys. Rev. D*, vol. 86, no. 8, 084033, p. 084 033, Oct. 2012. DOI: 10.1103/PhysRevD.86.084033. arXiv: 1206.3015 [gr-qc].

[91] A. Tsokaros and K. Uryū, "Binary black hole circular orbits computed with cocal", *Journal of Engineering Mathematics*, vol. 82, no. 1, pp. 133–141, 2012, ISSN: 1573-2703. DOI: 10.1007/s10665-012-9585-6. [Online]. Available: http://dx.doi.org/10.1007/s10665-012-9585-6.

[92] A. Tsokaros, K. Uryū, and L. Rezzolla, "New code for quasiequilibrium initial data of binary neutron stars: Corotating, irrotational, and slowly spinning systems", *Phys. Rev. D*, vol. 91, no. 10, 104030, p. 104 030, May 2015. DOI: 10.1103/PhysRevD.91.104030. arXiv: 1502.05674 [gr-qc].

[93] A. Tsokaros, B. C. Mundim, F. Galeazzi, L. Rezzolla, and K. Uryū, "Initial-data contribution to the error budget of gravitational waves from neutron-star binaries", *Phys. Rev. D*, vol. 94, no. 4, 044049, p. 044 049, Aug. 2016. DOI: 10.1103/PhysRevD.94.044049. arXiv: 1605.07205 [gr-qc].

[94] A. Tsokaros, K. Uryū, M. Ruiz, and S. L. Shapiro, "Constant circulation sequences of binary neutron stars and their spin characterization", *Phys. Rev. D*, vol. 98, no. 12, 124019, p. 124 019, Dec. 2018. DOI: 10.1103/PhysRevD.98.124019. arXiv: 1809.08237 [gr-qc].

[95] A. Tsokaros, M. Ruiz, V. Paschalidis, S. L. Shapiro, and K. Uryū, "Effect of spin on the inspiral of binary neutron stars", *Phys. Rev. D*, vol. 100, no. 2, 024061, p. 024 061, Jul. 2019. DOI: 10.1103/PhysRevD.100.024061. arXiv: 1906.00011 [gr-qc].

[96] M. Hannam, P. Schmidt, A. Bohé, L. Haegel, S. Husa, F. Ohme, G. Pratten, and M. Pürrer, "Simple Model of Complete Precessing Black-Hole-Binary Gravitational Waveforms", *Phys. Rev. Lett.*, vol. 113, no. 15, 151101, p. 151 101, Oct. 2014. DOI: 10.1103/PhysRevLett.113.151101. arXiv: 1308.3271 [gr-qc].

[97] M. Favata, "Systematic Parameter Errors in Inspiraling Neutron Star Binaries", *Phys. Rev. Lett.*, vol. 112, no. 10, 101101, p. 101 101, Mar. 2014. DOI: 10.1103/PhysRevLett.112.101101. arXiv: 1310.8288 [gr-qc].

[98] M. Agathos, J. Meidam, W. Del Pozzo, T. G. F. Li, M. Tompitak, J. Veitch, S. Vitale, and C. Van Den Broeck, "Constraining the neutron star equation of state with gravitational wave signals from coalescing binary neutron stars", *Phys. Rev. D*, vol. 92, no. 2, 023012, p. 023 012, Jul. 2015. DOI: 10.1103/PhysRevD.92.023012. arXiv: 1503.05405 [gr-qc].

[99] I. Harry and T. Hinderer, "Observing and measuring the neutron-star equation-of-state in spinning binary neutron star systems", *Classical and Quantum Gravity*, vol. 35, no. 14, 145010, p. 145 010, Jul. 2018. DOI: 10.1088/1361-6382/aac7e3. arXiv: 1801.09972 [gr-qc].

[100] X. Zhu, E. Thrane, S. Osłowski, Y. Levin, and P. D. Lasky, "Inferring the population properties of binary neutron stars with gravitational-wave measurements of spin", *Phys. Rev. D*, vol. 98, 043002, p. 043 002, Aug. 2018. DOI: 10.1103/PhysRevD.98.043002. arXiv: 1711.09226 [astro-ph.HE].

[101] B. Margalit and B. D. Metzger, "Constraining the Maximum Mass of Neutron Stars from Multi-messenger Observations of GW170817", *Astrophys. J. Lett.*, vol. 850, L19, p. L19, Dec. 2017. DOI: 10.3847/2041-8213/aa991c. arXiv: 1710.05938 [astro-ph.HE].

[102] A. Bauswein, O. Just, H.-T. Janka, and N. Stergioulas, "Neutron-star Radius Constraints from GW170817 and Future Detections", *Astrophys. J. Lett.*, vol. 850, L34, p. L34, Dec. 2017. DOI: 10.3847/2041-8213/aa9994. arXiv: 1710.06843 [astro-ph.HE].

[103] L. Rezzolla, E. R. Most, and L. R. Weih, "Using Gravitational-wave Observations and Quasi-universal Relations to Constrain the Maximum Mass of Neutron Stars", *Astrophys. J. Lett.*, vol. 852, L25, p. L25, Jan. 2018. DOI: 10.3847/2041-8213/aaa401. arXiv: 1711.00314 [astro-ph.HE].

[104] M. Ruiz, S. L. Shapiro, and A. Tsokaros, "GW170817, general relativistic magnetohydrodynamic simulations, and the neutron star maximum mass", *Phys. Rev. D*, vol. 97, no. 2, 021501, p. 021 501, Jan. 2018. DOI: 10.1103/PhysRevD.97.021501. arXiv: 1711.00473 [astro-ph.HE].

[105] E. Annala, T. Gorda, A. Kurkela, and A. Vuorinen, "Gravitational-Wave Constraints on the Neutron-Star-Matter Equation of State", *Phys. Rev. Lett.*, vol. 120, no. 17, 172703, p. 172 703, Apr. 2018. DOI: 10.1103/PhysRevLett.120.172703. arXiv: 1711.02644 [astro-ph.HE].

[106] E. R. Most, L. R. Weih, L. Rezzolla, and J. Schaffner-Bielich, "New Constraints on Radii and Tidal Deformabilities of Neutron Stars from GW170817", *Phys. Rev. Lett.*, vol. 120, no. 26, 261103, p. 261 103, Jun. 2018. DOI: 10.1103/PhysRevLett.120.261103. arXiv: 1803.00549 [gr-qc].

[107] S. De, D. Finstad, J. M. Lattimer, D. A. Brown, E. Berger, and C. M. Biwer, "Tidal Deformabilities and Radii of Neutron Stars from the Observation of GW170817", *Physical Review Letters*, vol. 121, no. 9, 091102, p. 091 102, Aug. 2018. DOI: 10.1103/PhysRevLett.121.091102. arXiv: 1804.08583 [astro-ph.HE].

[108] B. P. Abbott, R. Abbott, T. D. Abbott, F. Acernese, K. Ackley, C. Adams, T. Adams, P. Addesso, R. X. Adhikari, V. B. Adya, and et al., "GW170817: Measurements of Neutron Star Radii and Equation of State", *Physical Review Letters*, vol. 121, no. 16, 161101, p. 161 101, Oct. 2018. DOI: 10.1103/PhysRevLett.121.161101. arXiv: 1805.11581 [gr-qc].

[109] G. Montaña, L. Tolós, M. Hanauske, and L. Rezzolla, "Constraining twin stars with GW170817", *Phys. Rev. D*, vol. 99, no. 10, 103009, p. 103 009, May 2019. DOI: 10.1103/PhysRevD.99.103009. arXiv: 1811.10929 [astro-ph.HE].

[110] C. Raithel, F. Özel, and D. Psaltis, "Tidal Deformability from GW170817 as a Direct Probe of the Neutron Star Radius", *Astrophys. J.*, vol. 857, L23, p. L23, Apr. 2018. DOI: 10.3847/2041-8213/aabcbf. arXiv: 1803.07687 [astro-ph.HE].

[111] I. Tews, J. Margueron, and S. Reddy, "Critical examination of constraints on the equation of state of dense matter obtained from GW170817", *Physical Review C*, vol. 98, no. 4, 045804, p. 045 804, Oct. 2018. DOI: 10.1103/PhysRevC.98.045804. arXiv: 1804.02783 [nucl-th].

[112] T. Malik, N. Alam, M. Fortin, C. Providência, B. K. Agrawal, T. K. Jha, B. Kumar, and S. K. Patra, "GW170817: Constraining the nuclear matter equation of state from the neutron star tidal deformability", *Physical Review C*, vol. 98, no. 3, 035804, p. 035 804, Sep. 2018. DOI: 10.1103/PhysRevC.98.035804. arXiv: 1805.11963 [nucl-th].

[113] M. Shibata, E. Zhou, K. Kiuchi, and S. Fujibayashi, "Constraint on the maximum mass of neutron stars using GW170817 event", *Phys. Rev. D*, vol. 100, no. 2, 023015, p. 023 015, Jul. 2019. DOI: 10.1103/PhysRevD.100.023015. arXiv: 1905.03656 [astro-ph.HE].

[114] A. Nathanail, E. R. Most, and L. Rezzolla, "GW170817 and GW190814: Tension on the Maximum Mass", *Astrophys. J. Lett.*, vol. 908, no. 2, L28, p. L28, Feb. 2021. DOI: 10.3847/2041-8213/abdfc6. arXiv: 2101.01735 [astro-ph.HE].

[115] B. D. Metzger and R. Fernández, "Red or blue? A potential kilonova imprint of the delay until black hole formation following a neutron star merger", *Mon. Not. R. Astron. Soc.*, vol. 441, pp. 3444–3453, Jul. 2014. DOI: 10.1093/mnras/stu802. arXiv: 1402.4803 [astro-ph.HE].

[116] B. D. Metzger, "The Kilonova Handbook", *ArXiv e-prints*, Oct. 2016. arXiv: 1610.09381 [astro-ph.HE].

[117] ——, "Kilonovae", *Living Reviews in Relativity*, vol. 20, 3, p. 3, May 2017. DOI: 10.1007/s41114-017-0006-z. arXiv: 1610.09381 [astro-ph.HE].

[118] M. Zevin, M. Spera, C. P. L. Berry, and V. Kalogera, "Exploring the Lower Mass Gap and Unequal Mass Regime in Compact Binary Evolution", *arXiv e-prints*, arXiv:2006.14573, arXiv:2006.14573, Jun. 2020. arXiv: 2006.14573 [astro-ph.HE].

[119] T. Ertl, S. E. Woosley, T. Sukhbold, and H. .-. Janka, "The Explosion of Helium Stars Evolved with Mass Loss", *Astrophys. J.*, vol. 890, no. 1, 51, p. 51, Feb. 2020. DOI: 10.3847/1538-4357/ab6458. arXiv: 1910.01641 [astro-ph.HE].

[120] J. Alsing, H. O. Silva, and E. Berti, "Evidence for a maximum mass cut-off in the neutron star mass distribution and constraints on the equation of state", *Mon. Not. R. Astron. Soc.*, vol. 478, no. 1, pp. 1377–1391, Jul. 2018. DOI: 10.1093/mnras/sty1065. arXiv: 1709.07889 [astro-ph.HE].

[121] M. Agathos, F. Zappa, S. Bernuzzi, A. Perego, M. Breschi, and D. Radice, "Inferring prompt black-hole formation in neutron star mergers from gravitational-wave data", *Phys. Rev. D*, vol. 101, no. 4, 044006, p. 044 006, Feb. 2020. DOI: 10.1103/PhysRevD.101.044006. arXiv: 1908.05442 [gr-qc].

[122] A. Bauswein, S. Blacker, V. Vijayan, N. Stergioulas, K. Chatziioannou, J. A. Clark, N.-U. F. Bastian, D. B. Blaschke, M. Cierniak, and T. Fischer, "Equation of state constraints from the threshold binary mass for prompt collapse of neutron star mergers", *arXiv e-prints*, arXiv:2004.00846, arXiv:2004.00846, Apr. 2020. arXiv: 2004.00846 [astro-ph.HE].

[123] R. Kashyap, A. Das, D. Radice, S. Padamata, A. Prakash, D. Logoteta, A. Perego, D. A. Godzieba, S. Bernuzzi, I. Bombaci, F. J. Fattoyev, B. T. Reed, and A. da Silva Schneider, "Numerical relativity simulations of prompt collapse mergers: threshold mass and phenomenological constraints on neutron star properties after GW170817", *arXiv e-prints*, arXiv:2111.05183, arXiv:2111.05183, Nov. 2021. arXiv: 2111.05183 [astro-ph.HE].

[124] A. Bauswein, S. Blacker, G. Lioutas, T. Soultanis, V. Vijayan, and N. Stergioulas, "Systematics of prompt black-hole formation in neutron star mergers", *Phys. Rev. D*, vol. 103, no. 12, 123004, p. 123 004, Jun. 2021. DOI: 10.1103/PhysRevD.103.123004. arXiv: 2010.04461 [astro-ph.HE].

[125] S. Blacker, N.-U. F. Bastian, A. Bauswein, D. B. Blaschke, T. Fischer, M. Oertel, T. Soultanis, and S. Typel, "Constraining the onset density of the hadron-quark phase transition with gravitational-wave observations", *arXiv e-prints*, arXiv:2006.03789, arXiv:2006.03789, Jun. 2020. arXiv: 2006.03789 [astro-ph.HE].

[126] C. Ecker and L. Rezzolla, "A general, scale-independent description of the sound speed in neutron stars", Jul. 2022. arXiv: 2207.04417 [gr-qc].

[127] ——, "Impact of Mass Constraints on Neutron Star Properties ", in preparation, 2022.

[128] S. Altiparmak, C. Ecker, and L. Rezzolla, "On the Sound Speed in Neutron Stars", *ApJL, in press*, arXiv:2203.14974, arXiv:2203.14974, Mar. 2022. arXiv: 2203.14974 [astro-ph.HE].

[129] T. Demircik, C. Ecker, and M. Järvinen, "Dense and Hot QCD at Strong Coupling", *Phys. Rev. X*, vol. 12, no. 4, p. 041 012, 2022. DOI: 10.1103/PhysRevX.12.041012. arXiv: 2112.12157 [hep-ph].

[130] J. Wheeler, "Geometrodynamics and the issue of the final state.", in *Relativity, Groups, and Topology (Les Houches, France, 1964)*, C. DeWitt and B. DeWitt, Eds., New York: Gordon and Breach, 1964, pp. 316–520.

[131] W. Tichy, "The initial value problem as it relates to numerical relativity", *Reports on Progress in Physics*, vol. 80, no. 2, 026901, p. 026 901, Feb. 2017. DOI: 10.1088/1361-6633/80/2/026901. arXiv: 1610.03805 [gr-qc].

[132] W. Tichy, "Initial data for binary neutron stars with arbitrary spins", *Phys. Rev. D*, vol. 84, no. 2, 024041, p. 024 041, Jul. 2011. DOI: 10.1103/PhysRevD.84.024041. arXiv: 1107.1440 [gr-qc].

[133] H. P. Pfeiffer *et al.*, "Reducing orbital eccentricity in binary black hole simulations", *Class. Quantum Grav.*, vol. 24, S59–S82, 2007. DOI: 10.1088/0264-9381/24/12/S06. arXiv: gr-qc/0702106.

[134] M. Emma, F. Schianchi, F. Pannarale, V. Sagun, and T. Dietrich, "Numerical Simulations of Dark Matter Admixed Neutron Star Binaries", Jun. 2022. arXiv: 2206.10887 [gr-qc].

[135] B. Wardell, I. Hinder, and E. Bentivegna, *Simulation of GW150914 binary black hole merger using the Einstein Toolkit*, Zenodo, Sep. 2016. DOI: 10.5281/zenodo.155394. [Online]. Available: https://doi.org/10.5281/zenodo.155394.

[136] I. Hinder and et al., "Error-analysis and comparison to analytical models of numerical waveforms produced by the NRAR Collaboration", *Class. Quantum Grav.*, vol. 31, no. 2, 025012, p. 025 012, Jan. 2013. DOI: 10.1088/0264-9381/31/2/025012. arXiv: 1307.5307 [gr-qc].

[137] H. Togashi, K. Nakazato, Y. Takehara, S. Yamamuro, H. Suzuki, and M. Takano, "Nuclear equation of state for core-collapse supernova simulations with realistic nuclear forces", *Nucl. Phys.*, vol. A961, pp. 78–105, 2017. DOI: 10.1016/j.nuclphysa.2017.02.010. arXiv: 1702.05324 [nucl-th].

[138] F. Foucart *et al.*, "High-accuracy waveforms for black hole-neutron star systems with spinning black holes", Oct. 2020. arXiv: 2010.14518 [gr-qc].

[139] S. Banik, M. Hempel, and D. Bandyopadhyay, "New Hyperon Equations of State for Supernovae and Neutron Stars in Density-dependent Hadron Field Theory", *Astrohys. J. Suppl.*, vol. 214, 22, p. 22, Oct. 2014. DOI: 10.1088/0067-0049/214/2/22. arXiv: 1404.6173 [astro-ph.HE].

[140] S. Bernuzzi, A. Nagar, S. Balmelli, T. Dietrich, and M. Ujevic, "Quasiuniversal Properties of Neutron Star Mergers", *Phys. Rev. Lett.*, vol. 112, no. 20, 201101, p. 201 101, May 2014. DOI: 10.1103/PhysRevLett.112.201101. arXiv: 1402.6244 [gr-qc].

[141] T. Dietrich, S. Bernuzzi, M. Ujevic, and B. Brügmann, "Numerical relativity simulations of neutron star merger remnants using conservative mesh refinement", *Phys. Rev. D*, vol. 91, no. 12, 124041, p. 124 041, Jun. 2015. DOI: 10.1103/PhysRevD.91.124041. arXiv: 1504.01266 [gr-qc].

[142] T. Dietrich, S. Bernuzzi, and W. Tichy, "Closed-form tidal approximants for binary neutron star gravitational waveforms constructed from high-resolution numerical relativity simulations", *Phys. Rev. D*, vol. 96, no. 12, 121501, p. 121 501, Dec. 2017. DOI: 10.1103/PhysRevD.96.121501. arXiv: 1706.02969 [gr-qc].

[143] E. R. Most, L. Jens Papenfort, V. Dexheimer, M. Hanauske, H. Stoecker, and L. Rezzolla, "On the deconfinement phase transition in neutron-star mergers", *European Physical Journal A*, vol. 56, no. 2, 59, p. 59, Feb. 2020. DOI: 10.1140/epja/s10050-020-00073-4. arXiv: 1910.13893 [astro-ph.HE].

[144] V. Paschalidis, W. E. East, F. Pretorius, and S. L. Shapiro, "One-arm spiral instability in hypermassive neutron stars formed by dynamical-capture binary neutron star mergers", *Phys. Rev. D*, vol. 92, no. 12, 121502, p. 121 502, Dec. 2015. DOI: 10.1103/PhysRevD.92.121502. arXiv: 1510.03432 [astro-ph.HE].

[145] W. E. East, V. Paschalidis, and F. Pretorius, "Equation of state effects and one-arm spiral instability in hypermassive neutron stars formed in eccentric neutron star mergers", *Classical and Quantum Gravity*, vol. 33, no. 24, 244004, p. 244 004, Dec. 2016. DOI: 10.1088/0264-9381/33/24/244004. arXiv: 1609.00725 [astro-ph.HE].

[146] L. Lehner, S. L. Liebling, C. Palenzuela, and P. M. Motl, "m =1 instability and gravitational wave signal in binary neutron star mergers", *Phys. Rev. D*, vol. 94, no. 4, 043003, p. 043 003, Aug. 2016. DOI: 10.1103/PhysRevD.94.043003. arXiv: 1605.02369 [gr-qc].

[147] D. Radice, S. Bernuzzi, and C. D. Ott, "One-armed spiral instability in neutron star mergers and its detectability in gravitational waves", *Phys. Rev. D*, vol. 94, no. 6, 064011, p. 064 011, Sep. 2016. DOI: 10.1103/PhysRevD.94.064011. arXiv: 1603.05726 [gr-qc].

[148] V. Nedora, S. Bernuzzi, D. Radice, A. Perego, A. Endrizzi, and N. Ortiz, "Spiral-wave Wind for the Blue Kilonova", *Astrophys. J. Lett.*, vol. 886, no. 2, L30, p. L30, Dec. 2019. DOI: 10.3847/2041-8213/ab5794. arXiv: 1907.04872 [astro-ph.HE].

[149] K. Takami, L. Rezzolla, and L. Baiotti, "Constraining the Equation of State of Neutron Stars from Binary Mergers", *Phys. Rev. Lett.*, vol. 113, no. 9, 091104, p. 091 104, Aug. 2014. DOI: 10.1103/PhysRevLett.113.091104. arXiv: 1403.5672 [gr-qc].

[150] A. Bauswein, H.-T. Janka, K. Hebeler, and A. Schwenk, "Equation-of-state dependence of the gravitational-wave signal from the ring-down phase of neutron-star mergers", *Phys. Rev. D*, vol. 86, no. 6, 063001, p. 063 001, Sep. 2012. DOI: 10.1103/PhysRevD.86.063001. arXiv: 1204.1888 [astro-ph.SR].

[151] S. Bernuzzi, A. Nagar, T. Dietrich, and T. Damour, "Modeling the Dynamics of Tidally Interacting Binary Neutron Stars up to the Merger", *Phys. Rev. Lett.*, vol. 114, no. 16, 161103, p. 161 103, Apr. 2015. DOI: 10.1103/PhysRevLett.114.161103. arXiv: 1412.4553 [gr-qc].

[152] C. Palenzuela, S. L. Liebling, D. Neilsen, L. Lehner, O. L. Caballero, E. O'Connor, and M. Anderson, "Effects of the microphysical equation of state in the mergers of magnetized neutron stars with neutrino cooling", *Phys. Rev. D*, vol. 92, no. 4, 044045, p. 044 045, Aug. 2015. DOI: 10.1103/PhysRevD.92.044045. arXiv: 1505.01607 [gr-qc].

[153] L. Rezzolla and K. Takami, "Gravitational-wave signal from binary neutron stars: A systematic analysis of the spectral properties", *Phys. Rev. D*, vol. 93, no. 12, 124051, p. 124 051, Jun. 2016. DOI: 10.1103/PhysRevD.93.124051. arXiv: 1604.00246 [gr-qc].

[154] N. T. Bishop and L. Rezzolla, "Extraction of gravitational waves in numerical relativity", *Living Reviews in Relativity*, vol. 19, 2, p. 2, Oct. 2016. DOI: 10.1007/s41114-016-0001-9. arXiv: 1606.02532 [gr-qc].

[155] D. Grossman, O. Korobkin, S. Rosswog, and T. Piran, "The long-term evolution of neutron star merger remnants - II. Radioactively powered transients", *Mon. Not. R. Astron. Soc.*, vol. 439, pp. 757–770, Mar. 2014. DOI: 10.1093/mnras/stt2503. arXiv: 1307.2943 [astro-ph.HE].

[156] R. T. Wollaeger, O. Korobkin, C. J. Fontes, S. K. Rosswog, W. P. Even, C. L. Fryer, J. Sollerman, A. L. Hungerford, D. R. van Rossum, and A. B. Wollaber, "Impact of ejecta morphology and composition on the electromagnetic signatures of neutron star mergers", *Mon. Not. R. Astron. Soc.*, vol. 478, pp. 3298–3334, Aug. 2018. DOI: 10.1093/mnras/sty1018. arXiv: 1705.07084 [astro-ph.HE].

[157] L. Rezzolla and K. Takami, "Black-hole production from ultrarelativistic collisions", *Class. Quantum Grav.*, vol. 30, no. 1, p. 012 001, Jan. 2013. DOI: 10.1088/0264-9381/30/1/012001. arXiv: 1209.6138 [gr-qc].

[158] C. Breu and L. Rezzolla, "Maximum mass, moment of inertia and compactness of relativistic stars", *Mon. Not. R. Astron. Soc.*, vol. 459, pp. 646–656, Jun. 2016. DOI: 10.1093/mnras/stw575. arXiv: 1601.06083 [gr-qc].

[159] L. J. Papenfort, S. D. Tootle, E. R. Most, and L. Rezzolla, "Impact of extreme spins on the postmerger observables of high-mass binary neutron stars near prompt collapse", *to be submitted to MNRAS*, Sep. 2021.

[160] L. R. Weih, E. R. Most, and L. Rezzolla, "On the stability and maximum mass of differentially rotating relativistic stars", *Mon. Not. R. Astron. Soc.*, vol. 473, pp. L126–L130, Jan. 2018. DOI: 10.1093/mnrasl/slx178. arXiv: 1709.06058 [gr-qc].

[161] J. García-Bellido, A. Linde, and D. Wands, "Density perturbations and black hole formation in hybrid inflation", *Phys. Rev. D*, vol. 54, pp. 6040–6058, 10 Nov. 1996. DOI: 10.1103/PhysRevD.54.6040. [Online]. Available: https://link.aps.org/doi/10.1103/PhysRevD.54.6040.

[162] H. T. Cromartie, E. Fonseca, S. M. Ransom, P. B. Demorest, Z. Arzoumanian, H. Blumer, P. R. Brook, M. E. DeCesar, T. Dolch, J. A. Ellis, R. D. Ferdman, E. C. Ferrara, N. Garver-Daniels, P. A. Gentile, M. L. Jones, M. T. Lam, D. R. Lorimer, R. S. Lynch, M. A. McLaughlin, C. Ng, D. J. Nice, T. T. Pennucci, R. Spiewak, I. H. Stairs, K. Stovall, J. K. Swiggum, and W. W. Zhu, "Relativistic Shapiro delay measurements of an extremely massive millisecond pulsar", *Nature Astronomy*, vol. 4, pp. 72–76, Jan. 2020. DOI: 10.1038/s41550-019-0880-2. arXiv: 1904.06759 [astro-ph.HE].

[163] H. Falcke and L. Rezzolla, "Fast radio bursts: the last sign of supramassive neutron stars", *Astron. Astrophys.*, vol. 562, A137, A137, Feb. 2014. DOI: 10.1051/0004-6361/201321996. arXiv: 1307.1409 [astro-ph.HE].

[164] K. Taniguchi, T. W. Baumgarte, J. A. Faber, and S. L. Shapiro, "Black hole-neutron star binaries in general relativity: Effects of neutron star spin", *Phys. Rev. D*, vol. 72, p. 044 008, 2005. DOI: 10.1103/PhysRevD.72.044008. eprint: arXiv:astro-ph/0505450.

[165] L. Rezzolla and O. Zanotti, *Relativistic Hydrodynamics*. Oxford, UK: Oxford University Press, 2013, ISBN: 9780198528906. DOI: 10.1093/acprof:oso/9780198528906.001.0001.

[166] F. Foucart, T. Hinderer, and S. Nissanke, "Remnant baryon mass in neutron star-black hole mergers: Predictions for binary neutron star mimickers and rapidly spinning black holes", *Phys. Rev. D*, vol. 98, no. 8, 081501, p. 081 501, Oct. 2018. DOI: 10.1103/PhysRevD.98.081501. arXiv: 1807.00011 [astro-ph.HE].

[167] F. Foucart, M. B. Deaton, M. D. Duez, E. O'Connor, C. D. Ott, R. Haas, L. E. Kidder, H. P. Pfeiffer, M. A. Scheel, and B. Szilagyi, "Neutron star-black hole mergers with a nuclear equation of state and neutrino cooling: Dependence in the binary parameters", *Phys. Rev. D*, vol. 90, no. 2, 024026, p. 024 026, Jul. 2014. DOI: 10.1103/PhysRevD.90.024026. arXiv: 1405.1121 [astro-ph.HE].

[168] B. D. Metzger, A. Bauswein, S. Goriely, and D. Kasen, "Neutron-powered precursors of kilonovae", *Mon. Not. R. Astron. Soc.*, vol. 446, pp. 1115–1120, Jan. 2015. DOI: 10.1093/mnras/stu2225. arXiv: 1409.0544 [astro-ph.HE].

[169] E. Troja, H. van Eerten, B. Zhang, G. Ryan, L. Piro, R. Ricci, B. O'Connor, M. H. Wieringa, S. B. Cenko, and T. Sakamoto, "A thousand days after the merger: Continued X-ray emission from GW170817", *Mon. Not. R. Astron. Soc.*, vol. 498, no. 4, pp. 5643–5651, Oct. 2020. DOI: 10.1093/mnras/staa2626. arXiv: 2006.01150 [astro-ph.HE].

[170] A. Akmal, V. R. Pandharipande, and D. G. Ravenhall, "Equation of state of nucleon matter and neutron star structure", *Phys. Rev. C*, vol. 58, no. 3, pp. 1804–1828, Sep. 1998. DOI: 10.1103/PhysRevC.58.1804. arXiv: nucl-th/9804027 [nucl-th].

[171] M. Hempel and J. Schaffner-Bielich, "Statistical Model for a Complete Supernova Equation of State", *Nucl. Phys. A*, vol. 837, pp. 210–254, 2010. DOI: 10.1016/j.nuclphysa.2010.02.010. arXiv: 0911.4073 [nucl-th].

[172] K. Hebeler, J. M. Lattimer, C. J. Pethick, and A. Schwenk, "Equation of state and neutron star properties constrained by nuclear physics and observation", *Astrophys. J.*, vol. 773, p. 11, 2013. DOI: 10.1088/0004-637X/773/1/11. arXiv: 1303.4662 [astro-ph.SR].

[173] E. S. Fraga, A. Kurkela, and A. Vuorinen, "Interacting Quark Matter Equation of State for Compact Stars", *Astrophys. J. Lett.*, vol. 781, L25, p. L25, Feb. 2014. DOI: 10.1088/2041-8205/781/2/L25. arXiv: 1311.5154 [nucl-th].

[174] H. T. Cromartie *et al.*, "Relativistic Shapiro delay measurements of an extremely massive millisecond pulsar", *Nature Astron.*, vol. 4, no. 1, pp. 72–76, 2019. DOI: 10.1038/s41550-019-0880-2. arXiv: 1904.06759 [astro-ph.HE].

[175] E. Fonseca *et al.*, "Refined Mass and Geometric Measurements of the High-mass PSR J0740+6620", *Astrophys. J. Lett.*, vol. 915, no. 1, p. L12, 2021. DOI: 10.3847/2041-8213/ac03b8. arXiv: 2104.00880 [astro-ph.HE].

[176] T. E. Riley *et al.*, "A $NICER$ View of PSR J0030+0451: Millisecond Pulsar Parameter Estimation", *Astrophys. J. Lett.*, vol. 887, no. 1, p. L21, 2019. DOI: 10.3847/2041-8213/ab481c. arXiv: 1912.05702 [astro-ph.HE].

[177] M. C. Miller *et al.*, "PSR J0030+0451 Mass and Radius from $NICER$ Data and Implications for the Properties of Neutron Star Matter", *Astrophys. J. Lett.*, vol. 887, no. 1, p. L24, 2019. DOI: 10.3847/2041-8213/ab50c5. arXiv: 1912.05705 [astro-ph.HE].

[178] J. Nättilä, M. C. Miller, A. W. Steiner, J. J. E. Kajava, V. F. Suleimanov, and J. Poutanen, "Neutron star mass and radius measurements from atmospheric model fits to X-ray burst cooling tail spectra", *Astron. Astrophys.*, vol. 608, A31, 2017. DOI: 10.1051/0004-6361/201731082. arXiv: 1709.09120 [astro-ph.HE].

[179] M. C. Miller *et al.*, "The Radius of PSR J0740+6620 from NICER and XMM-Newton Data", *Astrophys. J. Lett.*, vol. 918, no. 2, p. L28, 2021. DOI: 10.3847/2041-8213/ac089b. arXiv: 2105.06979 [astro-ph.HE].

[180] T. E. Riley *et al.*, "A NICER View of the Massive Pulsar PSR J0740+6620 Informed by Radio Timing and XMM-Newton Spectroscopy", *Astrophys. J. Lett.*, vol. 918, no. 2, p. L27, 2021. DOI: 10.3847/2041-8213/ac0a81. arXiv: 2105.06980 [astro-ph.HE].

[181] *Compose website*, https://compose.obspm.fr/.

[182] G. Veneziano, "Some Aspects of a Unified Approach to Gauge, Dual and Gribov Theories", *Nucl. Phys. B*, vol. 117, pp. 519–545, 1976. DOI: 10.1016/0550-3213(76)90412-0.

[183] ——, "U(1) Without Instantons", *Nucl. Phys. B*, vol. 159, pp. 213–224, 1979. DOI: 10.1016/0550-3213(79)90332-8.

[184] M. Panero, "Thermodynamics of the QCD plasma and the large-N limit", *Phys. Rev. Lett.*, vol. 103, p. 232 001, 2009. DOI: 10.1103/PhysRevLett.103.232001. arXiv: 0907.3719 [hep-lat].

[185] T. Alho, M. Jarvinen, K. Kajantie, E. Kiritsis, and K. Tuominen, "Quantum and stringy corrections to the equation of state of holographic QCD matter and the nature of the chiral transition", *Phys. Rev. D*, vol. 91, no. 5, p. 055 017, 2015. DOI: 10.1103/PhysRevD.91.055017. arXiv: 1501.06379 [hep-ph].

[186] N. Jokela, M. Järvinen, and J. Remes, "Holographic QCD in the Veneziano limit and neutron stars", *JHEP*, vol. 03, p. 041, 2019. DOI: 10.1007/JHEP03(2019)041. arXiv: 1809.07770 [hep-ph].

[187] L. R. Weih, M. Hanauske, and L. Rezzolla, "Postmerger Gravitational-Wave Signatures of Phase Transitions in Binary Mergers", *Phys. Rev. Lett.*, vol. 124, no. 17, p. 171 103, 2020. DOI: 10.1103/PhysRevLett.124.171103. arXiv: 1912.09340 [gr-qc].

[188] M. Alcubierre, "Introduction to 3+1 numerical relativity", *Introduction to 3+1 Numerical Relativity*, Apr. 2006. DOI: 10.1093/acprof:oso/9780199205677.001.0001.

[189] C. Reisswig, C. D. Ott, U. Sperhake, and E. Schnetter, "Gravitational wave extraction in simulations of rotating stellar core collapse", *Phys. Rev. D*, vol. 83, no. 6, 064008, p. 064 008, Mar. 2011. DOI: 10.1103/PhysRevD.83.064008. arXiv: 1012.0595 [gr-qc].

[190] B. P. Abbott *et al.*, "GW170817: Observation of Gravitational Waves from a Binary Neutron Star Inspiral", *Phys. Rev. Lett.*, vol. 119, no. 16, p. 161 101, 2017. DOI: 10.1103/PhysRevLett.119.161101. arXiv: 1710.05832 [gr-qc].

[191] G. Ghirlanda *et al.*, "Compact radio emission indicates a structured jet was produced by a binary neutron star merger", *Science*, vol. 363, p. 968, 2019. DOI: 10.1126/science.aau8815. arXiv: 1808.00469 [astro-ph.HE].

[192] K. Takami, L. Rezzolla, and L. Baiotti, "Constraining the Equation of State of Neutron Stars from Binary Mergers", *Phys. Rev. Lett.*, vol. 113, no. 9, p. 091 104, 2014. DOI: 10.1103/PhysRevLett.113.091104. arXiv: 1403.5672 [gr-qc].

[193] Y. Sekiguchi, K. Kiuchi, K. Kyutoku, and M. Shibata, "Effects of hyperons in binary neutron star mergers", *Phys. Rev. Lett.*, vol. 107, p. 211 101, 2011. DOI: 10.1103/PhysRevLett.107.211101. arXiv: 1110.4442 [astro-ph.HE].

[194] D. Radice, S. Bernuzzi, W. Del Pozzo, L. F. Roberts, and C. D. Ott, "Probing Extreme-Density Matter with Gravitational Wave Observations of Binary Neutron Star Merger Remnants", *Astrophys. J. Lett.*, vol. 842, no. 2, p. L10, 2017. DOI: 10.3847/2041-8213/aa775f. arXiv: 1612.06429 [astro-ph.HE].

[195] A. Bauswein, N.-U. F. Bastian, D. B. Blaschke, K. Chatziioannou, J. A. Clark, T. Fischer, and M. Oertel, "Identifying a first-order phase transition in neutron star mergers through gravitational waves", *Phys. Rev. Lett.*, vol. 122, no. 6, p. 061 102, 2019. DOI: 10.1103/PhysRevLett.122.061102. arXiv: 1809.01116 [astro-ph.HE].

[196] S. Mukherjee, N. K. Johnson-McDaniel, W. Tichy, and S. L. Liebling, "Conformally curved initial data for charged, spinning black hole binaries on arbitrary orbits", Feb. 2022. arXiv: 2202.12133 [gr-qc].

[197] *Geometrized unit system*. [Online]. Available: https://en.wikipedia.org/wiki/Geometrized_unit_system.

[198] L. Blanchet, "Gravitational Radiation from Post-Newtonian Sources and Inspiralling Compact Binaries", *Living Reviews in Relativity*, vol. 17, 2, p. 2, Feb. 2014. DOI: 10.12942/lrr-2014-2. arXiv: 1310.1528 [gr-qc].